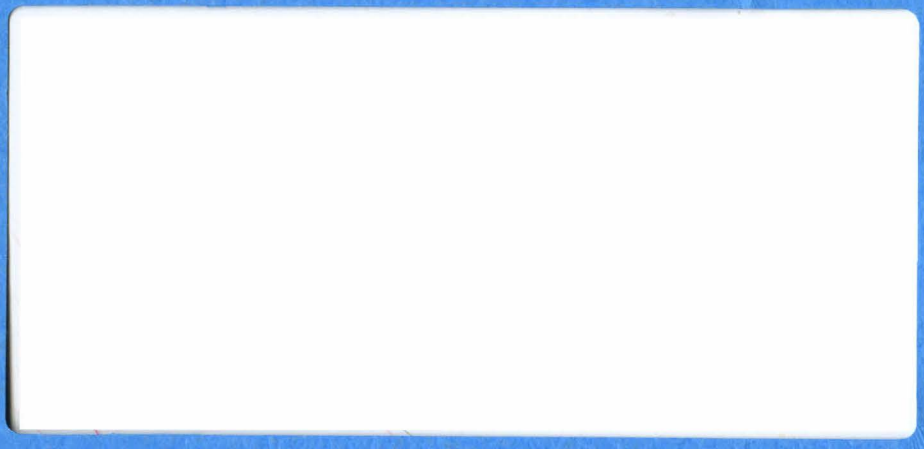

CALIFORNIA INSTITUTE OF TECHNOLOGY

PASADENA, CALIFORNIA

EXPERIMENTAL STUDY OF UNSTEADY HYDRODYNAMIC FORCE MATRICES ON WHIRLING CENTRIFUGAL PUMP IMPELLERS

Belgacem Jery
Division of Engineering and Applied Science
1987

Report No. 200.22

on

Contract NAS 8-33108

EXPERIMENTAL STUDY OF UNSTEADY HYDRODYNAMIC FORCE MATRICES ON WHIRLING CENTRIFUGAL PUMP IMPELLERS

Thesis by

Belgacem Jery

Division of Engineering and Applied Science

In partial fulfillment

of the Requirements for the Degree of

Doctor of Philosophy

California Institute of Technology

Pasadena, California

1987

(Submitted October 31, 1985)

ACKNOWLEDGEMENTS

I would like to express my deepest thanks to my advisors, Professors Christopher Brennen, Allan Acosta and Thomas Caughey. Not only did they provide me with the best technical assistance but they also expressed friendship and genuine concern for my welfare during the years of my education.

The help of several other people was instrumental in the success of various phases of this experimental work. I am particularly indebted to Dr. Haskell Shapiro from Shapiro Scientific Instruments, Corona Del Mar, California, for his assistance in the design of various electronic systems. Among the personnel of the Institute's Central Engineering Services my thanks go to N. Keidel, L. Johnson, G. Yamamota and M. Gerfen for their expert help with the design and construction of most of the mechanical components. Thanks also to G. Lundgren from the Aeronautics shop for directing the delicate task of machining the rotating dynamometer. Just as delicate was the task of instrumenting this dynamometer, which was successfully carried out by J. Hall from Microengineering II, Upland, CA. Thanks for many years of reliable operation.

Thousands of hours were spent preparing the test rig and collecting data from the various experiments. Many of these hours were contributed by student colleagues and friends D. Adkins, R. Franz, N. Arndt, W. Goda, D. Brennen, S. Moriarty, M. Karyeaclis and P. Chen. I very much appreciated their efforts. The help of C. Lin with the graphics and S. Berkeley with the administrative tasks was also greatly appreciated.

It takes substantial financial support to bring to term an experimental project of this magnitude. This support was generously provided by NASA's George C. Marshall Space Flight Center, Huntsville, Alabama. My advisors and I are very thankful for it. Rocketdyne Division of Rockwell International, Canoga Park, CA, provided a diffuser volute and half an SSME's HPOTP's double suction impeller for testing. Byron-Jackson Pumps Division of Borg-Warner Industrial Products Corp., Long Beach, CA, offered two test impellers. We are very grateful for these contributions.

My personal financial needs were met through a grant from the Foundation ENSAM, a scholarship from the Scientific Mission of Tunisia, a Graduate Research Assistantship from the California Istitute of Technology and a Research Fellowship from Byron-Jackson Pumps Division. I am forever indebted to all these sources.

Some contributions are hard to describe with words, let alone quantifiy. These came from my family and close friends whose love, patience and encouragement meant so much to me. I say: thank you all for being there when I needed you most.

This thesis is dedicated to my mother and father Fatma and Ammar, who never had a chance to learn how to read or write, but who taught me so much.

ABSTRACT

An experimental facility was constructed and instrumented. A study was conducted on a set of centrifugal flow pumps whose impellers were made to follow a controlled circular whirl motion. The aim was to characterize the steady and unsteady fluid forces measured on the impeller under various pump operating conditions. The postulation was that the unsteady lateral forces result from interactions between the impeller and the surrounding diffuser and or volute (via the working fluid), and that under certain flow regimes these forces can drive unstable lateral motions of the pump rotor.

The lateral hydrodynamic forces were decomposed into their steady and unsteady parts, the latter being further expressed in terms of a generalized fluid stiffness matrix. A study of this matrix as a function of the whirl to pump speed ratio supported the following chief conclusions:

i) the common assumption of matrix skew-symmetry is justified;

ii) the magnitudes and signs of the matrix elements are such that rotor whirl can indeed be caused by the hydrodynamic forces, in pumps operated well above their first critical speed,

iii) as expected, the matrix is very sensitive to the value of the flow coefficient, especially at flow rates below the design;

iv) the commonly postulated quadratic variation of the matrix elements with the reduced whirl frequency, resulting in the so-called rotordynamic coefficients (stiffness, damping and inertia) is not justified for flow coefficients significantly below design; and

v) surprisingly, it was discovered that the presence, number and orientation of diffuser guide vanes have little effect on the forces.

Conclusions regarding the effect of impeller geometry could not be reached given the similarity of the tested designs. However, other results on phenomena such as skin friction and leakage flow are presented. Some of the findings are compared to experimental and theoretical data from other sources. Finally, the rotordynamic consequences of the results are discussed as the present data were applied by another author to the case of the Space Shuttle Main Engine's (SSME) High Pressure Oxidizer Turbopump (HPOTP).

TABLE OF CONTENTS

LIST OF SYMBOLS

a = side dimension of square cross sectional area of dynamometer's post

b_2 = impeller discharge width

$[A]$ = dimensionless hydrodynamic force matrix

$[C]$ = hydrodynamic damping matrix as defined by Eq. (1.8)

c = impeller face seal clearance, also volute ring clearance

$\{F\}$ = generalized six-component force vector

F_1, F_2 = components of instantaneous lateral force on impeller in the rotating dynamometer reference frame (1,2)

F_x, F_y = components of instantaneous lateral force on impeller in fixed laboratory reference frame (X,Y) non-dimensionalized by $\rho\pi r_2^3\omega^2 b_2$

F_{ox}, F_{oy} = values of F_x and F_y when impeller axis remains coincident with the origin of the (X,Y) coordinate system

F_N, F_T = components of lateral force on impeller normal to and tangential to the whirl orbit, non-dimensionalized by $\rho\pi r_2^3\omega^2 b_2\varepsilon$ and averaged over one whirl orbit

I, J = integers such that $\Omega = I\omega/J$

$[K]$ = hydrodynamic stiffness matrix as defined by Eq. (1.8)

$[M]$ = hyrodynamic inertia matrix as defined by Eq. (1.8)

N = pump rpm = $60\omega/2\pi$

r_2 = impeller discharge radius

t = time

x, y = instantaneous coordinates of impeller center in fixed laboratory reference frame, (X,Y), non-dimensionalized by r_2

$x, y, \dot{x}, \dot{y}$ = first and second time derivatives of impeller position non-dimensionalized using Impeller X's radius, r_2, and the time ω^{-1}

(X,Y) = fixed laboratory reference frame

ε = radius of circular whirl orbit

ρ = density of water

Φ = pump flow coefficient based on impeller discharge area and tip speed

Ψ = pump total head coefficient = total head rise $/\rho r_2^2 \omega^2$

ω = radian frequency of pump shaft rotation = $2\Pi N/60$

Ω = radian frequency of whirl motion = $I\omega/J$

LIST OF FIGURES

Appendix figures:

Tables:

CHAPTER 1

INTRODUCTION

Perhaps one of the most striking characteristics of modern turbomachine technology is the constant search for higher and higher power densities. This is especially true in space applications where payload considerations dictate severe weight and size limitations[1]. Since power is proportional to the square of the dimensions and to the cube of the velocity, the moving parts must be operated at extremely high speeds in order to achieve the required power levels, while maintaining compact size. At the same time, to be truly competitive, high performance turbomachines have to meet stringent cost effectiveness, efficency, reliability and safety requirements. Delicate compromises must usually be made in the various phases of the research and development process before the product is finally put in service. Unfortunately, it is not until then that the real problems start to manifest themselves. These are the kind that designers had no reason to anticipate and that component testing or even prototype testing could not reveal. This scenario is typical of cases where new design concepts and new materials are introduced, in an effort to take the state of the art a step higher. The literature abounds with reports of such instances.

An area of particular interest in this regard is that of rotordynamic instability problems and their relation to the fluid dynamics of pumping systems. These are the problems addressed by the present research work.

1.1 Presentation of the Problem:

Rotordynamic instabilities have been receiving ever increasing attention among designers, manufacturers and operators of high performance turbomachines. Although the days when the

[1] As an example, Appendix A summarizes the design and performance data of the turbomachinery in NASA's Space Shuttle Main Engines (SSME).

shaft first critical speed appeared to be an unsurmountable barrier are long gone[2], it remains true that rotor instabilities continue to dictate the most severe limitations on the performance of pumping systems. Difficulties such as rough running (noise and vibration), eccessive loads and wear on both stationary and rotating components, loss of performance (drop in head), and in some cases catastrophic failures, can often be caused by some kind of rotor vibration.

Most commonly, these vibrations are referred to as rotor "whirl" or "whip." Originally, the term rotor whirl was used by rotordynamicists to describe the lateral deflections of a rotating shaft. The term rotor whip is more specific to the terminology of turbomachine practitioners. It was originally used to describe turbomachine rotor vibrations inside oil and gas bearings, (oil whip and gas whip). It should be emphasized however, that both terms refer to lateral (transverse) vibrations only. Although other motions such as longitudinal (axial) or torsional (angular) vibrations have been encountered, and could account for some of the instability problems, a choice has been made to confine the scope of the present research work to the study of the lateral vibrations. Also, from here on, only the term rotor whirl will be used when referring to these vibrations.

In the remainder of this chapter, the terminology of rotor whirl is reviewed. Some prominent cases of whirl-related rotor instability problems that motivated this study are then described. A brief survey of analytical and experimental efforts aimed at understanding rotor instability symptoms, mechanisms and remedies is presented. Finally, the specific scope and goals of the present work are delineated.

1.2 Terminology of Rotor Whirl:

As far as rotordynamics is concerned, an ideal turbomachine is one in which the rotor centerline coincides with the machine axis of rotation at all times, irrespective of rotational speed or load distribution. This requires either that all structures (rotor and stator) be perfectly rigid, aligned and close fitted, or that all loads have a perfectly symmetric distribution. In practice, neither

---

[2] Gustave de Laval was first to demonstrate experimentally, in 1895, that a steam turbine was capable of sustained operation above the rotor's first critical speed (see Section 1.2 for definition of critical speed).

is ever the case. All real turbomachines operate with a certain amount of whirl [3] owing to dynamic rotor deflections generated , for instance, by inevitable imbalance forces. The question is : How much whirl is acceptable?

Theoretically, the ultimate limit is the minimum rotor deflection that would result in (i) damage to internal parts due to violation of radial clearances, or (ii) structural failure of the shaft. Whether this limit will be reached in any particular application depends only on (i) the ratios of rotor rotational speed to rotor critical speeds, and (ii) the net balance of excitative over dissipative forces at play.

Critical Speeds:

Most textbooks introduce the concept of critical speeds through the classical, idealized system sketched in Fig.1.1-top. A disk of mass m, concentrated at its center of gravity, G, is tied to a vertical, weightless shaft in such a way that the center G is a distance d from the shaft centerline, O. Neglecting gravity, and assuming that the shaft is rotated at a constant angular velocity, ω (rad/sec), the disk is in lateral equilibium under two transverse forces, acting at G:

(i) a centrifugal force equal to $m(\varepsilon+d)\omega^2$, where ε is the deflection of the shaft centerline away from the axis of rotation, O' (these two lines are one when the shaft is at rest), and

(ii) a restoring force proportional to the deflection ε, with a proportionality factor, K, that depends on the shaft dimensions, its material, method of support and load configuration. In this illustrative example $K=EI/l^3$; where E is the modulus of elasticity of the shaft material, I is the moment of inertia of the shaft, and l its length. Usually K is called the stiffness, spring constant or elastic constant.

As mentioned above, it is important to determine the relation between ε and ω. This is done by equating the two forces:

$$m(\varepsilon+d)\omega^2 = K\varepsilon \qquad (1.1)$$

which yields:

[3] By definition, whirl describes motion of a rotor combining both (i) pure rotation of the rotor around its deflected centerline, and (ii) random or organized excursions (in time and space) of this centerline around its undeflected position. Herein, the word whirl will sometimes be used to refer to the second motion alone.

$$\varepsilon = md\omega^2/(K-m\omega^2). \tag{1.2}$$

Thus, there is one particular value of ω for which ε becomes infinite, and the shaft should theoretically break. This value of ω, usually denoted ω_c, is by definition the critical angular velocity for that particular shaft, in that particular configuration. To this critical angular velocity corresponds a critical speed, n_c, in revolutions per minute. Clearly,

$$\omega_c = (K/m)^{1/2} \tag{1.3}$$

and

$$n_c = 30(K/m)^{1/2}/\Pi \tag{1.4}$$

from which one gets:

$$\varepsilon = \omega^2(\omega_c^2-\omega^2)d = n^2(n_c^2-n^2)d \tag{1.5}$$

which indicates that if the operating speed n goes above n_c , the deflection ε changes sign and decreases in magnitude. This is better illustrated by Fig.1.1-top, which adds important information about the phase angle between the centrifugal force vector and the bending plane. Namely, one notices that below the critical speed, the vector is in line with the bending plane (in an outwards direction), and at speeds above the critical it is 180^o ahead of the bending plane. When the speed is infinite, ε equals -d, and the center of mass G exchanges places with the center of rotation. At the critical speed, ε is infinite and the angle is not defined. Another very important observation is that the period of shaft rotation at the critical speed is identical to that of its natural or free transverse vibration.

Thus far, the candidate shaft has been a purely hypothetical one. What then becomes of the concept of critical speed in a real turbomachine?. In real life, gravity cannot be neglected and all masses and loads are distributed. Rotors may assume any position in space, they may have any type and number of supports, and any number of structural components. These components may be fastened to the rotor in various ways and may have different sizes, shapes and materials. They

may also be rubbing against stationary parts or be submerged in fluids having various viscous properties; and most importantly, be subjected to any type and configuration of loads, both steady and unsteady (gravitational, mechanical, thermal, fluid dynamic, etc...). How does one go about finding the critical speeds of such rotors?. A complete treatment of this question is obviously beyond the scope of this thesis. However, the following remarks may prove helpful in avoiding some of the common misconceptions about critical speeds.

First, it should be emphasized that, in theory, every turbomachine rotor, no matter how simple and well balanced, has an infinite number of critical speeds. Each of them corresponds to a particular mode of rotor transverse vibration. Furthermore, the exact values of these speeds are never known: solving the vibration problem for a non-homogeneous continuum with nonlinear properties is impossible.

In practice, the best one can hope for is an estimate of the first few most predominant modal frequencies. This estimate is usually obtained by solving a simplified vibration problem, in which the rotor and its supports are discretized and replaced by a system of masses, springs and dashpots. How good such an estimate is clearly depends on how realistic the mathematical modeling was. Particularly crucial is the evaluation of spring and dashpot coefficients. The role of phenomena such as viscous damping, hysteresis, friction and fluid-structure interactions has not yet been mastered, despite considerable efforts by the turbomachine community.

The most useful piece of information one gets from solving the simplified vibration problem is the value of the first critical speed. This is important since, by definition, this speed corresponds to the vibration mode in which the shaft undergoes maximum deflections[4]. However, a complete design study should use all computed critical speeds and mode shapes. Selection of the operating speed(s) is then subject to verification of the structural integrity of rotor and stator components under the expected loads.In particular, provision should be made for comfortable

[4] With the simplifications made, the problem ends up approaching theoretical textbook cases in which the number and shape of modes is determined by the number and relative arrangement of disks and supports. For example, a shaft freely supported at both ends and carrying two disks will have two vibration modes. In the first, the shaft's deflected shape resembles a bow. In the second, a vibration node (point of zero deflection) appears between the two disks and there are two bows, one on each side of the node.

margins between the frequencies of the dynamic loads and the rotor's own critical frequencies to account for design uncertainties and possible speed and load transients.

In practice, if all goes according to design, the rotor components and environment should provide enough damping to keep all but a few most predominant modes of vibration below perceptible levels. When regimes of operation take the rotor through one of these predominant modes, the lateral deflections are usually restrained by the close internal fits inside the machine.

Even in machines with no closely fitted internal parts, vibration energy can usually be dissipated due to internal friction of rotor material and external friction and damping from the surrounding medium. Strong vibration may be observed, but the structural integrity of rotor and stator components will not be menaced. It is important to realize that (i) mathematically, a critical speed is a point on both sides of which the rotor regains its ability to resist deflection, and (ii) when the rotor is merely traversing a critical speed (such as occurs during startup and shutdown), there is usually not enough time for the maximum deflection to develop.

Synchronous Versus Non-Synchronous Whirl:

A rotor need not be running at or very near one of its critical speeds, for whirl to be present. Let Ω denote the whirl frequency, ω the rotation frequency and ω_i the rotor i^{th} critical frequency. If $\Omega=\omega$, the whirl is said to be *synchronous*. If $\Omega\neq\omega$, the whirl is said to be non-synchronous (or asynchronous), *subsynchronous* when $\Omega<\omega$, and *supersynchronous* when $\Omega>\omega$. The theoretical example in Fig.1.1 was a bit misleading in the sense that whirl due to simple mass unbalance is inherently synchronous and hence only one frequency was needed to describe the motion.

In principle, all values of Ω are possible, sometimes several occurring simultaneously. So, not only does whirl not have to be synchronous, but also the whirl frequency does not have to coincide with one of the rotor's critical frequencies. Considered from a vibration point of view, synchronous whirl is simply a forced vibration problem in which the frequencies of the forcing functions can fall anywhere in the spectrum. In practice, however, excitations whose frequencies are coherent with one of the rotor's critical frequencies usually dominate (and are thus referred to as synchronous), owing to amplification of their effects through the phenomenon of resonance.

As a general rule, designers should avoid operating speeds close to an integer fraction or a multiple of one of the rotor's critical speeds (especially the first).

Forced Versus Self-Excited Whirl:

The excitatory forces responsible for synchronous whirl are inherently different from those responsible for non-synchronous whirl. The origins and mechanisms of action of both types will be discussed in more detail later. The focus here is mainly on the terminology. From a purely descriptive point of view, the two kinds of whirl differ in the way their frequency, amplitude, and direction are related to the rotor operating and critical speeds and to its direction of rotation.

Firstly, the frequency of forced whirl is synchronous with, or is a multiple or a rational fraction of, the frequency of the shaft rotation, whereas the frequency of self-excited whirl is independent of the latter and falls usually at or near one of the rotor critical frequencies[5]. Secondly, the amplitude of self-excited whirl is not perceptible until the rotor speed reaches a certain value (called Onset Speed of Instability, or O.S.I.), at which point it will suddenly rise. Above O.S.I. the amplitude growth rate is exponential at first, which means that the damping is negative and so is the logarithmic decrement[6]. As a result, internal machine clearances are sometimes violated before system non-linearities enter into play and a limit cycle is reached.

The amplitude of forced whirl, on the other hand, behaves in a more conventional manner. As in any forced vibration phenomenon, the amplitude peaks occur when there is resonance between the forcing frequency (in this case the rotation frequency or multiples or integral fractions thereof, as mentioned above) and the system's own natural frequency (rotor critical frequency). Finally, compared to the rotor concentric motion, the whirl (precession) motion can be either in the same direction or in the opposite direction. In the first case, the whirl motion is said to be *forward*,

---

[5] With the rotor running above its first critical, self-excited whirl usually "locks on" the first natural frequency, which makes it essentially subsynchronous.

[6] The logarithmic decrement (denoted δ) is usually supplied by manufacturers as a vibration characteristic of commercial units. By definition, $\delta=\log[(x(t)/x(t+T)]$, where $x(t)$ is the vibration amplitude at time t, and T is its period.

or *positive*. In the second, it is termed *backward*, *negative* or *reverse*. Forced whirl is always forward. Self-excited whirl is also mostly forward[7].

This concludes this section on the terminology of whirl. It should be clear at this point that, of the two types of rotor whirl, the forced one would be easier to predict and deal with. It is simply a case of classical forced vibration. Even if one fails to understand and eliminate the underlying forcing mechanisms, one can usually avoid strong vibrations (resonance) by proper selection of operating speed(s) and startup procedure.

The same cannot be said of self-excited whirl. Not only the underlying mechanisms are much less understood, making it harder to predict, but also once initiated, the motion is inherently unstable. Also, being non-synchronous, the whirl motion imposes continuous stress reversal on the rotor fibers (at the rate ω-Ω for forward whirl). Thus, it is no surprise to find that among the numerous cases of rotor instability problems reported by high performance turbomachine operators, the most severe and puzzling of them fit the description of self-excited whirl.

1.3 Cases of Rotor Instability Problems:

Over the past ten to fifteen years, the turbomachine community has become aware that serious fundamental problems stand in the way of higher performance levels. As hinted above, the most severe among these problems has been self-excited subsynchronous rotor whirl. Reports show that the machines affected cover such a wide range of applications and fields, including the space, nuclear and petroleum industries. Most of the case histories are now well publicized and need not be described in any detail. Following are brief summaries of a few representative cases. Attention should focus mainly on the conclusions drawn by those who investigated the incidents.

The SSME Turbopumps:

Both the High Pressure Fuel Turbopump (HPFTP) and the High Pressure Oxidizer Turbopump (HPOTP) of the Space Shuttle Main Engine (SSME) suffered from severe,

[7] A. Stodola was first to demonstrate experimentally that reverse synchronous precession is possible.

unexpected vibration problems. The HPFTP was designed to run between its second and third critical speeds (37,000 rpm at Full Power Level). During early engine tests, nonsynchronous rotor whirl became acute at speeds above 19,000 rpm; with accelerometer cutoff at around 22,000 rpm. In one case, "the characteristics of the vibration were remarkably consistent and were marked by a forward precession at less than shaft speed with bearing loads rapidly increasing in a nonlinear manner at a frequency typically 0.5 to 0.6 of the shaft speed until a destructive limit cycle was attained."

In another case, "the inception (of the whirl) occurred at a shaft speed of approximately twice the first critical speed, and the whirl frequency thereafter followed the critical speed of the system at approximately one-half the shaft speed." An extensive investigation was initiated, delaying the project for six months, at an estimated cost of nearly half a million dollars a day. Among the conclusions of the investigation were: (i) "in spite of the views of some optimists in the field of rotor instability, prediction of stability in a new design must be viewed with skepticism. A prediction of instability should, however, be taken very seriously" and (ii) " as much component testing as possible to define/confirm model parameters should be planned as part of a basic program" [51].

High Pressure Compressors:

High pressure compressors have also experienced whirl problems in which fluid dynamic effects may play a part. For example, for over seven months, full-load plant startup was delayed in the Chevron-owned Kaybob natural-gas plant. The problem was due to rotor instabilities in a set of nine-stage high pressure centrifugal compressors designed to operate just below their third critical speed [151].

The Phillips Petroleum Company faced similar rotor whirl problems in two of its installations. The first involved 15 MW eight-stage compressors used to boost gas pressure from 7 to 63 MPa, at the Ekofisk oilfield in the North Sea. The second incident occurred at the Hewett Gas Plant in England, and involved six identical 3 MW centrifugal compressors pumping gas from wells located 17 miles offshore. In both cases, valuable time was wasted before ad-hoc solutions were improvised and a major shortfall was averted. The author who documented the case had this final

comment: "I am certain that many improvements have been made, but there is need for many more. I hope that such improvements will be forthcoming because the need is great and the potential penalty very high" [47].

Feed Pumps:

In power stations, the single most critical component is the feed pump -whether a reactor feed pump in a Boiling-Water Reactor (BWR), a steam generator feed pump in a Pressurized Water Reactor (PWR), or a boiler feed pump in a conventional fossil-fuel plant. The Electric Power Research Institute (EPRI) has determined that feed pump failures were the cause of hundreds of power trip-outs [108]. A comprehensive study was conducted showing that "The hydraulic forces involved are very large -great enough, in fact, to fracture heavy metal components and to erode surfaces in pumps which would run for decades in less exacting fluid systems." Bearing and seal failures have been attributed to such high fluid forces.

The most pertinent conclusion of this study was that "specifying and realizing good performance at the Best Efficiency Point (BEP) is not sufficient protection against failures. Even specifying performance at two operating points adds little reliability. Needs for operating flexibility sooner or later will put the pump at an off-design flow rate where all of a unit's feed capacity can be destroyed within a few hours or even a few minutes."

Other Cases and Concluding Remarks:

These have been some of the most famous cases. The turbomachine literature abounds with reports on equally severe and costly incidents, albeit less well publicised. For instance, two out of four cases reported by Wachel [151] concerned steam turbines on which several modifications had to be made before nonsynchronous whirl was reduced to acceptable levels. In his introduction Wachel writes, "The threshold of instability can be fully defined only from testing over the full performance range of the machine, and even this approach is not always completely adequate. Some units have run satisfactorily for several years before serious instability trip-outs occurred. After one year of satisfactory operation, one compressor failed eight times in the next

three years from instabilities. Because the stability margin on some units is so delicately balanced, its characteristics can be drastically changed whenever small changes are made in factors such as pressure ratio, flow, bearing clearance, oil temperature, unbalance, alignment, etc., or upsets in the process such as liquid slugs, surge transients, or electrical trip-outs."

The list could continue for much longer. The one important fact that emerged from the investigations of these incidents was that the state of knowledge was not adequate enough. It could not satisfactorily explain all the facets of the problems encountered. Nor could it provide proper design guidelines that would assure trouble free operation. The seriousness of the situation prompted concerted efforts from turbomachine practioners, as witnessed by the numerous conferences, symposia and workshops that were subsequently organized.

The next section presents a brief assessment of the state of knowledge.

1.4 Survey of Current Knowledge:

This survey is not intended to be complete or exhaustive. The aim is simply to present an adequate picture of what was known about turbomachine rotor instabilities at the time the present research work was initiated (1978-79). The more recent contributions will be discussed in parallel with the results of the present investigation. Also, only some of the references listed will be quoted.

Consider the resultant, F(t), of the instantaneous lateral (in-plane) forces acting on the center of a turbomachine rotor running at an angular velocity, ω. Unless the rotor is infinitely rigid, or the value of this resultant is always zero (perfectly axi-symmetric loads), the center of the rotor, O, will be displaced an amount, $\varepsilon(t)$, away from its undeflected position, O' (see Fig. 1.2-top). *Whirling* motion will ensue in which the center, O, describes a path or orbit around O'. Relative to this orbit, the lateral force vector, $\underline{F}(t)$, can be separated into a normal component, $\underline{F}_N(t)$, and a tangential component, $\underline{F}_T(t)$; and so can the time derivative of the displacement vector, $\dot{\underline{\varepsilon}}(t)$ (i.e., the velocity vector). Rotordynamics (in the context of lateral whirl) is simply the study of the temporal

relationship between $\underline{F}(t)$ and $\underline{\varepsilon}(t)$. More specifically, the local stability of the whirl motion is determined by the directions of $F_N(t)$ and $F_T(t)$ relative to the normal and tangential velocity components, respectively[8]. When the force is in the direction of the velocity, its effect on the whirl motion is excitatory or aggravating. When the force opposes the velocity, the effect is dissipative or moderating.

In the case of forced whirl, the steady-state angular velocity of the whirl, Ω, is controlled by the frequency of the forcing mechanism. The steady-state amplitude of the whirl, ε, is strongly affected by the amount of damping present in the system and reaches its peaks at resonance. The simplest illustration is presented in Fig. 1.1-bottom. The model in this figure is identical to the one presented in Fig. 1.1-top, except for the addition of external damping. This damping introduces an important new feature represented by the change in the phase relation between the centrifugal force vector (the forcing vector) and the displacement vector, as described by the phase angle, β. Clearly, the tangential component of the lateral force is highest when the shaft rotation (i.e., the forcing mechanism) occurs at a frequency equal to the frequency of its transverse vibration. For this reason, additional damping may reduce the peak amplitude of vibration but will not affect its frequency.

In the case of self-excited whirl, damping plays a different role. However, it is important frist to understand that, in this case, the tangential force will not appear as long as the rotor is centered. In other words, self-excited whirl is not self-starting; it needs a starting mechanism. Thus, a better name for it would be "self-perpetuating" or "self-aggravating." In practice, the initial deflection is provided by any number of forcing mechanisms. The most common are static deflection, misalignment or pure mass unbalance of the rotor assembly. Once initiated, self-excited whirl is basically insensitive to damping. Additional damping can only delay (to a higher rotor speed) the transition to a destabilizing positive tangential force.

---

[8] The positive direction is defined to be radially outward for the normal component. For the tangential components it is defined as the direction of a tangential velocity that would result in positive whirl ($\Omega>0$, see Fig. 1.3).

Thus, it seems that the whirl problem can be circumvented either by sufficiently reducing the peak amplitude, or by sufficiently delaying the Onset Speed of Instability. All that is needed is enough damping in the system. Is this true, and if so, why is it that designers of turbomachines seem incapable of achieving either?.

The answer to the first part of this question is affirmative. The second part is best answered by the following facts:

(i) energy dissipated by damping is wasted energy which has to be supplied by the drive system,

(ii) in many applications, dampers can be too bulky, costly and hard to implement, especially if the initial design did not provide enough room for additions, bringing up a most important point, namely, that

(iii) in many high performance turbomachine designs, the instability mechanisms are either new and unexpected or, if known, insufficiently understood and prepared for.

For a turbomachine rotordynamic analysis to be successful, the designer needs to be aware of, and understand, all possible instability mechanisms applicable to the configuration and components at hand. Furthermore, data on the so-called rotordynamic coefficients must be available with enough accuracy for all the components involved (mechanical and other).

In its simplest linearized form, the equation of motion of the whirling rotor can be written as:

$$\underline{F}(t) = \underline{F}_0(t) + [A]\,\underline{\varepsilon}(t) \tag{1.6}$$

or, referred to the stationary (X,Y)-frame of Fig.1.2-top,

$$\begin{pmatrix} F_x(t) \\ F_y(t) \end{pmatrix} = \begin{pmatrix} F_{ox}(t) \\ F_{oy}(t) \end{pmatrix} + [\,A(?)\,] \begin{pmatrix} x(t) \\ y(t) \end{pmatrix} \tag{1.7}$$

where the lateral force vector components are assumed to be comprised of two parts: (i) a "fixed" part, which would be the only one present should the rotor be perfectly centered; and (ii) a part which is "proportional" to the displacement of the rotor center away from its undeflected position.

The fixed part is called the radial force and can in turn be decomposed into a (i) steady part, such as caused by gravity, buoyancy or unbalanced static pressure forces; and (ii) an unsteady part, such as caused by roller bearing reaction, rotating centrifugal loads or flow disturbances. The proportionality factor is a second order matrix referred to as the generalized stiffness matrix. Lumped in this matrix are the effects of all the forces (steady and otherwise) which are functions of at least the displacement of the rotor center and/or its time derivatives (in addititon to other possible variables, such as rotor and stator geometries and machine operating parameters).

Although the evaluation of the radial force vector, $\underline{F}_o(t)$, is an important step in a comprehensive rotordynamic analysis, the stability of the rotor motion depends solely on the characteristics of the generalized stiffness matrix, [A]. It is not surprising then to see the bulk of the research efforts focus on one aspect or another of this matrix. Also, although there is no fundamental reason for it to follow such simple behavior, most rotordynamic models start by assuming a series expansion of this matrix, writing the instantaneous force components as:

$$\begin{Bmatrix} F_x \\ F_y \end{Bmatrix} = \begin{Bmatrix} F_{ox} \\ F_{oy} \end{Bmatrix} - [K] \begin{Bmatrix} x \\ y \end{Bmatrix} - [C] \begin{Bmatrix} \dot{x} \\ \dot{y} \end{Bmatrix} - [M] \begin{Bmatrix} \ddot{x} \\ \ddot{y} \end{Bmatrix} + \text{higher order terms} \qquad (1.8)$$

where time has been dropped for simplification, and where the matrices, [K], [C] and [M], are called the *pure* stiffness, the damping and the inertia matrices, respectively. The term rotordynamic coefficients mentioned above refers to the elements of these three matrices. To visualize the role played by the individual coefficients, it is convenient to consider a simple radial motion of the rotor center, say along the X-axis[9]. Suppose that at time, t, this center is a unit displacement away from its undeflected position, and is moving with a unit velocity and a unit acceleration (x=x=x=1); then, disregarding the higher order terms:

$$F_x(t) = F_{ox}(t) - K_{xx} - C_{xx} - M_{xx} \qquad (1.9)$$

and

---

[9] clearly, the same reasoning can be carried out for a motion along the Y-axis.

$$F_y(t) = F_{oy}(t) - K_{yx} - C_{yx} - M_{yx}. \qquad (1.10)$$

In other words, a simple radial motion induces not only a radial force acting along the line of motion but also a "cross" force acting perpendicularly to this line. It is important to notice that the cross-diagonal terms of the rotordynamic matrices make up the proportional part of this cross force. One can already anticipate the connection between this force and the tangential force acting on a whirling rotor.

For instance, a rotor operating with a slight static deflection (due to, say, its own weight), may experience a lateral force perpendicular to the plane of deflection capable of initiating whirling motion. For this to happen, all that is required is that the pure stiffness matrix have non-zero off-diagonal elements (or cross-coupled terms, as they are sometimes called). However, the subsequent history of this whirling motion cannot be determined by the pure stiffness alone. Damping, inertia and other effects play an important role. Indeed, the study of turbomachine rotor instability problems is simply the study of the mechanisms by which such cross forces can arise, and of the ways in which the rotordynamic coefficients combine to affect the the overall stability of the rotor lateral motion.

Several such mechanisms have been discovered and documented[10]. In general, those traceable to purely mechanical causes seem to have received most of the attention. They include:

(i) internal damping and hysteresis in the rotor and shaft assembly [93],

(ii) non-isotropic shaft stiffness or rotor inertia [66],

(iii) rotor mass unbalance [69],

(vi) system nonlinearities, such as lateral-torsional coupling [152], and finally

(v) rub between rotating and stationary parts [63, 110].

[10] A recent article by Ehric and Childs [50] provides an introduction to some of the most prominent among these mechanisms. Another excellent reference is the Freemann lecture by Greitzer [67] which presents a comprehensive survey of mechanisms affecting the stability of pumping systems.

On the subject of mechanisms of fluid dynamic origin, however, the literature contained little certainty and much speculation at the time the present research program was initiated. Some information existed on the following mechanisms:

(i) cross forces in fluid bearings and seals [30, 37, 83,100,107],

(ii) the Alford (or Thomas) effect in axial flow pumps [6, 140, 145, 146, 155],

(iii) fluid trapped in rotors [49], and

(iv) cross forces in centrifugal pumps and compressors [5, 16, 19, 41, 43, 46, 72, 141,].

Among these mechanisms, (iv), cross forces in centrifugal machines was the least understood. Indeed, it was not clear that these cross forces existed. These are the forces that the present research program was designed to address, under the sponsorship of NASA. Centrifugal flow pumps scaled to high performance applications were selected for the study, which planned for parallel theoretical and experimental investigations. The motivation came from the severe subsynchronous whirl problems encountered during the development of the SSME's HPFTP and HPOTP, described in an earlier section of this chapter; however, this study is of sufficient generality for its results to apply to more conventional turbomachines. The basic questions to be answered were:

(i) Are there simplified turbomachine flow models that may help to clarify the origins of these whirl-exciting forces and the possible mechanisms of their action?

(ii) Are there indeed hydrodynamic, whirl-exciting forces in a real centrifugal pump? More specifically, can the flow through an impeller-volute system generate sub-synchronous disturbances (such as propagating stall, or asymmetric pressure or velocity distributions) capable of driving unstable whirl motions of the rotor? What role, if any, do the various pump components and operating parameters play in such disturbances?

(iii) Are direct measurements of these excitatory forces possible, either on a free-vibrating pump rotor, or on a rotor that is artificially made to whirl? What form would these measurements take? What information would they contain, and how could it be interpreted

and applied to the design or operation of real machines? Could this information be extended to other types of instabilities in other machines?

Consider the flow through a centrifugal pump impeller/volute system[11] (disregarding other pump components such as cylindrical sleeve bearings and seals, which are not part of this study). Lateral hydrodynamic forces (steady or unsteady) acting on the impeller may arise due to :

(i) operation of the impeller at fixed, eccentric position inside the volute,

(ii) whirling of the impeller inside the volute,

(iii) form and shape of the volute,

(iv) number of blades on the impeller, and/or

(v) modulation of the flow due to the combined effect of (i) and (ii).

If the motion of the impeller inside the volute frame is known, it is possible, in theory at least, to identify these different forces due to their different frequencies. For example, consider the situation in which the impeller is whirling. The lateral forces on the impeller, for any position, $(x(t),y(t))$, of the impeller center, O (see Fig. 1.2-top), may be represented by the same equation introduced earlier, Eq. (1.7). The only difference is that, here, only fluid forces generated within the impeller/volute system are to be considered

In both this equation and all the equations and results which follow, dimensionless forces and deflections are used (see Nomenclature for definitions). Implicitly, Eq. (1.7) assumes small offsets, $x(t)$ and $y(t)$, of the impeller center so that the force variations can be represented by such a linear equation (little, if anything, is known of possible nonlinear effects). It follows that the lateral forces, $F_x(t)$ and $F_y(t)$, can be represented by forces, $F_{ox}(t)$ and $F_{oy}(t)$, generated when the impeller

[11] A sketch of a centrifugal flow pump is presented in Fig. 1.2-bottom. It shows the main components of the pump (volute and impeller), and their positions in the reference frame, (X,Y), when the rotor whirls.

center coincides with the volute center[12] (or at least some fixed laboratory position) plus a generalized fluid stiffness matrix, [A], multiplying the displacement vector. Both should be functions of the flow conditions as represented by the flow coefficient, ϕ. Furthermore, one could hypothesize that the matrix, [A], should depend on the characteristics of the whirl motion, in terms of its frequency, Ω.

To be more specific, consider the case of a centrifugal flow impeller whirling around the volute center, O_v, at a constant angular velocity, Ω, in a circular orbit with constant radius, ε; while rotating around its own center, O_i, at the constant rate,ω (see Fig.1.3, notice the choice of the X-axis as the line joining the volute center to the volute cutwater, or tongue; disregard F_1 and F_2 for now). Normalizing the displacements by the impeller discharge radius, r_2 , one gets:

$$x(t) = \varepsilon(\cos\Omega t)/r_2 \tag{1.11}$$

and

$$y(t) = \varepsilon(\sin\Omega t)/r_2, \tag{1.12}$$

in which case, Eq. (1.7) can be rewritten as:

$$\begin{pmatrix} F_x(t) \\ F_y(t) \end{pmatrix} = \begin{pmatrix} F_{ox}(t) \\ F_{oy}(t) \end{pmatrix} + (\varepsilon/r_2)\,[\,A(\Omega/\omega)\,] \begin{pmatrix} \cos\Omega t \\ \sin\Omega t \end{pmatrix} \tag{1.13}$$

where the generalized hydrodynamic stiffness matrix, $[A(\Omega/\omega)]$, is now a function of the ratio of whirl frequency to impeller rotating frequency, (Ω/ω), as well as the flow coefficient. Expansion of Eq. (1.13) in a fashion similar to that of Eq. (1.7) would yield pure fluid stiffness, [K], fluid damping, [C], and fluid intertial, [M], matrices. Here, given the particular type of whirl motion chosen, the expansion is simply a polynomial in powers of the reduced frequency, (Ω/ω). The individual elements of these matrices are then readily determined from Eq. (1.8) and (1.13), namely:

---

[12] Volutes are designed to "match" the impeller at its design speed and discharge flow rate, which usually correspond to the Best Efficiency Point (B.E.P) of pump operation. Ideally, radial forces should balance when the impeller is centered in the volute, both at design and at off-design conditions. In practice this is hardly ever the case, especially at off-design conditions. However, there is always a point in the volute at which these forces will balance on the impeller. The closer this point is to the volute center, the better the design.

$$A_{xx} = M_{xx}\Omega^2/\omega^2 - C_{xy}\,\Omega/\omega - K_{xx}$$

$$A_{xy} = M_{xy}\Omega^2/\omega^2 + C_{xx}\,\Omega/\omega - K_{xy}$$

$$A_{yx} = M_{yx}\Omega^2/\omega^2 - C_{yy}\,\Omega/\omega - K_{yx} \qquad (1.14)$$

$$A_{yy} = M_{yy}\Omega^2/\omega^2 + C_{yx}\Omega/\omega - K_{yy}.$$

It should be observed that there is no known fundamental reason why the generalized hydrodynamic stiffness matrix should follow such a simple quadratic behavior. Investigators who postulate this form of the matrix in their models should be aware of its implications.

The foregoing example involved what might be considered an artificially well-organized motion of the pump impeller. Monitoring of the lateral vibration of actual pump rotors shows that the locus of the impeller center is far from being a perfect circle (the frequency of vibration, on the other hand, is usually more consistent). What then are the prospects for an investigator who wants to study these fluid phenomena using, for example, a small perturbation approach?. From both theoretical and experimental points of view, an organized perturbation, in time and space, can simplify matters a great deal. For instance, if one can somehow prescribe the circular whirling motion described in the example to a real pump rotor and somehow isolate and measure the resulting steady and unsteady impeller hydrodynamic forces for different values of the whirl frequency, then, by correlationg these force measurements with the impeller position and speed along the orbit, one can, in principle, completely determine not only the radial forces but also the complete generalized hydrodynamic stiffness matrix for the particular pump and operating conditions used. Notice that the imposition of a circular orbital motion is analogous to performing a forced vibration experiment in a mechanical system, with the consequence that the rotordynamic coefficients extracted for that impeller/volute combination can be used in a more general dynamic analysis of that system (such as a determination of pump critical speeds and O.S.I.).

Alternatively, one might consider the "free" vibration approach. One might attempt to measure whirl-induced forces directly on a machine which is known to whirl. If such a machine cannot be afforded or accommodated in a laboratory environment, one might simulate whirl on a model scale by applying the dynamic scaling laws. Then, by control of the experimental model parameters, the hydrodynamic forces can be inferred indirectly.

The free vibration approach has the appeal of authenticity. On the other hand, the forced vibration approach gives the experimentator control over an important parameter, namely, the displacement. This second approach has been adopted in the present investigation. To this author's knowledge, there should be no fundamental reason for the two approaches not to yield the same results. One has to keep in mind that, from a practical standpoint, the basic information sought concerns the response of the flow through an impeller/volute system to outside disturbances (in terms of the way fluid stiffness damping and inertia affect the stability of the rotor vibration). Having made this choice, one has then to devise a way to implement the whirling motion and to isolate and measure the fluid forces.

As far as the motion is concerned a preliminary study settled the choice on an eccentric drive mechanism consisting of a double bearing cartridge in which the entire rotor assembly is made to whirl parallel to the machine axis.The motive power could be provided by an auxiliary motor (whose motion is independent of the main pump motor), as described in the next chapter. The same preliminary study determined two basic ways of measuring the impeller forces:

(i) in a stationary frame, and

(ii) in a frame rotating with the impeller.

Method (i) is easier to implement but has the disadvantage for dynamical measurements that one has to contend with large inertia forces and possible fluctuating moments due to the drive system. Method (ii) is somewhat more difficult to implement but has the advantage of minimizing the inertia of the moving parts. In addition, any possible drive system fluctuations are taken by the bearings and will not interfere with the primary measurements. Both methods were implemented during the course of the study, as explained next.

When the present research program was initiated, a substantial body of data existed on the lateral forces, F_{ox} and F_{oy}, thanks to the work of Domm and Hergt [46], Agostinelli et al. [5] and Iverson et al. [81] among others. On the other hand, very little information existed on the hydrodynamic stiffness matrix, [K]; and even less on the hydrodynamic damping and inertia matrices, [C] and [M].

The present program of research at the California Institute of Technology began with measurements of both the lateral forces, F_{ox} and F_{oy}, and the pure fluid stiffness matrix [K], together with a simplified theoretical analysis. The details of this first stage of research have been reported by Chamieh [32] under the supervision of Prof. A. J. Acosta and will not be repeated here. The experimental results were obtained by very slowly moving the impeller center around a circular orbit and measuring the lateral forces at each location, using an externally mounted stationary force balance. The theoretical analysis used a two-dimensional irrotational flow model in which the impeller was represented by an actuator disk having an infinite number of blades, and a vortex distribution was substituted for the volute.

The main finding in this first stage was that the hydrodynamic stiffness matrix, [K], is statically unstable. The direct stiffness terms were equal in magnitude and had the same negative sign, resulting in a radially outward fluid force. The cross-coupled stiffness elements were equal in magnitude and their opposite signs were such as to produce a tangential fluid force capable of driving forward whirl motion of the impeller, should the system lack adequate damping. The theory did not completely confirm these experimental findings, which is not surprising, in retrospect, given the simplifications used (irrotationality).

These interesting findings paved the way for the second stage of research geared toward the study of the unsteady aspects of these potentially destablizing fluid forces. A theoretical study was planned as part of this second satge and is being carried out by a separate investigator, D. Adkins, under the supervision of Prof. C. E. Brennen. The model used in this analysis and the

results obtained will be discussed later. The focus here is on the experimental work for which the present author is responsible.

Herein, the aim is to extend the results of the first stage to the case of non-negligible velocity of the orbiting motion, so that the complete generalized stiffness matrix can be measured.

1.5 Scope and Goals of Present Research:

More specifically, it was decided to artificially prescribe variable speed, circular whirling motions on the impellers of various centrifugal flow pumps, and to measure the resulting steady and unsteady fluid forces, using a rotating dynamometer mounted immediately behind the impeller. The aim was to study the behavior of the generalized stiffness matrix under various pump geometric and operating conditions. The idea was to use as much of the existing hardware as possible. However, the following specific requirements had to be provided for in the test setup:

(i) the experiments had to be carried out on centrifugal flow pumps that are scaled to high performance applications such as the SSME's HPFTP,

(ii) the facility had to be capable of measuring all components of both steady and unsteady rotor forces (using rotating dynamometer and associated intrumentation), and have sufficient flexibility to allow separate investigation and evaluation of their various sources,

(iii) both the direction and the angular velocity of the circular whirl motion should be prescribed independently of the drive shaft angular velocity, so that the entire range of sub-synchronous and a representative range of supersynchronous speeds should be explored in both whirl rotational directions,

(iv) various impeller and volute geometries had to be accommodated and provision made for adjustable impeller face seal clearances, in order to study the influence on the measurements of pump component geometry and pump leakage,

(v) close phase monitoring was needed to provide instantaneous information on rotor location and orientation for correct synchronization with the data acquisition,

(vi) possibility of varying pump flow rate and overall system pressure, and finally,

(vii) full instrumentation to monitor impeller motions and pump parameters.

The ultimate goal of the project was to provide high performance turbomachine practioners with a deeper understanding of the relations between rotor dynamic instabilities and impeller/volute hydrodynamic interactions. From a practical standpoint, the intention was to supply a body of data on the dynamic coefficients of impeller/volute systems which designers could input into their rotordynamic codes[13].

In the next chapter the modifications and additions implemented to ready the test setup for the unsteady measurements of this second stage will be described. The main feature of the experiment is the rotating dynamomter. Chapter 3 and Appendix B are devoted to a detailed description of the design and realization of this instrument. The various experiments performed are summarized in Chapter 4. The data acquisition and reduction techniques used to handle dynamometer and other system raw measurement signals are explained in Chapter 5 and Appendix C. Their results are described and discussed in Chapter 6; and comparisons are made with other available experimental and theoretical data. An addendum to this thesis illustrates the use of such results in an actual rotordynamic analysis, see Appendix D. Finally, the important findings of the study are summarized and final conclusions are drawn, in Chapter 7.

[13] After the present program was initiated, two other studies were reported by Ohashi et al. [122], and Bolleter et al [21]. The scope and the results of these studies will be discussed with the results of the present work.

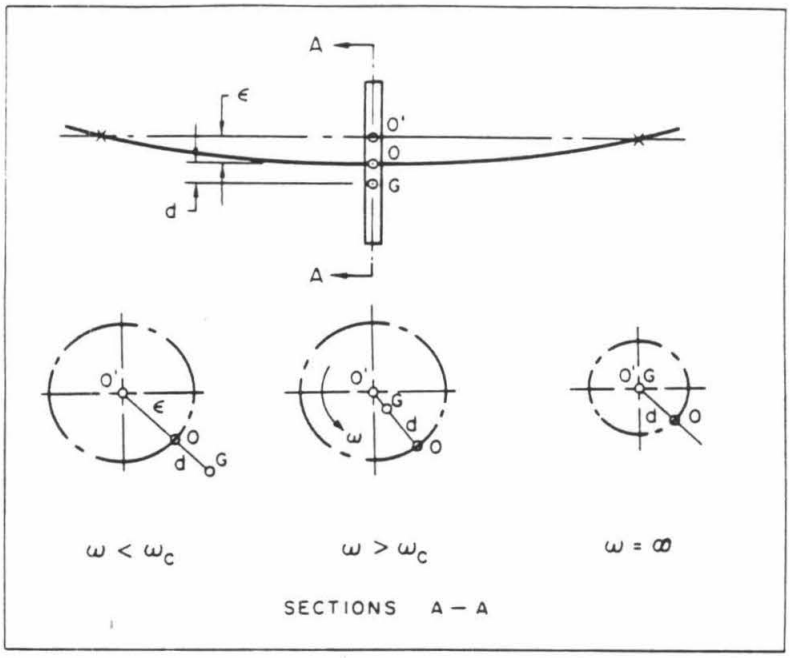

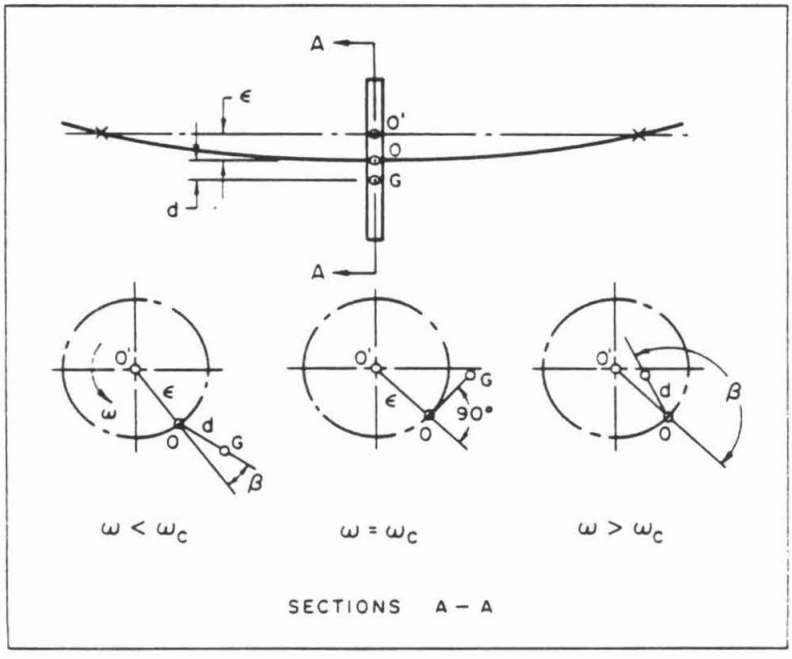

Fig.1.1 Idealized case of rotor whirl due to pure mass unbalance of a weightless vertical shaft. Top: without damping. Bottom: with damping.

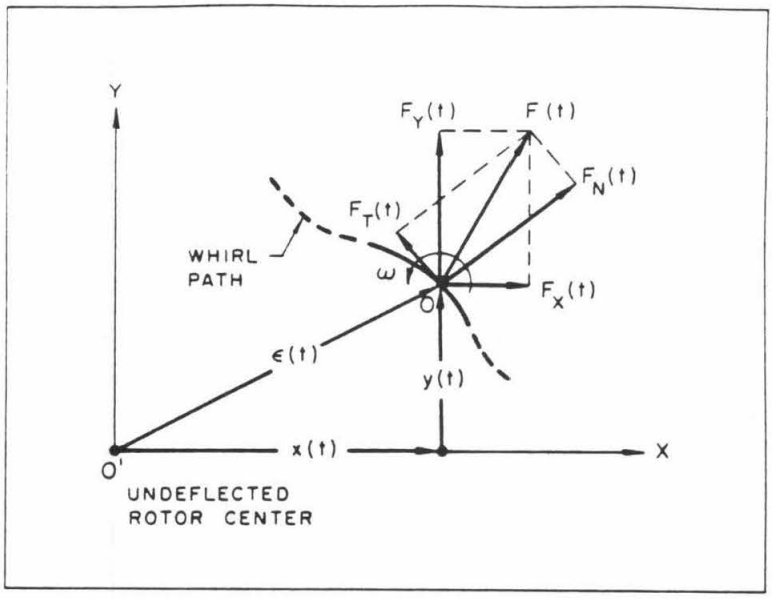

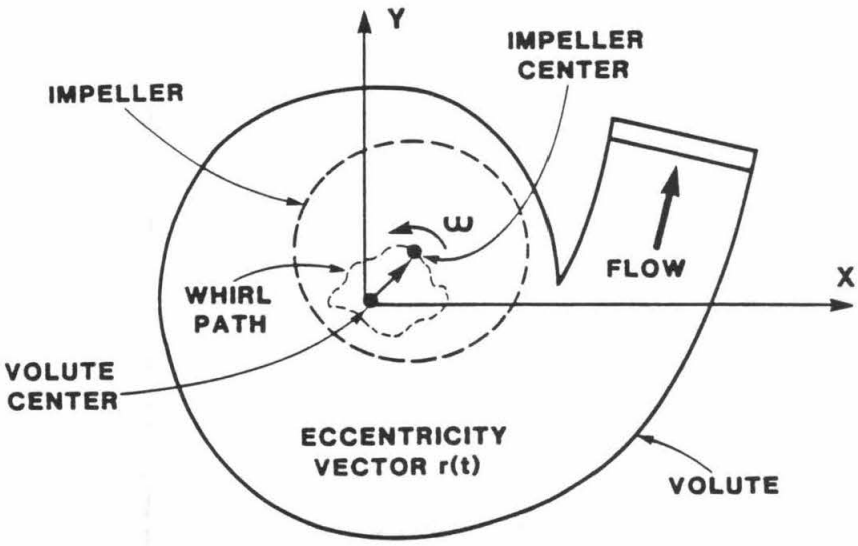

Fig. 1.2 Top: diagram of the in-plane forces acting on a whirling impeller at its center, O. Bottom: schematic of a centrifugal pump whith a whirling impeller, ω = pump speed (rad/sec).

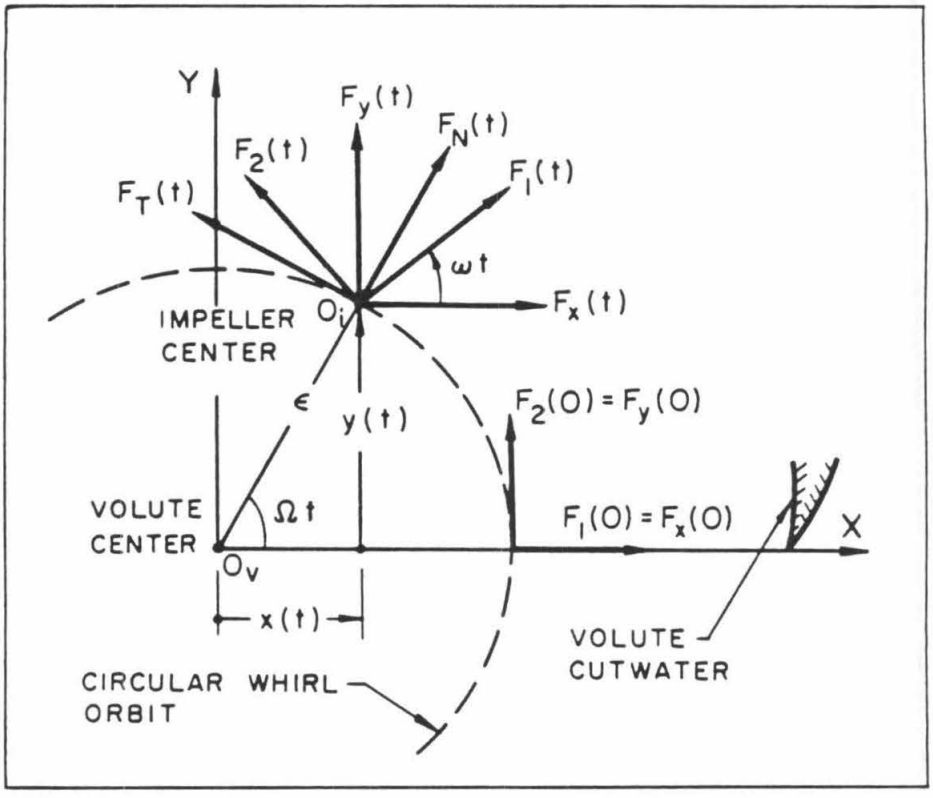

Fig. 1.3 Circular whirl for a centrifugal flow pump. F_x and F_y are the impeller forces in the laboratory reference frame, (X,Y), where the X-axis is the line joining volute center to volute tongue. F_1 and F_2 are the lateral impeller forces sensed in the rotating frame of the impeller, (1,2). F_N and F_T are the normal and tangential (to the circular whirl orbit) components of the impeller lateral forces.

Chapter 2

EXPERIMENTAL FACILITY

As mentioned in the introduction, the present work is the second stage in an extensive research program. The experimental part in this program was planned with the idea that the same pre-existing pump loop, the Dynamic Pump Test Facility, or DPTF, will be used with as little alteration and addition as possible, for obvious budgetary reasons. The steady force and pure stiffness measurements, carried by Chamieh in the first stage, introduced what was called the Rotor Force Test Facility, or RFTF. The RFTF replaced the axial flow pump test section of the DPTF (see Fig. 2.1).

However, the dynamic measurements proposed in this second stage have their own hardware and software requirements. Also, although several major components from the RFTF (as designed in the first stage) were reuseable, it was necessary to design and build a number of new and highly customized mechanical and electronic components. In the following descriptions, more emphasis will be put on these new components.

2.1 The Dynamic Pump Test Facility:

The DPTF has been described in detail elsewhere in the literature, Ng [119], Braisted [27]. It is basically a closed, water recirculating pump loop containing flow control and measurement systems. It was originally used to collect data on the transfer matrices of various cavitating inducers, Ng and Brennen [120]. The major components of this facility are depicted in Fig. 2.1. Also shown in this figure are the sites of the major alterations that had to be implemented in order to meet the requirements of this second stage of research. The alterations needed for the first stage were described in detail by Chamieh [32]. Most of them apply to the unsteady measurements of this second stage and will be preserved. These will not, however, be described in detail again.

The Rotor Force Test Facility (RFTF) was installed in the lower left hand corner of the loop. Two of the RFTF major design constraints are worth reiterating here. The first one was the 20.3 cm (8 in) distance between the piping centerline and the base mount of the existing DPTF, dictating that the maximum volute radius be less than this distance. The second one resulted from the decision to keep the existing 15 kW (20 hp) D.C. motor as the main pump drive. These two constraints combined with the 0.6 line of specific speed pumps proposed for the measurements dictated a maximum pump shaft speed of about 3500 rpm (f=58 Hz), necessitating a change in the gearing ratios of the existing gear box. The maximum pressure rise across the pump (using simple single suction impellers and single volutes) was then estimated to be around 4.8×10^5 N/m^2 (70 psi). Taking into account the structural capabilities of the loop and the fact that force measurements under cavitation are contemplated, it was decided to design the pump housing for a maximum pressure of 10^6 N/m^2 (150 psi). This maximum value allows sufficient flexibility in setting a datum pressure for the system.

The bulk of the present modifications and additions took place within the RFTF part of the DPTF. However, one major modification was separate from the RFTF. It is the inclusion of an auxiliary pump in the upper left hand corner of the DPTF. These and other modifications are described in the following sections.

2.2 The Rotor Force Test Facility:

Detailed description of the original version of this facility can be found in Reference [32]. It was designed by Chamieh with some help from the present author. Basically, it consisted of a centrifugal flow pump in which the rotor could be driven into a very slow whirling motion, along a constant radius circular orbit. The steady and quasi-steady forces experienced by the impeller were measured by means of an externally mounted stationary force balance, also referred to as the External Balance. The current version of this facility is depicted in Fig. 2.2. A photograph is included in Fig. 2.10.

Essentially, this new version of the RFTF provides (i) a precisely controlled, constant radius circular whirl motion of the rotor at speeds equal to integer fractions (smaller as well as bigger than unity) of the main pump speed, and (ii) an accurate way of measuring the steady and unsteady hydrodynamic forces experienced by the impeller under these two motions combined, for a variety of pump geometries and a wide range of pump operating conditions.

The differences between the new and the old version, visible in Fig. 2.2, include a new 1.5 kW (2 hp) whirl motor with its optical encoder, a set of slip-rings, an air bearing, and an optical encoder attached to the main motor gear box. A major difference not visible in Fig. 2.2 is the inclusion of a rotating dynamometer inside the pump itself. Detailed descriptions of these components will be given, as noted in the following list which summarizes the specific changes implemented by the present author in order to prepare the RFTF for the unsteady measurements of this second stage. These included:

(i) A more powerful whirl motor to develop speeds ranging from subsynchronous to supersynchronous in both rotational directions. This motor drives the eccentric mechanism described in Section 2.3.

(ii) A customized electronics package to assure precise control of both concentric and eccentric impeller motions, including synchronization with the data acquisition. Descriptions can be found in Section 2.6.

(iii) An internally mounted rotating dynamometer to measure all six components of both steady and unsteady impeller fluid forces (the chief interest is in the two lateral ones). The design, construction and calibration of this dynamometer are described in detail in Chapter 3 and Appendix B.

(iv) Complete instrumentation to transmit, amplify, condition and monitor the raw measurement signals output by this rotating dynamometer. Refer to Section 2.7 for details.

(v) Major upgrading of the microprocessor-based data acquisition system was necessary, and interfacing of this system with the newly acquired desktop computer ended the dependence on the Institute's Computing Center for data storage and processing. More

flexibility and reliability were achieved, in addition to budgetary savings. See details in Chapter 5.

(vi) An auxiliary pump to allow the investigatin of leakage flows and the operation of the main test pump in all four quadrants. Section 2.5 describes this pump.

(vii) Additional test volutes and impellers to explore the effect of various pump component geometrie, as explained in Section 2.4. Some of the volutes were fitted with a set of taps for mapping static pressure distributions. Details on these taps and the associated manometers are presented in Chapter 4.

A set of conventional flow control and measurement devices and instruments, including a flow rate control servo-valve, a pneumatic system for control of overall loop pressure, turbine and electromagnetic flow meters, accelerometers and upstream and downstream pressure transducers and gages, already existed in the test loop and needed little or no modification.

2.3 The Eccentric Drive Mechanism:

The whirling motion imposed on the impeller is powered by the above-mentioned 1.5 kW whirl motor via the chain, sprocket wheels and eccentric drive mechanism described schematically in Fig. 2.2.and photographically in Fig.2.11. Further description of this eccentric drive mechanism is best followed by referring to Fig. 2.3 in which an assembly drawing of the main test section is presented. The main pump shaft (10) rotates in a double bearing system (8,9,12,13) designed so that rotation of the sprocket (11) attached to the intermediate bearing cartridge causes the orbiting motion. The radius of the orbiting motion, ε, is set at a constant value of 0.126 cm (.050 in).

At first, use of a variable eccentricity was contemplated, but soon it became evident that its implementaion would be very troublesome. The choice of a suitable (single) value for ε, then became a design issue. Too high an ε would put the whirling motion outside the "linear," "small"perturbation range, which is implicit in the way the measurements will be interpreted. Too small an ε would result in forces too small to measure accurately (especially the tangential force).

As in any engineering problem, a compromise had to be found. A preliminary study settled the choice on the above-mentioned value of 0.126 cm.

Another question was that of powering the eccentric drive mechanism. Two basic solutions were contemplated: (i) using the main pump motor and a second gear box, or (ii) using an auxiliary motor and a chain/sprocket wheel or belt/pulley system. The first had the advantage of accuracy and reliability, but lacked flexibility (considering the range of whirl speeds contemplated, many gear ratios would be needed).

The second solution presented the problem of synchronizing[1] the motions of the two motors, the problem of accuracy should a belt be used, and finally the problem of noise and safety in the case of a chain. The second solution was adopted after it was determined that accurate digital control (using angular position and speed feedback from optical encoders, see Section 2.6) could be achieved. A chain/sprocket wheel system was chosen over the belt/pulley solution. Also, to reduce noise and avoid excessive vibration on the eccentric drive assembly, it was deemed necessary to limit the highest whirl speed to 1200 rpm. Finally, the power transmission assemblies from both motors were covered by a protective grid, for safety reasons.

Among the problems associated with the eccentric drive assembly were (i) the failure of inner bearing (13) as a result of a water leak, and (ii) excessive noise in the spectral analysis of the response of the assembly recorded during simultaneous whirl and rotation tests in air. This second problem was traced to excessive chain tension, which was easily remedied.

2.4 Housing, Volutes and Impellers:

The study planned for investigation of several pump geometries. Of particular interest was the determination of the role played in these forces by the two main pump components, namely, the impeller and the volute. Answers to the following questions were sought:

---

[1] It will become clear from the descriptions of the data acquisition and processing techniques (Chapter 5) that precise control of the impeller location and orientation are necessary at each instant in time. This in turn requires precise synchronization and control of both concentric and eccentric shaft rotations. See also Section 2.6 of this chapter.

(i) What is the influence of the impeller geometry, in terms of blade angle, solidity, presence or absence of shroud, number of vanes, etc...?

(ii) What role, if any, is played by the volute? In particular, what would happen to the impeller forces if there was no volute? Will there be a difference between forces measured with a real volute and those measured with a simple diffuser? What are the effects of (a) volute and diffuser cross-section design, (b) the presence, size, orientation and number of diffuser guide vanes?

This desire to explore so many unknowns was reflected in the flexibility of the pump design, as described in Fig. 2.3. It was decided to pressurize the volute (2) inside a large cast aluminum housing (1) stressed to 1 MPa (150 psi, as mentioned earlier). This allows the volutes to be made economically out of lightweight materials (except for the one donated by Rocketdyne, all volutes were made in house, out of fiberglass). The geometry of the impeller (5) is also flexible. The characteristics of the various impeller and volute designs tested are presented in Fig. 2.4 and Fig. 2.5, respectively. Also Fig. 2.6 presents a graphic summary of the the cross-sectional geometries of the volutes. Photographs of the various impellers are shown in Fig. 2.14, those of the various volutes in Fig. 2.15.

It can be seen that the variety in types and geometries was bigger in terms of volutes. Removal and installtion of both the impeller and the volute were made easy by fastening the flow inlet connection (3) and inlet bell (4) to the casing front cover, so that the whole assembly can be removed and replaced in little time. Figs. 2.12 and 2.13 show the test pump as viewed from the inlet side, with and without the casing cover

The impeller is mounted directly on the rotating dynamometer (6) (or Internal Balance as it is sometimes referred to), which is new to the present experiments and is discussed more fully in Chapter 3 and Appendix B. Face seals on both inlet (15) and discharge (16) sides of the impeller were backed off to prescribed clearances in order to minimize their contribution to the forces on the impeller. Also, by performing tests at various seal clearance settings, one could measure the influence of the leakage flows. In a particular set of tests, these seals were supplemented with

circular rings mounted on the volute, near the impeller discharge (see Fig. 4.1 for more detalils on this arrangement).

2.5 Auxiliary Pump:

Another investigation of the leakage flow involved the use of a special impeller and an auxiliary pump, as described below. First, a 10 cm (4 in) butterfly valve was inserted some distance downstream of the main pump discharge. A type "TLH" Byron-Jackson centrifugal flow pump, driven by a 5.6 kW (7.5 hp) Marathon motor, was then installed as a bypass to this butterfly valve. Additional valves and piping allow the pump to circulate water in either direction through this bypass. This pump and the associated piping and valves[2] are described by the isometric sketch of Fig. 2.7.

The purpose of this addition is two-fold. First, it permits leakage flow to be generated even when a non-functional impeller (such as the consolidated dummy impeller, Impeller S) is installed inside the main test pump. A separate investigation of the role played by the leakage flows in the measured rotordynamic forces and force matrices is then possible. There are some indications in the SSME flight hardware tests that modifications (e.g., anti-swirl vanes) to the leakage flow pathways may indeed have significant rotordynamic consequences, Ek [51]. The second reason is to allow measurements of the forces for an actual impeller over a wider range of operating conditions (i.e., to allow some four-quadrant testing).

2.6 System Controls:

Unsteady fluid force measurements such as those attempted here require sufficient control to permit data to be taken over many cycles of both the whirl and main shaft frequencies. In particular, at all times in the reference cycle used to control the data sampling process (described in Ch. 5), it

---

[2] The installation of these components was carried out by R. Fanz and D. Adkins, whose help was very much appreciated.

is necessary to determine precisely the orientaion of the dynamometer and its location on the whirl orbit, so that the forces measured in this rotating frame could be resolved correctly. This demands close control of both concentric and eccentric rotor motions, which was achieved by means of the control system shown diagrammatically in Fig. 2.8.

A single frequency generator feeds a frequency multiplier/divider which uses two integers, I and J input by the operator to produce various reference waves, having various frequencies. One output signal at a frequency ω drives the main shaft motor, a feedback control system ensuring close adherence to that driving signal. Another output at a frequency $\Omega=I\omega/J$ controls the eccentric drive motor which is also provided with a feedback control system. The block diagram in Fig. 2.9 describes these systems (in a generic fashion).

Essentially, the frequency and phase of the slave motor (main pump motor or whirl motor, as the case may be) are closely controlled by means of a Phase Lock Loop (PLL). During startup, the motor speed is slowly increased to near its prescribed value (command rpm) using the ramp generator (in an open loop fashion). Two wave signals output by the optical encoder provide information on both motor speed (high frequency channel: 1024 x rpm) and phase (low frequenncy channel: 1 x rpm).

As the motor reaches the prescribed speed for the first time, phase coincidence is detected between the command signal and the feedback signal. The phase detector then orders the actuator to freeze the ramp voltage and release the frequency counter and the integrator. The counter corrects for deviations in frequency and the integrator corrects for deviations in phase, by feeding into the summation junction a voltage (amplified before reaching the motor) proportional to the error. The loop is thus closed.

Synchronization of the two motors is implicit from the choice of the driving frequencies. Three other outputs from the frequency multiplier/divider at frequencies of $\omega\pm\Omega$, or $(J\pm I)\omega/J$, and ω/J are used in the data acquisition and processing systems described in Chapter 5.

Bringing the complete control system to a satisfactory state of operation was no easy task. Complications were encountered due to (i) the range of the basic main motor frequency covered (0.2 to 60 Hz), and (ii) the later-to-be-regretted choice of not building completely new components, and instead try to salvage part of some old, poorly documented pieces of electronic hardware. These existed as part of the old flow fluctuator control system (siren valve phase-lock drive shown in the upper right-hand corner of the DPTF, Fig. 2.1) which has not been used in the present research program.

2.7 Instrumentation:

The main feature of the test setup is the rotating dynamometer which will be described separately in the next chapter. Herein, brief descriptions of various other instruments are presented.

Pump flow rates are controlled by a servo valve (`silent' throttle valve shown in Fig. 2.1) in which the flow rate as sensed by a turbine flow meter is continuously matched to the reference flow level selected by the operator. When negative flow rates were used (auxiliary pump), the flow was manually controlled using the by-pass valve and an Electromagnetic Flow Meter (EFM), the turbine meter being reliable only in one flow direction. Both of these meters were calibrated using a pitot tube.

Overall system pressure was regulated by the amount of pressurized air allowed inside a submerged rubber bladder. Upstream and downstream pump pressures were registered by two pressure transducers, supplemented by a dial gage and a Heise gage, respectively, for visual control. Another dial gage displays the pressure in the cavity surrounding the dynamometer. Monitoring of this pressure was necessary as a preventive measure against accidental water leaks to the inside of the dynamometer[3].

---

[3] Originally, the design provided for air (compressed to a regulated pressure slighty higher than the one prevailing in this cavity) to be fed inside the dynamometer, through an air bearing (item (21), Fig. 2.3 right), in order to assist positive sealing. After calibration and preliminary checks, this measure proved unnecessary. The dynamometer seals (described later) were sufficient for the task.

Chamieh [32] evaluated the contribution, to the radial force and the pure stiffness matrix, of uneven static pressure distribution at the impeller periphery. This evaluation was based on readings from a set of static pessure taps placed on both sides of the volute, just near the impeller discharge, as described in Fig. 4.1. It was decided to refine these measurements and extend them to more volutes. Given the range of pressures anticipated, water manometers were used to give a good resolution. A battery of twenty-two such manometers was provided so that static pressure displays from all twenty-two taps used can be "frozen" and read simultaneously.

Finally, it should be noted that the three optical probes (item (7), Fig.2.3), originally designed to monitor the impeller motions inside the volute, did not fill their function properly, due to irregularities in the reflectivity of the impeller surfaces, which makes accurate calibration impractical. They were superseded by the electronic control system described in Section 2.6 of this chapter.

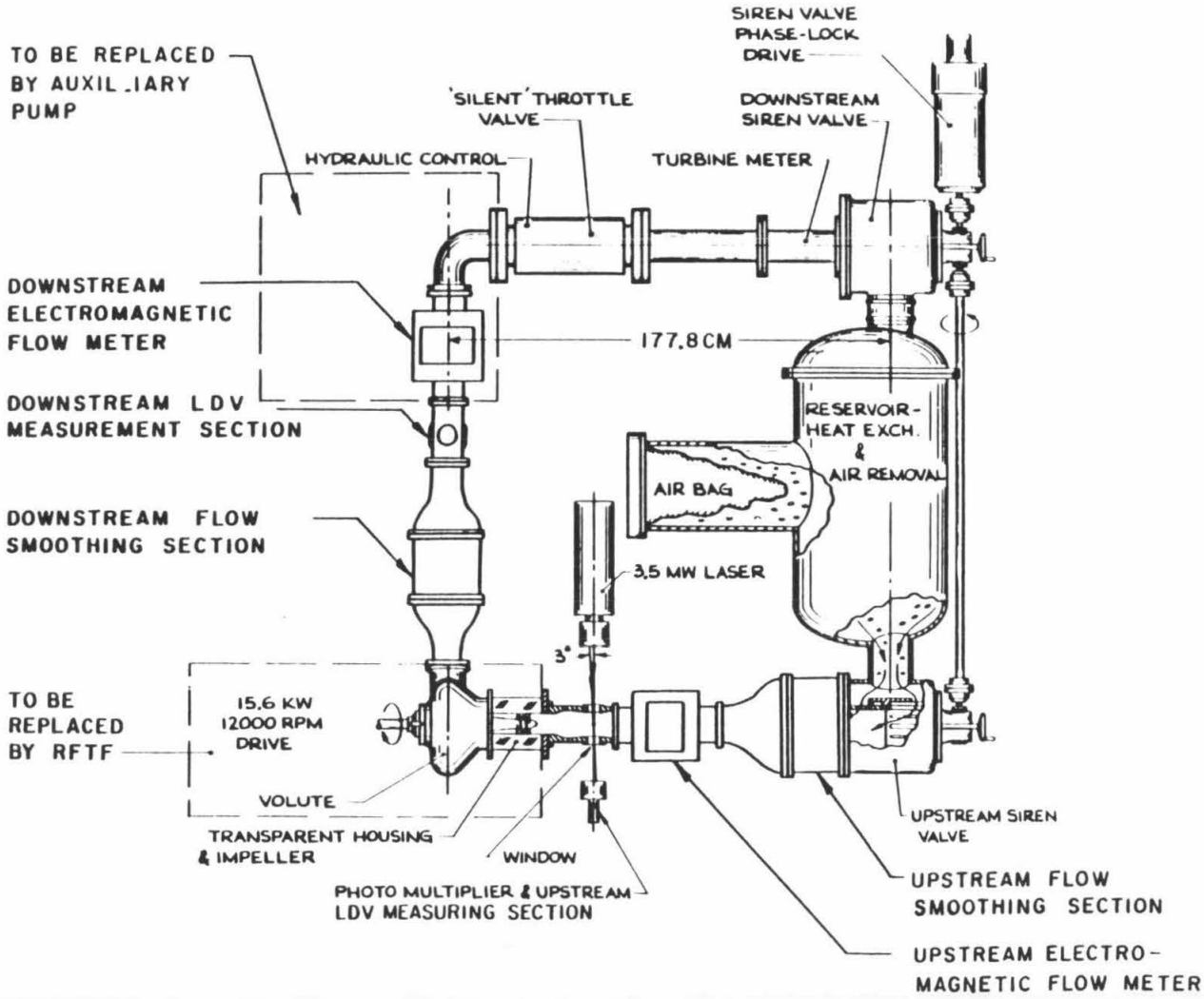

Fig. 2.1 Schematic top view of the Dynamic Pump Test Facility (DPTF), before the addition of the Rotor Force Test Facility (RFTF) at bottom left corner, and the auxiliary pump at the top left corner.

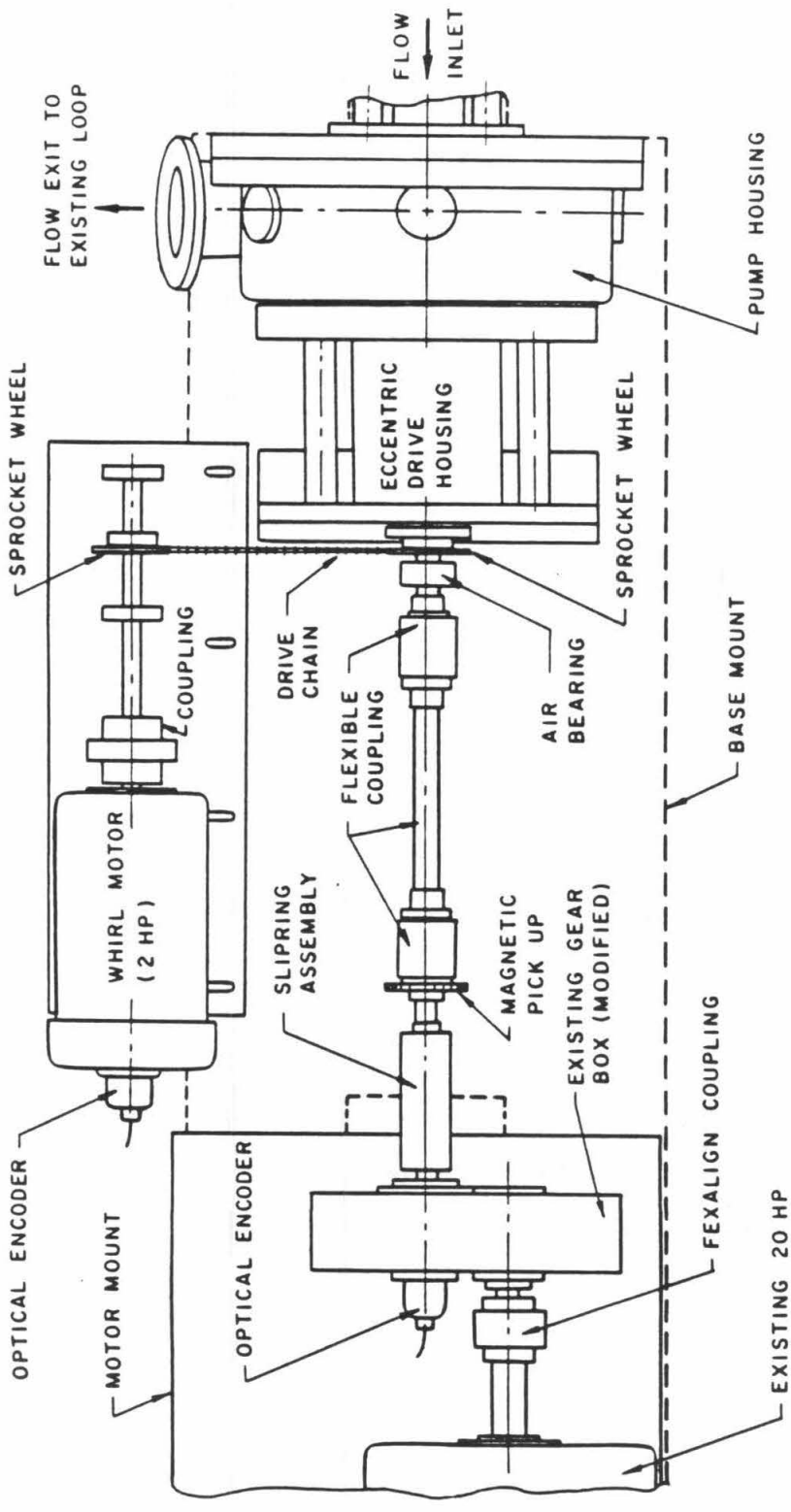

Fig. 2.2 Schematic layout of the main components of the Rotor Force Test Facility (RFTF).

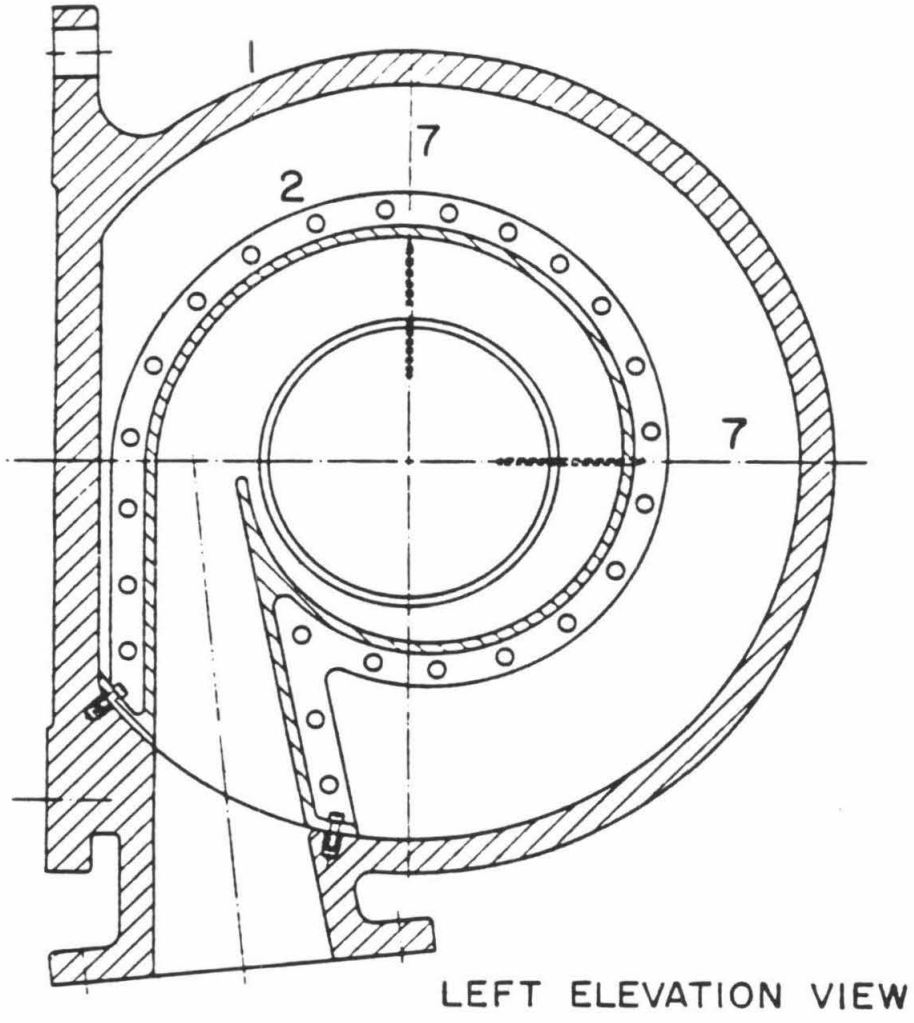

Fig. 2.3 Left: left elevation view of the Rotor Force Test Facility (RFTF) test section.

Right: plan view of RFTF test section showing pump casing, 1, volute, 2, inlet section, 3, inlet bell, 4, impeller, 5, rotating dynamometer, 6, proximity probes, 7, eccentric drive outer and inner bearing cartridges, 8 and 9, shaft, 10, sprocket wheel, 11, outer and inner bearing sets, 12 and 13, flexible bellow, 14, impeller front and back face seals, 15 and 16, inner and outer bearing seals, 17 and 18, strain gage cable connector, 19, flexible coupling 20, and air bearing stator, 21.

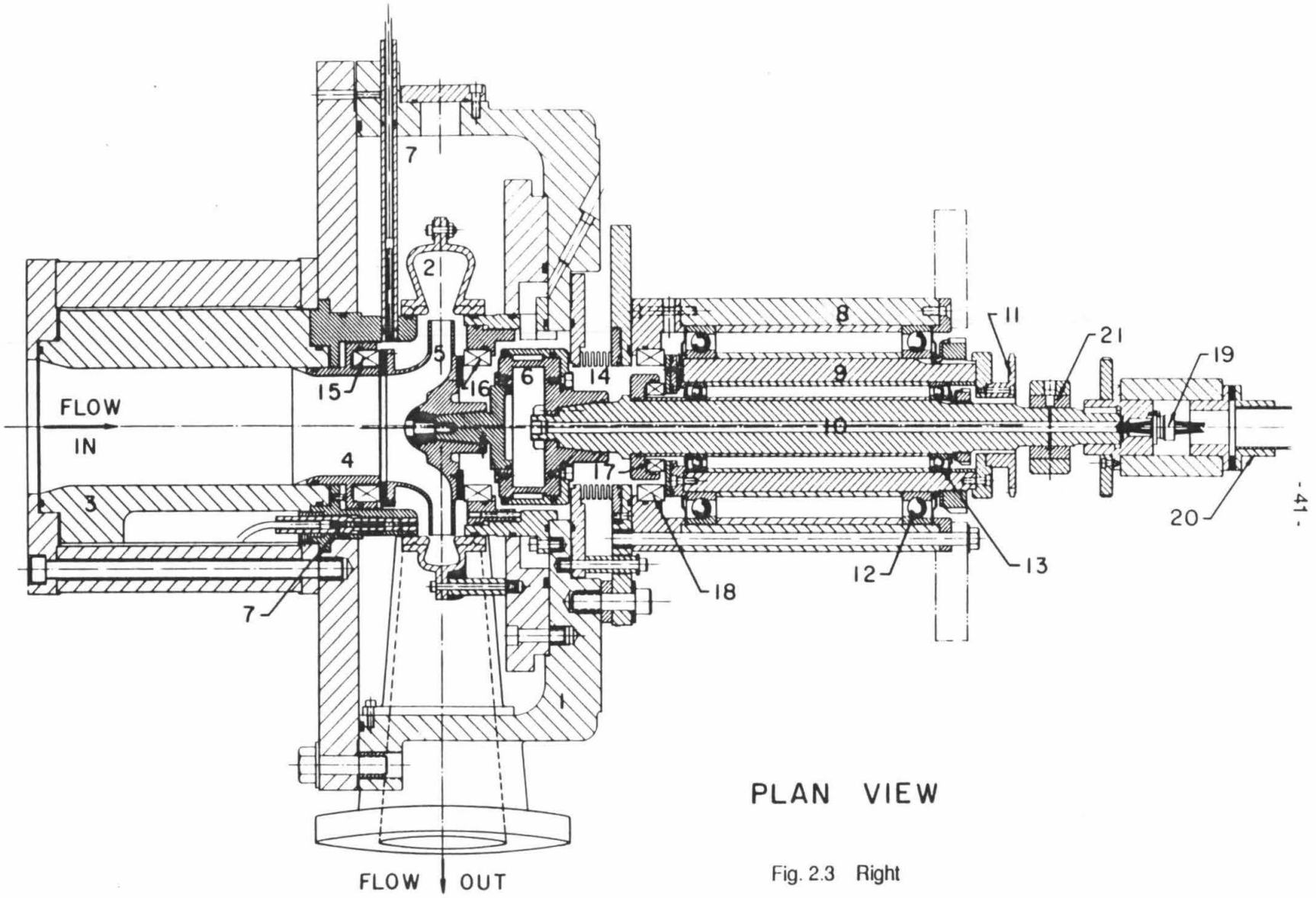

PLAN VIEW

Fig. 2.3 Right

IMPELLER NAME	X	Y	K	S
OUTLET DIAMETER (mm)	161.9	162.1	SOLID DISK: OUTSIDE DIAMETER = 161.9 mm THICKNESS = 6.3 mm	CONSOLIDATED DUMMY DUPLICATING OUTSIDE GEOMETRY OF IMPELLER X
OUTLET WIDTH (mm)	15.8	16.5		
BLADE ANGLE (deg)	23	30		
NUMBER BLADES	5	6		
SPECIFIC SPEED	0.57	0.59		
DESIGN FLOW COEFFICIENT	0.092	0.095		

Fig. 2.4 A table summary of the characteristics of the various "impellers" tested. Only Impeller X and Impeller Y are true impellers.

VOLUTE NAME	VOLUTE TYPE	CROSS SECTION SHAPE	SPIRAL ANGLE (deg)	TONGUE ANGLE (deg)	NUMBER VANES	VANE SECTOR (deg)
A	VOLUTE	TRAPE-ZOIDAL	4	174	0	NA
B	VOLUTE	CIRCULAR	NA	117	0	NA
C	VOLUTE	TRAPE-ZOIDAL	4	176	0	NA
D (D-0)	VANELESS DIFFUSER	TRAPE-ZOIDAL	4	168	0	NA
E	VANED DIFFUSER	ELLIPTIC	5	140	17	26
F (D-F6)	VANED DIFFUSER	TRAPE-ZOIDAL	4	168	6	42
G (D-G6)	VANED DIFFUSER	TRAPE-ZOIDAL	4	168	6	33
H (D-H12)	VANED DIFFUSER	TRAPE-ZOIDAL	4	168	12	33

Fig. 2.5 A table summary of the characteristics of the various volutes tested. Volutes D, F, G and H differ only by the number and arrangement of diffuser guide vanes. Tongue angle is the angle between the upward vertical and the line joining volute center to volute tongue. Vane sector is the angle subtended by the vane.

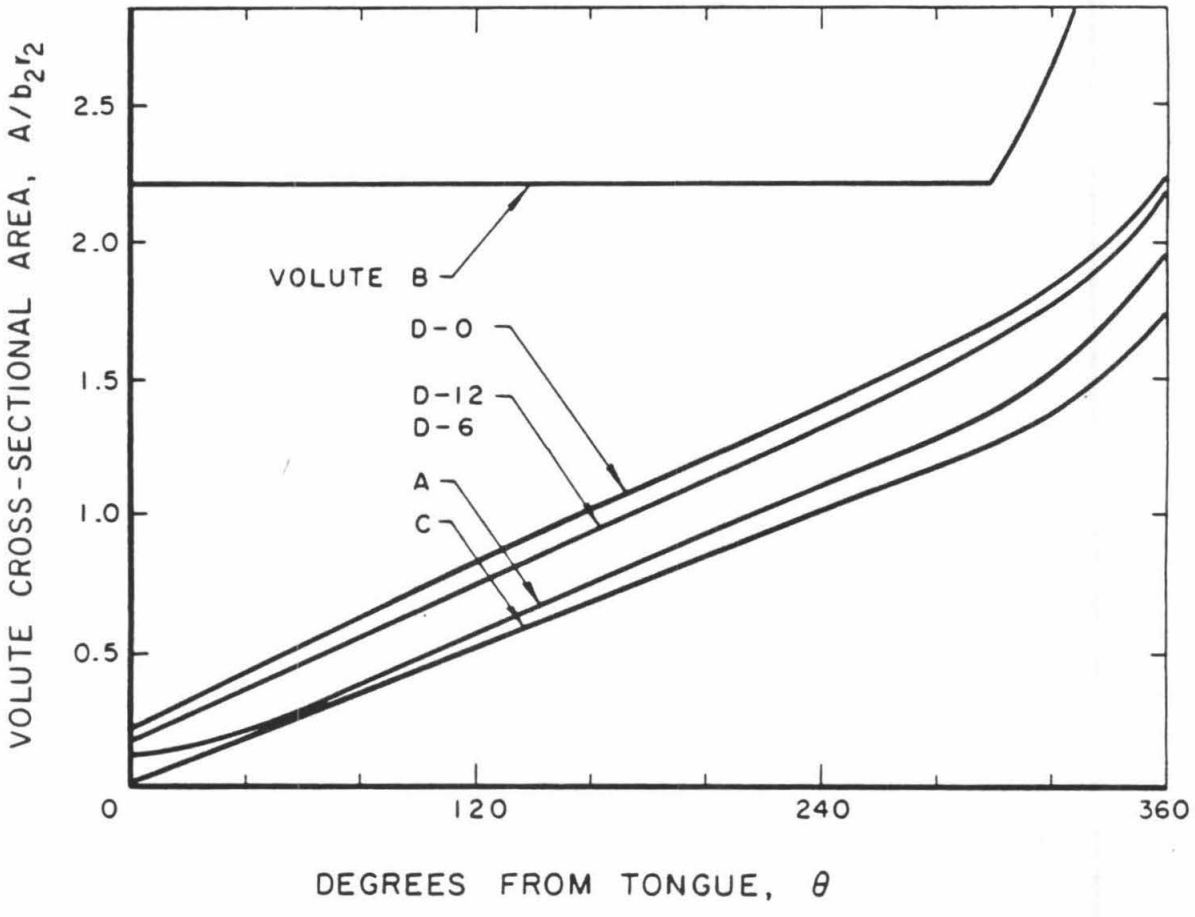

Fig. 2.6 Graphic summary of the cross-sectional geometries of the various volute designs tested.

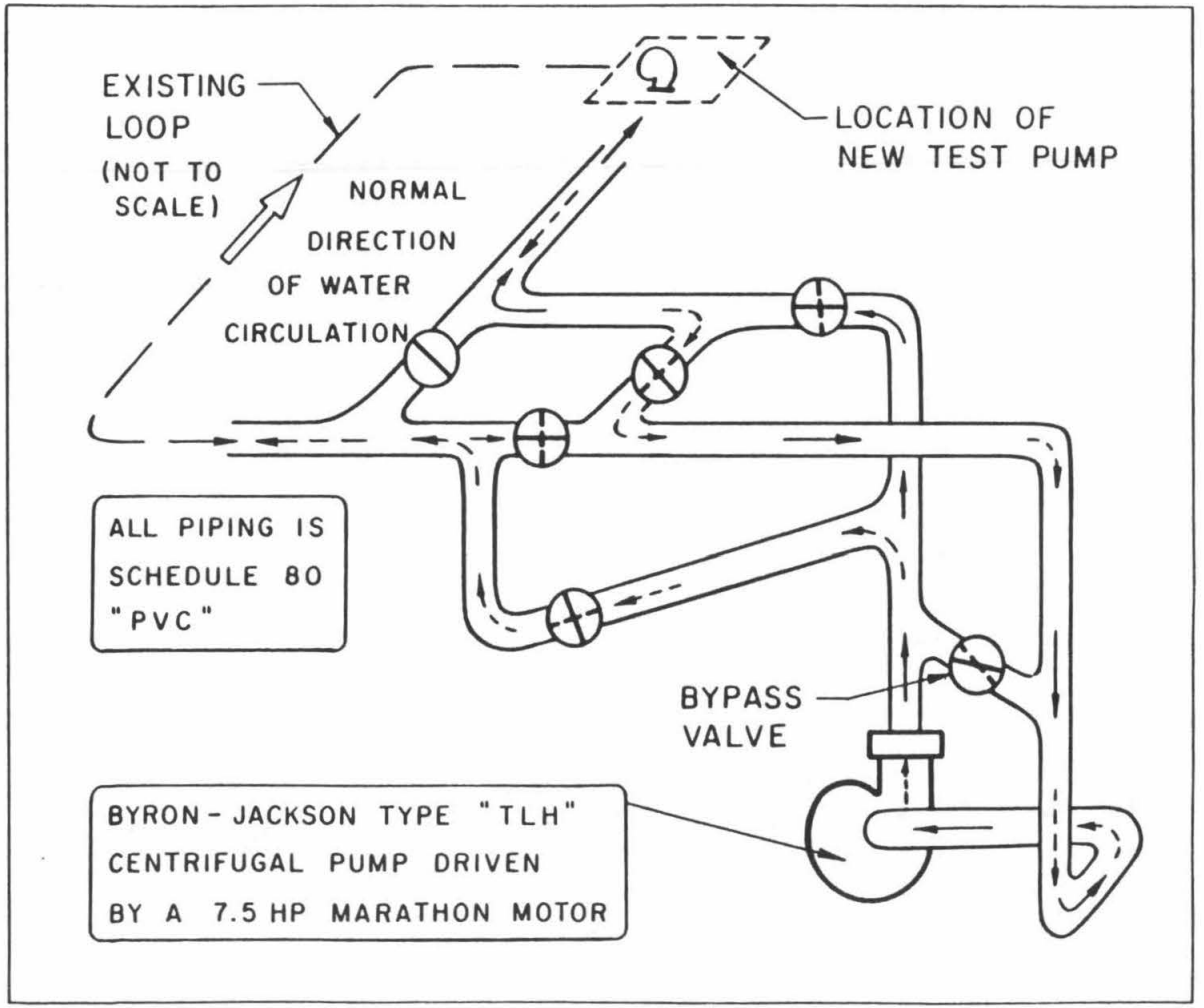

Fig. 2.7 Isometric sketch of auxiliary pump and associated piping and valves. This pump is used to circulate water in the loop in either direction allowing four quadrant operation of the main test pump.

SYSTEM CONTROLS

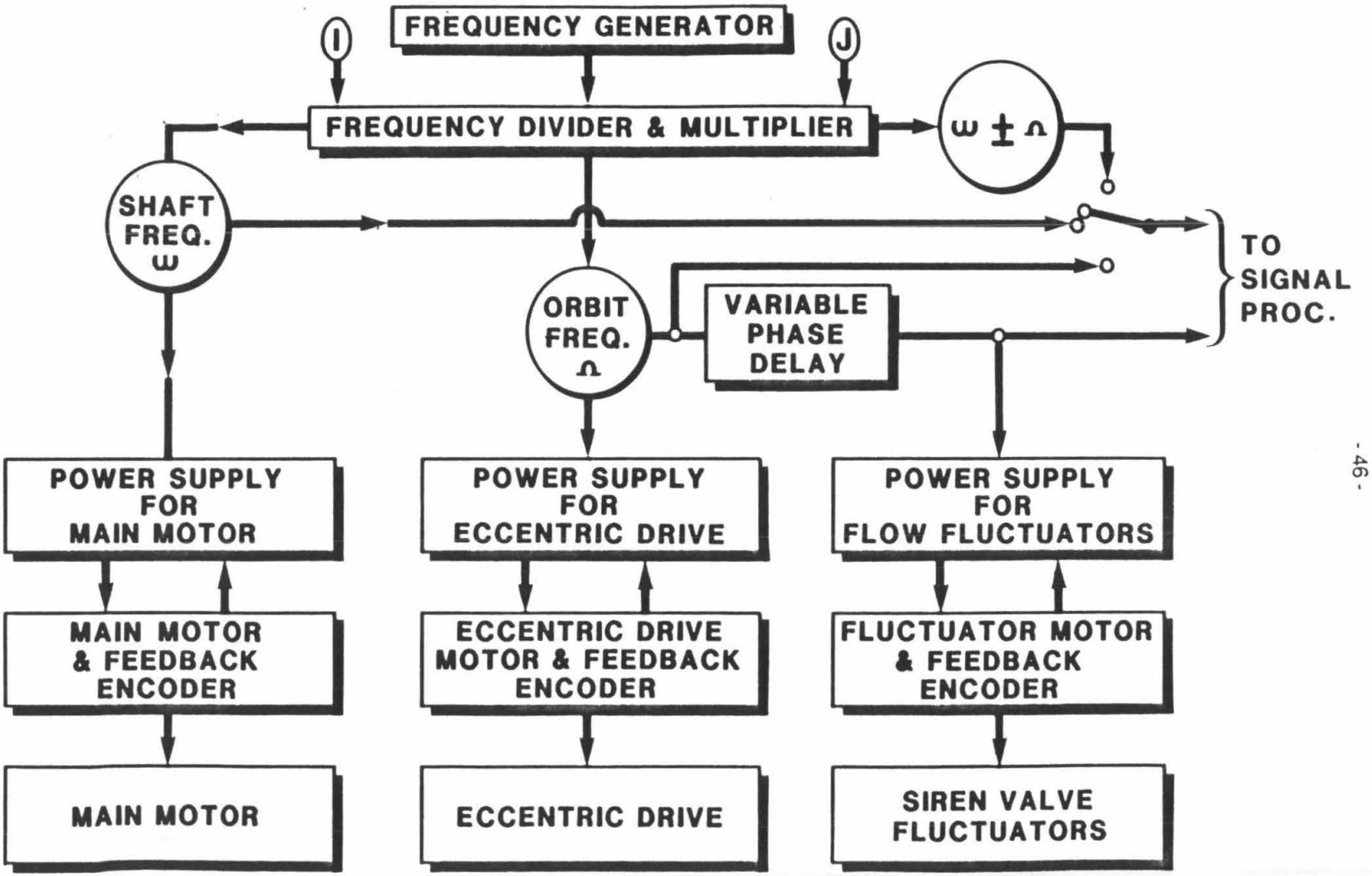

Fig. 2.8 Diagram of the Rotor Force Test Facility (RFTF)'s system controls (siren valve fluctuators were not used in the present experiments). Integers I and J are input by the operator to set the ratio of whirl-to-pump speed: $\omega = I\Omega/J$.

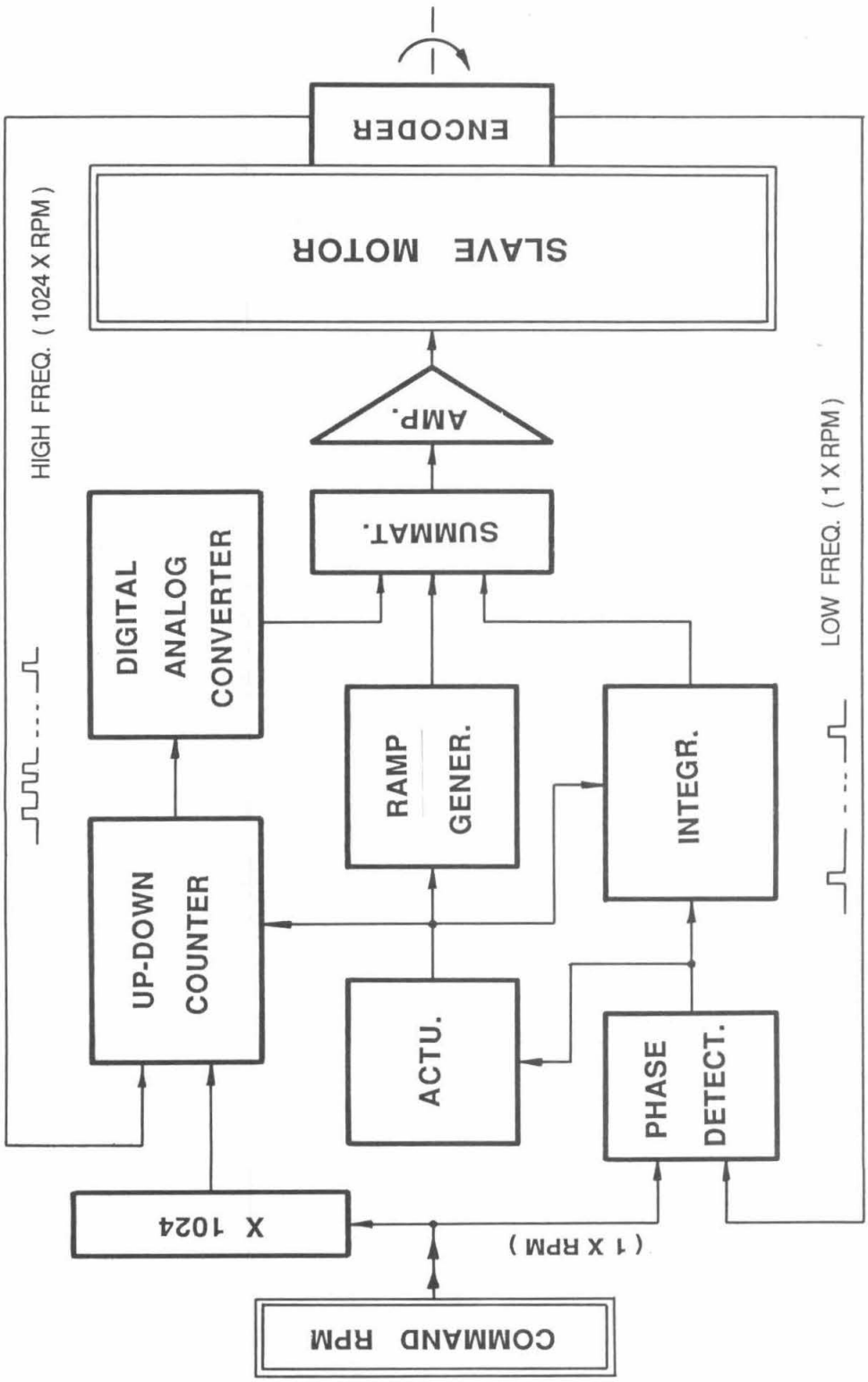

Fig. 2.9 Block diagram of main motor closed loop control system. The desired pump rpm is set by the operator via a frequency generator not shown. The same feedback control system is used for the whirl motor. The command whirl rpm is derived from the command pump rpm by use of a frequency divider/multiplier (not shown) and the two integers, I and J.

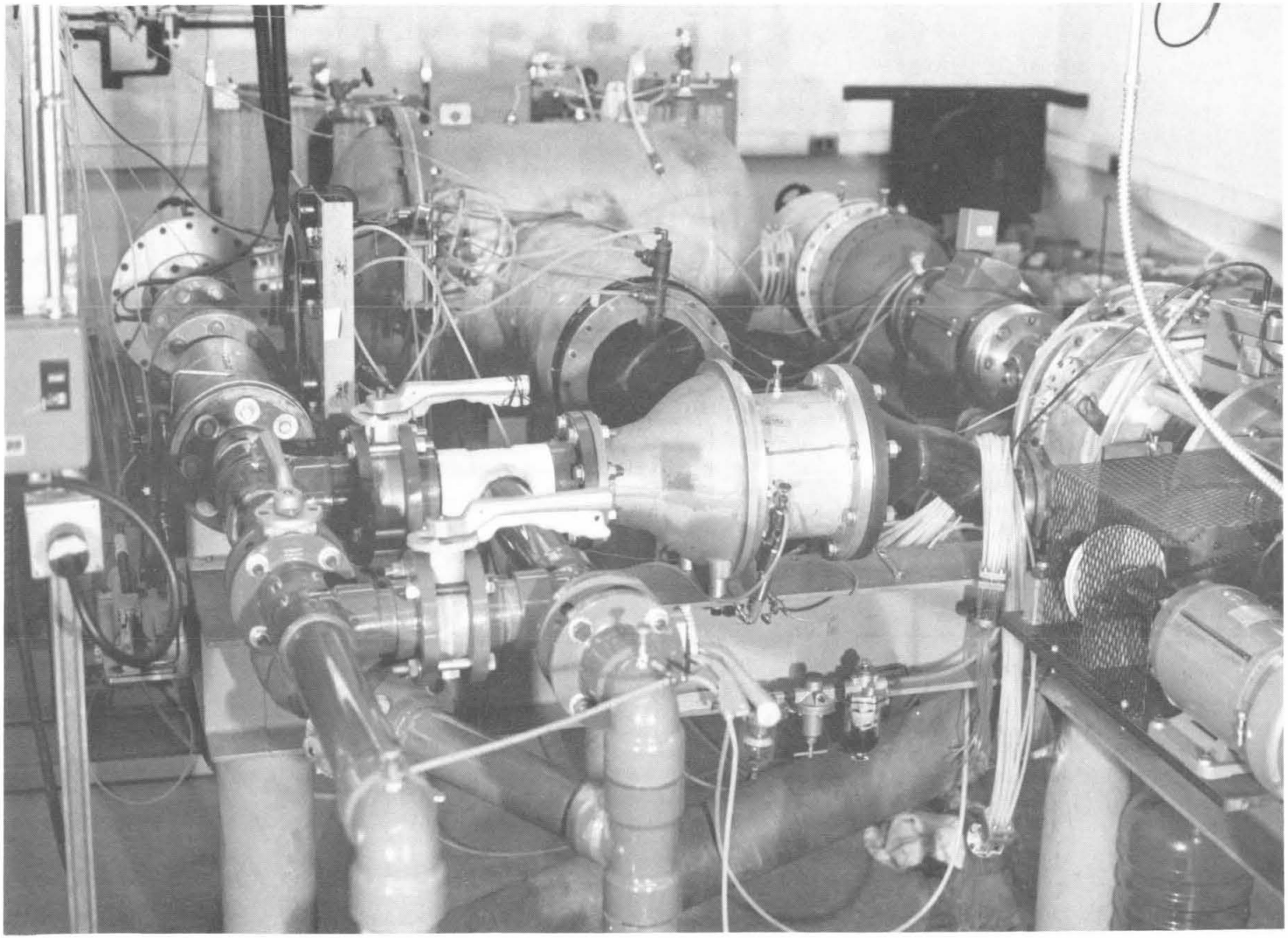

Fig. 2.10 Photograph of current Dynamic Pump Test Facility, including the RFTF's test section (right side) and auxiliary pump (foreground, left).

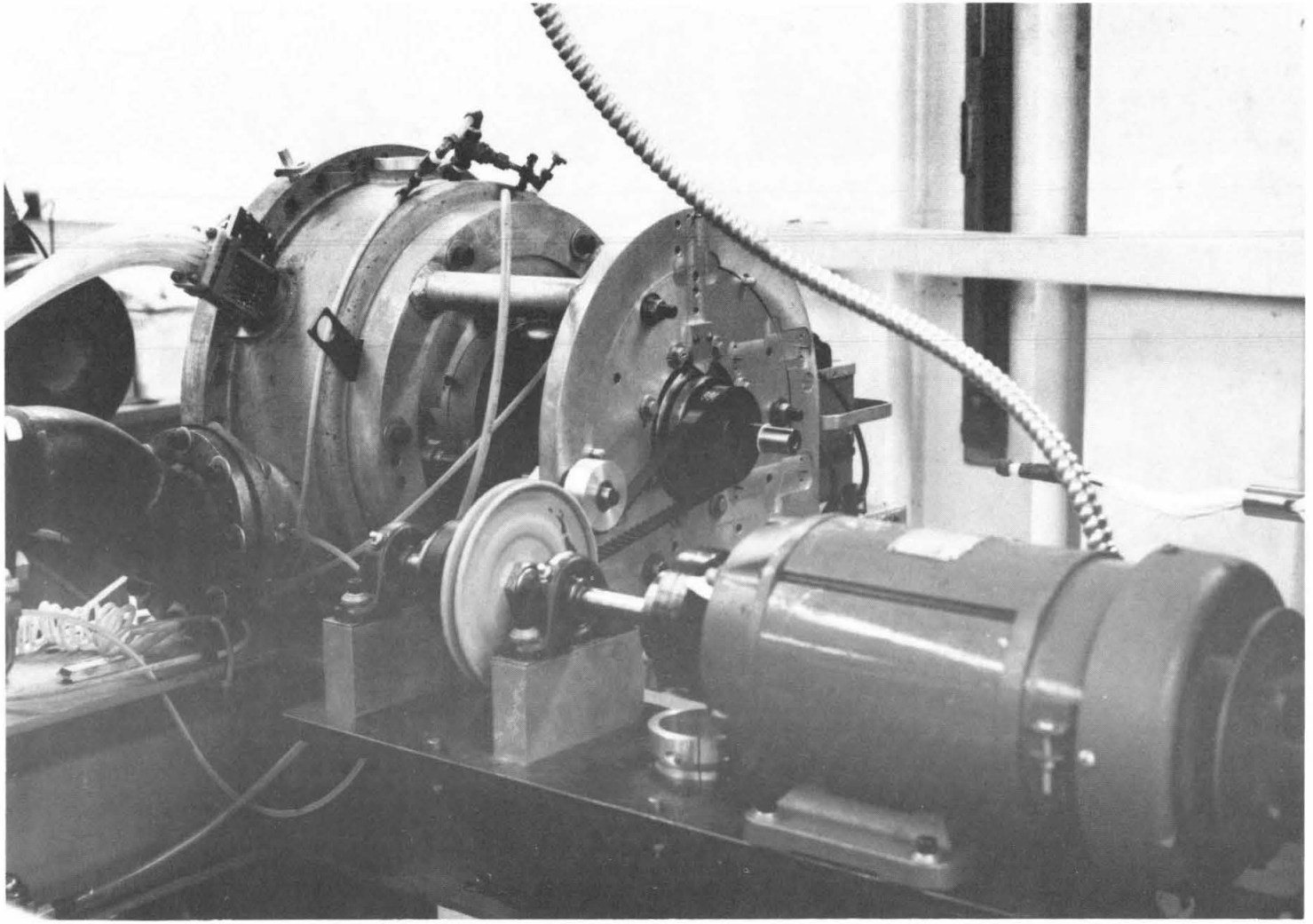

Fig. 2.11 Photograph of the RFTF part of the DPTF. Visible are the pump casing and discharge section, the eccentric drive motor and transmission (the picture was taken after the chain was replaced by a belt). The flexible coupling in the main shaft assembly is removed and the slip-ring side of the dynamometer cable can be seen in the far right.

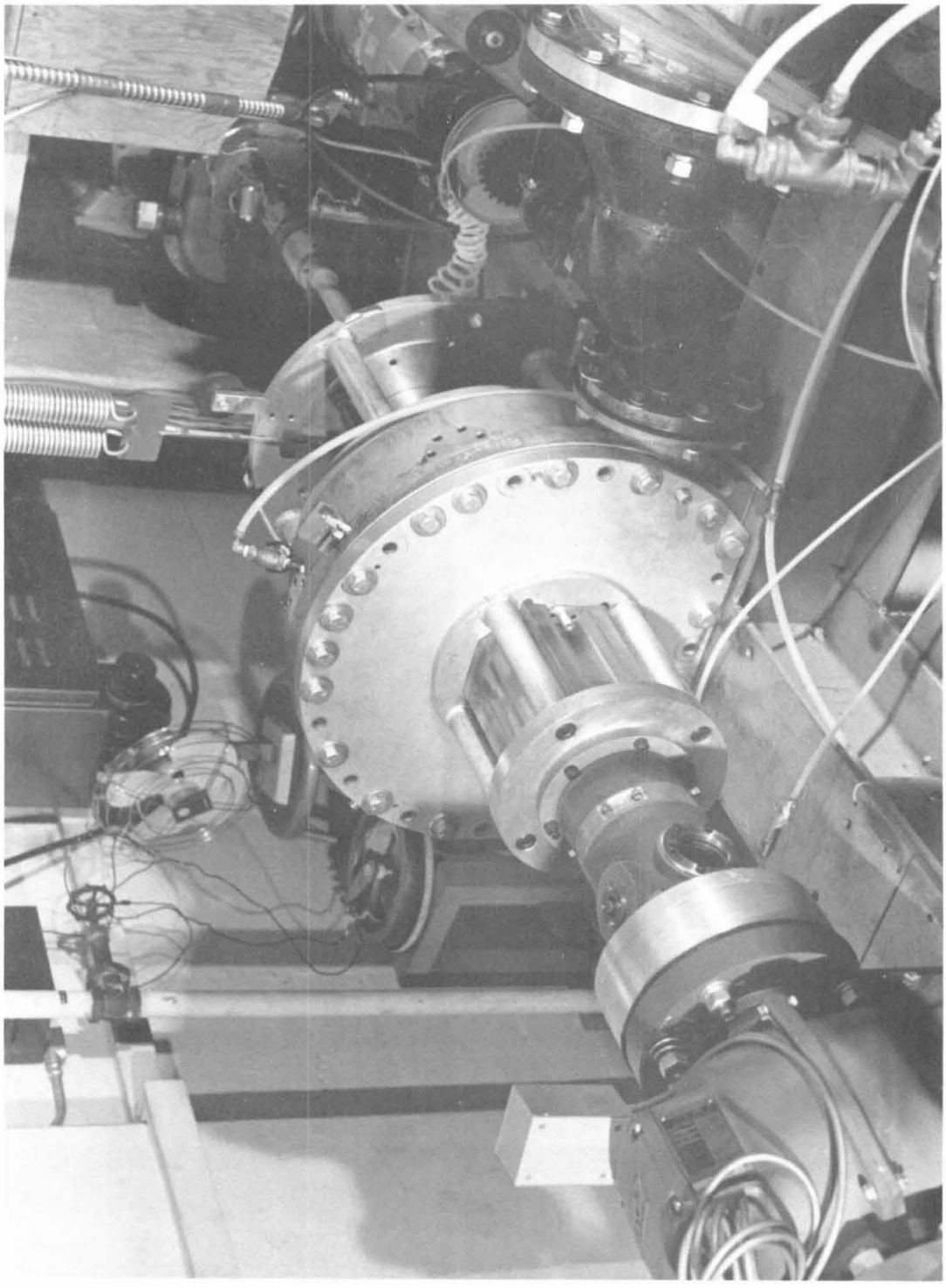

Fig. 2.12 Photograph of the test pump as viewed from the inlet side, with the casing cover bolted in place.

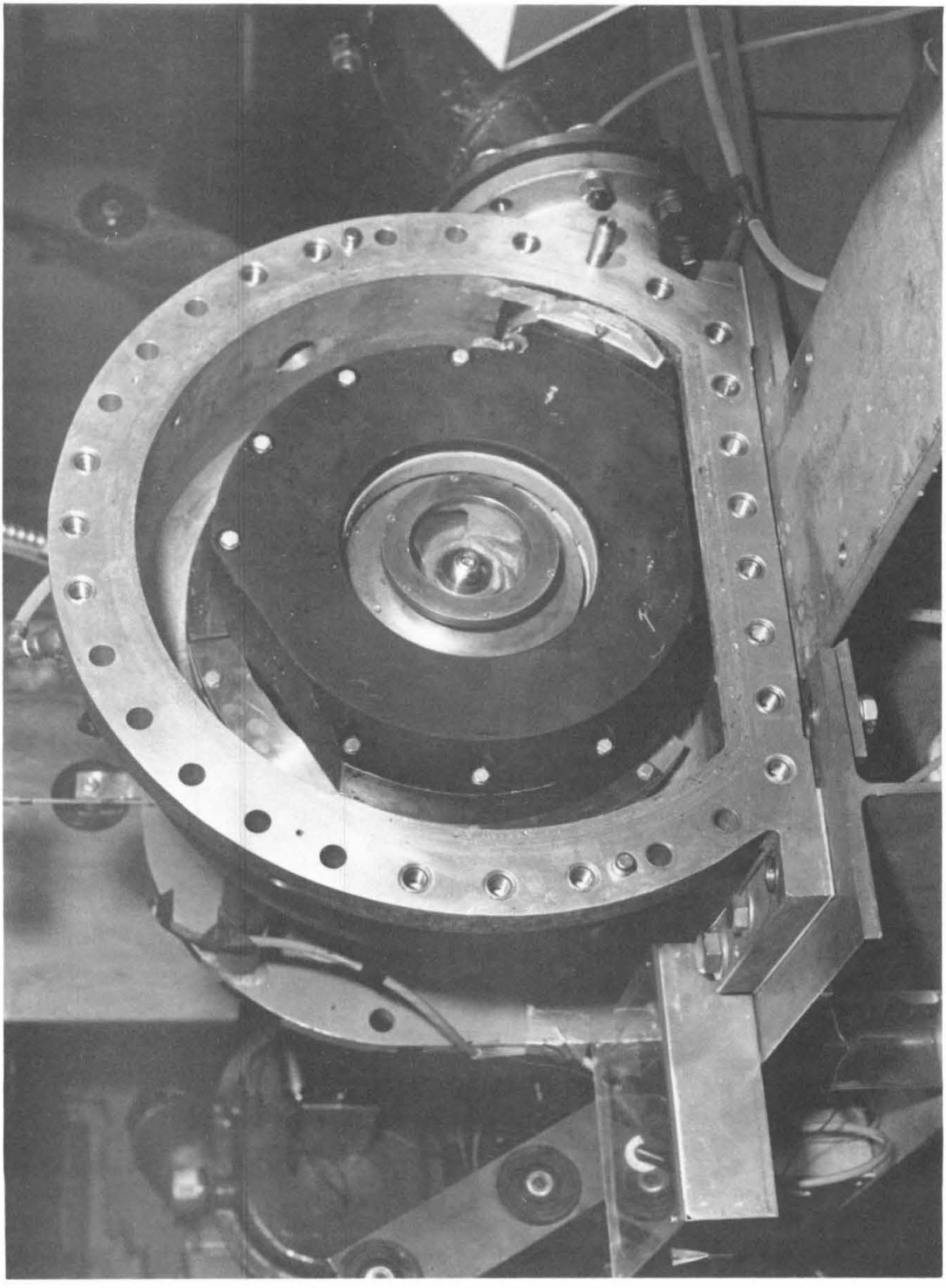

Fig. 2.13 Photograph of the test pump. The casing cover is removed, showing Impeller X seated inside Rocketdyne Diffuser Volute E.

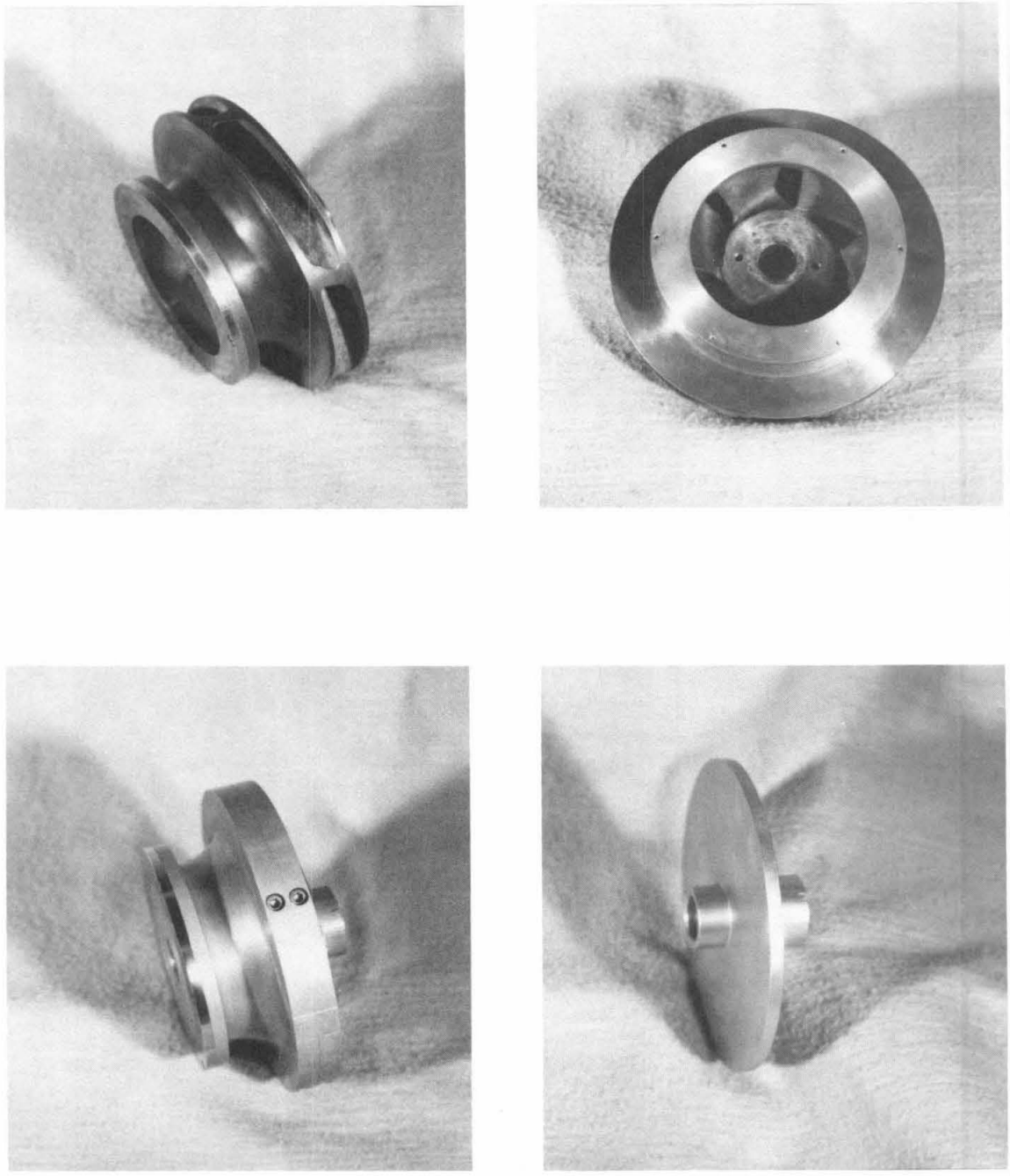

Fig. 2.14 Photographs of the various "impellers" tested. From top left: Byron-Jackson five-bladed Impeller X, Byron-Jackson six-bladed Impeller Y, solid dummy impeller, Impeller S, duplicating the outside geometry of Impeller X, and thin cirular disc, Impeller K.

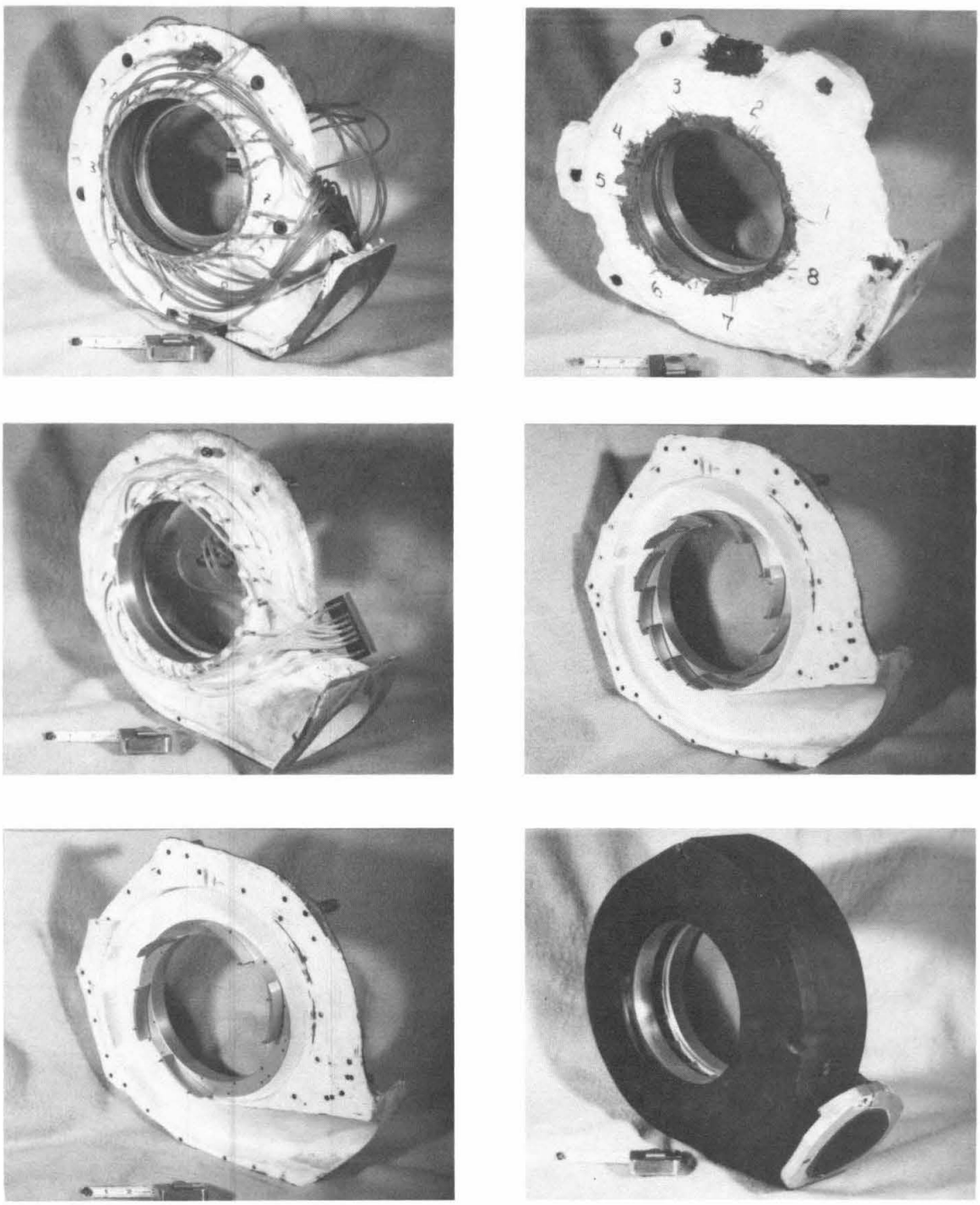

Fig. 2.15 Photographs of the various volutes tested. From top left: Volute A, Volute B, Volute C, Diffuser Volute H, Diffuser Volute G, and Rocketdyne Diffuser Volute E.

Chapter 3

ROTATING DYNAMOMETER

3.1 Introduction and Basic Design Features:

The particularly unique feature of the test setup is the incorporation of a dynamometer mounted directly between the impeller and the drive shaft (see photograph in Fig. 3.5 for location of dynamometer in rotor assebly). Clearly, proper design of this instrument is vital to the success of the entire project. This dynamometer rotates at shaft speed. Also, having adjustable impeller back seal clearance as an option implies that the dynamometer structure will be rotating in a water-filled cavity.

The other primary design requirements and constraints include (i) assurance of proper sensitivity given the anticipated low values of the measured forces (high signal-to-noise ratio), (ii) guarantee of good dynamic characteristics within the desired frequency range, and (iii) sufficent accurary: 1to 2% is considered good, 5% acceptable.

The magnitudes of the fluctuating forces which will be encountered by the dynamometer during deliberate whirl excitation are very difficult to estimate a priori. This is particularly true of the most important measurement, namely, that of the tangential force. Under these circumstances, the design was necessarily tentative and the risk of a redesign was implicit. Fortunately, the first candidate design proved to be adequate, as will be seen later. Following is a brief description of this candidate dynamometer. A design analysis is outlined in Appendix B and shoud be consulted for specific design figures. Also included in this appendix is a machine drawing of the dynamometer.

The basic structure of this dynamometer was chosen for its relative simplicity. It consists of four equally spaced elements (or posts) placed at a radius, R, of 4.76 cm (1.875 in), with their axes

parallel to the shaft axis (Fig. 3.1-top, and photograph in Fig. 3.6-bottom). The elements have (i) a square cross section, with side dimensions, a, of 0.51 cm (0.2 in); (ii) a length, L, of 2.54 cm (1.0 in), and (iii) are built into rigid base plates at both ends. Indeed, the four posts and the two end plates form a single monolithic stainless steel structure.

Although difficult to machine, this structure has some clear advantages. It is symmetric and easy to analyze (in terms of stress-strain relationships). It avoids the dynamic nuisances of shrink fits and other fastening devices, and provides more flexibility in grouping the strain gages into bridges. The choice of the material is appropriate in terms of modulus of elasticity, corrosion resistance and heat evacuation.

The elements were instrumented with strain gages in such a way as to record all six components of force and moment on the impeller. The requirements of small deflections and high sensitivities dictated the use of semi-conductor gages. Altogether thirty-six such gages were used forming nine complete Weatstone bridges (refer to Appendix B for details). This choice (i) assures adequate temperature compensation, (ii) accounts for all force interactions, and (iii) provides spare bridges (trouble-shooting and repairing damaged bridges can be very time-consuming, if at all possible).

One of the nine bridges is primarily sensitive to the thrust. It consists of four gages placed on the external faces of the posts, at mid-length, and having a gage resistance of 250 ohms and a nominal gage factor of about 60 (two gages have a positive gage factor and two gages have a negative gage factor). The eight other bridges are each sensitive to two of the remaining five generalized force components. The gages forming these bridges are placed at the quarter- and three-quarter length points from the ends of the elements, that is to say, near t the points of maximum element curvature. They have a gage resistance of 350 ohms and a nominal gage factor of 130. The excitation voltage was set at 5 volts on all bridges. The output signal amplification took place outside the test section and varied from 50 to 200 depending on load range (no amplification prior to slip-rings).

Waterproofing of the dynamometer was assured by means of two o-rings fitted between the dynamometer end plates and an enveloping cylindrical sleeve, in addtion to the two that seal it at the impeller and the drive shaft ends (Fig. 3.1 bottom). The implementation of the quasi-static seal presented some difficulties which will be described shortly. It was imperative that both this ring and the protecting sleeve do not interfere with the dynamic measurements, within the planned frequency range.

3.2 Fabrication:

The dynamometer main structure and the impeller mount (mandrel) were machined out of 17-4 PH stainless steel. Heat treating consisted of aging for one hour at 900° F, to a final Rockwell hardness of C40-41. Achieving as good a geometry as practical was a must, and very close tolerances had to be imposed. Providing adequate supporting and selecting the proper machining sequence were necessary in order to comply with these tolerances. The machining was done in-house, but the heat treating was contracted out.

Micro Engineering II of Upland, CA, was selected to carry out the task of instrumenting the dynamometer, including (i) surface preparation, (ii) gage bonding, baking, electric insulation, protection and waterproofing (against accidental leaks), and (iii) internal wiring of the nine full bridges. A fifty-conductor cable (14 out of the 50 conductors are spares) was connected to the dynamometer to carry the bridge input and output signals through the shaft center hole. The conductors are type AWG 30, solid, silver-plated copper, insulated with a wall of Goretex binder 0.1 mm (0.004 in) thick. They are protected by a PVC jacket having an outside diameter of 7.5 mm (0.3 in) and a thickness of 0.9 mm (0.035 in).

As mentioned above, waterproofing of the dynamometer was necessary but presented some difficulties. The quasi-static ring has to have a minimum squeeze in order to seal correctly. However, the deformation has to remain within a small "linear" range in order for the ring not to interfere with the deflections of the dynamometer (ring stiffness and damping negligible compared to those of posts). Also, the protecting sleeve (seen in photograph in Fig. 3.6 top) has

to be rigid enough so that the extraneous hydrodynamic forces generated in the surrounding cavity are not transmitted to the dynamometer.

The ring groove dimensions were determined through guestimates of expected forces and deflections. The sleeve was machined out of aluminum and had a wall thickness of 4.3 mm (0.17 in). It was anodized for protection against corrosion. It took a great deal of experimenting to find the right material with the right elastic properties for the quasi-static ring. It was discovered that this ring was acting as a nonlinear shunt between the dynamometer and the protecting sleeve, and that it was affecting the dynamic force measurements in terms of both magnitude and phase. The final choice was a 70-durometer neoprene ring.

3.3 Calibration:

A preliminary set of tests were conducted, in order to verify proper wiring and to determine initial working values for excitation and gain levels, before the actual calibration was performed. The purpose of the calibration procedure was to produce a six-by-six calibration matrix, [B], which would include all possible dynamometer interactions. The six-component force vector, {F}, can then be obtained from the measured bridge output voltages by use of the simple relation,

$$\{F\} = [B]\{V\} \tag{3.1}$$

where {V} is a six-component voltage vector. Six out of the nine Wheatstone bridges were selected so that {V} registers the effects of all six force components present during any particular test. The outputs of the remaining three bridges were monitored and stored as a back-up.

The matrix, [B], is simply the inverse of the matrix of slopes, [S], in which an element, S_{ij}, represents the output voltage,V_i of bridge, i, under a unit load of the j^{th} force component, F_j. Thus, if the bridges are ordered in such a way that bridge number i is primarily sensitive to at least the i^{th} force component, then matrix, [S], will be diagonally dominated. The off-diagonal elements of [S] represent dynamometer interactions. It is important to remark that the presence of

interactions is not necessarily indicative of poor design, and that interactions do not introduce any measurement errors, as long as they are linear, and that they are taken into account through a full calibration matrix. This is the case in the present measurements.

The slopes, S_{ij}, for both the six essential (i=1 to 6) and the three spare (i=7 to 9) bridges were determined through six sets of individual ("pure") force loadings, one for each generalized force component. A rig of pulleys, cables and weights (see photograph in Fig. 3.7) was devised to apply these pure loads, of both positive and negative signs, *in situ*. Each set comprised fifteen such loadings, with smaller increments for the smaller load values[1].

Presented in Fig. 3.1-top, are two typical calibration graphs. Since bridge number one is primarily sensitive to force compocent F1 and marginally to force component F2, the circles in this figure correspond to a primary effect, whereas the triangles correspond to an interaction (or secondary) effect. Two important facts are worth emphasizing. The first is that the primary response is about two orders of magnitude larger than the secondary response. The second is that both responses are perfectly linear (correlation coefficients are typically 0.999 for the primary graphs and 0.9 for the interction graphs, for all six sets of loadings).

This static calibration was supplemented with a number of tests including measurements of (i) drift (in time) under constant loads, (ii) response to much larger load values (200 to 500 N), response to combined loads, and (iii) response to hysteretic loading cycles. All of these tests proved to be very satisfactory. A typical hysteresis loop in response to a lateral loading cycle is shown in Fig. 3.2-bottom. The total cycle was completed in about thirty minutes. Also tested were the effects of bridge excitation voltage and bridge output amplifier gain levels. In fact, three separate calibration matrices were used, one for each gain level (50,100 and 150).

However, due to the dynamic nature of the primary forces to be measured, these static calibration matrices are useless unless the dynamic characteristics of the dynamometer are tested and found satisfying within the range of frequencies for which measurements are planned.

---

[1] For the two lateral forces, F1and F2, and the thrust (axial force), P (or F3), the load values were varied from -89 N to + 89 N (-20 lbf to +20 lbf). For the two bending moments, M1 and M2 (or F4 and F5), and the torque, T (or F6), the load ranged from -6.8 N-m to +6.8 N-m (-60 lbf-in to +60 lbf-in).

3.4 Dynamic Characteristics:

To this end further dynamic calibration tests were carried out under rotating and whirling conditions. First, a smooth aluminum flywheel with "hidden," but known, off-centered brass weights was substituted for the impeller, and the shaft was rotated in air without any whirl motion, at different speeds. This corresponds to a static loading in the rotating frame of the dynamometer. The forces obtained by processing the output signals through the static calibration matrix exactly matched the calculated values of the centrifugal forces.

Secondly, the balanced impeller was rotated in air without whirl motion so that the impeller weight is seen by the dynamometer as a periodic (dynamic) lateral force. This allowed evaluation of the dynamic response of the balance up to about 50 Hz (3000 rpm). The magnitude and phase of the response remained unchanged up to this frequency. Results from this test are presented in Fig. 3.3. The weight of the impeller was recovered to within two percent, and phase angle fluctuations remained within one degree.

Similar dynamic checks were conducted using only whirl motion. The resulting magnitudes and phase angles of the centrifugal force due to the mass of the impeller displayed the same satisfactory behavior. As mentioned above, it took a great deal of experimenting with various sealing rings before these results were reached.

The last set of dynamic tests consisted of spectral analyses of various analog recordings of bridge output signals. These tests covered the entire range of concentric and eccentric motions of the rotor, both separate and combined. Also performed were analyses of rotor responses to lateral force impulses (hammer shocks). The conclusion of these tests was that below a rotational frequency of about 160 Hz resonance , free operation can be expected.

The graphs in Fig. 3.4 show sample spectra from these tests. The top graph shows the system's natural frequency of transverse motion obtained from a hammer test. This frequency was lower than expected. The explanation is overestimation of bearing stiffness. However, this did not

have an impact on the experimental scope. Only the data related to blade passage were affected (for a six-bladed impeller the highest pump speed would be less than about 1600 rpm). The bottom graph in Fig. 3.4 shows the spectrum of a recording obtained for bridge number one while the pump was running dry at 800 rpm. The magnitude of the primary response (-17 Db, at 13 Hz) is about ten times that of the highest noise spike (-36 Db, at 180 Hz).

Altogether, the dynamometer performed extremely well under these dynamic tests. The static calibration matrices were thus sufficient to process the dynamic measurements.

ROTATING DYNAMOMETER

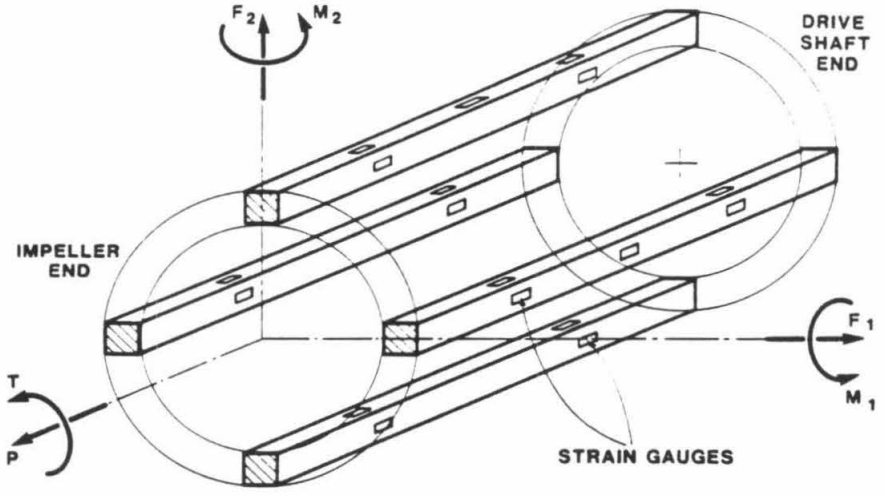

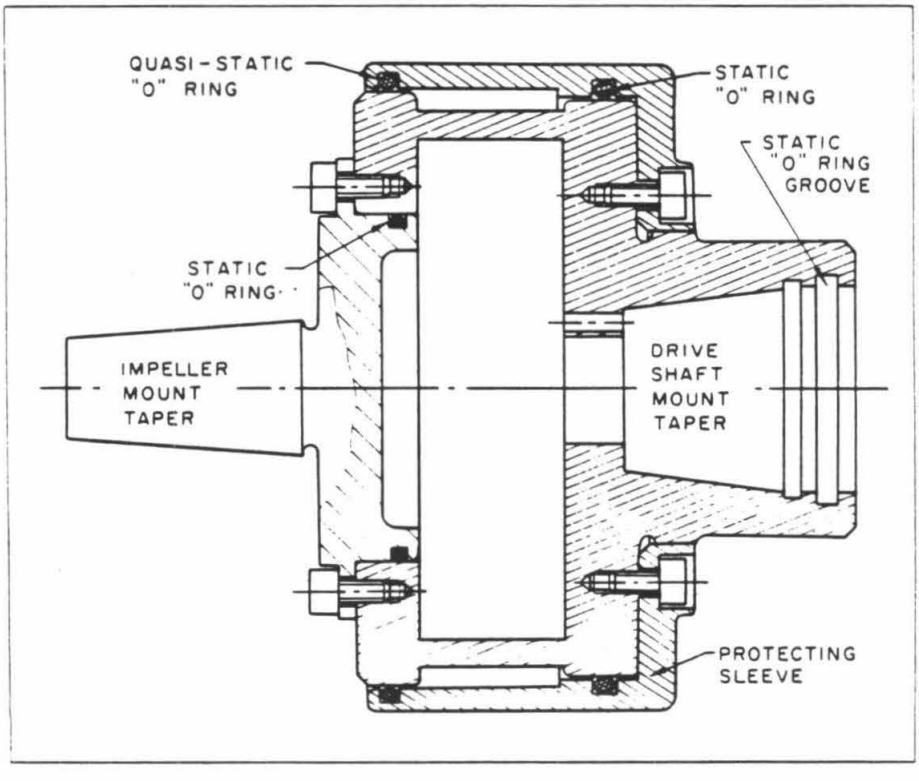

Fig. 3.1 Top: schematic of rotating dynamometer's basic four-post configuration showing strain gage location and generalized force sign conventions. Bottom: assembly drawing of rotating dynamometer with protecting sleeve, impeller mounting mandrel, and various o-rings used to seal dynamometer cavity.

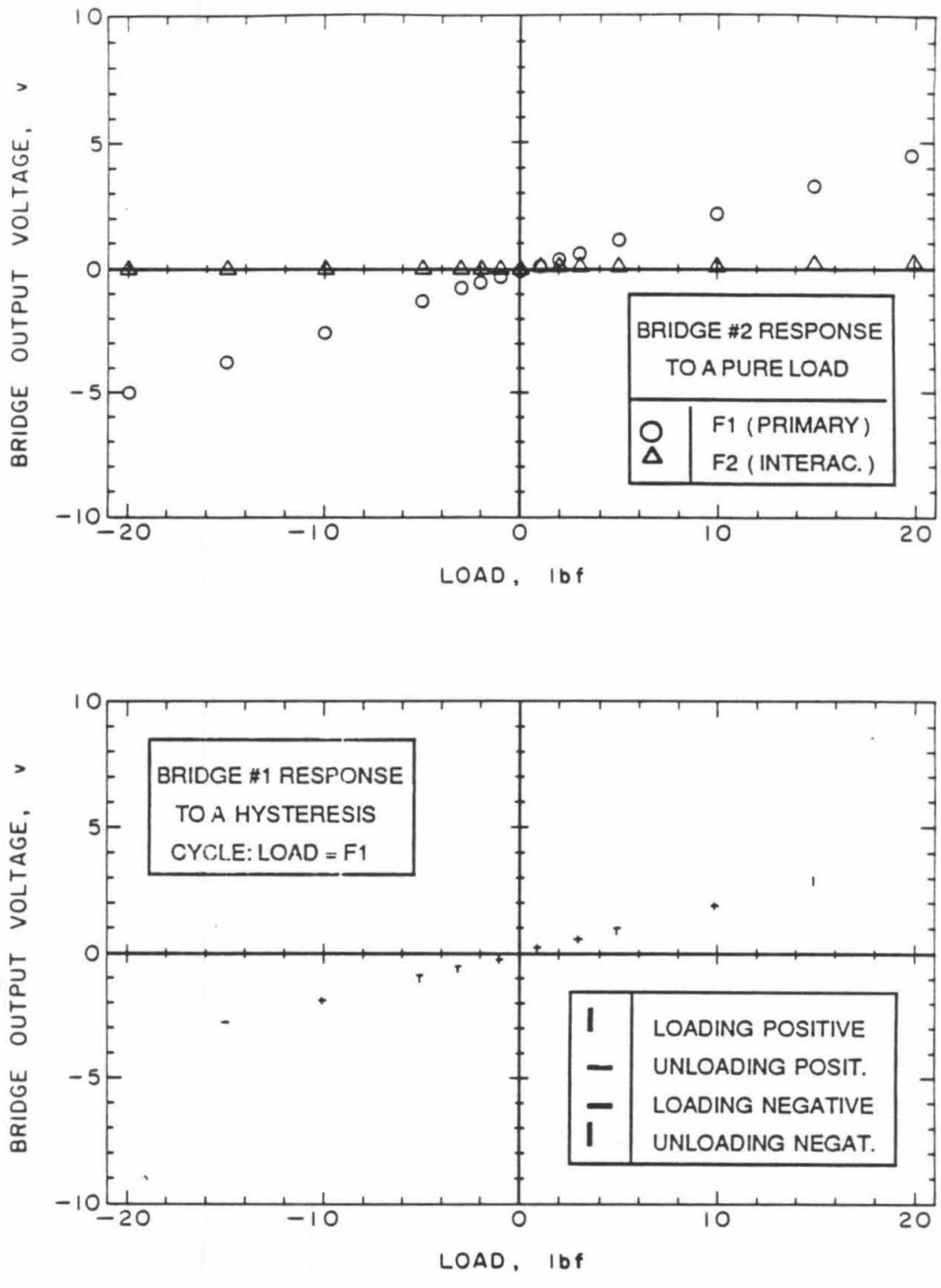

Fig. 3.2 Top: typical *in-situ* static calibration loading graphs. Bridge #1 is primarily sensitive to loading in the F_1 direction. Bottom: typical response of same bridge to a hysteresis loading cycle in primary direction.

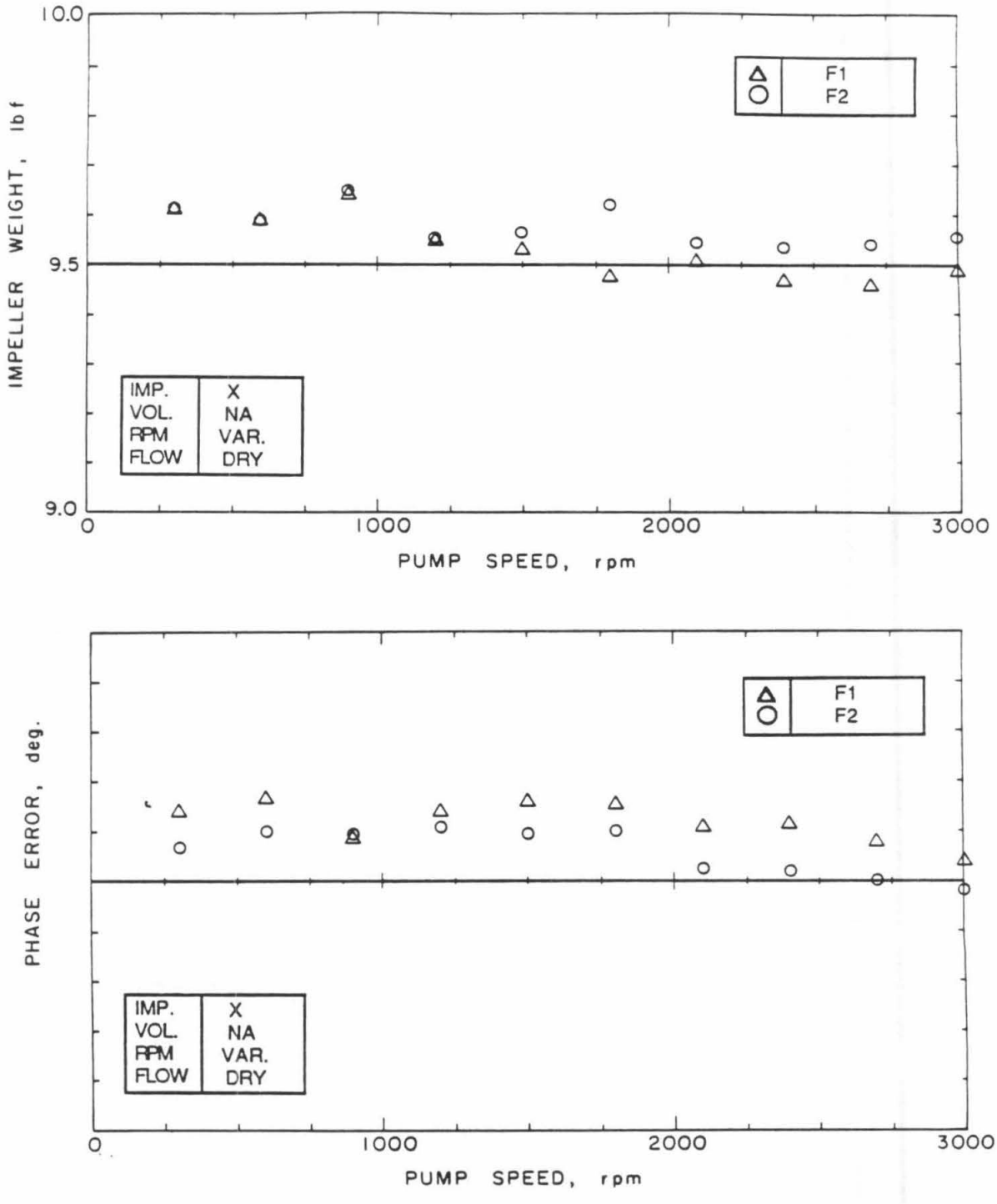

Fig. 3.3 The weight of Impeller X is sensed as a rotating force vector in the frame of the dynamometer (F_1,F_2), when the shaft is rotating. Plotted are: magnitude of gravity vector (top) and phase angle (bottom, referenced to upward vertical), for various shaft rotational speeds in air (up to 3000 rpm).

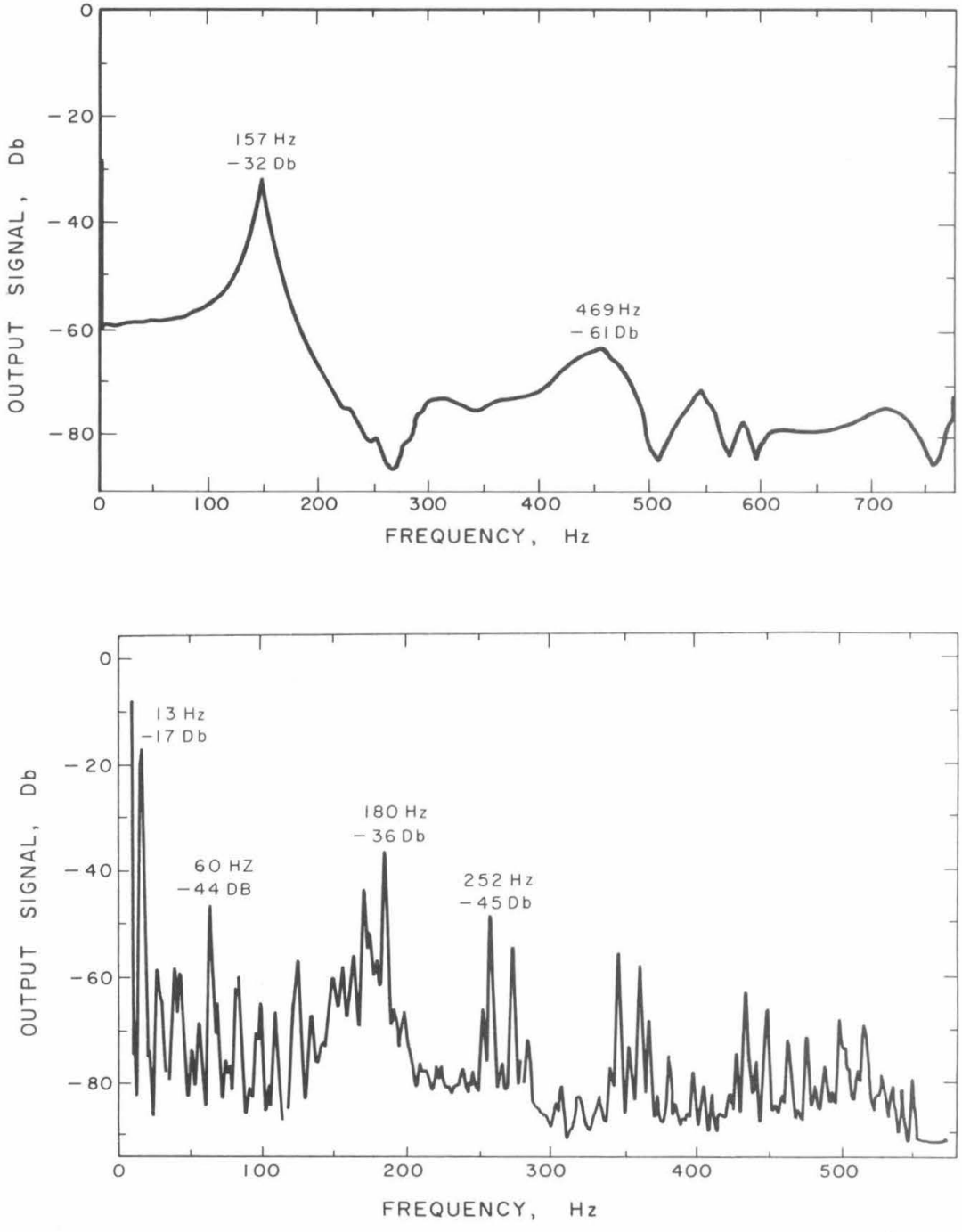

Fig. 3.4 Top: spectral response of the installed impeller-dynamometer-shaft-eccentric-drive system after a lateral impulse (hammer shock) is applied to the impeller. System damped natural frequency is shown to be near 160 Hz. Bottom: typical spectral analysis of bridge output signal recorded during shaft rotation in air at 800 rpm. Synchronous response is at 13 Hz (peak at -17 Db).

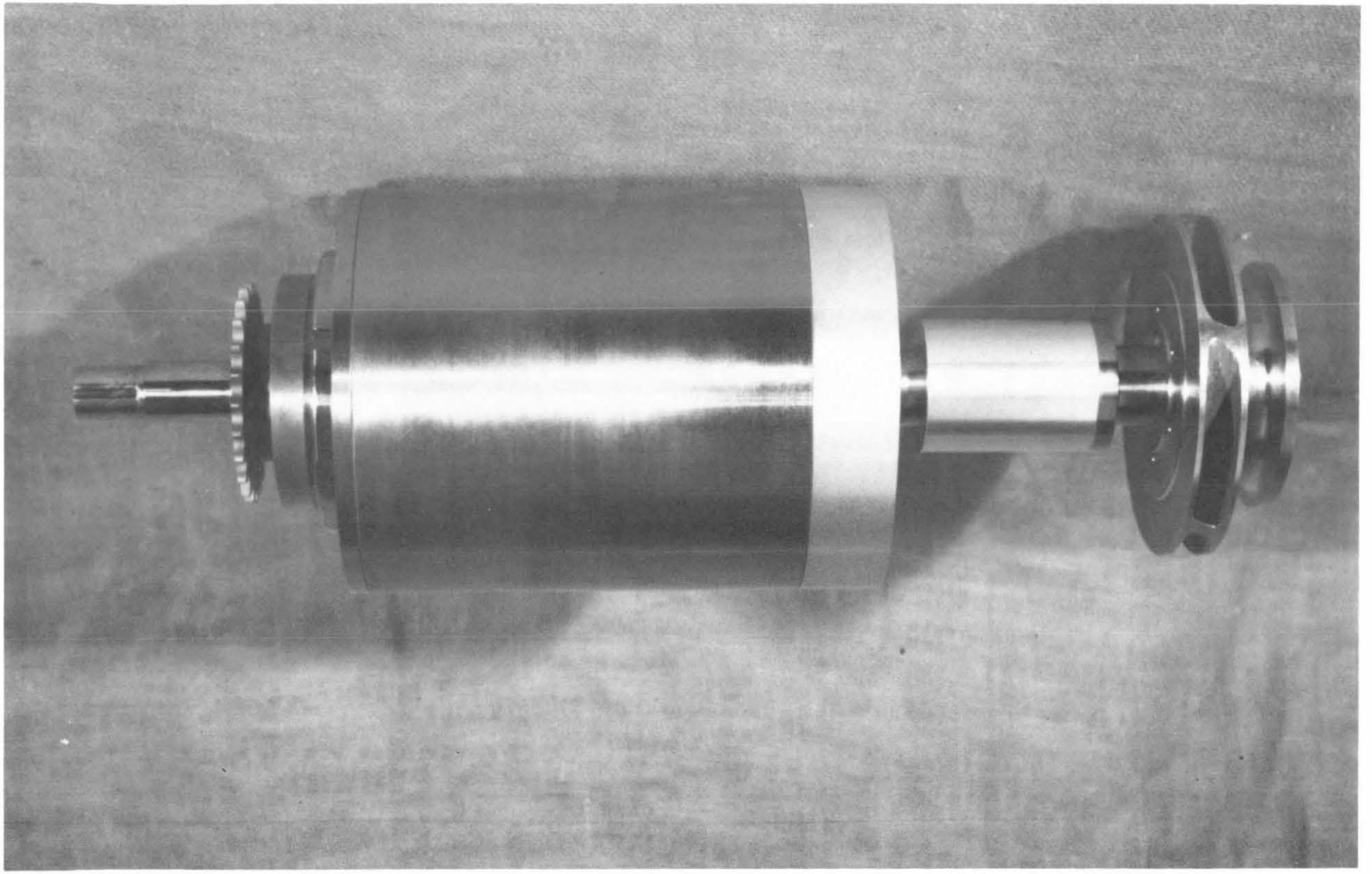

Fig. 3.5 Photograph of the eccentric drive disassembled from the Rotor Force Test Facility. Visible are (from left to right) the sprocket wheel, the main double bearing housing, a dummy replacing the actual dynamometer, and Impeller X mounted at the end of the drive shaft.

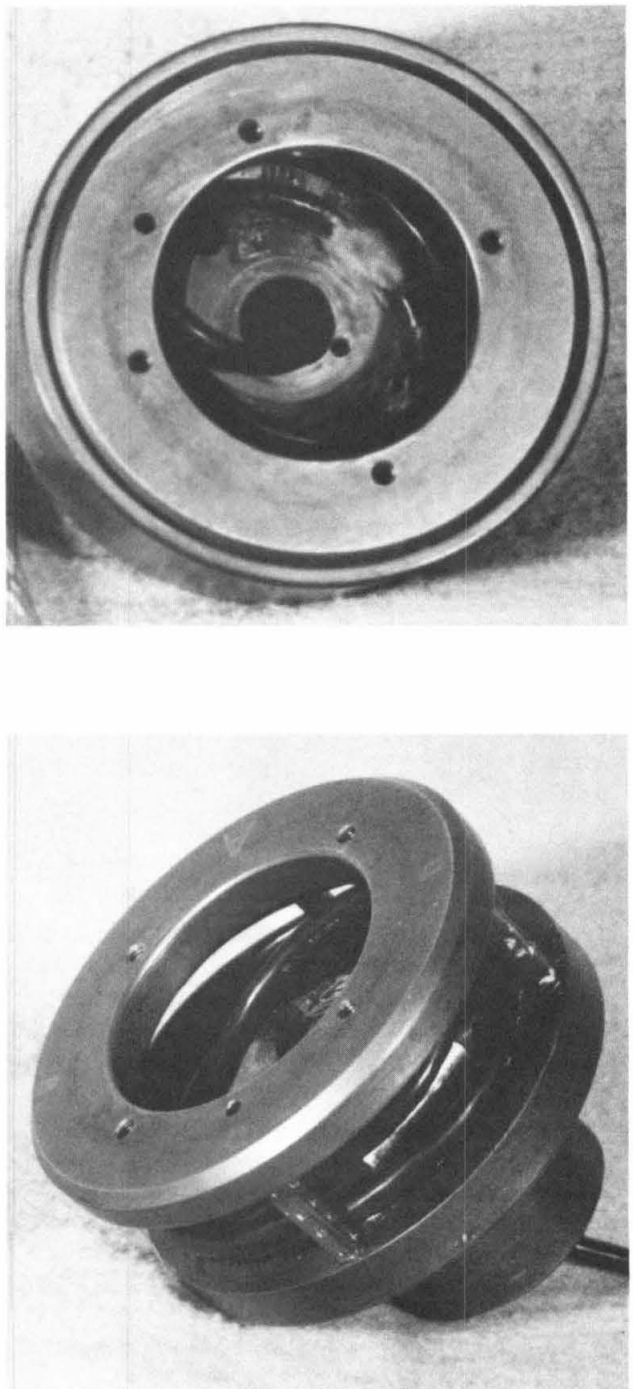

Fig. 3.6 Photographs of the rotoating dynamometer with (top), and without (bottom) its protecting sleeve.

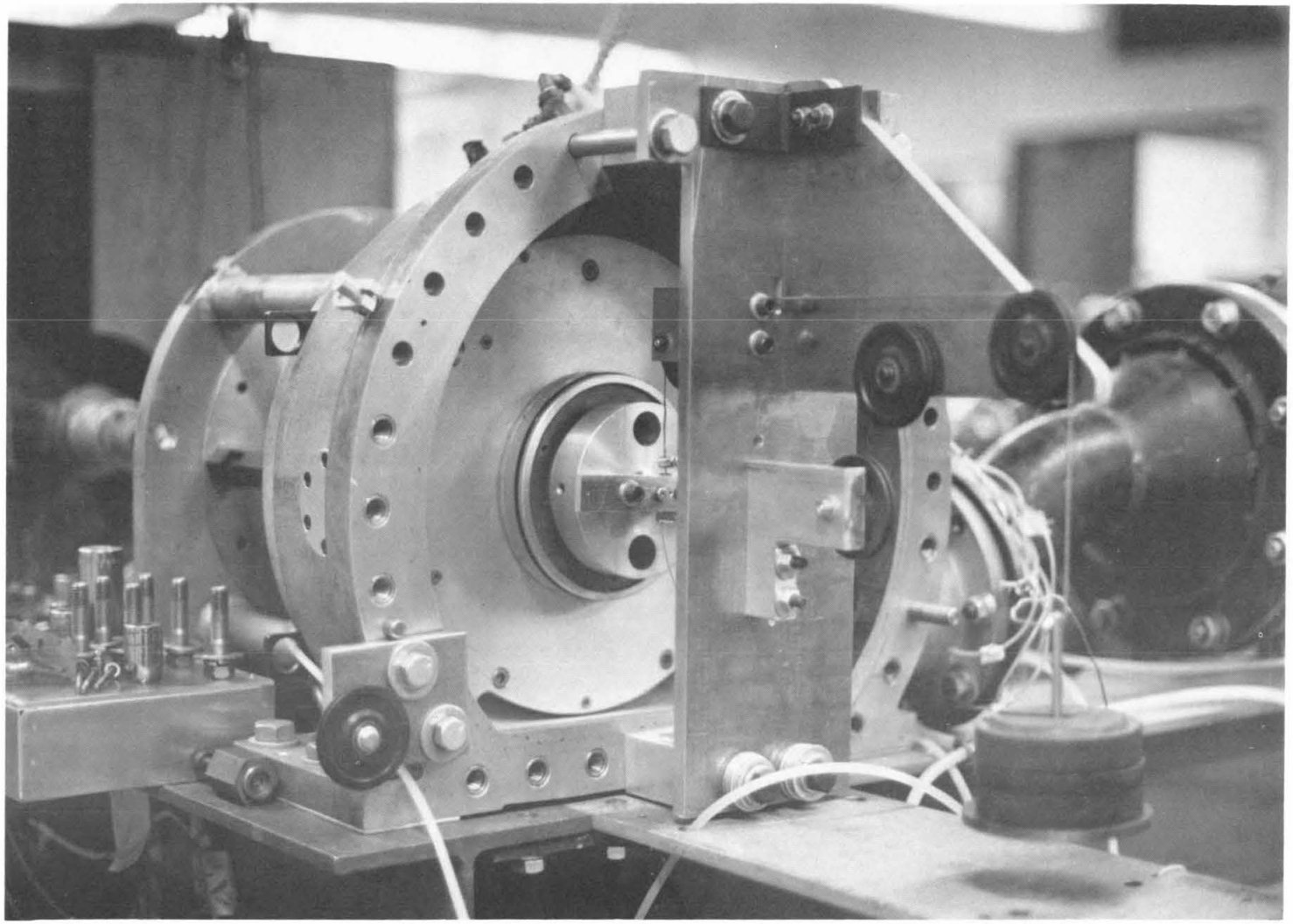

Fig. 3.7 Photograph of typical arrangement of the static calibration rig, employing loading plate, brackets, pulleys, cable and weights. Arrangement shown is for loading in the positive F_1 direction (upward vertical in laboratory frame).

Chapter 4

MATRIX OF EXPERIMENTS

Due to the size and complexity of the experimental setup, extreme caution had to be exercised in order to ensure error-free measurements. One had to make certain that what was intended to be measured had actually been measured. The preparatory work and preliminary testing took a surprisingly large amount of time compared to the main measurements.

This chapter is comprised of four sections. In the first section, the test hardware and variables are briefly reviewed. The second section contains a description (and a summary of some results) of preliminary test measurements, including a discussion of how parasitic and tare forces are dealt with. Various auxiliary tests are presented in the last section, Section 4.4, following the description of the main fluid force measurement tests in Section 4.3.

4.1 Test Hardware and Variables:

A fair amount of effort went into planning the test matrix. A compromise had to be reached in determining a suitable number and range of test variables to be explored. The idea was to achieve representative and conclusive results, while keeping the number of individual test runs within practical limits,, and taking into account the available test hardware. A quick review of this test hardware and the associated test variables is in order at this point.

The design characteristics of the various impellers and volutes tested are summarized in Figs. 2.4, 2.5 and 2.6. Essentially, two real impellers were available for testing. They are designated Impeller X and Impeller Y. Both are of the three-dimensional, shrouded type. They are very similar in most regards (specific speed, main dimensions,...), the only exception being the number of vanes, five for X and six for Y. The impellers designated 'S' and 'K' are not real impellers. They were used in various auxiliary tests designed to supplement the data gathered with X and Y.

On the other hand, a large variety of volute designs were available, beginning with Volute A which was designed to match Impeller X at its nominal flow. The combination Impller X-Volute A represents a typical industrial unit, and was tested more extensively than any other. Volute D (with its various diffuer-vane configurations, D-0, D-F6, D-G6 and D-H12) nearly matches Impeller X. All other volutes are mismatched to X (and Y), deliberately (in the case of wider than normal Volute B and tighter than normal Volute C, which were made in-house) or otherwise (Volute E was donated by Rocketdyne). Volutes A and D have a trapezoidal cross-section, Volute B a circular cross-section, and Volute E an elliptic one. All volutes are of the spiral type, except for Volute B, which has a constant radius. Other pump design features included the arrangement of impeller front and back face seals, and the arrangement of leakage-limiting rings fitted to Volute A near the impeller discharge; see Fig. 4.1. The pump operating variables included:

(i) the pump speed, variable from zero to 3000 rpm,

(ii) the pump flow rate (which determines the non-dimensional flow coefficient), variable from zero at shut-off, to maximum flow when the throttle is fully open,

(iii) the pump inlet pressure, variable from near zero to 480 kN/m^2 (low vacuum to 70 psia); this was intended as a test variable for measurements under cavitating conditions, however, since none were performed this pressure was simply kept well above vapor pressure for all tests.

As far as the whirl motion is concerned, the whirl speed and direction were effectively the only test variables. The choice of a constant setting for the whirl orbit radius has already been discussed in Chapter 2, Section 2.3. The phase of the whirl motor was directly related to that of the pump motor by virtue of the feed-back control system described in Chapter 2, Section 2.6. An upper limit of 1200 rpm was set for the whirl speed as a precautionary measure to limit the inertial loads and mechanical vibrations on the rotor assembly. Subsequently, the following ranges were selected for the reduced whirl frequency, Ω/ω:

(a) $-0.4 \leq \Omega/\omega \leq 0.4$ for 3000 rpm pump speed,

(b) $-0.6 \leq \Omega/\omega \leq 0.6$ for 2000 rpm pump speed,

(c) $-0.8 \leq \Omega/\omega \leq 0.8$ for 1500 rpm pump speed,

(d) $-1.1 \leq \Omega/\omega \leq 1.1$ for 1000 rpm pump speed, and

(e) $-2.2 \leq \Omega/\omega \leq 2.2$ for 500 rpm pump speed;

the negative sign in the inequalities refers to the negative whirl direction. Thus, both subsynchronous and supersynchronous whirl motions could be explored in both directions.

4.2 Preliminary Measurements:

Hydraulic Performance Data:

One of the objectives of the study was that the pumps tested be representative of those used in high performance applications. For the sake of completeness, hydraulic performance data in the form of graphs of head coefficient versus flow coefficient were collected on all impeller-volute combinations tested, either from stand-alone performance tests or as by-products of the fluid force measurement tests.

Representative results from these tests are included in Chapter 6. Also included in Chapter 6 are data on other performance variables (torque and efficiency coefficients) supplied by the manufacturer of impellers X and Y.

Treatment of Tare Forces:

Two primary sources of tare forces were identified:

(a) gravitational and pure mass inertial loads on rotor, and

(b) the buoyancy force on the submerged impeller and attached dynamometer.

Forces (a) were removed by subtracting the forces measured in a "dry" run, where the impeller was operated in air, from the forces measured in a "wet" run where the same impeller was operated in water at the same speeds Ω and ω. Thus, each eventual data point was determined from the results of two separate tests.

As a side benefit, these dry runs provided a reliable, independent means of dynamically calibrating the force measurement system. This was done by comparing the predicted values of the lateral force (knowing the rotor mass and the whirl radius and speeds) to those measured by the dynamometer for various shaft concentric and eccentric rotation speeds.

When the measured forces are presented in terms of an average (over the whirl orbit) normal force, F_N, and an average tangential force, F_T, plotted versus the reduced whirl frequency, Ω/ω (see Fig. 4.2, RPM refers to the speed of concentric rotation), the following statements can be readily verified:

(i) Shaft concentric rotation does not make a difference. The force whose frequency is coherent with the whirl frequency is a purely centrifugal one, depending only on the whirl radius and frequency, and on the impeller mass (if present, rotor mass imbalance would result in a stationary force in the frame of the dynamometer, and would affect the measurements only during synchronous whirl).

(ii) The average normal force displays a perfect quadratic variation with whirl speed, and the average tangential force remains zero at all times, which means that no shift in the phase of the radial force vector occurs inside the band of frequencies tested.

Provision was also made in the software to subtract out force (b) which is simply equal to the weight of the dry rotor minus that of the submerged rotor (as measured by the dynamometer when the rotor is still).

Parasitic Hydrodynamic Forces:

These are hydrodynamic forces acting on the external surfaces of the submerged dynamometer. Preliminary tests showed that these forces could reach significant levels and *hence interfere* with the primary impeller-volute forces. It became necessary that these forces be dealt with in some way. Two options were available: (i) measure these forces and subtract them

from the impeller-volute forces, or (ii) modify the original design so as to eliminate them or at least keep their magnitudes below significant levels.

This second option was chosen and was implemented by enlarging the gap surrounding the dynamometer's shield. Before this modification, these forces represented as much as 10% of the impeller-volute forces. This percentage is now less than 3% at the higher negative whirl speeds, and practically null at the lower negative whirl speeds and throughout the the entire positive whirl speed region (which is of more interest); see Fig. 4.3 for results and Chapter 6 for explanation of format and notation. Thus it was safe to neglect these parasitic hydrodynamic forces.

Notice that option (i) would have required a much higher processing effort. It should also be pointed out that these parasitic forces were evaluated from the results of two force measurement tests performed at the same combinations of concentric and eccentric rotation speeds: a wet run without the impeller and a dry run without the impeller.

4.3 Fluid Force Measurements:

These measurements constitute the bulk of the effort. Essentially, they can be placed in either of two categories. Those performed with the impeller center located at a fixed postion on the whirl orbit, and those performed with the impeller whirling around the circular orbit. The first ones yield data on the radial forces for various (fixed) positions of the impeller center inside the volute; these forces can be further processed to yield pure stiffness matrices. The second ones yield data from which both steady and unsteady forces (in the form of a generalized stiffness matrix) can be extracted.

It is of fundamental importance to realize that the first measurements are not absolutely necessary, in the sense that the information they contain could be derived from the second measurements. Thus, the latter are of most interest in this study since they completely characterize the phenomenon of whirl. This will become clearer once the data reduction technique has been explained; see next chapter.

However, since the former measurements are much less involved in terms of data acquisition and processing, they were systematically performed for all impeller-volute combinations tested. Their results are useful in two ways: (i) they provide an idependent means of checking the performance of the rotating dynamometer (through comparison with the results obtained by Chamieh [32], who used an entirely different force balance and data acquisiton and processing software), and (ii) they provide an indication on the validity of the technique used to reduce the measurements made on the whirling impeller (as the whirl speed gets smaller and smaller, the measured forces should approach those obtained for fixed positions of the impeller center inside the volute).

Typically, results from both types of measurements are combined in single graphs of force versus reduced whirl frequency, the no-whirl measurements providing the single data point at the origin, $\Omega/\omega=0$.

Measurements in the Absence of Whirl:

For each selected combination of impeller, volute, pump speed (as represented by the shaft radian frequency ω), and pump flow rate (as represented by the flow coefficient Φ), a wet run is taken for each position of the impeller center on the whirl orbit. A few clarifying remarks are in order:

(i) A run consists of a complete cycle of data acquisiton in which all data channels are sampled in a manner described in the next chapter, Chapter 5. Also recorded during the run are readings from various auxiliary system instruments.

(ii) The number of orbit positions for which runs are taken varied from 24, at first, to 4, corresponding to locations which were 15 to 90 degrees apart. It was verified that little accuracy is lost in going from 24 to 4. Four is however the minimum number of runs needed to determine all elements of the two-by-two pure stiffness matrix from these tests.

(iii) Only wet runs are needed in these 'static' tests since, as will be explained in the data reduction technique, results from runs taken at locations diametrically opposite each other (on the circular whirl orbit) can be processed in such a way as to eliminate the need for explicitly measuring and subtracting out the tare forces (obtainable from a dry run).

Measurements in the Presence of Whirl:

For each selected combination of impeller, volute, pump speed (as represented by the shaft radian frequency ω), and pump flow rate (as represented by the flow coefficient Φ), a set of wet runs is taken, one run for each value of whirl speed (as represented by the whirl motor radian frequency, Ω, or equivalently Ω/ω, in normalized notation). In this case, however, the results of dry runs performed for the measurement of the tare forces, at the same ω and Ω, are subtracted from the results of these wet runs, leaving only purely hydrodynamic forces and force matrices. The data reduction process is explained in Chapter 5.

Considering the wide variety of test hardware and the number of test variables, the total number of runs would be well in the five digits, if all possible combinations were tested (based on the following 'typical' figures: 2 to 4 impellers, 8 volutes plus the no-volute case, 1 to 5 pump speeds, 3 to 6 flow rates, and 9 to 20 whirl speeds). As mentioned earlier, compromises were sought by which a maximum number of representative tests were achieved from a manageable number of runs. For example, when verifying the scaling of forces with pump speed, only one impeller, one volute, two flow rates (at and off- design), and nine whirl speeds were used; when studying the effect of the flow coefficient, only one impeller, two volutes, one pump speed, and nine whirl speeds were explored; when studying the effect of volute design, only one impeller, one pump speed, and nine whirl speeds were explored; ...etc.

Despite these compromises, however, no less than twelve hundred individual test runs were performed. The exact combinations of test hardware and variables used in these tests can be determined from the figure legends in Chapter 6, for those test runs whose results are explicitly

reported. Clearly, the main test variable is the reduced whirl frequency, Ω/ω; and, although three tests at three values of this variable would, theoretically, suffice to get an indication on the stiffness, damping and inertia effects, as many as twenty values were used at times in an effort to capture possible localized behavior (especially near the origin). All considered, it is safe to assume that the generalizations implicit in some of the conclusions drawn from the results are fully justifiable.

4.4 Auxiliary Measurements:

These mesurements are auxiliary only in the sense that they did not deal directly with the pump's main components (impeller and volute) or main operating variables (flow rate and speed). Instead, they concentrated on what might be considered secondary aspects of pump geometry and operation. These included measurements of static pressure distributions, blade-passage forces, and more importantly leakage-flow-dependant forces.

Here, again, the measurements fell in either of two categories, those performed in the absence of whirl and those performed in the presence of whirl. Although a full study of the contents of these measurements was not possible in the time frame of this thesis, their preliminary results provide clear evidence on how important they are to a fundamental understanding of the phenomenon of pump whirl.

Blade-Passage Forces:

These masurements consisted of analog recordings of dynamometer bridge output voltages, performed during the no-whirl runs described in the previous section. Both five-bladed Impeller X and six-bladed Impeller Y were tested inside Volute A. Three flow coefficients (shut-off,design and full flow) and four impeller center positions (ninety degrees apart, starting with the point on the whirl orbit closest to the volute tongue) were explored. These recording were processed using a Fourier analyzer.

Static Pressure Distributions:

The knowedge of the circumferential static pressure distribution is useful in determining the average radial force exerted on the impeller. This distribution was measured at the front and back walls of the volute, just downstream of the impeller discharge; see Fig. 4.1 for exact arrangement of the measurement taps. A total of twenty-two such taps were fitted to Volute A, eleven at each wall. The taps, were connected to a battery of inverted water manometers for good resolution. Two impellers were used, Impeller X and the consolidated dummy, Impeller S. Both whirl and no-whirl cases were explored at three different flow settings (shut-off, design and full flow, using the auxiliary pump in the case of Impeller S).

Leakage Flow, Shroud Forces:

These tests were designed in an attempt to further understand the makeup of the total lateral force measured on the impeller. Complex flow phenomena such as occur in the leakage pathways or in the region near the volute tongue are very difficult to approach, experimentally or analytically. Typically, experimental studies have difficulty adressing each possible source of impeller force separately, while analytical studies have difficulty accounting for all possible sources in any one model. As a result, meaningful comparisons of experimental and theoretical data cannot be carried out. With this concern in mind, the following sets of measurements were performed (on both whirling and statically offset impellers):

(i) using Impeller X, Volute A and two new impeller face seal clearance settings, 0.64 mm and 1.3 mm (all previous measurements used the nominal setting of 0.13 mm),

(ii) using Impeller X and Volute A fitted with leakage limiting rings (see Fig. 4.1),

(iii) using Impeller S, Volute A and the flow from the auxiliary pump, and

(iv) using Impeller K, Volute A and the flow from the auxiliary pump.

Details on the test purpose and procedure can be found in Chapter 6, where the test results are discussed.

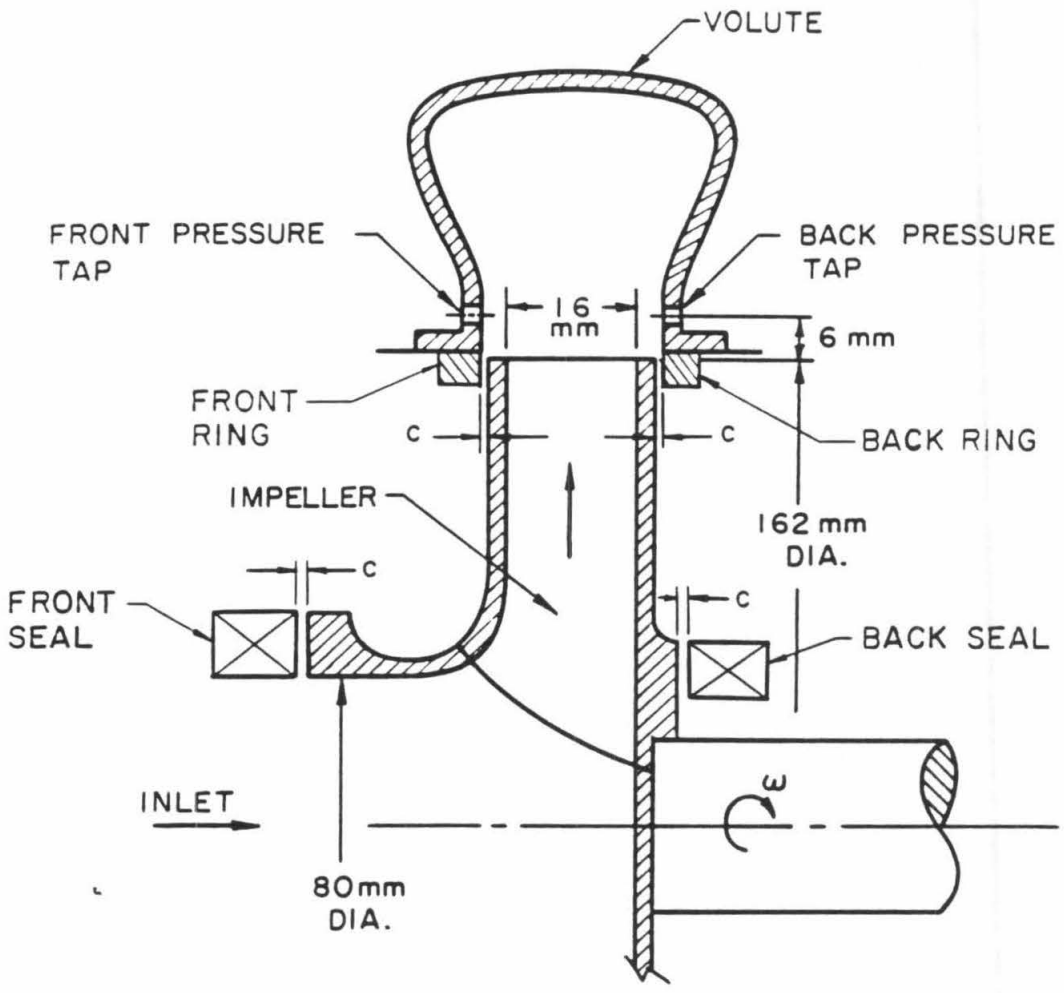

Fig. 4.1 Schematic of volute A and impeller X showing main dimensions, static pressure measurement points within the volute (front: 11 taps, back: 11 taps), impeller face seals, and leakage limiting rings at impeller discharge.

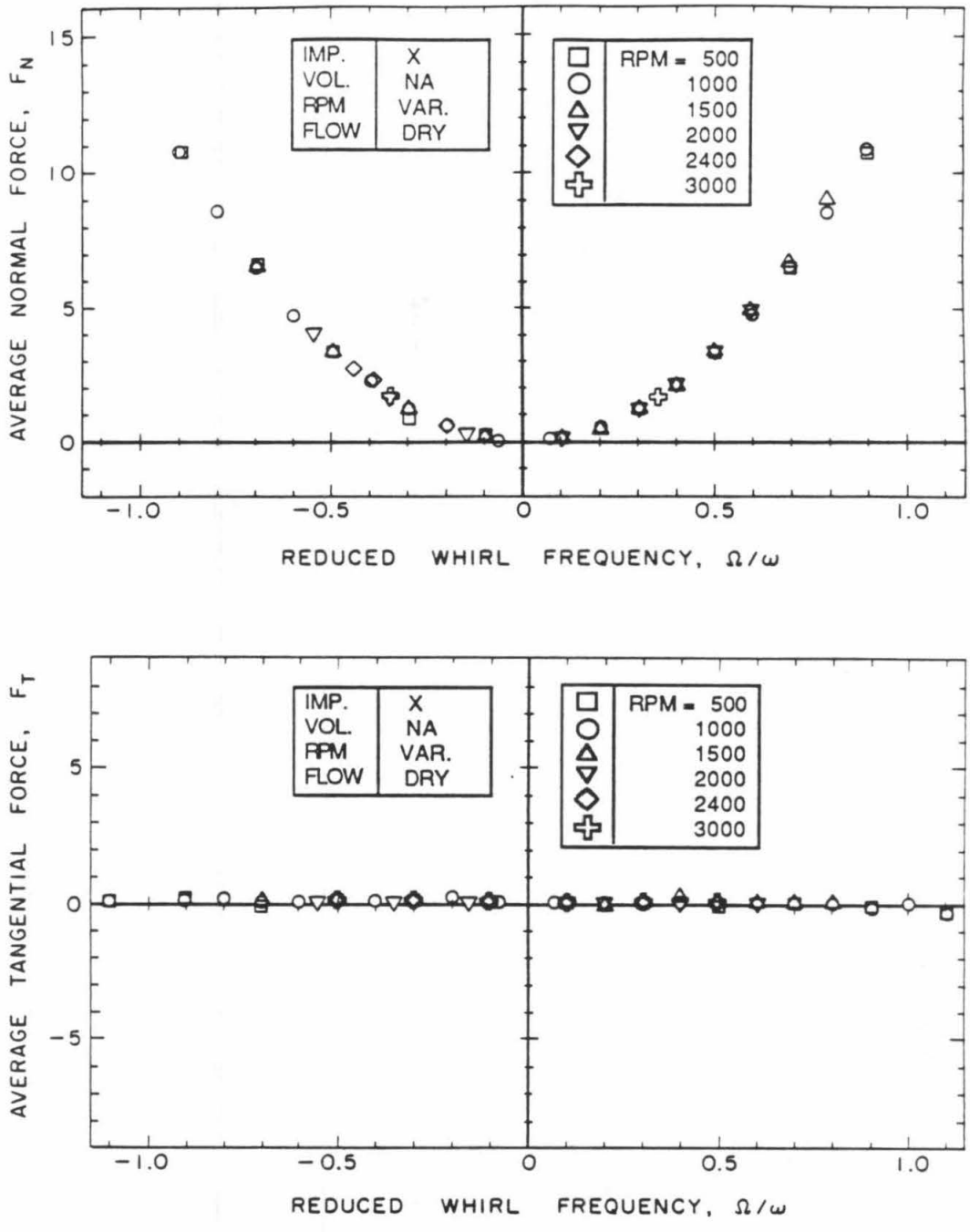

Fig. 4.2 Evolution with the reduced whirl frequency of the normal (top) and tangential (bottom) components of the orbit-averaged lateral force sensed by the dynamometer during simultaneous whirl and concentric motions of Impeller X in air, for various shaft speeds (500 to 3000 rpm).

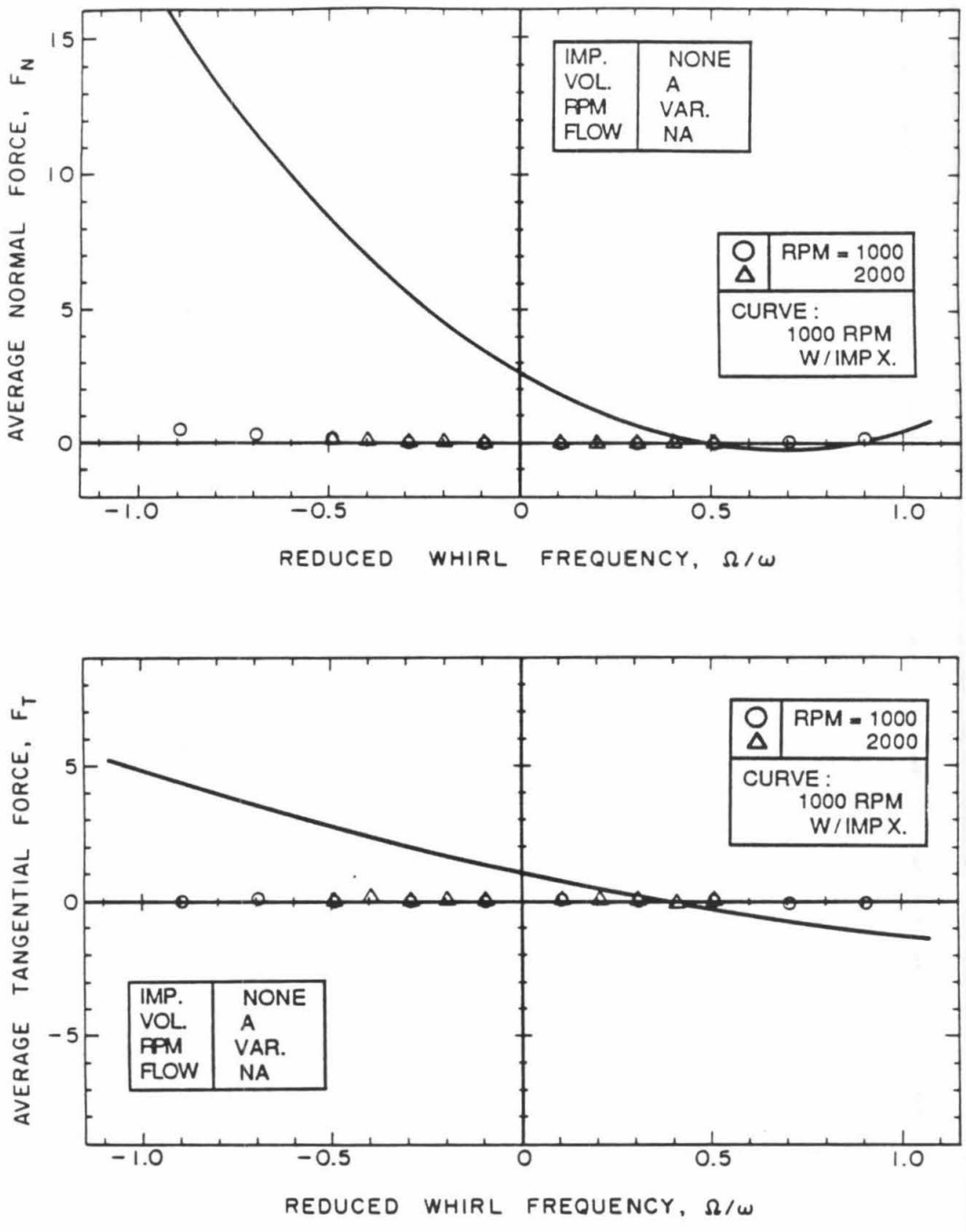

Fig. 4.3 Evolution with the reduced whirl frequency of the normal (top) and tangential (bottom) components of the orbit-averaged lateral parasitic hydrodynamic force sensed by the dynamometer during simultaneous whirl and concentric motions of the submerged pump shaft (in the absence of an impeller), for two pump speeds (circles:1000 rpm, triangles: 2000 rpm). Comparison is made with the corresponding components of the actual impeller-induced hydrodynamic force (curve: Volute A, Impeller X at design flow and 1000 rpm).

Chapter 5

DATA ACQUISITION AND REDUCTION TECHNIQUES

This chapter describes the steps followed by the various raw signals, from the time they are generated inside the dynamometer and other system instruments to the time they are processed into meaningful numerical values. A diagram of the complete signal processing system is presented in Fig. 5.1, and a photograph of the instrumentation is included in Fig. 5.2.

There are three major steps to this process. The first step (Section 5.1) consists of the routing, and conditioning of all data and control signals, in preparation for input to the data acquisition and storage system. The second step (Section 5.2) takes place inside the Shapiro Digital Signal Processor (SDSP) which is responsible for the acquisition and temporary storage of data from individual test runs. Permanent mass storage of the collected data is done with the help of a Zenith Z120 desktop computer. This same computer is used for the last step (Section 5.3), namely, the processing of the digitized data into tables and graphs of numerical values.

5.1 Signal Conditioning:

The four possible reference signals that could drive the SDSP are generated as part of the control system already described in Ch. 2, Section 2.6 and need no further description. It should, however, be noted that all four waves have coherent phases: the leadig edges of all four waves coincide at time intervals equal to their lowest common period. This measure assures proper timing of the sampling process, and subsequently, correct resolution of the forces sensed in the rotating and whirling dynamometer frame. Which one of these waves should be fed into the reference channel of the SDSP depends on the needs of the particular measurements to be made (this will become clear later).

The measurement signals fed into the 16 data channels of the SDSP come primarily from the dynamometer output signal conditioning amplifiers. Nine such amplifiers were provided, one for

each Wheatsone bridge. Amplifier gain was set alternately at 50, 100, or 150, depending on signal level (usually determined by pump speed). Before reaching these amplifiers, these output signals (together with the bridge excitation signals) follow a long path, which takes them first through the central hole of the main drive shaft (item (10), Fig. 2.3 right), to a miniature connector (item (19), Fig. 2.3 right), and then to the slip-ring assembly (Fig. 2.2). There the connection is made between the rotating and the stationary wiring. The signals are finally routed along the laboratory ceiling, down to the amplifiers. Care had to be taken so that this path does not introduce any noise in the raw signals. Overall, these signals were very clean and needed no filtering whatsoever.

The remaining seven data channels were fed various inputs, generated inside more conventional instruments, such as pressure transducers, flowmeters and accelerometers. As previously mentioned, the idea of using optical probes to monitor the motion of the impeller was abandoned.

5.2 Data Acquisition and Storage:

The central component of the signal processing system is the SDSP. Its design is based on a Motorola 68000 microprocessor. Sixteen data channels are scanned in a sequence controlled by a clock signal whose frequency is coherently derived from that of the reference wave signal (ω, $\Omega=l\omega/J$, ω/J or $\omega\pm\Omega$). Up to 64 samples can be taken for each data channel, during any reference cycle (sampling rate variable from 0.25 to 60 kHz) . The conversion from analog to digital and the writing to the memory are part of the sampling process. For each channel, samples from up to 4096 reference cycles can be accumulated, representing an "average" data cycle (this averaging process constitutes a very effective filter). The end result for each "run" is in the form of 1024 (64 data points x 16 channels) digital values stored in the internal memory of the SDSP.

These digital values are subsequently transferred to floppy diskettes, for mass storage and further processing. Several analog recordings were also made, either simultaneously with or separately from the above digitization process. Their results (stored on magnetic tape) were

processed separately, through a Fourier spectrum analyzer, yielding information on the frequency contents of various data signals.

5.3 Data Reduction Technique and Software:

It was explained in the previous chapter that, apart from some preliminary checks and some auxiliary measurements, the bulk of the data collected fall in either of two categories: froce measurements on the whirling impeller, or force measurements on the statically offset impeller. It was also mentioned that dry runs did not need to be performed in the case of the no-whirl measurements, the reason being that the only information sought from these measurements is in the form of pure stiffness matrices. Thus, only differences in force due to differences in displacement (as the impeller center is moved from one fixed position on the whirl orbit to another) are needed.

The process of extracting these pure stiffness matrices from the raw data is straightforward. Essentially, the sets of raw data from all the test runs are grouped in pairs corresponding to locations of the impeller center diametrically opposite each other on the whirl orbit. The reference cycle in these tests was chosen to be a shaft revolution. Thus, each data point in the cycle corresponds to a precise angular position of the impeller (and of the attached reference frame), so that point by point substraction of the raw data pairs can be perfomed in a consistent manner. The changes in the magnitude and direction of the lateral force vector are derived and related to the lateral displacement vector, yielding pure lateral stiffness coefficients.

The processing of the raw data collected while the impeller is whirling is much more involved. On the one hand, tare forces have to be subtracted (this is done on a point by point basis, before any further processing). On the other hand, there is the complication of consistently resolving the lateral forces under the combined concentric and eccentric motions of the impeller. The primary information sought from these data are the values (averaged over the whirl orbit) of the steady lateral force components, F_{ox} and F_{oy}, and the four components of the generalized stiffness matrix, A_{xx}, A_{xy}, A_{yx}, and A_{yy}. In what follows, a brief description of how these six unknowns are

extracted from the raw data is presented. A more detailed description can be found in Appendix C.

The lateral forces detected by the dynamometer are in a rotating reference frame. Denoting the lateral force components in the dynamometer frame by F_1, F_2 (see Fig. C.1 in Appendix C), it is clear that F_x and F_y are related to F_1 and F_2 by:

$$\begin{aligned} F_x(t) &= F_1(t) \cos \omega t - F_2(t) \sin \omega t \\ F_y(t) &= F_1(t) \sin \omega t + F_2(t) \cos \omega t. \end{aligned} \tag{5.1}$$

The angle ϕ_m is assumed to be zero, for simplification. As a first step in the data processing, the digitized values of $F_1(t)$ and $F_2(t)$ (sampled by the SDSP) are Fourier-analyzed using the reference frequency ω/J so that:

$$\begin{aligned} F_1(t) &= F_1^0 + \sum_{k=1}^{\infty} \left(F_{1P}^k \sin k\omega t/J + F_{1Q}^k \cos k\omega t/J \right) \\ F_2(t) &= F_2^0 + \sum_{k=1}^{\infty} \left(F_{2P}^k \sin k\omega t/J + F_{2Q}^k \cos k\omega t/J \right) \end{aligned} \tag{5.2}$$

where the second subscript on the force component refers to the Fourier component, P for in-phase and Q for quadrature. The superscript refers to the order of the harmonic. Components F_1^0, F_2^0, F_{1P}^k, F_{1Q}^k and F_{2Q}^k are available up to some limiting value of k, determined from the number of samples per channel. Theoretically, if 64 samples were taken, the thirty-second harmonic could be resolved. Eliminating F_1 and F_2 from Eq. (5.1) and Eq. (5.2), substituting the resulting expressions for F_x and F_y into Eq. (1.13) of Chapter 1, and then integrating over one cycle of frequency ω/J results in the following relations:

$$
\begin{aligned}
F_{ox} &= -(F_{2P}^{J} - F_{1Q}^{J})/2 \\
F_{oy} &= (F_{1P}^{J} + F_{2Q}^{J})/2 \\
A_{xx} &= (1/2\varepsilon) (- F_{2P}^{(J-I)} + F_{1Q}^{(J-I)} - F_{2P}^{(J+I)} + F_{1Q}^{(J+I)}) \\
A_{xy} &= (1/2\varepsilon) (- F_{1P}^{(J-I)} - F_{2Q}^{(J-I)} + F_{1P}^{(J+I)} + F_{2Q}^{(J+I)}) \\
A_{yx} &= (1/2\varepsilon) (F_{1P}^{(J-I)} + F_{2Q}^{(J-I)} + F_{1P}^{(J+I)} + F_{2Q}^{(J+I)}) \\
A_{yy} &= (1/2\varepsilon) (- F_{2P}^{(J-I)} + F_{1Q}^{(J-I)} + F_{2P}^{(J+I)} - F_{1Q}^{(J+I)}),
\end{aligned}
\qquad (5.3)
$$

thus, evaluation of the J^{th}, $(J-I)^{th}$ and $(J+I)^{th}$ harmonics was necessary. The usual value chosen for J was 10, though the data points at the lowest whirl frequency used J=20,18,16,14 and 12. Values of the integer I ranged typically from -11 to +11, and from -20 to + 20 exceptionaly.

A large number of relatively long and complex programs had to be developed for the various needs of the data acquisition and processing tasks. They included:

(i) programs in machine language (assembler for the Motorola 68000 microprocessor) to control channel data sampling, conversion from analog to digital, and storage in the internal microprocessor memory,

(ii) communication programs (assembler for the Zenith Z120's 8086 microprocessor) to control the two-way data and command transfer between the SDSP and the Z120, via a serial RS232 bus, and

(iii) programs in high level language (Basic and Fortran 77) for data management and processing, including Fourier analysis, data calibration, analysis, and plotting.

Listings of these programs are not included in this thesis but can be made available upon request.

4.4 Measurement Errors:

Electric noise, parasitic forces, and dynamic interference between measurement instruments and system components are likely sources of error, unless proper care has been taken to either eliminate them, or isolate their effect and account for it in the primary results.

The design of the rotating dynamometer (discussed earlier) assured that the last item (i.e., dynamic interference) will not be an issue. Direct measurements confirmed that both dynamometer and system natural frequencies are above the highest frequency for which force measurements were planned. Similarly, extensive checks were performed which proved that electric noise (ground loops, capacitive coupling, etc...) will not interfere with the data signals. One of the most conclusive tests involved the following steps:

(i) generate waves of various (but known) shapes and frequencies, at the data acquisition and processing side of the facility;

(ii) send these electrical signals along the bridge excitation wire pairs, to the input terminals of the slip-ring assembly;

(iii) collect these signals at the output terminals of this assembly, and send them back to the data acquisiton system along the bridge output wire pairs, and finally,

(iv) process them in the same fashion as the other raw data and compare their results to the original signal.

One hundred percent success was met in all variations tried. The original signals were recovered to within the accuracy of the digital processor (1 in 4096), regardless of shaft speed.

Other measurement errors are simply related to conventional instrument accuracies. The accuracy of the primary instrument, i.e., the dynamometer has already been discussed. The next important instruments are the optical encoders. Phase errors in these devices are less than 1 part in 1024, or 360:1024 degree.

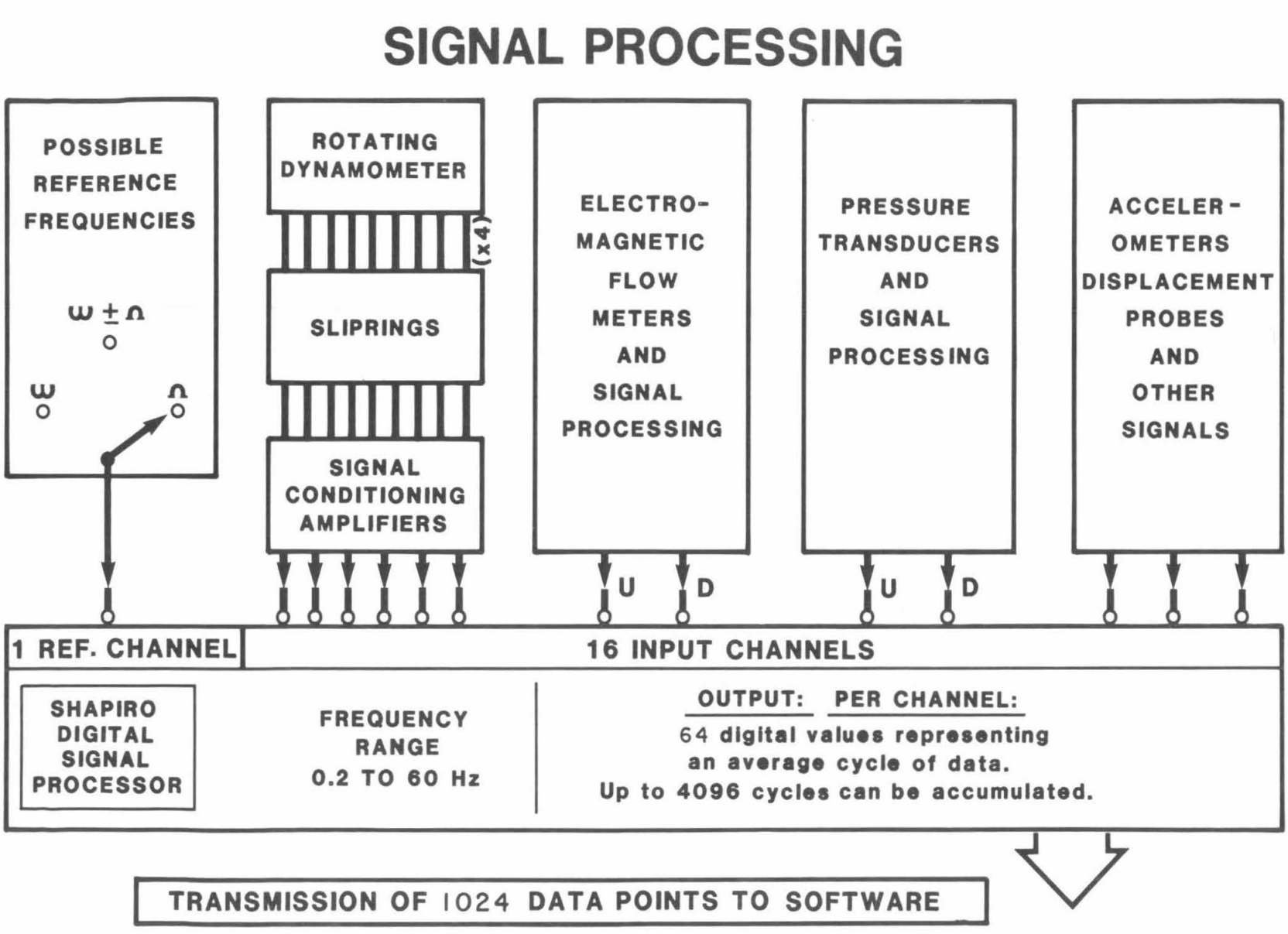

Fig. 5.1 Flow chart of signal processing. The Shapiro Digital Signal Processor is a Motorola 68000-based microprocessor. The reference signal is synchronized with the motions (concentric and eccentric) of the rotor. The 16 input channels are sampled sequentially, and readings are cumulated and averaged over several reference cycles. A maximum of 1024 average digital values (16 channels x 64 data points per channel) are stored in each run and then transmitted to the Zenith Z-120 desktop computer for further processing.

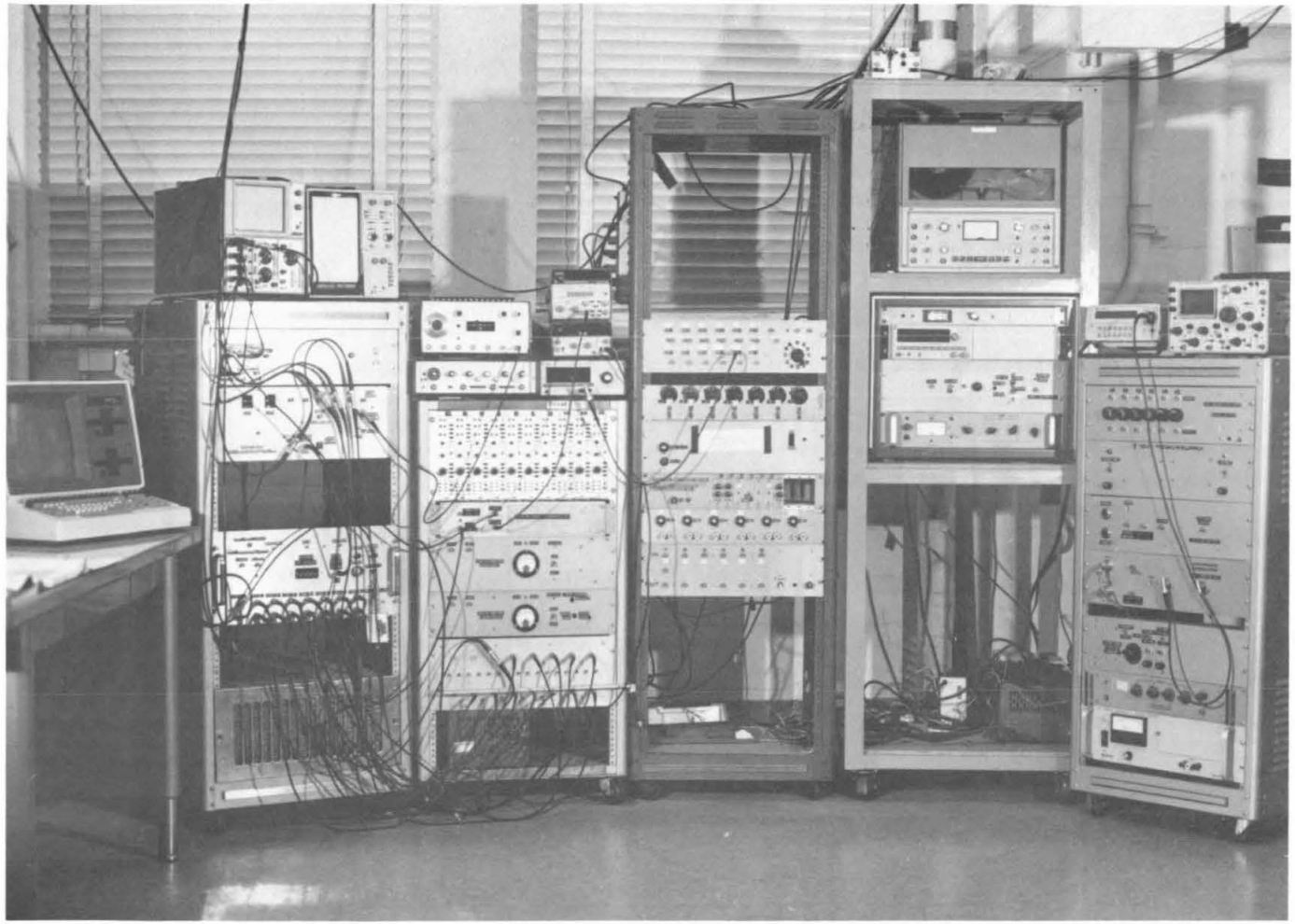

Fig. 5.2 Photograph of the instrumentation racks. Visible are, in particular, the Zenith Z-120 computer (far left), the Shapiro Digital Signal Processor (middle of leftmost rack), a battery of10 signal conditioning amplifiers (top of second rack), and the servo-controls for whirl and pump motors (bottom of second rack).

Chapter 6

RESULTS AND DISCUSSION

Preliminary test data such as the hydraulic performance curves, $\Psi(\phi)$, the steady forces, F_{ox} and F_{oy}, and the fluctuations of thrust, torque and bending moments are briefly presented, first. Emphasis is then placed on the hydrodynamic force matrices, $[A(\Omega/\omega)]$, which contain the essence of the information sought. Auxiliary data on blade passage, leakage flow and static pressure forces are also included. A presentation of the results in a format suitable for rotordynamic analysis is then discussed (in conjunction with Appendix D, where the present results are applied to the case of the SSME's HPOTP by Childs, and Moyer [39]). Also, some of the main measurement results are compared with limited experimental and theoretical data available from other sources. This chapter closes with a brief discussion highlighting some of the most important findings of the study.

6.1 Preliminary Test Results:

Some of these results have already been described in Chapter 4. Essentially, it was shown that the tests performed with the impeller running in air served a double purpose. Not only were they necessary as part of the procedure used to remove the tare forces, but as witnessed by the data in Fig. 4.2, they provided a reliable and accurate dynamic calibration check of the rotating dynamometer.

The tests whose results were presented in Fig. 4.3, on the other hand, proved that the hydrodynamic tare forces can be safely neglected in comparison with the impeller-volute forces. Although this conclusion did nothing to reduce the total number of runs (the tests had to be performed, in the first place), it brought by a significant reduction in the number of the data

processing steps, and hence the processing time and cost[1]. In the remainder of this section, the results of the other preliminary tests are described.

Hydraulic Performance Data:

In terms of performance, a pump is completely characterized by three functional relationships describing the evolution of the pump's non-dimensional head, Ψ, torque, τ, and efficiency, η, coefficients with the non-dimensional flow coefficient, Φ.

For the sake of completeness, Fig. 6.1 provides a graphical representation of these three coefficients (in a dimensional form, however) as a function of the pump flow rate in gallons per minute, and for two different impellers, designated Impeller X and Impeller Y. It should be pointed out that this designation is slightly misleading in the sense that the measurements shown were performed by the manufacturer, using impellers identical to X and Y except for their discharge diameters. The volute, on the other hand, is the manufacturer's test volute and does not necessarily have the same characteristics as any of the volutes tested in the present study.

More relevant here are the graphs presented in Fig. 6.2, obtained from measurements in which the actual test volute and impellers were used. The data in Fig. 6.2-top represent a conventional $\Psi(\Phi)$ graph for Impeller X when operated within Volute A at 1000 rpm. Those in Fig. 6.2-bottom correspond to Impeller Y, Volute A and two different speeds, 1000 and 2000 rpm.

Two features are worth pointing out in this bottom plot. First, observe that data at two different speeds fall on what would be the same $\Psi(\Phi)$ curve, which confirms proper scaling with pump speed. Second, notice that the data at 1000 rpm extend into the negative head region. This is an example of how the auxiliary pump (described in Chapter 2) could be used to explore quadrants other than the conventional positive flow-positive head one.

[1] Each eventual data point is now obtained from the following subtraction: [(results of wet run with impeller) - (results of dry run with impeller)], as opposed to: {[(results of wet run with impeller) - (results of dry run with impeller)] - [(results of wet run without impeller) - (results of dry run without impeller)]}.

Steady Forces:

Before embarking on a systematic analysis of the force measurement results, it is necessary to verify the validity of the model described by Eq. (1.7), in terms of the steady force components, F_{ox} and F_{oy}. It is to be pointed out that, in the context of the data processing scheme described in Appendix C, the word "steady" refers to both a temporal and spacial average of the lateral components of the hydrodynamic impeller-volute force vector sensed by the dynamometer as the impeller's geometric center orbits the volute's geometric center.

In this sense, F_{ox} and F_{oy} represent what is conventionally known as the average volute forces and hence they should be essentially independent of the whirl speed. Their magnitudes at any particular pump operating point are a reflection of the quality of the pump design in terms of how well impeller and volute are matched to each other. Ideally, the lateral force components should remain null at all times, when the impeller is operating at the volute center. In practice, however, this is never the case, especially away from the pump design point.

These considerations are confirmed in the graphs of Fig. 6.3 where values of F_{ox} (top) and F_{oy} (bottom) from typical test runs are presented as a function of the reduced whirl frequency, Ω/ω. Impeller X is operated inside Volute A at 1000 rpm and three flow coefficients, Φ=.000: shut-off, Φ=.092: design, and Φ=.132: throttle fully open. To get a feel for the actual size of these forces, notice that for the 1000 rpm pump speed, unity on the vertical scale corresponds to 285 N (64 lbf).

Clearly, these forces are insensitive to the whirl speed. Also, they both vanish for Φ=.092, an indication of good match between Volute A and Impeller X. Furthermore, the values of F_{ox} and F_{oy} at zero whirl agree with those measured by Chamieh [32], on the same pump, but using entirely different force balance and data processing software. Overall, these force components displayed a very regular and predictable behavior. It was essential for the rest of the project that these results be established beyond any doubt.

Thrust, Torque, and Moment Fluctuations:

Although the use of a complete six-by-six calibration matrix assures that all possible dynamometer interactions are accounted for, it is interesting to look at the magnitudes of the fluctuations of force components other than the two primary lateral ones.

Presented (as a function of the reduced whirl frequency) in Fig. 6.4 are typical fluctuations of the normalized thrust, P, torque, T, and bending moments, M_1 and M_2, in terms of their first harmonic content relative to the whirl orbit. Data are for Impeller X, Volute A, 1000 rpm, and design flow. Clearly, the values shown in Fig. 6.4 are two orders of magnitude lower than the nominal values (as are those measured in all other tests).

6.2 Unsteady Force Measurement results:

The forces described in this section can be viewed as the reaction of the flow to the lateral displacements of the impeller center away from the volute center. In the case of a purely static offset (no-whirl) these forces are actually steady in the volute frame and are processed in a manner different from the one used for the measurements performed in the presence of whirl. However, as explained in Chapter 4, it is convenient and logical to group both results in a single presentation: hydrodynamic impeller-volute forces as a function of Ω/ω ($\Omega/\omega=0$ corresponding to the no-whirl case). This can be done in either of three formats:

(a) graphs of individual elements of the matrix $[A(\Omega/\omega)]$, averaged over the whirl orbit,

(b) graphs of the average normal and tangential forces F_N, F_T given by:

$$F_N = (A_{xx} + A_{yy}) / 2$$
$$F_T = (- A_{xy} + A_{yx}) / 2 \qquad (6.1)$$

(c) tables of stiffness, damping and inertia coefficients obtained from polynomial fits to the elements of $[A(\Omega/\omega)]$; see Eqs. (1.8) and (1.14).

The first format has the advantage of reporting the data in their raw and complete form but is not always convenient to work with. When presented in the second format, the forces are easier

to interpret physically. However, this second format presupposes a particular symmetry in the elements of the matrix, as explained later. Rotordynamicists favor the third format since it provides information that can be readily input into standard linear dynamic analysis codes. All three formats will be used in the course of this presentation.

6.2.1 Generalized Hydrodynamic Force Matrix:

The origin of this matrix was explained in Chapter 1. Essentially, in the linearized (small displacements of the impeller center inside the volute) model of the impeller-volute forces, this matrix represents that part of the hydrodynamic force (imparted by the flow onto the impeller) which is proportional to the displacement. Appendix C contains a summary of the procedure by which the average values (over the whirl orbit) of the elements of this matrix are extracted from the raw data. Equation (6.1) shows how these average elements are related to the orbit-averaged, orbit-referenced impeller normal and tangential forces.

Typical results from what will be sometimes referred to as the "standard case" (Impeller X, Volute A, 1000 rpm, design flow: .092) are presented in Fig. 6.5, for this matrix[2]. The diagonal elements, A_{xx} and A_{yy}, are grouped in the top graph, and the off-diagonal elements, A_{xy} and A_{yx}, in the bottom graph. Both are plotted against the reduced whirl frequency, Ω/ω, whose values span the entire range from negative supersynchronous, to positve supersynchronous.

Examination of the graphs shows that matrix $[A(\Omega/\omega)]$ has almost equal diagonal terms, and off-diagonal terms which are almost equal but opposite in sign. This skew-symmetry of the hydrodynamic matrix is remarkable, since there is no known fundamental reason why this should be the case. It has often been assumed, but this is the first confirmation that the present author is aware of. It is this property of the matrix that makes the above-mentioned (F_N, F_T) format very convenient. It conveys the same amount of information in half the number of graphs. Also, since it

[2] It should be recallled that Volute A was designed to match Impeller X, at the design flow condition, Φ=.092.

was verified that this property is common to all cases tested, the (F_N,F_T) format will be used exclusively from here on.

The values of F_N and F_T corresponding to the data in Fig. 6.5 are pesented in Fig. 6.6. Several general features of these results should be emphasized. Considering first F_N, note that the hydrodynamic force is almost always in the radially outward direction. At zero whirl frequency it has a positive value which is in close agreement with the results of Chamieh [32]. This corresponds to a negative stiffness at zero whirl speed. The sign of the tangential force, F_T, is such as to produce a rotordynamically stabilizing effect at negative whirl speeds and for the larger positive whirl speeds. However, it is important to notice that there is a region of positive reduced whirl speeds, between zero and Ω/ω=.4, in which the tangential force is destabilizing rotordynamically. This is perhaps the single most important finding of this study.

A simplifying assumption often used by rotordynamicists, in particular, is that whirl-induced forces vary quadratically with the whirl speed. This assumption appears to be well justified, judging by how well the curve obtained from a least-squares quadratic approximation fits the raw data in Fig. 6.6. However, departures from this behavior did occur in some instances and will be discussed later.

Conventional scaling of the hydrodynamic forces with pump speed implies that data obtained when varying only the pump speed should be identical when plotted in the appropriate dimensionless form. For the range of pump speeds used (500 to 3000 rpm, in 500 rpm increments), Figs. 6.7 and 6.8 demonstrate that this is indeed the case for both F_N and F_T, both at and away from the design flow conditions (Φ=.092 and Φ=.060). Contrary to the scaling with whirl speed, scaling with pump speed was verified to prevail in all cases. This is important since it

means that the measured forces are not affected by the value of the Reynolds number (at least not in the range explored in the present tests).

6.2.2 Effect of Flow Coefficient:

When a pump is throttled, the flow patterns at both impeller inlet and discharge are affected. The farther away from the design point the pump is operated, the stronger these distortions can be. It is thus natural to expect that the flow-induced forces acting on the impeller be dependent on the fow coefficent. This dependence is illustrated in Figs. 6.9 though 6.11. Impeller X is operated at 1000 rpm in two different volutes. The data in Fig. 6.9 are obtained with a simple volute, Volute A. The data in Fig. 6.10 and 6.11 are obtained with a diffuser volute, Rocketdyne Diffuser Volute E. In both cases the flow was varied in steps, from shut-off to maximum, and the entire range of whirl speeds was explored.

Consider first the data in Fig. 6.9 and 6.10, the difference being the type of volute employed. In both cases, both F_N and F_T show a dependence on the value of the flow coefficent, ϕ, throughout the entire whirl speed range. This dependence is, however, much more pronounced in the case of Volute E. This could be attributed to the fact that, unlike Volute A which was matched to Impeller X, Volute E was designed independently of Impeller X, and, as such, has a higher potential for distorting the impeller discharge flow.

In particular, consider the value of Ω/ω at which F_T changes sign. At shut-off (ϕ=.000), this value is negative (Ω/ω=-.2), indicating a whirl stabilizing tangential force for <u>all</u> positive speed ratios. Notice that there exists in this case a small region in the negative whirl domain where the tangential force is destabilizing. This has rarely been observed. As ϕ is increased to .060, the sign change occurs in the positive whirl region and at a much higher speed ratio (Ω/ω=+.5). Accordingly, F_T has a destabilizing effect in the positive subsynchronous whirl region between Ω/ω=0 and Ω/ω=.5. As ϕ is increased even further, however, an interesting reduction in the critical

value of Ω/ω is evident: at and above design (ϕ=.092 and $\phi=\phi_{max}$) the destabilizing effect is confined to the region $0 \leq \Omega/\omega \leq 0.3$.

Further study of these graphs reveals interesting information concerning the curvature of the average tangential force. At shut-off this curvature undergoes several changes (from positive, to negative, to positive again). As the flow coefficient is increased, these changes become less pronounced, ending in a uniform positive curvature at maximum flow.

To better illustrate this feature of the results, two additional sets of measurements were taken at selected intermediate values of ϕ, .030 and .110. The resulting data for F_T are presented separately in Fig.6.11, for clarity. Particularly noticeworthy is the fact that, at ϕ =0.030 , F_T changes sign twice in the positive whirl-speed region, first, sloping upward at around Ω/ω=.06, and then sloping downward at around Ω/ω=.3 (see Fig. 6.11-top). This brings back the issue of the dependence of the forces on whirl speeed. Clearly, the assumption of quadratic behavior cannot be justified at the lower flow rates. A higher order polynomial (see Fig. 6.11-bottom) or possibly a non-polynomial description would be more appropriate. No explanation other than the increased flow distortions near shut-off can be offered at this point. It should be mentioned, however, that an attempt was made to monitor the inlet flow using threads distributed around the inlet bell. It was thus observed that departures from the quadratic behavior do seem to be triggered by, or at least closely associated with, the onset of inlet flow distortions.

Nonetheless, it is correct to conclude that the value of the flow coefficient does have an effect on the fluid forces acting on the impeller. This effect is stronger (i) when the pump operates away from its design flow, and (ii) when the volute is not matched to the impeller. Changes in these forces with changes in volute and impeller design (at constant flow coefficient) are discussed next.

6.2.3 Effect of Volute and Impeller Design:

One of the postulations in this study is that the forces arise as a result of an interaction between the impeller and the volute via the working fluid. It is then only natural to focus one's attention on the type of impeller and volute designs, when trying to characterize these fluid forces. The effect of the volute design is presented in Fig. 6.12 and Fig. 6.13. The effect of the impeller design is presented in Fig. 6.14 and Fig. 6.15.

Effect of Volute Design:

In Fig. 6.12, comparison is made between the results obtained when Impeller X is operated inside the pump casing (without any volute, crudely approximating the case where the impeller is whirling in an infinite medium), and when the same impeller is operated inside four different volutes. The same speed and flow conditions were maintained in all five tests. One clearly observes a much stronger interaction due to the presence of a volute, especially for the tangential force in the negative whirl region. Furthermore, notice that, in comparison to Volute A's data, (i) the tangential force obtained with Volute B is smaller, and (ii) that obtained with Volute C is larger.

This is important considering that, unlike Volute A, both Volute B and Volute C are deliberately mismatched to Impeller X. Volute B has a wider than normal, constant, circular cross section. Volute C by contrast has a tighter than normal, trapezoidal cross section. As one would legitimately expect, the higher rate of turning imposed on the flow discharged in the tighter volute results in a higher tangential force.

On the other hand, it is somewhat surprising that the presence of diffuser guide vanes (or their number or orientation) appears to has little effect on F_N and F_T, especially in the positive whirl region. This is witnessed by the data in Fig. 6.13, for which the same basic diffuser volute, D, was first tested with no vanes (D-0), then with two different sets of six vanes at two different angles

(D-F6 and D-G6), and, finally, with a set of twelve vanes (D-H12). Refer to Fig. 2.5 in Chapter 2 for more details on these vane configurations.

Effect of Impeller Design:

Impeller X and Impeller Y have similar geometric characteristics (see Fig. 2.5). Their hydraulic characteristics are quite similar (see Fig. 6.1). It is therefore not surprising that the forces measured on these two impellers have nearly the same magnitude and phase. This can be observed in Fig. 6.14, where the pump speed is 1000 rpm and the flow coefficient is kept at the Impeller X design value, .092.

However, it was possible to link one aspect of the measured forces directly to the impeller design, and more specifically to the number of impeller vanes (five for Impeller X and six for Impeller Y). This was done by performing a set of tests which are quite different from the ones described so far. They consisted of analog recordings of dynamometer bridge output with the impeller operating at fixed locations on the orbit (no whirl). These recordings are then processed through a Fourier analyzer, and their harmonic content is correlated with the blade-passing frequency.

Typical spectra obtained from this procedure are presented in Fig. 6.15-top for Impeller X at shut-off (Φ=.000), and Fig. 6.15-bottom for Impeller Y at the Impeller X design flow (Φ=.092). In both tests Volute A was used, and the pump was operated at 1000 rpm (16.7 Hz). The angular position, Φ_m (see Fig. C.1 in Appendix C),of the impeller center on the whirl orbit during the test was measured counterclockwise from the point closest to the volute tongue, and was 0° for Impeller X and 180° for Impeller Y.

Highlighted in Fig. 6.15 are the once-per-revolution spikes (ω=16.8), corresponding to the weight of the wet impeller. Since the frame of reference was rotating[3] with the impeller at the rate ω, the blade-passing forces produced spikes at 4ω and 6ω for five-bladed Impeller X, and 5ω and

[3] This results in a sine and cosine decomposition of the force vector, when referred to the volute frame, and hence the two frequencies: (number of blades -1)ω, and (number of blades +1)ω.

7ω, for six-bladed Impeller Y. Notice that the spectrum has a higher noise level when the pump is operating at shut-off. Notice also that the magnitude of the blade-passing forces is about an order of magnitude lower than that of the weight of the wet impeller, and furthermore, that these forces are stronger when the impeller is closer to the cutwater (Φ_m=0°).

6.2.4 Additional Test results:

Thus far, the focus has been on the main pump components (impeller and volute) and operating parameters (speed and flow rate). The fluid forces measured are real in the sense that the test hardware is typical of commercial units, with the possible exception of the impeller seals. In the design, a choice was made to use face seals instead of cylindrical seals, in an attempt to isolate the impeller-volute forces. Both front and back face seals were backed off to a nominal clearance setting of .13 mm (.005 in), enough to eliminate any direct interference with the fluid force measurements (no rubbing on impeller face).

However, these face seals could have an indirect effect on the impeller forces, not so much in terms of fluid forces developing in the sealing gaps, but in terms of the fluid forces acting on the impeller front and back shrouds (which are part of the total force sensed by the dynamometer). See Fig. 2.3-right for details. A full investigation of the fluid forces associated with this leakage flow was not intended as part of this thesis work. However, some preliminary measurements were made which might shed some light on this intricate issue. The results of these measurements are described next.

Effect of Seal Clearance:

Presented in Fig. 6.16, in the usual (F_N,F_T)-format, are typical results from measurements conducted for three impeller front and back seal clearance settings, .13, .64, and 1.3 mm (.005, .025, and .050 in). Impeller X was operated within Volute A at 1000 rpm. In all three cases, the net flow through the pump was adjusted to the design value (corresponding to the nominal clearance

setting of .13 mm). Both F_N and F_T are affected by the value of the seal clearance, but only in the negative whirl region. In the case of F_N, the trend is more consistent and could make intuitive sense: the smaller the clearance, the higher the rate of flow entering the volute, and the higher the radial force. One could only speculate at this point. The fluid mechanics of the flow in the leakage path does not easily lend itself to analysis.

The data presented in Figs. 6.17 and 6.18 show how inconclusive some of these results could be. In these experiments two additional rings were fitted to the volute at the impeller discharge (see Fig. 4.1), in an attempt to reduce the leakage flow even further. Again, both F_N and F_T are affected. However, with the rings in place, the effect extends to the positive whirl region, as well.

Consider first F_N, both at (Fig. 6.17-top) and off (Fig. 6.18-top) the design flow conditions. Notice that there is a value of Ω/ω for which the trend is reversed. This value appears to be near the minimum of the data set. Also, if and where a comparison could be made with the data in Fig. 6.17-top, one would notice that the relation between the magnitude of the force and the amount of leakage is reversed.

As far as F_T is concerned (see Fig. 6.17-bottom and Fig. 6.18-bottom), notice that (i) at design flow, the slope of the data is smaller (in absolute value) with rings than without rings, (ii) the opposite is true at maximum flow, and (iii) in both cases, the destabilizing region is smaller with than without rings. No meaningful comparison could be made with data in Fig. 6.16-bottom.

Static Pressure Distributions:

The data presented in Fig. 6.19 and Fig. 6.20 give an indication on the static pressures prevailing at the volute front and back walls, just near the impeller discharge (refer to Fig. 4.1 for arrangement of measurement taps). As expected, the region near the volute tongue is where the strong changes in slope and curvature occur. Volute A was used for both sets of measurements.

The main motor speed (or spin speed) was 1000 rpm, and the whirl speed 500 rpm. The difference between the two graphs is in the type of impeller used.

In Fig. 1.19, the normalized (by the dynamic head) static pressure distribution associated with Impeller X is plotted, as a function of the azimuthal position referred to the volute tongue, for three flow coefficients. Notice the shift in the average value with varying flow coefficients. The net radial force would, however, be given by integration around the periphery.

Impeller S (a consolidated dummy duplicating the outside geometry of Impeller X) was used for the data in Fig. 6.20. The auxiliary pump was operated so as to create the same pressure differential across Impeller S as the one prevailing across Impeller X, at the indicated flow coefficients. Here, again, the same reamrks apply.

Forces on Solid Impeller:

These forces are presented in Fig. 6.21. The auxiliary pump was operated in the same fashion just described. The flow coefficients indicated in the legend of Fig. 6.21 are for reference only. The idea is to get an approximation, however crude, of the contribution of the impeller shroud forces to the total force sensed by the dynamometer.

Judging by the values appearing in Fig. 6.21, this contribution is significant. As far as whirl excitation is concerned, however, the measured tangential force appears to have a stabilizing effect throughout the entire range of whirl speeds.

Forces on Thin Disk:

A 6.3 mm thick, flat circular disk having the same tip diameter as Impeller X (see Fig. 2.4) was used in this experiment. The flow rates are "real" in this case. They are identical to those generated by Impeller X at the indicated flow coefficients. However, they are generated by the auxiliary pump.

The interest here again is in determining whether or not a whirl-exciting tangential force could be measured. There appears to be no clear indication of any.

6.2.5 Rotordynamic Matrices:

As mentioned earlier, rotordynamicists much prefer the [K]-[C]-[M] format. Presented in Table 1 and Table 2 are dimensionless values of the elements of [K], [C], and [M] matrices obtained from second, third, and fifth order polynomial fits to the elements of $[A(\Omega/\omega)]$. It is clear from Fig.6.6 and Fig.6.7 that the curvature of the graphs of the average tangential force F_T is somewhat uncertain below the design flow rate. This results in appreciable departures from the pure quadratic behavior and hence discrepancies in the off-diagonal terms of some of the inertia matrices, [M]. On the other hand, the elements of the stiffness matrices, [K], are in good agreement with the measurements of Chamieh [32]. Also, it was verified that the added mass terms could be predicted with good accuracy using simple textbook formulae.

Selected values from Table 1 are used in the rotordynamic analysis of the SSME's High-Pressure Oxydizer Turbopump (HPOTP). This analysis was carried out by Childs et al. [39] and is appended to this thesis; see Appendix.D. The study provides an example of how the present results could be used in a practical application, and most importanly, it demonstrates that the rotordynamic analysis of a high performance turbomachine is not complete unless all the rotordynamic coefficients of all the system components are individually accounted for.

6.2.6 Comparison With Results From Other Sources:

As mentioned in the introduction, the literature contained little information on the unsteady hydrodynamic impeller-volute interaction forces at the time the present research work was initiated. Since then, some theoretical and experimental data became available thanks to the work

of Ohashi et al. [122], Bolleter et al. [21], Adkins [4], and Tsujimoto et al. [143,144]. Appropriately selected results from these sources will be compared to those of the present measurements.

Comparison with Other Experimental Results:

This comparison is carried out in Fig. 6.23. Ohashi et al.[122] measured the same forces on an impeller surrounded by an axisymmetric (double discharge) vaneless diffuser. Their forces are much smaller than those measured on Impeller X inside Volute A. This would be consistent with the postulation that the forces are primarily due to the volute asymmetry.

In support of this, the results from the tests where Impeller X was operated inside the pump casing with no volute around it have been reproduced. The agreement becomes significantly better. Notice that the pump casing is not symmetric either. Thus, although far from the impeller, it still exerts some destabilizing influence, unlike the symmetric diffuser.

The measurements of Bolleter et al. [21] display the same qualitative behavior. They were conducted on a symmetric vaned diffuser. The position of the impeller center position was perturbed in a quasi-linear fashion. The higher values of the measured forces seem to go against the above-mentioned postulation. However, it should be mentioned that in this case the pump inlet section is asymmetric and it is not unconceivable that this could account for part of the differences.

Although definite conclusions should not be made based on this limited evidence alone, it is important to remark that despite the differences in the experimental setups and approaches (the interested reader is urged to refer to these two studies) the central findings are quite similar.

Comparison With Theory:

This comparison is carried out in Fig. 6.24. The model used by Adkins [4] is a quasi-one-dimensional, inviscid one. The model used by Tsujimoto et al. [144] is a two-dimensional, distributed vortex one.

Both models yield qualitatively good predictions of both F_N and F_T. The latter, however, does slightly better from a quantitative standpoint. Also, notice that Adkins' model is limited in the range of whirl frequencies covered.

It is important to keep in mind that the present measurements include all the forces acting on the impeller, including front and back shroud forces. Adkins made a good attempt at distinguishing the various sources of contribution to the rotor forces and concluded that both the static pressure distribution at the impeller discharge and the interaction of the leakage flow with the impeller front shroud play a major role. This goes against the earlier interpretation by Chamieh which hinted at a major contribution from an asymmetric distribution of the momentum flux at the impeller discharge.

6.3 Discussion:

From the multitude of incidents and accidents reported in the high performance turbomachine literature regarding what was described as self-excited rotordynamic instabilities it was clear that the industry was faced with a new challenge. None but a few of the symptoms reported fit the descriptions of the problems turbomachine practitoners were accustomed to solving. Under these circumstances, progress toward the solution greatly depends on defining the problem and posing it in rational terms.

Preliminary investigations identified a number of mechanisms which should be studied further. These included annular seal forces, blade-tip clearance forces in axial flow machines, and impeller-volute forces in centrifugal flow machines. This thesis is part of an ongoing research

program aimed at the study of impeller/volute forces. The central issue this thesis addresses is whether or not the flow through an impeller-volute system is capable of creating and/or sustaining unstable motions of the rotor.

It has been determined that under certain circumstances destabillizing forces can be generated by the flow through the impeller and the volute. The destabilizing forces act at subsynchronous frequencies, the range of which tends to increase with decreasing flow coefficient.

It should be emphasized at this point that these findings are the result of direct measurements on real pumps, and as such are only limited by the assumptions underlying the experimental procedure employed. These were very few and have already been discussed. The only one worth invoking here is the assumption of "small motions of the impeller center" which was implicit in the data processing procedure[4]. Thus, it is clear that these new findings should impact the design of high performance turbomachines in a significant way: impeller-volute systems should no longer be considered as passive systems from a rotordynamics point of view.

[4] This assumption has been justified in Ref. [122], for instance, where different values of impeller center eccentricity were tested.

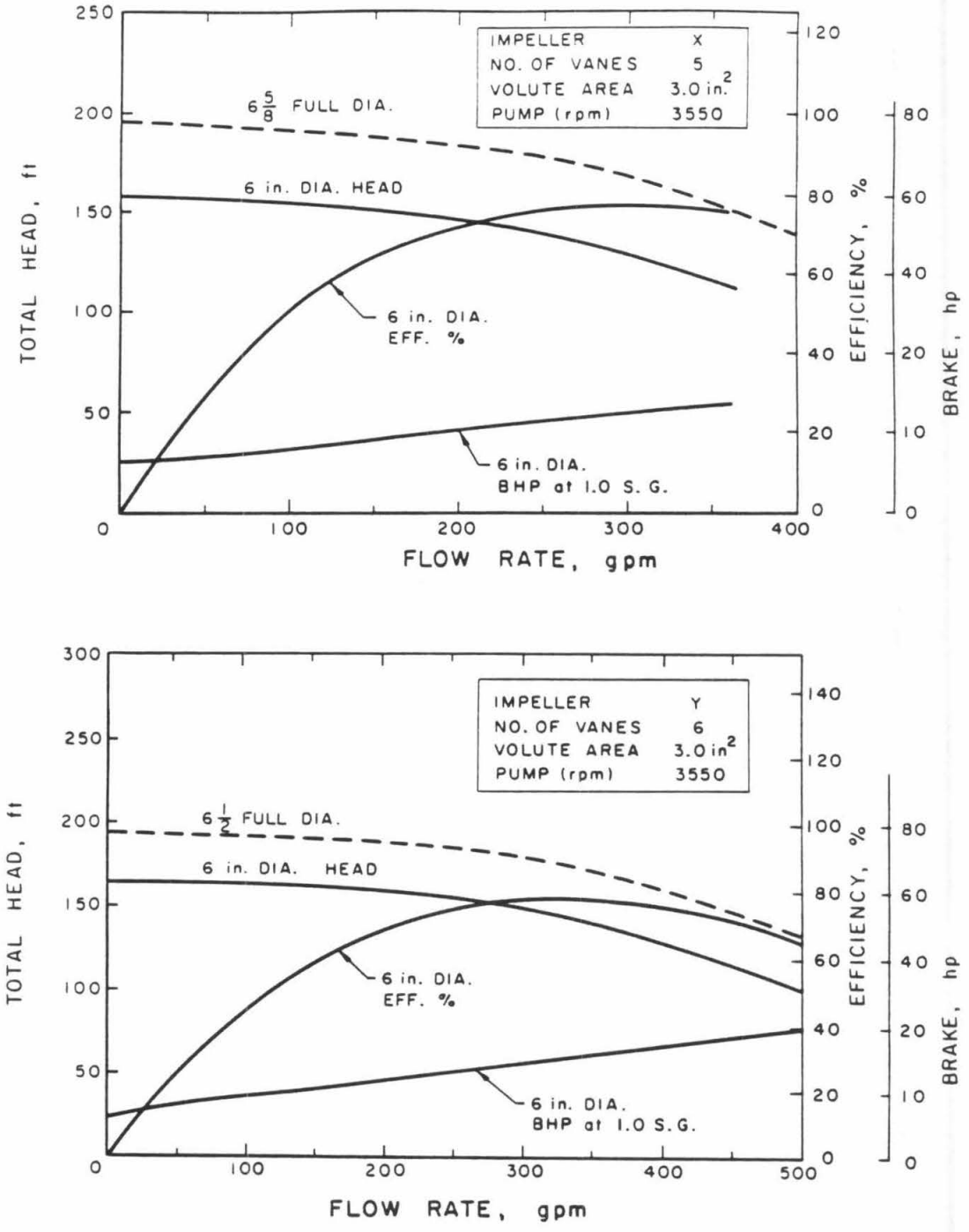

Fig. 6.1 Manufacturer-supplied dimensional hydraulic performance data of the two Byron-Jackson impellers tested; top: Impeller X, bottom: Impeller Y.

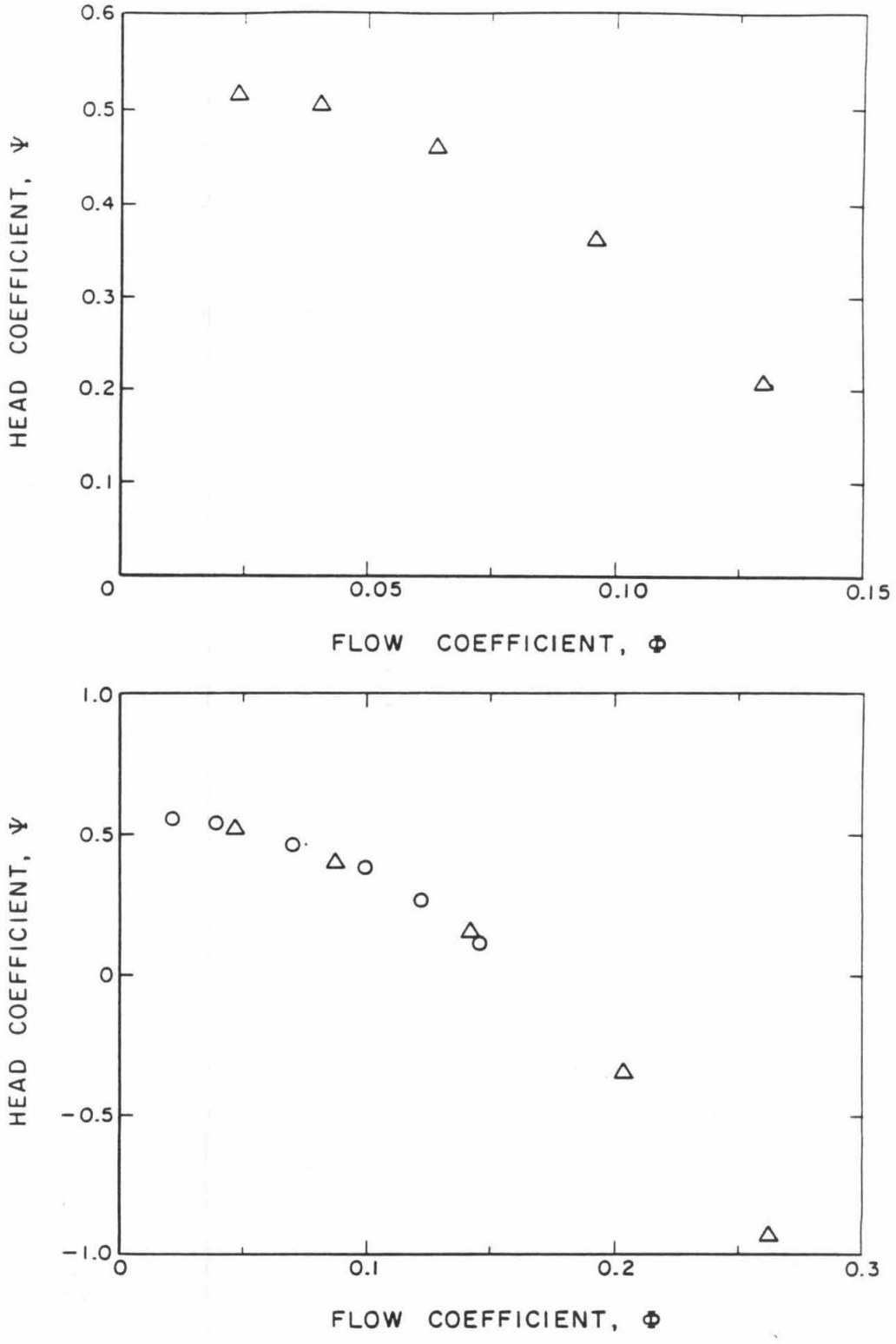

Fig. 6.2 Dimensionless performance data of Impeller X as tested inside Volute A. Top: in the conventional positive flow-positive head quadrant, at 1000 rpm using own flow. Bottom: using auxiliary pump to explore part of the positive flow-negative head region (two impeller speeds, triangles:1000 rpm, circles: 2000 rpm).

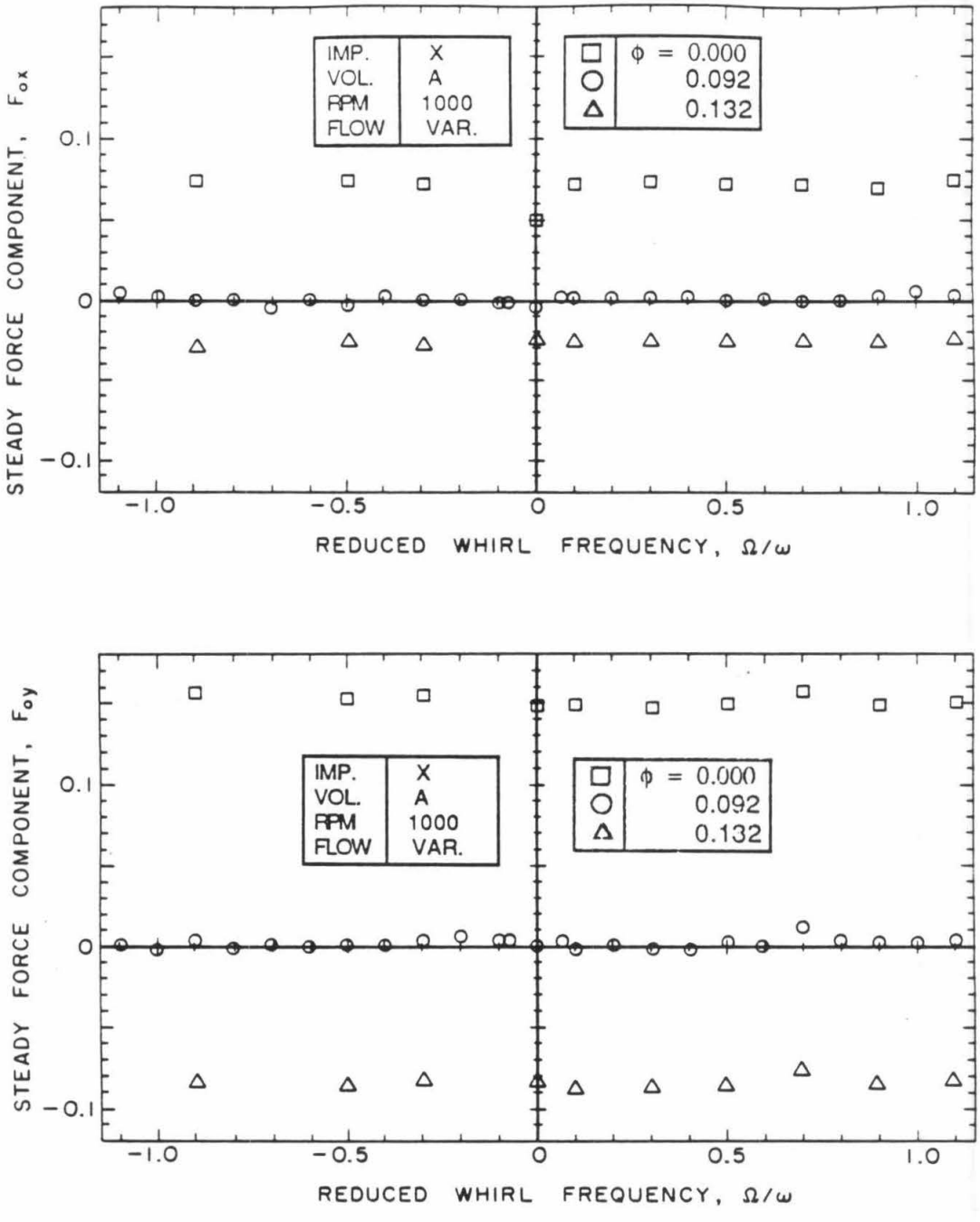

Fig. 6.3 Evolution with the reduced whirl frequency of the X (top) and Y (bottom) components of the steady hydrodynamic force measured, in the stationary (X,Y)-volute frame, on Impeller X operating within Volute A at 1000 rpm and three flow conditions (Φ= 0: shut-off, Φ=.092: Impeller X design flow coefficient, Φ=.132: full throttle).

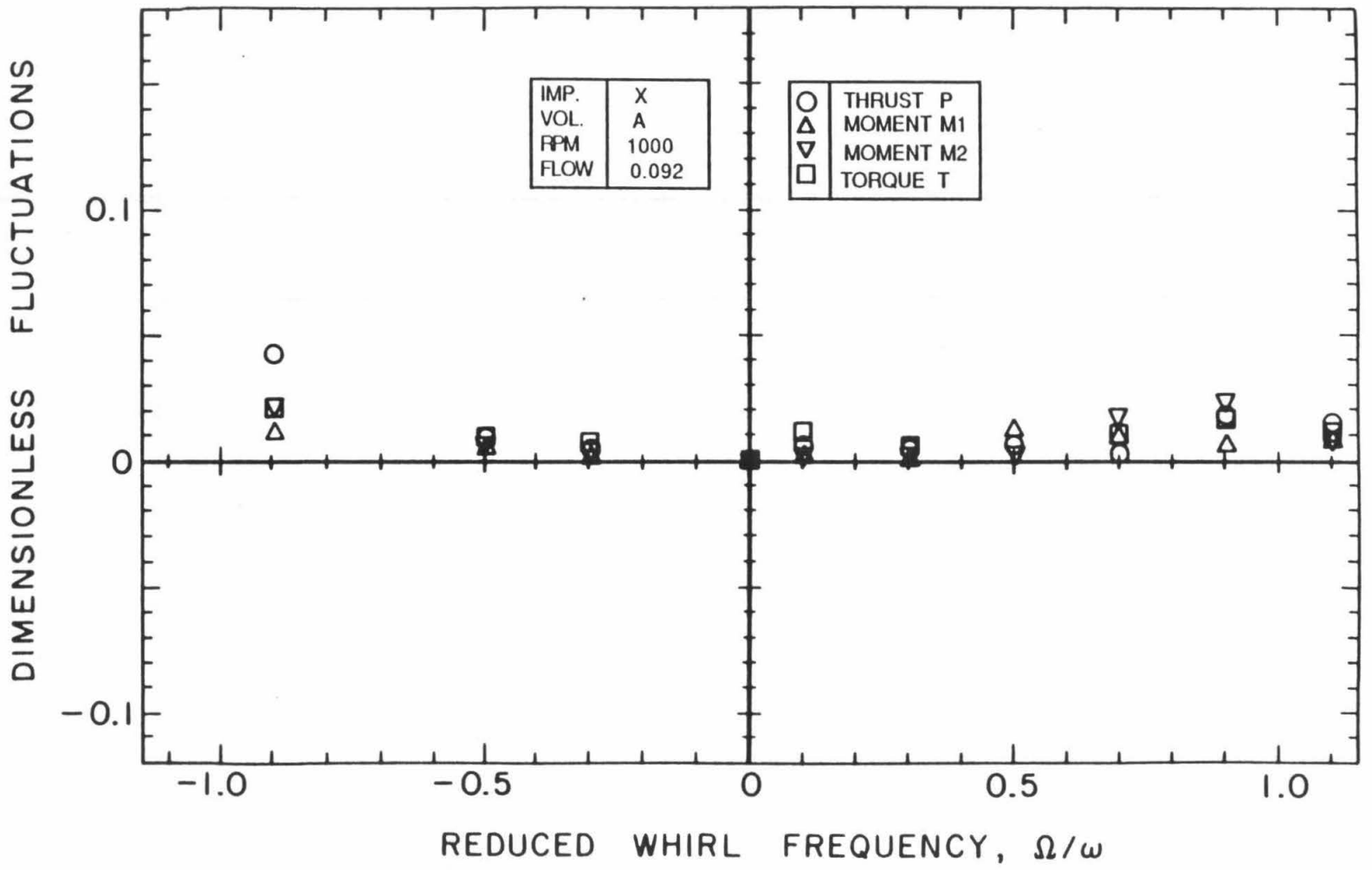

Fig. 6.4 Typical (Volute A, Impeller X at design flow and 1000 rpm) magnitudes of the fluctuations in normalized hydrodynamic impeller forces other than lateral. Data are for the first harmonic variation (referred to the whirl orbit) of the axial thrust, P, the two bending moments, M_1 and M_2, and the torque, T, with the reduced whirl frequency, Ω/ω.

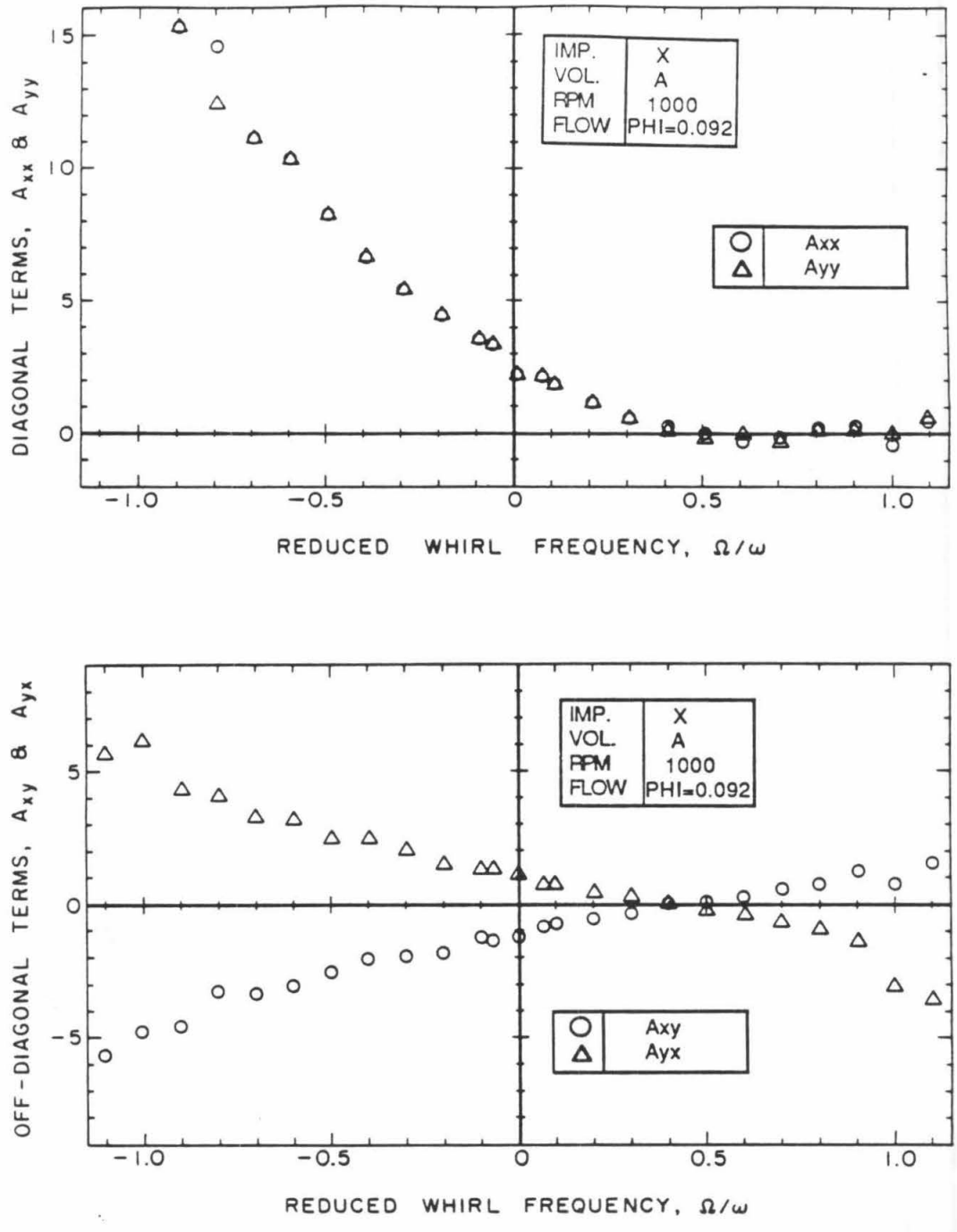

Fig. 6.5 The dimensionless, orbit-averaged diagonal (top) and off-diagonal (bottom) elements of the generalized hydrodynamic force matrix, [A], as a function of Ω/ω, measured for Impeller X operating within Volute A at 1000 rpm and design flow, ϕ=0.092.

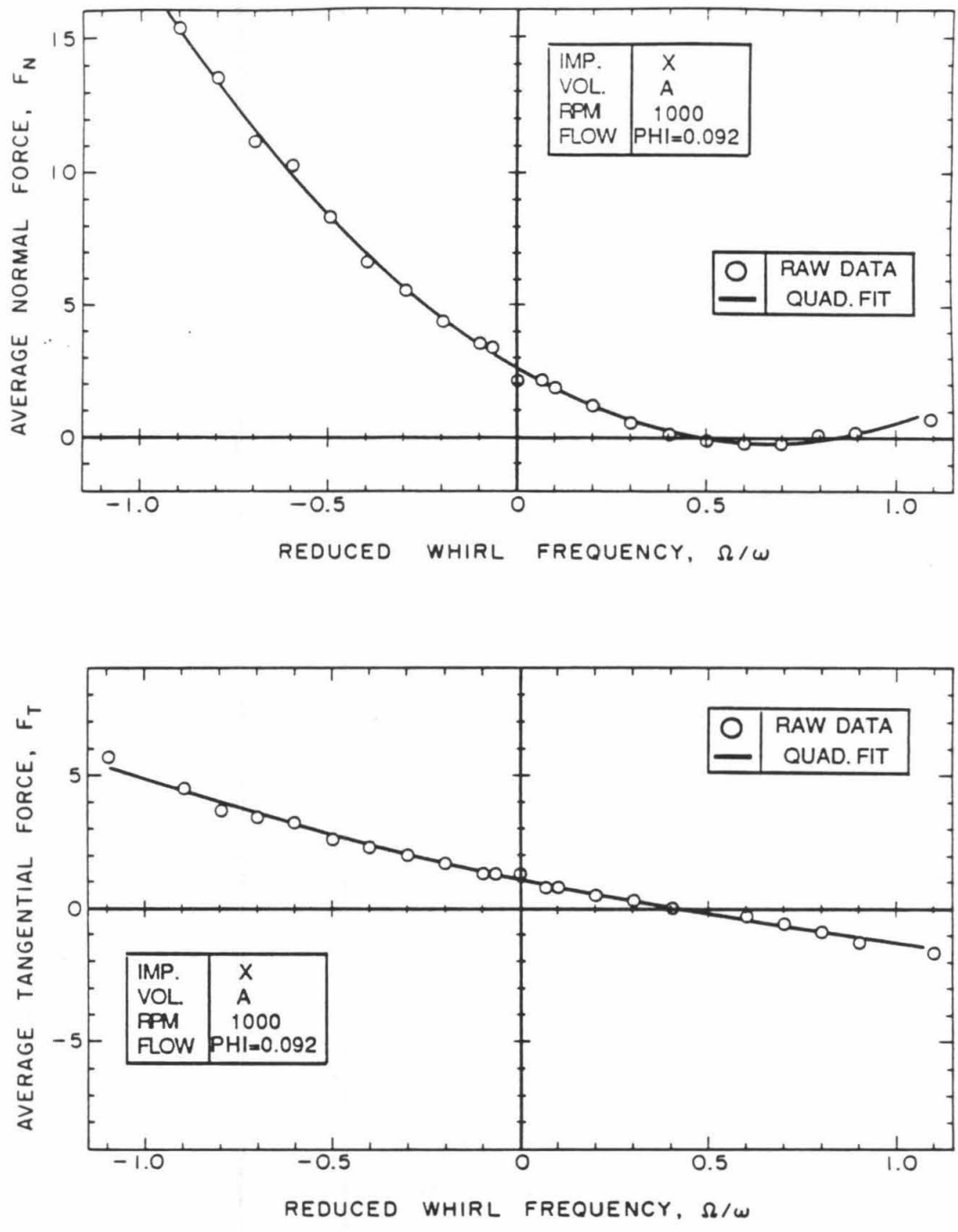

Fig. 6.6 The dimensionless, orbit-averaged normal (top: F_N) and tangential (bottom: F_T) components of the impeller lateral hydrodynamic force representing the data in Fig. 6.5. Least-squares quadratics (in Ω/ω) are fitted to both F_N and F_T.

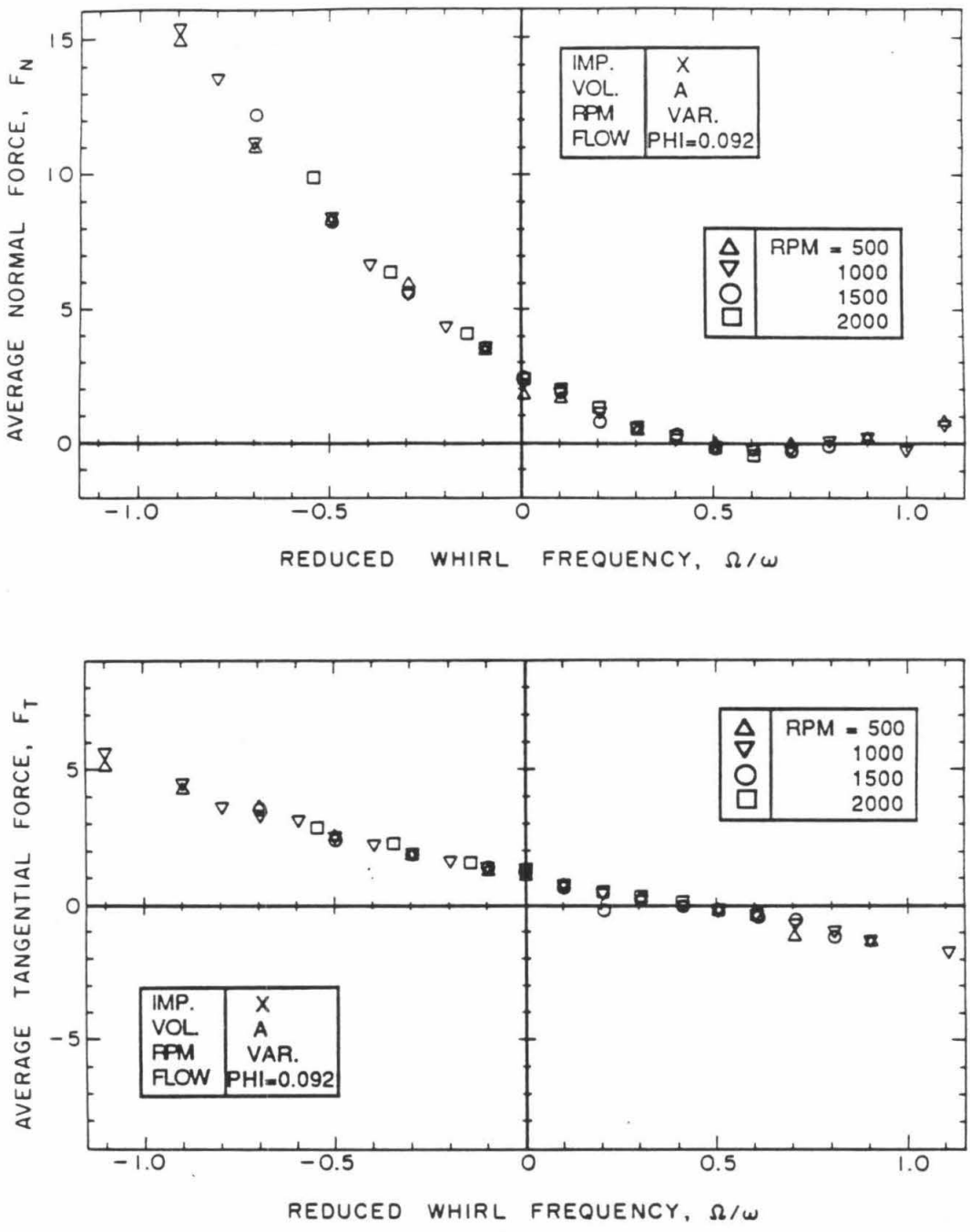

Fig. 6.7 Evolution (as a function of the reduced whirl frequency) of the dimensionless, orbit-averaged normal and tangential forces measured on Impeller X when operating within Volute A at design flow, ϕ=0.092, and four different pump speeds: 500,1000,1500 and 2000 rpm.

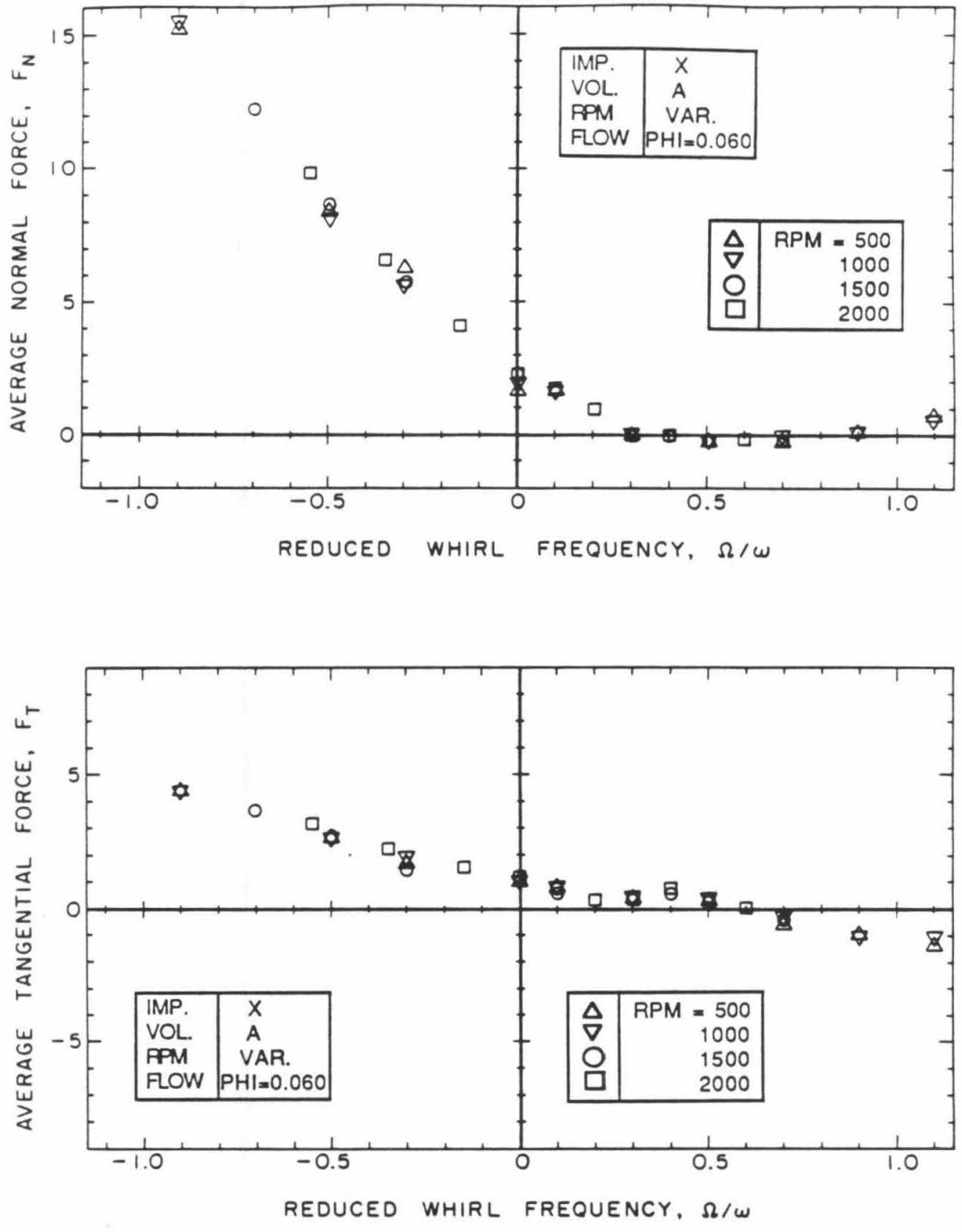

Fig. 6.8 Evolution (as a function of the reduced whirl frequency) of the dimensionless, orbit-averaged normal and tangential forces measured on Impeller X when operating within Volute A below design flow (ϕ=0.060), at four different pump speeds: 500,1000, 1500, and 2000 rpm.

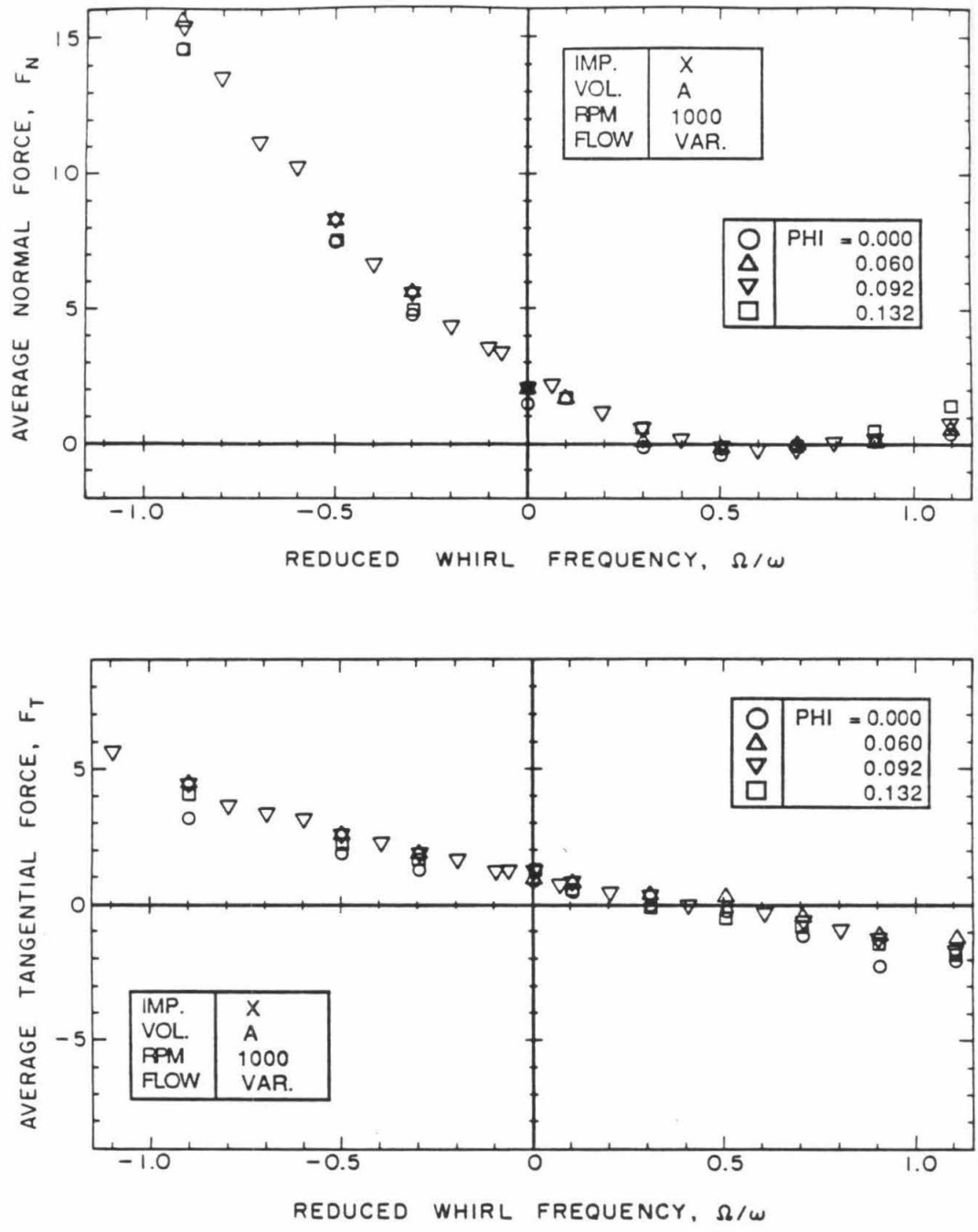

Fig. 6.9 Effect of the flow coefficient on the variation with reduced whirl frequency of the average normal and tangential forces. Data are for Impeller X operated within Volute A at 1000 rpm and four different flow conditions; from shut-off to full throttle: ϕ=0, 0.060, 0.092 and 0.132. Volute A is matched to Impeller X.

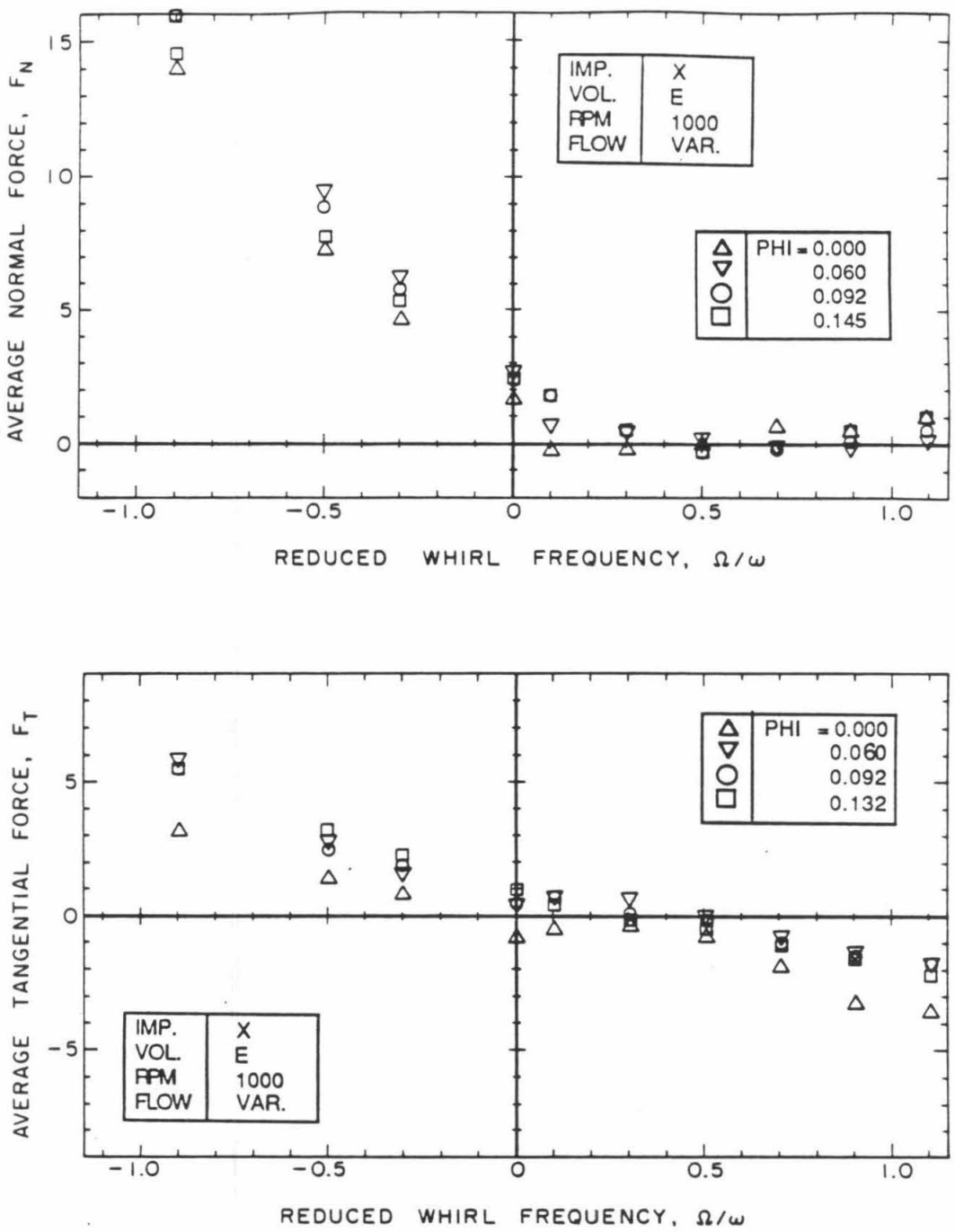

Fig. 6.10 Effect of the flow coefficient on the variation with reduced whirl frequency of the average normal and tangential forces. Data are for Impeller X operated within Volute E at 1000 rpm and four different flow conditions; from shut-off to full throttle: ϕ=0.000, 0.060, 0.092, and 0.145. Volute E was designed independently of Impeller X.

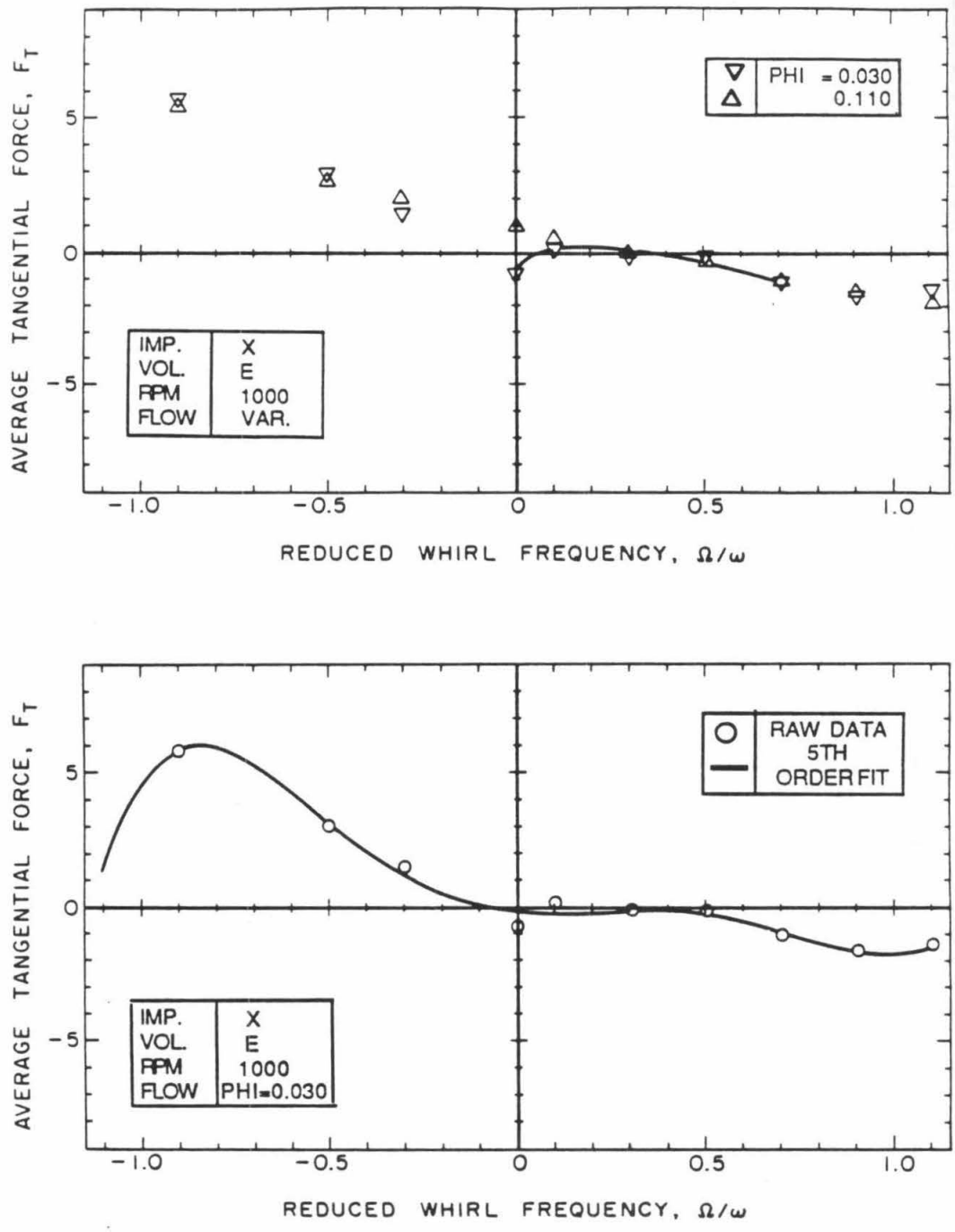

Fig. 6.11 The average tangential force measured on Impeller X operating within Volute E at 1000 rpm and two intermediate flow coefficients: ϕ=0.030 and ϕ=0.110 (top). A 5th order polynomial (in Ω/ω) is fitted to the Φ=.030 data (bottom).

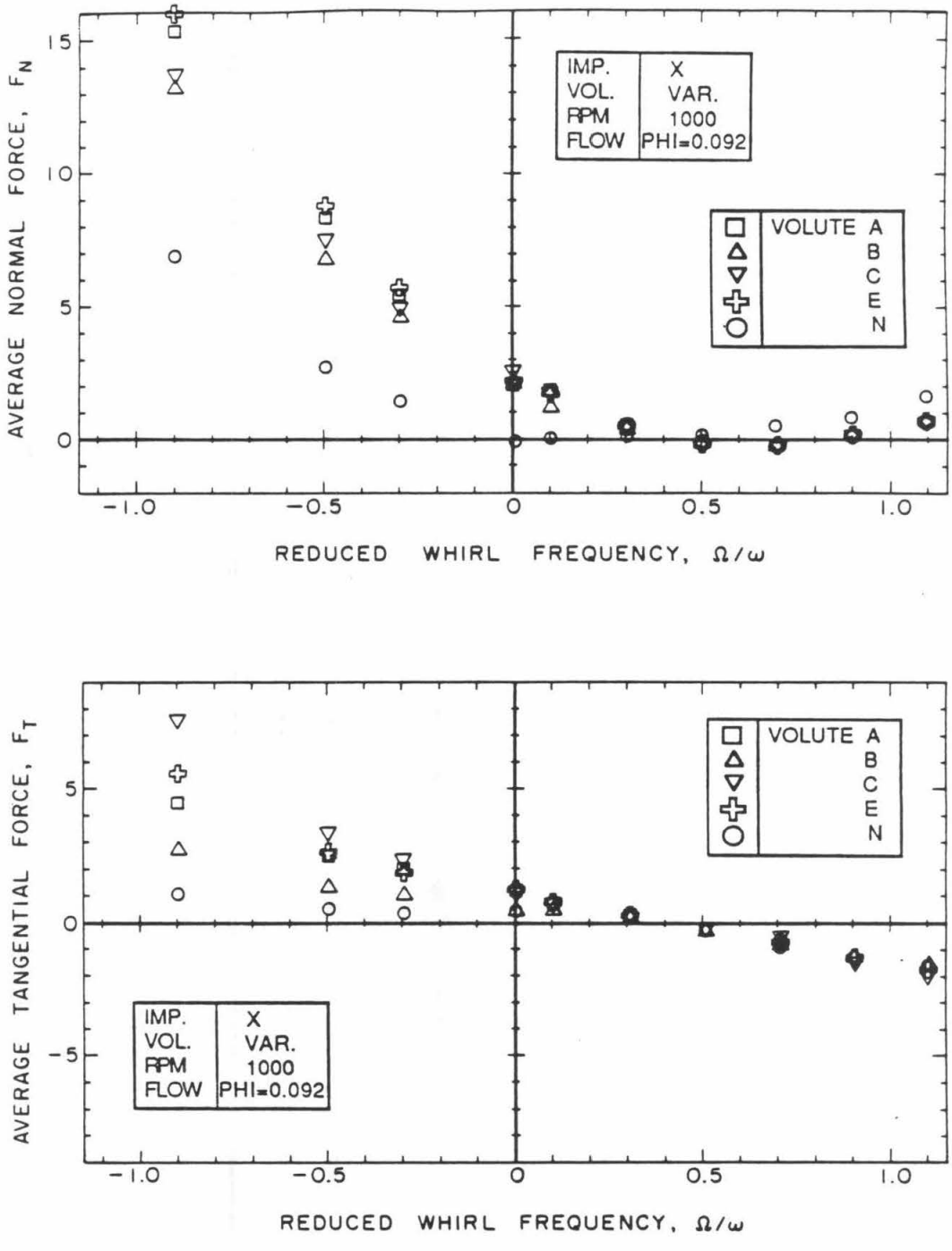

Fig. 6.12 Effect of the volute geometry on the evolution (with Ω/ω) of the average normal and tangential forces. Data are for Impeller X operated at 1000 rpm and design flow, in four different volutes (Volutes A, B and C, and Diffuser Volute E; see Fig. 2.5 for summary of volute and diffuser characteristics). The letter N refers to the case where the impeller is operated directly inside the pressure casing with no volute around it.

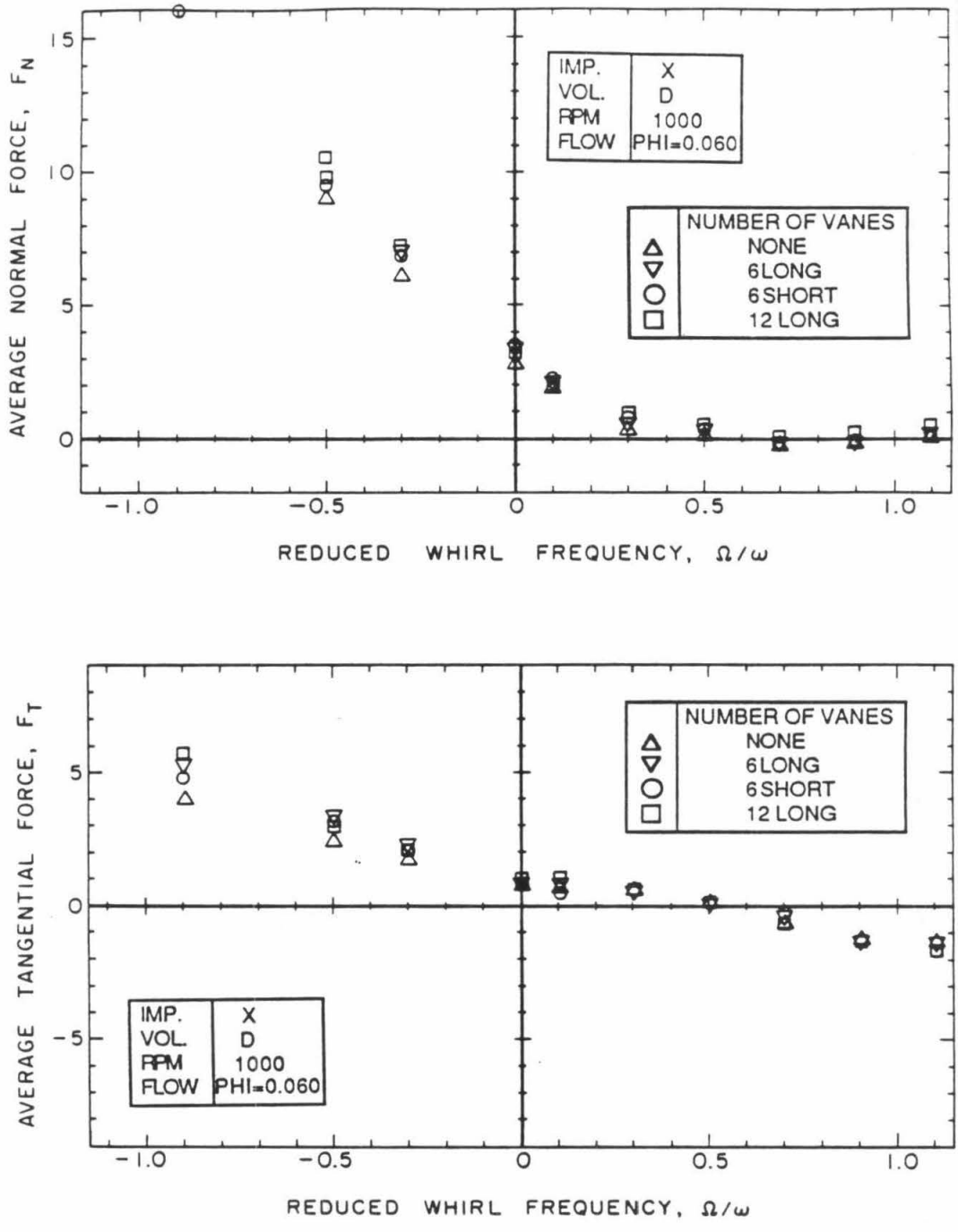

Fig. 6.13 Effect of the diffuser vane configuration on the evolution (with Ω/ω) of the average normal and tangential forces measured on Impeller X operating below design flow, at 1000 rpm, in Diffuser Volute D. Refer to Fig. 2.5 for details of the different vane configurations tested .

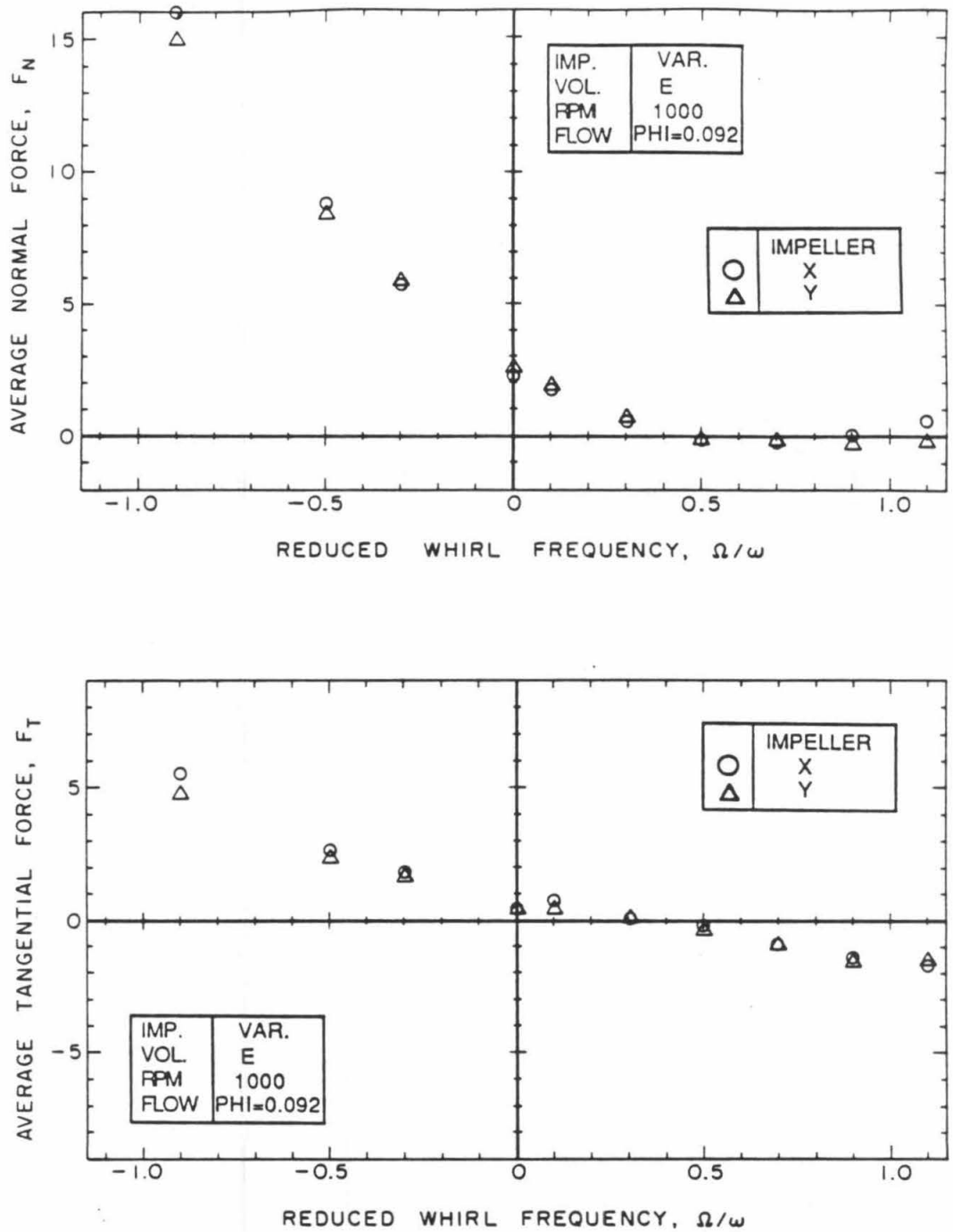

Fig. 6.14 Effect of the impeller design on the evolution (with Ω/ω) of the average normal and tangential forces. Data are for Diffuser Volute E and two different impellers (five-bladed Impeller X and six-bladed Impeller Y). The pump speed is 1000 rpm and the flow coefficient is ϕ=0.092= Impeller X design flow coefficient.

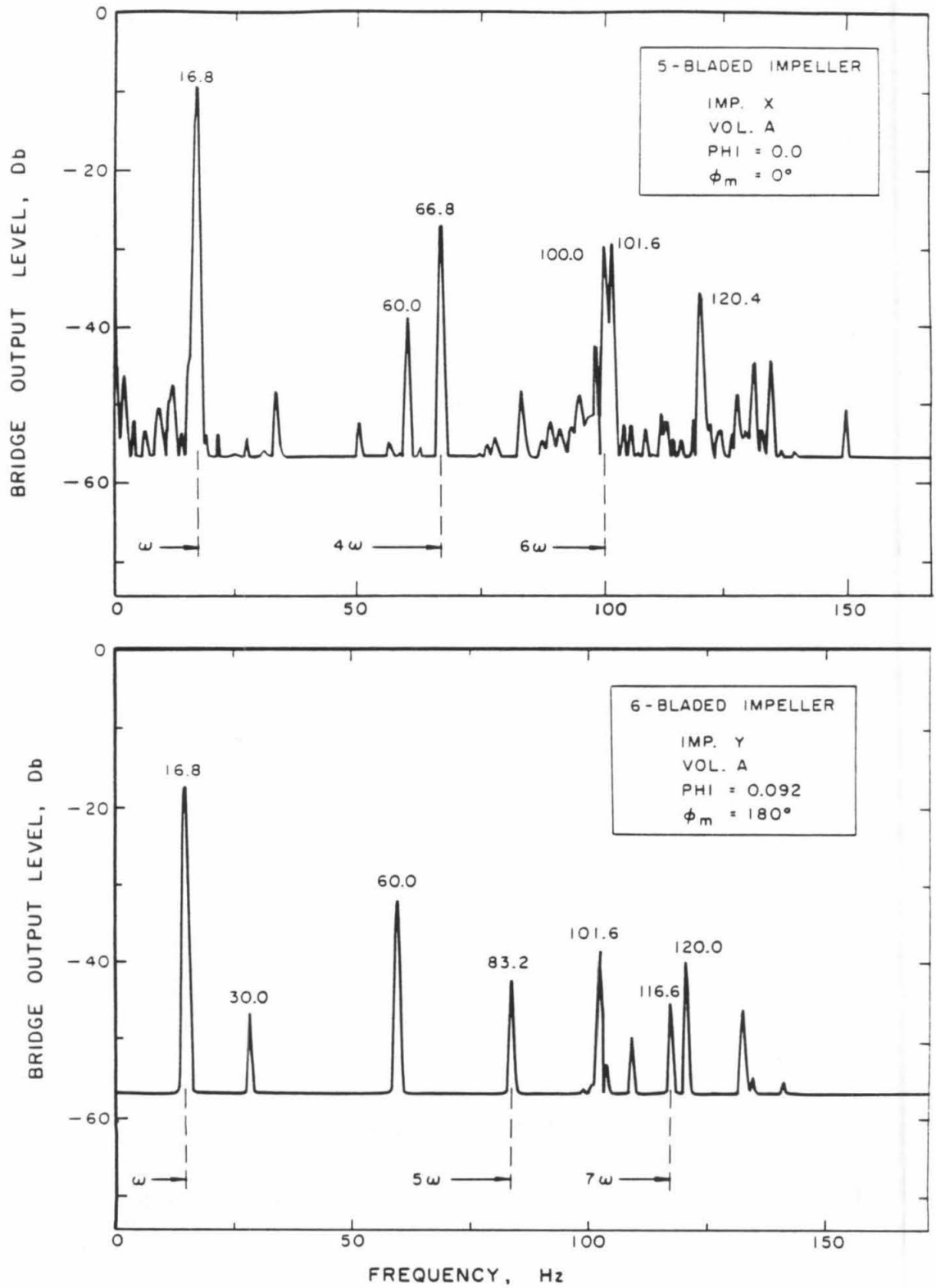

Fig. 6.15 Spectral analysis of analog recording of Bridge #1 output. The impeller is running at 1000 rpm (ω=16.7 Hz, no whirl: Ω=0) at a fixed location on the orbit, designated by the angle from the volute tongue, Φ_m (see Fig. C.1). Highlighted are the frequencies related to the blade passage. Top: 4ω and 6ω for the five-bladed Impeller X operated at shut-off. Bottom: 5ω and 7ω for the six-bladed Impeller Y operated at design flow.

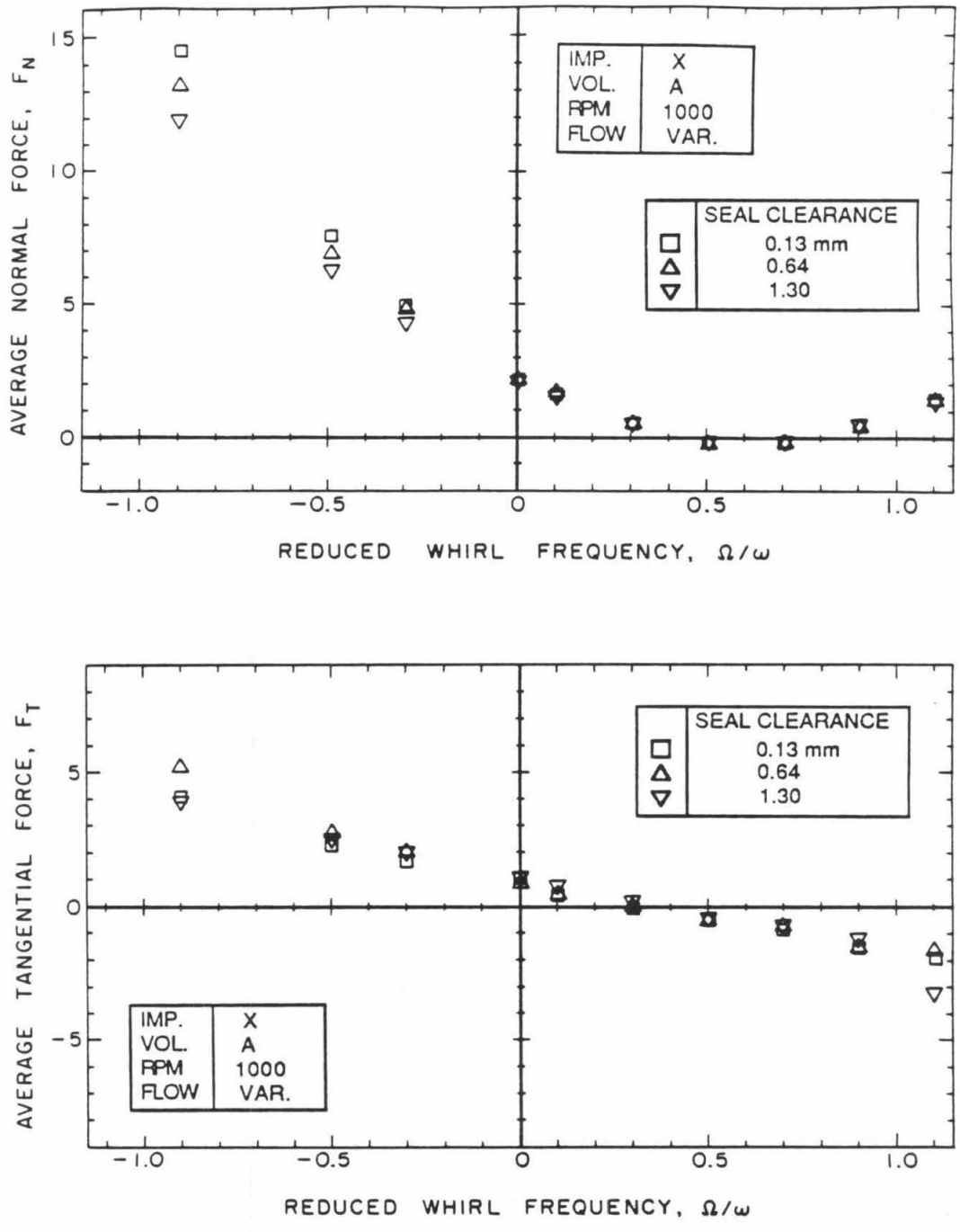

Fig. 6.16 Influence of the impeller face seal clearane setting on the variation of the impeller lateral force components with reduced whirl frequency. Both front and back seals are backed-off an equal amount (.13, .64 or 1.3 mm). Impeller X was operated inside Volute A at 1000 rpm. The pump net flow was adjusted to the value corresponding to Impeller X design condition and the nominal seal clearance setting of .13 mm.

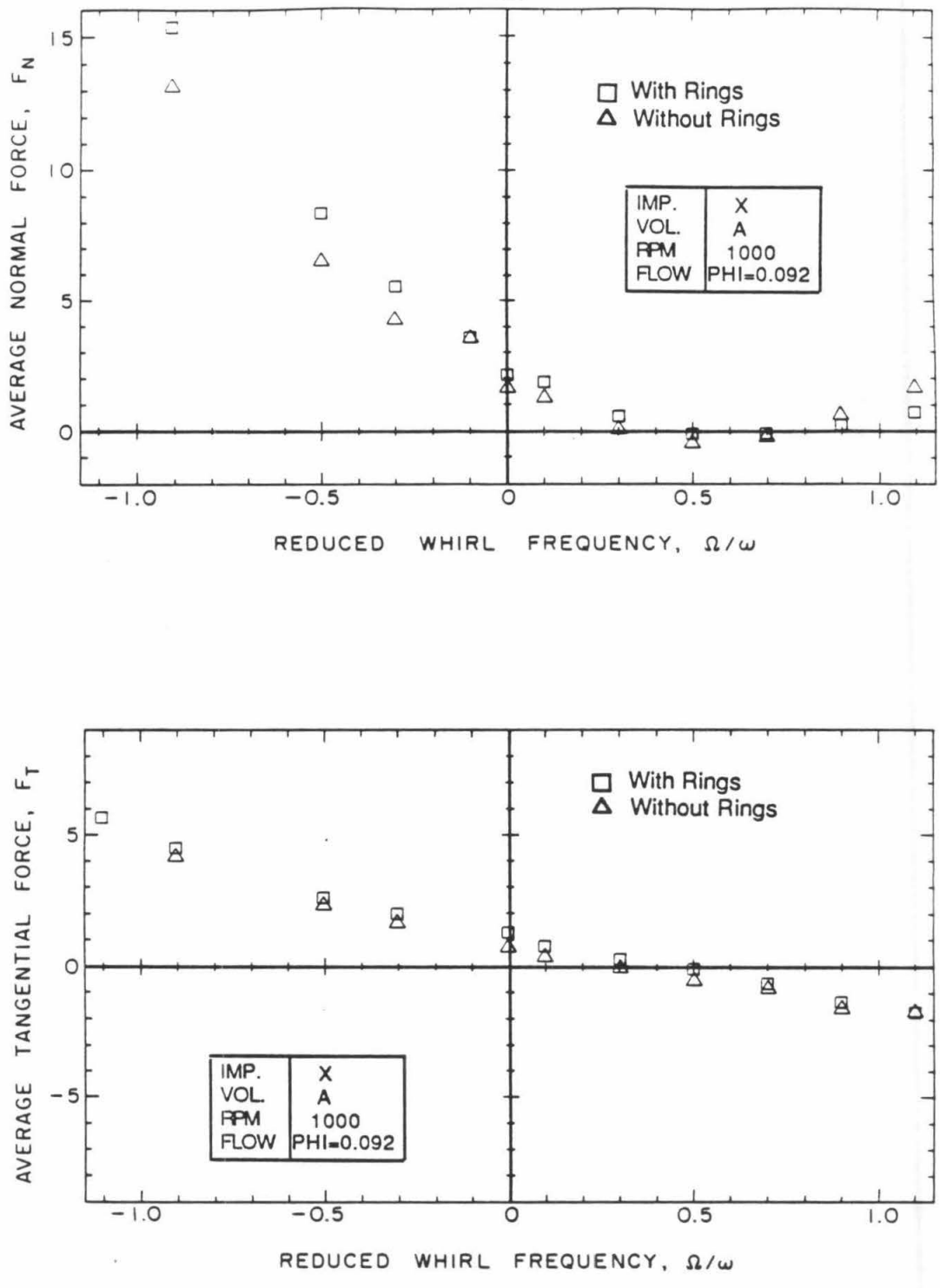

Fig. 6.17 Orbit-averaged normal (top) and tangential (bottom) components of the lateral hydrodynamic force measured on Impeller X in Volute A. Data from when Volute A is fitted with two circular rings (used to restrict the leakage area at the impeller discharge, see Fig. 4.1 for ring arrangement) are compared to those obtained in the standard case (no rings). Pump speed is 1000 rpm and the flow rate corresponds to Impeller X design condition.

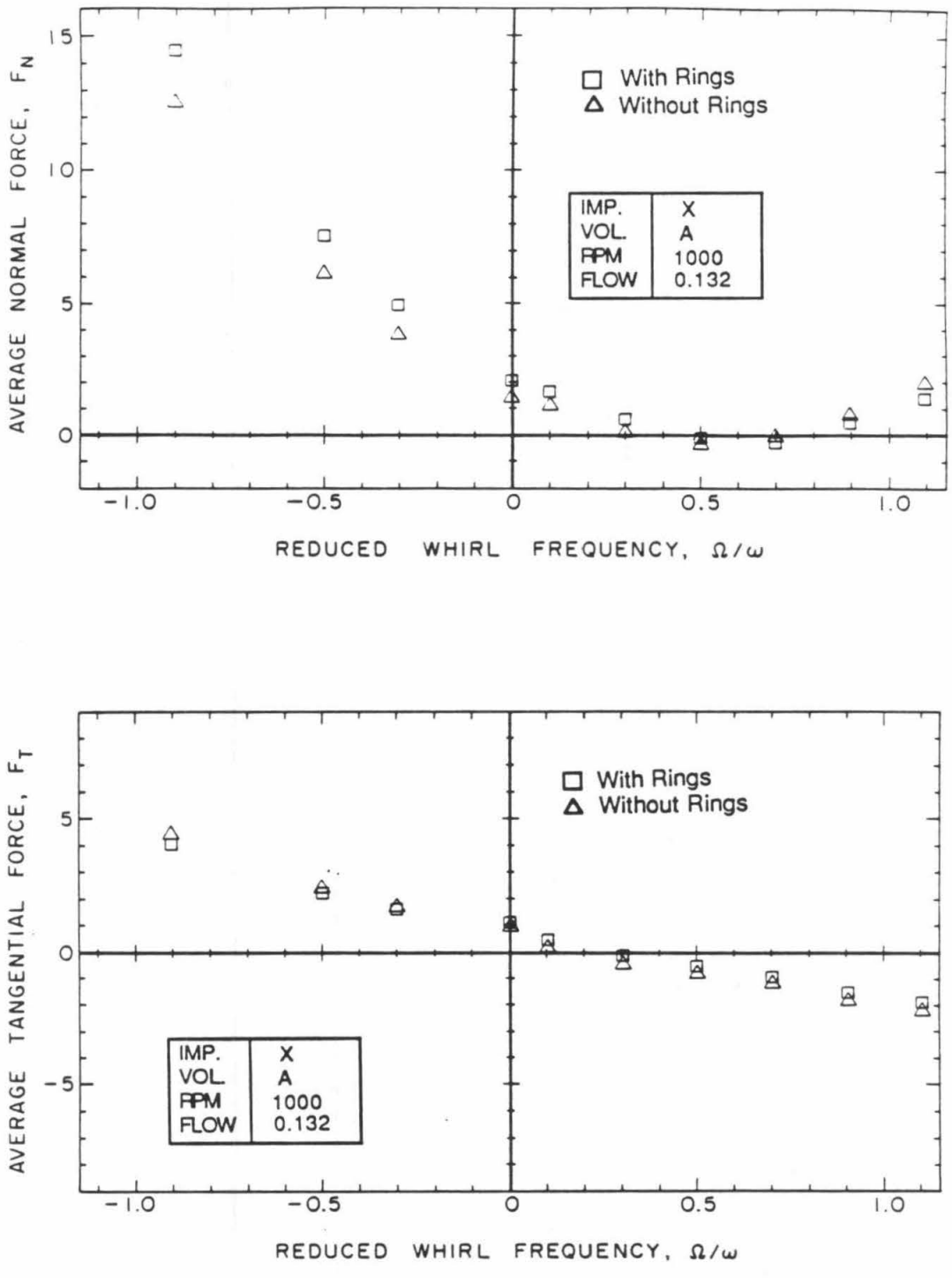

Fig. 6.18 Orbit-averaged normal (top) and tangential (bottom) components of the lateral hydrodynamic force measured on Impeller X in Volute A. Data from when Volute A is fitted with two circular rings (used to restrict the leakage area at the impeller discharge, see Fig. 4.1 for ring arrangement) are compared to those obtained in the standard case (no rings). Pump speed is 1000 rpm and the throttle is full open.

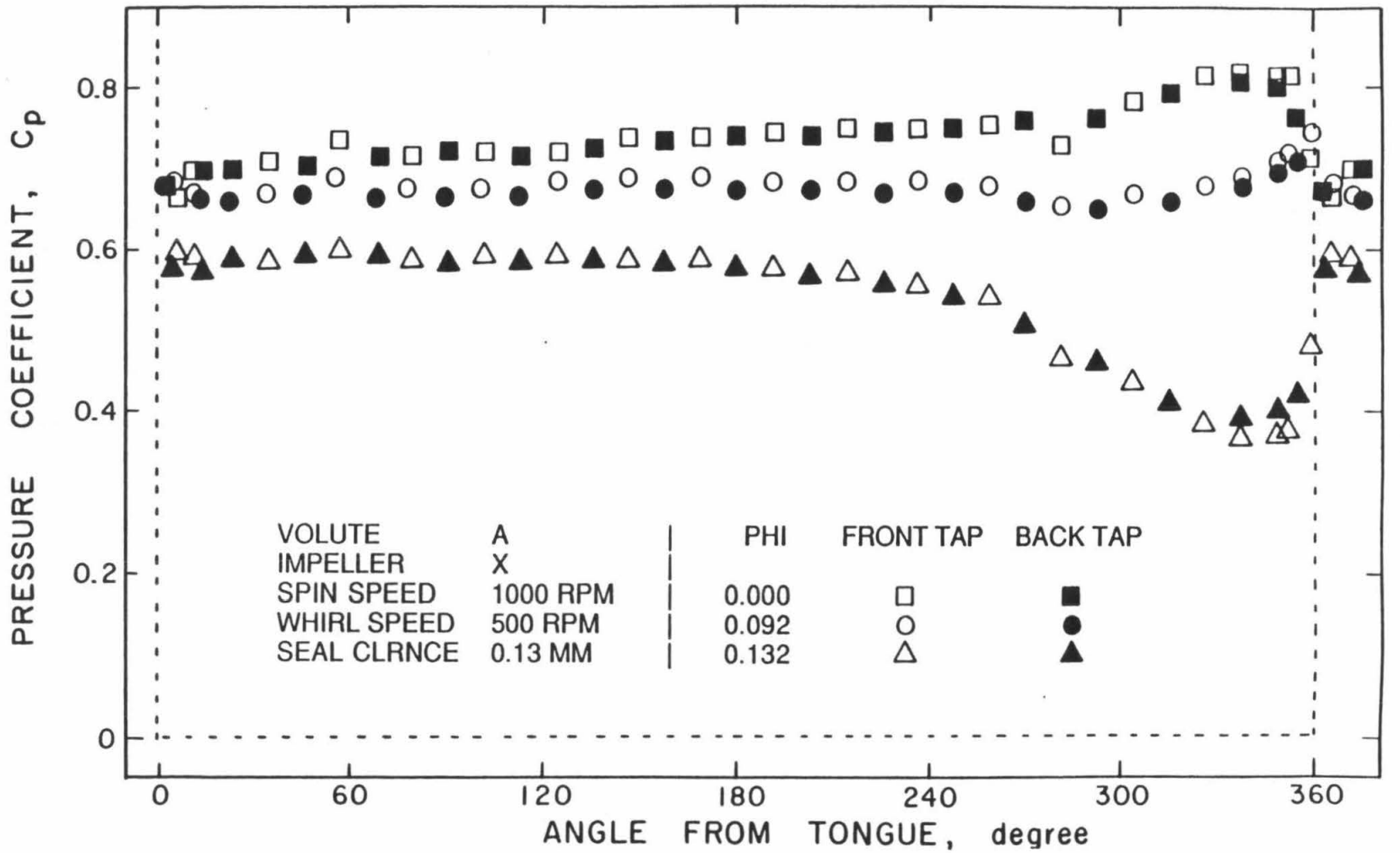

Fig. 6.19 Typical circumferential static pressure distributions measured at the front and back walls of Volute A immediately after the discharge of Impeller X. See Fig. 4.1 for details of tap arrangement. Pump speed is 1000 rpm and whirl speed is 500 rpm. Data are for three flow coefficients. .060, .092: design, and .132.

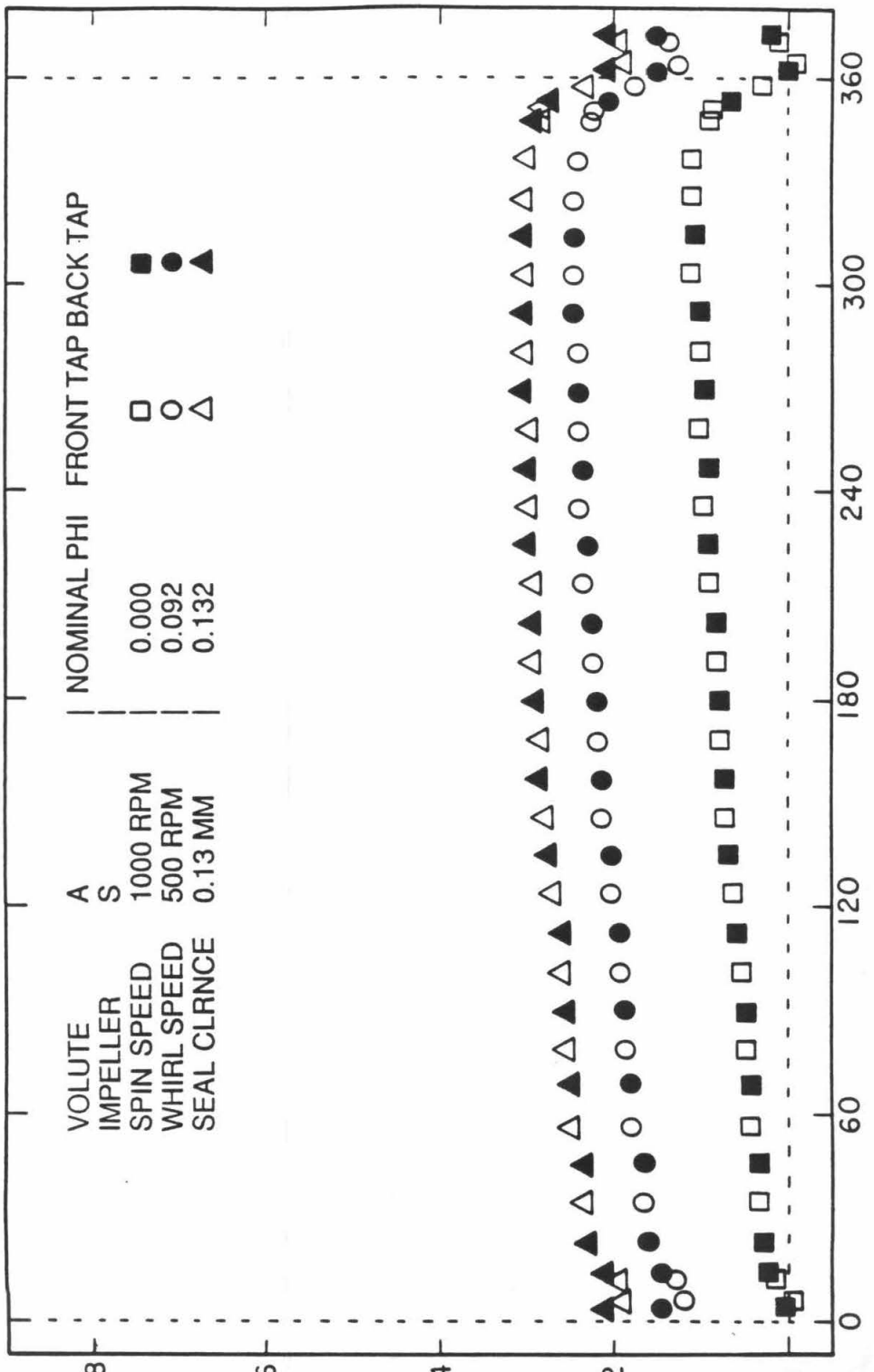

Fig. 6.20 Typical circumferential static pressure distributions measured at the front and back walls of Volute A. See Fig. 4.1 for details of tap arrangement. A solid impeller (Impeller S) is used (spin speed=1000 rpm, whirl speed=500 rpm). The auxiliary pump was operated so as to create the same pressure differentials across Impeller S as those prevailing across Impeller X at the indicated flow coefficents (.000, .092 and .132).

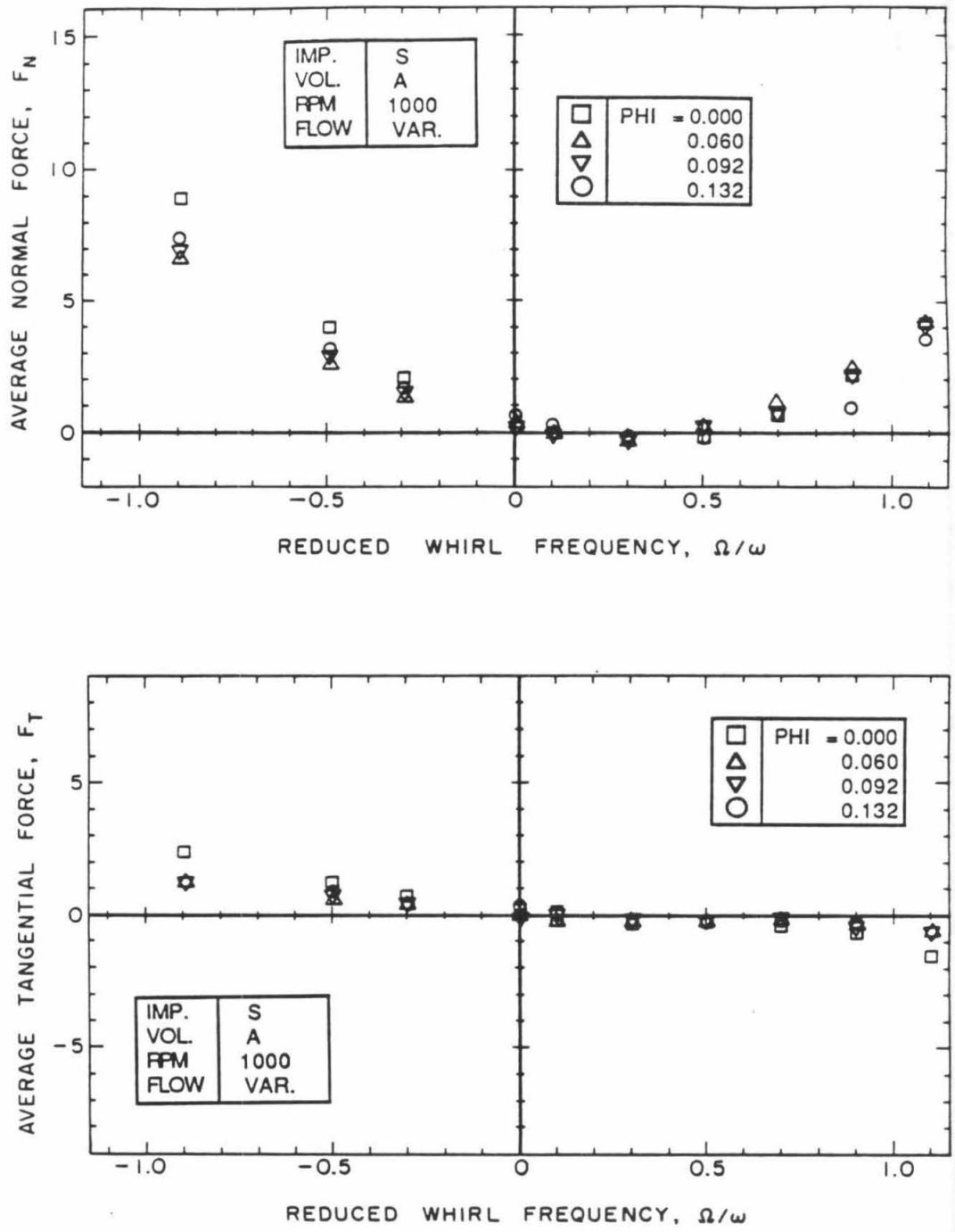

Fig. 6.21 Orbit-averaged normal (top) and tangential (bottom) components of the lateral hydrodynamic force measured on a consolidated dummy, Impeller S, duplicating the outside geometry of Impeller X. Impeller S was operated at 1000 rpm inside Volute A. The auxiliary pump was operated so as to create the same pressure differentials across Impeller S as those prevailing across Impeller X at the indicated flow coefficents (.000, .060, .092 and .132).

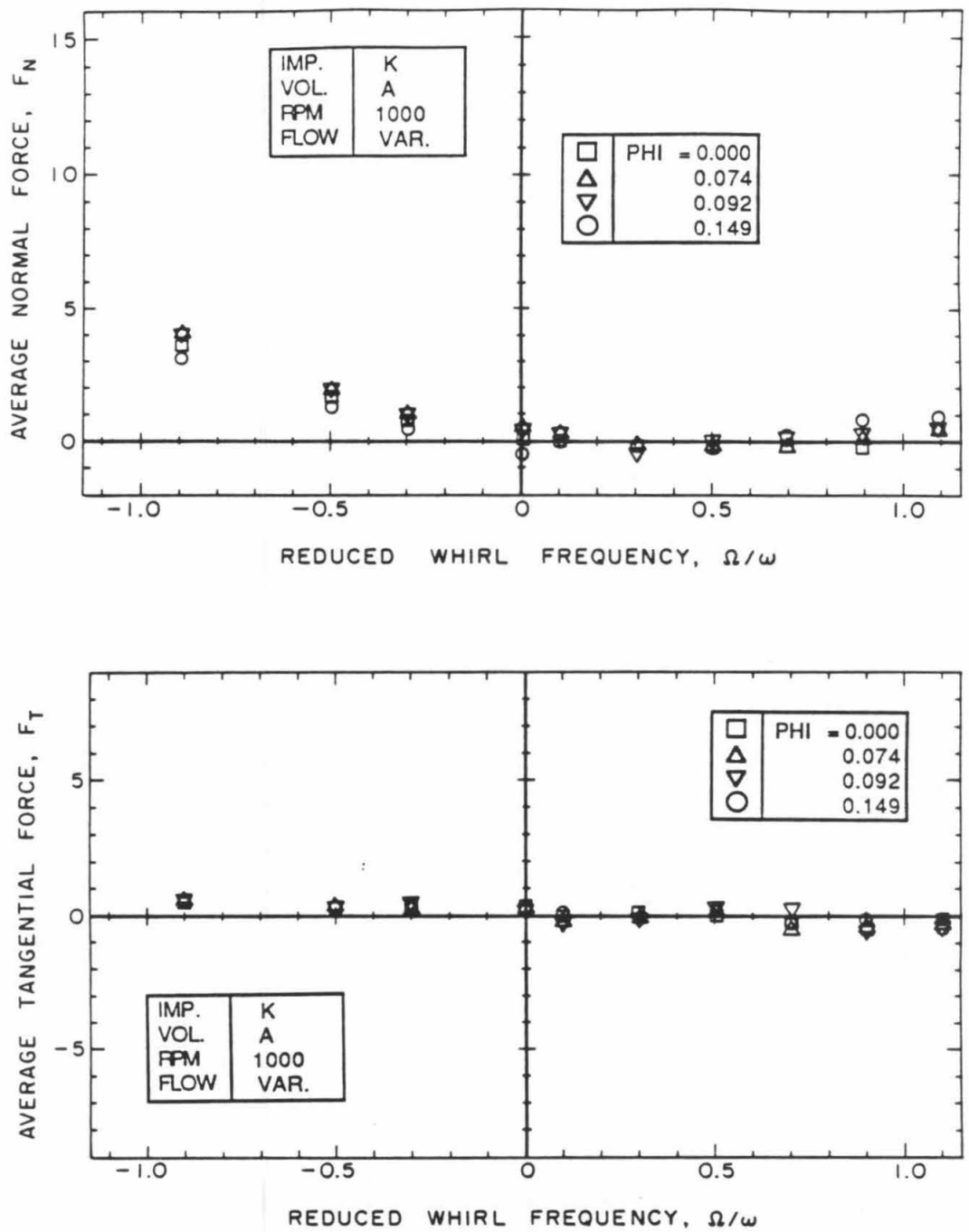

Fig. 6.22 Orbit-averaged normal (top) and tangential (bottom) components of the lateral hydrodynamic force measured on a thin circular disk, Impeller K (see Fig. 2. 4 for exact geometry), operating at 1000 rpm inside Volute A. The auxiliary pump was operated at flow rates equivalent to the indicated Impeller X flow coefficients,.000, .074, .092 and .149.

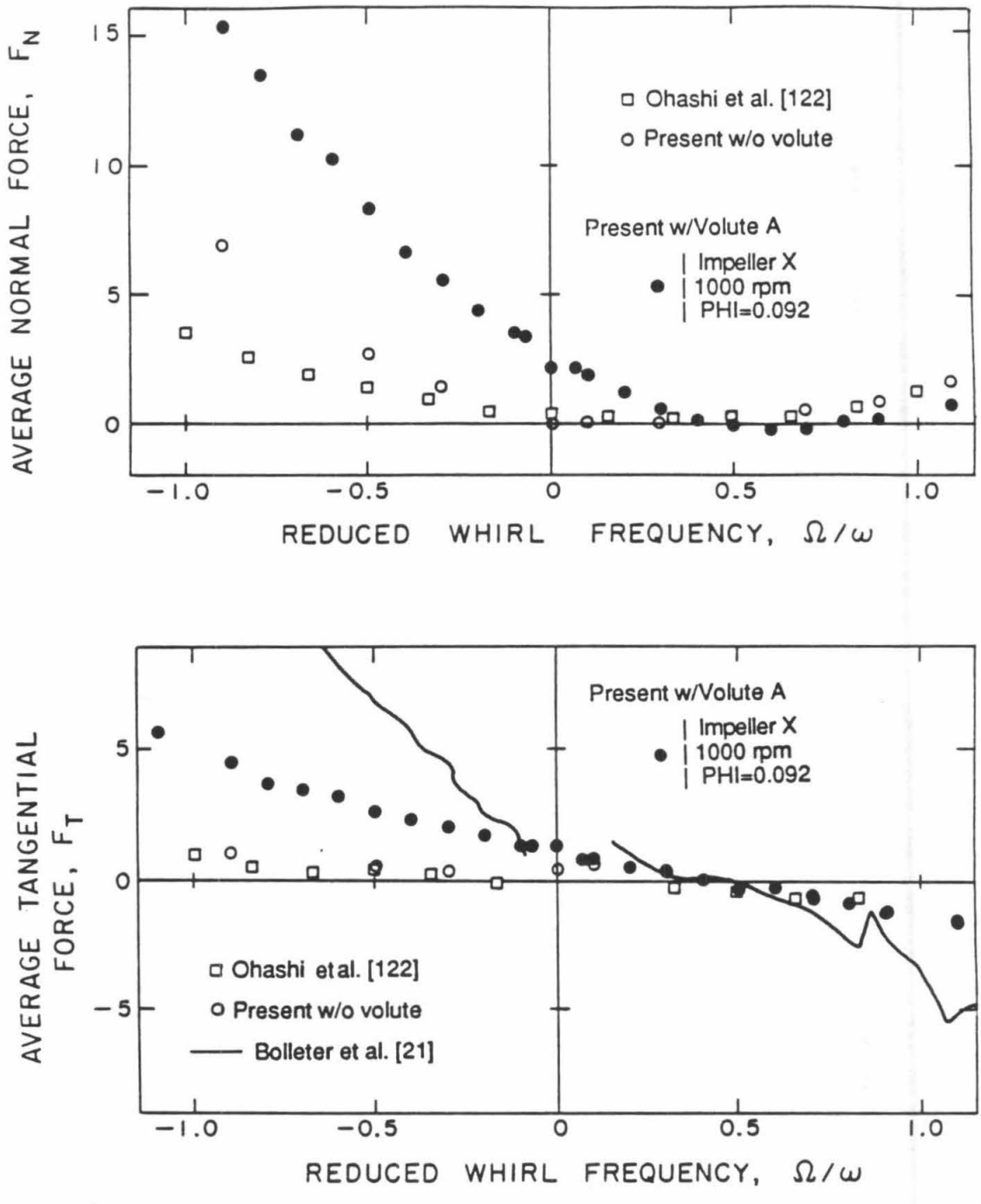

Fig. 6.23 Comparison of present data (standard case: Volute A, Impeller X, pump speed 1000 rpm) with experimental results from two other sources, Ohashi et al. [122], and Bolleter et al. [21].

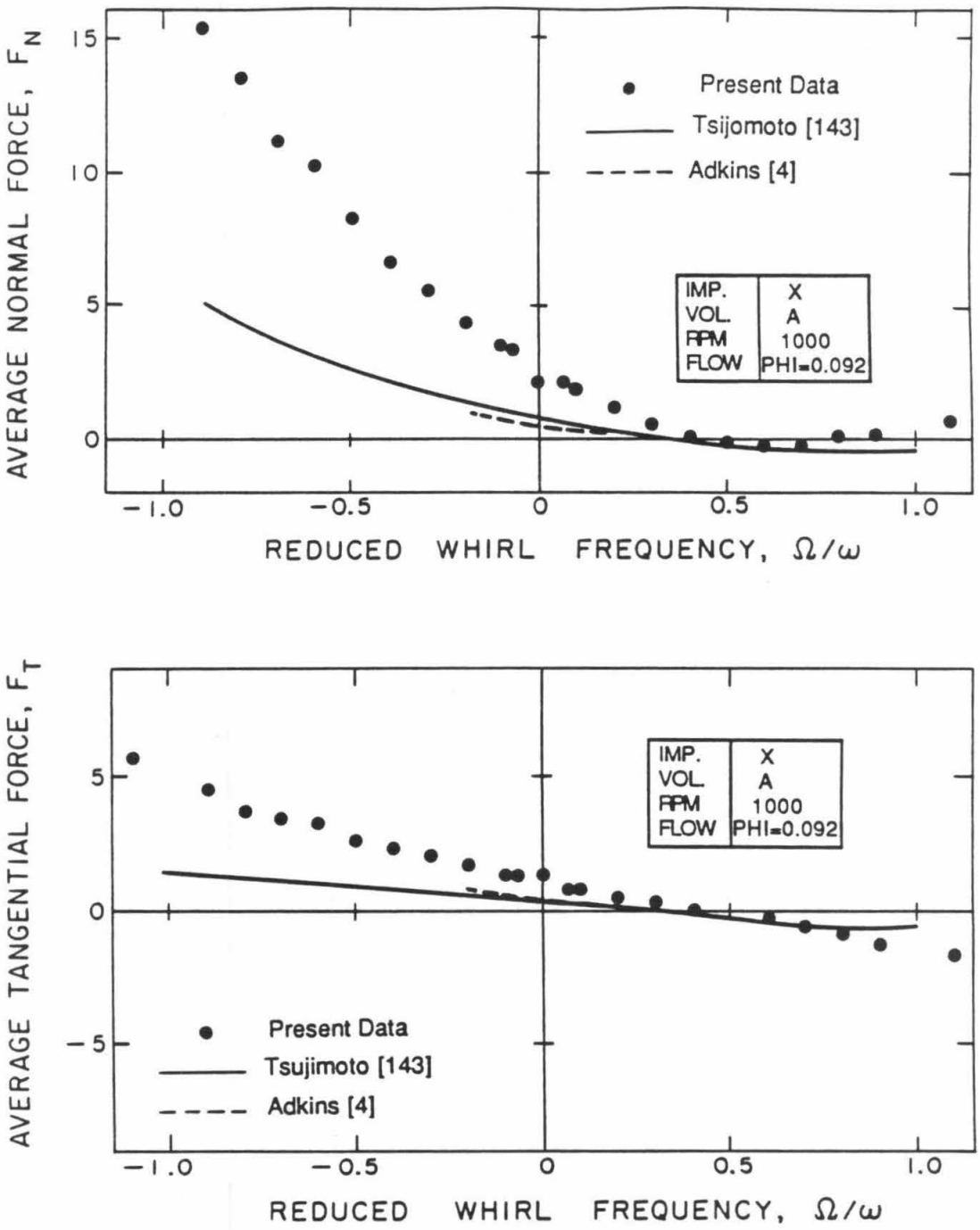

Fig. 6.24 Comparison of present data (standard case: Volute A, Impeller X, pump speed 1000 rpm) withresults from two theoretical studies, Adkins [4]], and Tsujimoto et al. [143].

Chapter 7

SUMMARY AND CONCLUSIONS

The need for the advancement of the state of knowledge in the area of rotor whirl-related instabilities in high performance turbomachines has been stressed, and the second stage of an extensive, multistage research program specifically designed to meet this need has been described. The efforts were aimed at a better understanding of the role played in these instabilities by hydrodynamic forces attributable to the presence of the rotor and/or to interactions between the rotor and the stator. Centrifugal flow pumps, in which deliberate circular whirl motions were forced upon the rotor, were chosen for the study.

In the first stage, Chamieh [32] investigated the quasi-steady fluid forces resulting from small, quasi-static displacement of the rotor center (very slow circular motion of the rotor center around the volute center), both theoretically and experimentally. His main conclusion was that the proportional (to the displacement) part of the steady impeller force results in a fluid stiffness matrix which is statically unstable. The direct stiffness terms were equal in magnitude and had the same negative sign, resulting in a radially outward fluid force. The cross-coupled stiffness elements were equal in magnitude and their opposite signs were such as to produce a tangential fluid force capable of driving forward whirl motion of the impeller, should the system lack adequate damping.

These interesting findings paved the way for the second stage of research geared toward the study of the unsteady aspects of these potentially destabilizing fluid forces. A theoretical study was planned as part of this second satge and was carried out by a separate investigator, D. Adkins [4]. The focus here is on the experimental work for which the present author is responsible.

The aim of this second experimental investigation was to provide a substantial body of data on a much wider variety of centrifugal flow pumps, in order to completely characterize the unsteady *hydrodynamic* forces measured under a much wider range of pump operating conditions, and in the presence of impeller whirl motions at finite speeds.

To do so, major modifications and additions had to be implemented in the test setup, including:

(i) an internally mounted rotating dynamometer capable of measuring all six components of both steady and unsteady impeller fluid forces (the chief interest is in the two lateral ones),

(ii) complete instrumentation of this dynamometer,

(iii) a more powerful whirl motor developing speeds ranging from subsynchronous to supersynchronous in either rotational directions,

(iv) a customized electronics package assuring precise control of both concentric and eccentric impeller motions, including synchronization with the data acquisition,

(v) major upgrading of the microprocessor-based data acquisition system, and interfacing of this system with the newly acquired desktop computer for data storage and processing,

(vi) an auxiliary pump making possible the investigatin of leakage flows and the operation of the main test pump in all four quadrants, and

(vii) additional test volutes and impellers to explore the effect of various pump geometries.

A set of conventional flow control and measurement devices and intruments, including a flow rate control servo-valve, a pneumatic system for control of overall loop pressure, turbine and electromagnetic flow meters, accelerometers and upstream and downstream pressure transducers, already existed in the test loop and needed little or no modification.

Comprehensive static and dynamic calibrations of the measurement system, and a set of preliminary tests were performed before the actual force measurements took place. These measurements included:

(i) for all pump and whirl speeds and combinations thereof, measurements of all tare forces which could affect the net lateral hydrodynamic forces imparted by the flow onto the impeller, and which included: (a) gravitational and pure inertial loads on the rotor, (b) the buoyancy force on the submerged impeller and dynamometer, and (c) parasitic hydrodynamic forces acting on the external surfaces of the submerged dynamometer,

(ii) with the impeller rotating at fixed locations on the whirl orbit (but not whirling), measurements of steady hydrodynamic forces covering the entire range of pump speeds and flow rates, and for three different values of impeller face seal clearance,

(iii) for each combination of pump speed, flow rate and seal clearance in (ii), measurements of steady and unsteady hydrodynamic forces for a number of whirl speeds ranging from subsynchronous to supersynchronous, in both whirl rotational directions,

(iv) various additional steady and unsteady hydrodynamic force measurements, associated with the pressure differentials (generated by the flow from the auxiliary pump) across both a consolidated dummy impeller and a thin circular disk (generating no flow of their own) rotating and/or whirling at the pump and whirl speeds and speed combinations used in (ii) and (iii); and finally,

(v) analog recordings of dynamometer, accelerometer and other pump instrument readings during representative tests selected from all four sets listed above.

Measurements (ii) and (iii) form the bulk of the study. They were conducted on two real impellers (one five-bladed, the other six-bladed) operating within a number of geometrically dissimilar volutes, including vaned and vaneless diffuser volutes. In these and all other measurements, data were averaged over several reference cycles represented by (a) one rotation of the impeller around its own axis, in the absence of whirl, or (b) one or more rotations of the impeller center around the whirl orbit, when whirl and concentric rotation are combined.

Among the six force components measured in each one of these tests, only the two lateral ones were directly used in the results to follow. Monitoring of the remaining components assured that they did not interfere in the measurement of these first two.

Measurements (ii) are analogous to the steady measurements of the first stage, and were processed in a similar manner, producing volute forces and "pure" stiffness matrices. Measurements (iii) are new but can be interpreted in the same fashion as measurements (ii). However, the resulting stiffness matrices are of the "generalized" type, containing hydrodynamic

damping, and inertial effects (due to whirl tangential velocity and normal acceleration), and possibly higher-order fluid effect, in addition to the pure fluid stiffness (due to eccentricity alone).

Measurements (vi) can produce either results, depending on whether whirl was present or not. Recordings (v) were processed through a Fourier spectrum-analyzer and provided information on the harmonic contents of the various signals, including blade-passage forces.

A study of the results of all these measurements supports the following chief conclusions:

(i) The steady hydrodynamic radial forces measured by the rotating dynamometer confirm the findings of previous investigators, especially those of Chamieh [32], and extend them to new pump geometries and operating conditions. In particular, it was found that (a) these forces scale with the square of pump speed as would be expected; (b) the fixed part of these forces vanishes at the design flow coefficient and is independent of the whirl motion (this second finding is new but should be expected); and (c) the proportional part of these forces results in a statically unstable pure fluid stiffness matrix which is the sum of a diagonal matrix and a skew-symmetric matrix.

(ii) Measurements of the average unsteady, lateral hydrodynamic impeller forces performed for various whirl speeds yielded generalized hydrodynamic stiffness matrices which (a) scale with the square of pump speed, and (b) whose elements confirm the common assumption of skew-symmetry[1], for the first time.

(iii) When interpreted in terms of average normal and tangential forces (with respect to the circular whirl orbit) and plotted against the reduced whirl frequency, these unsteady hydrodynamic forces display the following important properties: (a) the normal force has a pronounced quadratic variation with a positiive curvature, and is positive for all values of the

[1] The diagonal terms, A_{xx} and A_{yy}, are equal in magnitude and sign; the off-diagonal terms, A_{xy} and A_{yx}, are equal in magnitude but opposite in sign, which makes it possible to describe the results with two variables only: the average normal force, $F_N=(A_{xx}+A_{yy})/2$, and the average tangential force, $F_T=(A_{xy}+A_{yx})/2$.

reduced frequency except in a small region centered approximately around 0.6 in which a slightly negative normal force was registered; (b) the magnitude of this normal force is higher in the negative whirl region, as expected for a Bernouilli suction force[2]; (c) as for the tangential force (which plays a much more important role in the stability of the whirl motion), three distinct regions of reduced whirl frequency can be observed: for all negative whirl speeds and for the higher positive whirl speeds, the sign of this force is such as to dampen the whirl motion. On the other hand, there is a region of reduced positive whirl frequencies (between 0.0 and 0.2 to 0.6) in which this force has the same sign as the tangential whirl velocity, and as such has a destabilizing effect on the whirl motion. This is perhaps the single most important finding from these measurements, as it proves that self-excited whirl can be caused by the flow through the pump.

(iv) The unsteady forces measured were very sensitive to the value of the flow coefficient (especially below design conditions), the tangential force being higher for the higher flow coefficients[3], on the average.

(v) Several volutes were tested, and the results obtained show that the effect of volute geometry on the measured forces is very strong in the negative whirl region, and virtually null in the positive whirl region (which is of more interest). However, it is clearly demonstrated that operation of the impeller inside the wide pump casing, after completely removing the volute, makes a significant difference in the results for both whirl directions. The fundamental question was raised of whether an impeller whirling in an infinite medium would generate destabilizing forces. This experiment was the closest approximation to this condition and appears to show that that is indeed the case. The measured stiffness was basically zero but the damping was negative, with a small positive tangential force at low whirl

---

[2] For negative whirl, the concentric and the eccentric rotations combine to give a higher tip velocity for the impeller side closer to the volute which results in a lower pressure in the annular gap, thus sucking the impeller radially outward.

[3] The postulation was that these forces are mostly due to the interaction of the impeller with the surrounding volute via the flow in between; thus, the higher the flow, the higher the interaction.

speeds. Also, the presence, number or orientation of diffuser guide vanes had surprisingly little effect on these results.

(vi) As for the effect of the impeller geometry, no conclusion can be made until impellers with more dissimilar characteristics are tested.

(vii) There is a speculation that the leakage flow might play a role in the unsteady forces. Although no clear trend could be detected, measurable variations were registered in both normal and tangential forces, when the impeller face seal clearances were varied or when the volute was fitted with two leakage-limiting rings placed at the impeller discharge.

When recirculation from the high pressure side to the low pressure side of the impeller was simulated, using a consolidated dummy impeller and the flow from an auxiliary pump, the measured forces showed some change with changes in the equivalent flow coefficient. However, the tangential force always opposed the whirl tangential velocity (friction on all external faces of the dummy included), and thus had a stabilizing effect.

Similar measurements conducted on a thin disk (using the actual values of the flow rates) led to the same conclusion regarding the tangential force.

(viii) Spectral analysis of dynamometer output signals during operation of the impeller at fixed locations on the whirl orbit proved that blade passage forces are large enough to be detected. However, the radial forces (and rotordynamic forces) analysed in this thesis produced the dominant peaks an all spectra.

(ix) The main results of this study are in good qualitative (and in some instances quantitative) agreement with those of recent experimental and analytical investigations.

(x) Finally, the assumption of quadratic variation of the elements of the generalized stiffness matrix, often used in linearized rotor dynamic analyses, was found to hold well for the higher flow coefficients (as confirmed by the results of least-squares quadratic fits). However, near shut-off, a higher order polynomial fit appears to be more appropriate. It was also found that the measured added mass coefficients match those obtainable from simple textbook models. As an illustration of the practical use of the rotordynamic coefficients (elements of

the pure stiffness, the damping and the inertia matrices), the study (carried by Childs and Moyer, using results from the present measurements) appended to this thesis clearly shows that all rotordynamic coefficients have to be included in the computational model, before accurate predictions of the crititcal speeds and the Onset Speed of Instability can be achieved.

It is important to conclude by observing that, although the present measurements were conducted on centrifugal flow pumps, the approach is more general and can be applied to other types of turbomachines. It is also essential to emphasize that a fundamental fact has been established, namely, that the flow itself is capable of sustaining unstable rotor motions inside a turbomachine.

REFERENCES*

1. Adams, M. L., and Makay, E., "Development of Advanced Rotor-Bearing Systems for Feedwater Pumps, Phase 2," EPRI CS-2027, Project 1266-7-1, Final Report, Sept. 1981.

2. Adams, M. L., Makay, E., and Diaz-Tous, I.A., "Measurement of Interstage Fluid-Annulus Dynamical Properties," Second Workshop*,1982.

3. Adams, M. L., and Padovan, J. , "Insights into Linearized Rotor Dynamics," J. of Sound and Vibration, Vol.76 (1), pp. 129-142, 1981.

4. Adkins, R.D., "Analysis of Hydrodynamic Forces on Centrifugal Pump Impellers," Ph.D. Thesis, Division of Engineering and Applied Science, California Institute of Technology, 1986.

5. Agostinelli, A., Nobels, D., and Mockridge, C. R., "An Experimental Investigation of Radial Thrust in Centrifugal Pumps," Transactions of the ASME, pp. 120-126, April 1960.

6. Alford, J. S., "Protecting Turbomachinery From Self-Excited Rotor Whirl," J. of Eng. for Power, pp. 333-344, Oct. 1965.

7. Allaire, P.E., Flack,R.D., "Instability Thresholds for Flexible Rotors in Hydrodynamic Bearings," First Workshop*,1980.

8. Allaire, P.E., Sato, C.J., and Branagan, L.A., "Hydraulic Forces on a Centrifugal Impeller Undergoing Synchronous Whirl," Third Workshop*,1984.

9. Atkins, K.E., Tison, J.D.,and Wachel, J.C., "Critical Speed Analysis of an Eight-Stage Centrifugal Pump," Proc. of the Second International Pump Symposium, Houston,Texas, April 29 - May 2, 1985.

10. Barrett, L.E., Gunter, E.J., "Stabilization of Aerodynamically Excited Turbomachinery with Hydrodynamic Journal Bearings and Supports," First Workshop*,1980.

11. Baxter, N., "Case Studies of Rotor Instability in the Utility Industry," presented at ASME/The Applied Mechanics, Bioengineering and Fluids Engineering Conference, Houston, Texas, June 20-22, 1983 , AMD Vol. 55, 1983.

12. Beatty, R.F., and Rowan, B.F., "Determination of Ball Bearing Dynamic Stiffness," Second Workshop*,1982.

13. Benckert, H., and Wachter, J., "Flow-Induced Spring Coefficients of Labyrinth Seals for Application in Rotordynamics," First Workshop*,1980.

14. Bently, D.E., and Muszynska, A., "Dynamic Stiffness Characteristics of High Eccentricity Ratio Bearings and Seals by Perturbation Testing," Third Workshop*,1984.

15. Bhat, G.I., and Eierman, R.G., "Experimental On-Stream Elimination of Resonant Whirl in a Large Centrifugal Compressor," Third Workshop*, 1984.

* Several of the references cited herein can be found in the proceedings of workshops on Rotordynamic Instability Problems in High-Performance Turbomachinery organized biannually by the Turbomachinery Laboratories at Texas A&M University, College Station, Texas. The first took place May 12-14, 1980. The second took place May 10-12, 1982, NASA Conf. Pub. 2250. The third took place May 28-30,1984, NASA Conf. Pub. 2338.

16. Biheller, H. F., "Radial Force on the Impeller of Centrifugal Pumps with Volute, Semivolute, and Fully Concentric Casings," J. of Eng. for Power, pp. 319-323, July 1965.

17. Binder, R. C., and Knapp, R.T., "Experimental Determinations of the Flow Characteristics in the Volutes of Centrifugal Pumps," Trans. ASME, Vol.58, pp. 649-661, 1936.

18. Black, H. F., "Calculation of Forced Whirling and Stability of Centrifugal Pump Rotor Systems," Trans.of the ASME, pp. 1076-1084, August 1976.

19. Black, H. F., "Lateral Stability and Vibrations of High Speed Centrifugal Pump Rotors," International Union of Theoretical and Applied Mechanics, Dynamics of Rotors, Symposium Lyngby, Denmark, August 12-16, 1974, Springer Verlag, pp.56-74, 1975.

20. Bolleter, U., Frei, A., Florjancic, D., "Predicting and Improving the Dynamic Behavior of Multistage High Performance Pumps," Proceedings of the First International Pump Symposium, Texas A&M University, College Station, Texas, pp.1-8, May 1984.

21. Bolleter, U., Wyss, A., Welte, I., and Stuerchler, R., "Measurement of Hydrodynamic Interaction Matrices of Boiler Feed Pump Impellers," presented at the ASME Design Engineering Division Conference and Exhibit on Mechanical Vibration and Noise, Cincinnati, Ohio, Sept. 10-13, 1985.

22. Bonciani, L., Ferrara, P. L., and Timori, A., "Aero-induced Vibrations in Centrifugal Compressors," First Workshop*,1980.

23. Bonciani, L., and Terrinoni, L., "Influence of Stationary Components on Unsteady Flow in Industrial Centrifugal Compressors," Third Workshop*,1984.

24. Bonciani, L., Terrinoni, L., and Tesei, A., " Unsteady Flow Phenomena in Industrial Centrifugal Compressor Stage," Second Workshop*,1982.

25. Booth, D., "Phillip's Landmark Injection Project," Petroleum Engineer, pp.105-109, Oct. 1975.

26. Bowerman, R. D., and Acosta, A.J., "Effect of the Volute on the Performance of a Centrifugal Pump Impeller," Trans. ASME, Vol. 79, pp. 1057-1069, July 1957.

27. Braisted, D. M., "Cavitation Induced Instabilities Associated with Turbomachines," Ph. D. Thesis, Division of Engineering and Applied Sciences, California Institute of Technology, 1979.

28. Brennen, C.E., "On the Flow in an Annulus Surrounding a Whirling Cylinder," J. of Fluid Mech. , Vol. 75, Part 1, pp. 173-191, 1976 .

29. Brennen, C. E., Acosta, A.J., and Caughey, T.K., "A Test Program to Measure Fluid Mechanical Whirl-Excitation Forces in Centrifugal Pumps," First Workshop*, 1980.

30. Brown, D.R., and Black, H.F., "Limit Cycles of a Flexible Shaft with Hydrodynamic Journal Bearings in Unstable Regimes," First Workshop*, 1980.

31. Caignaert, G., "Contribution a l'Etude des Interactions entre le Bec de la Volute et la Roue d'une Pompe Centrifuge," Thesis Dissertation, L'Universite' des Sciences et Techniques de Lille, France, February 1978.

32. Chamieh, D.S., "Forces on a Whirling Centrifugal Pump-Impeller," Ph.D. Thesis, Division of Engineering and Applied Science, California Institute of Technology, 1983.

33. Chamieh, D.S., "Calculation of the Stiffness Matrix of an Impeller Eccentrically Located Within a Volute," Cavitation and Polyphase Flow Forum, Joint ASME/ASCE Conf., Boulder, Colorado, pp. 51-53, 1981.

34. Chamieh, D.S., Acosta, A. J., Brennen, C. E., and Caughey, T. K., "A Brief Note on the Interaction of an Actuator Cascade with a Singularity," First Workshop*, 1980.

35. Chamieh, D.S., Acosta, A.J., Brennen C.E., Caughey, T.K., and Franz, R., "Experimental Measurements of Hydrodynamic Stiffness Matrices for a Centrifugal Pump Impeller," Second Workshop*, 1982.

36. Childs, D.W., "The Space Shuttle Main Engine High-Pressure Fuel Turbopump Rotordynamic Instability Problem," Trans. of the ASME, J. of Eng. for Power, Vol. 100, pp. 48-57, Jan., 1978.

37. Childs, D.W., "Finite-Length Solutions for Rotordynamic Coefficients of Turbulent Annular Seals," Trans. of the ASME, J. of Lubrication Technology, Vol. 105, pp. 437-444, July 1983.

38. Childs, D.W., and Kim, C., "Analysis and Testing for Rotordynamic Coefficients of Turbulent Annular Seals with Different, Directionally Homogeneous Surface Roughness Treatment for Rotor and Stator Elements," Third Workshop*, 1984.

39. Childs, D.W., and Moyer, D.S., "Vibration Characteristics of the HPOTP (High-Pressure Oxygen Turbopump) of the SSME (Space Shuttle Main Engine)," Trans. ASME, J. of Eng. for Power, Paper No. 84-Gt-31, 1984.

40. Chow, S. K., Hou, A. Y., and Landweber, L., "Calculation of Flow Through a Two-Dimensional Centrifugal Impeller by the Method of Hydrodynamic Singularities," Chapter 6, "Pumps: Analysis Design and Application," Worthington Pump Inc., Vol.1, pp. 113-133, 1978.

41. Colding-Jorgensen, J., "Effect of Fluid Forces on Rotor Stability of Centrifugal Compressors and Pumps," First Workshop*, 1980.

42. Crandall, S.H., "The Physical Nature of Rotor Instability Mechanisms," presented at ASME/The Applied Mechanics, Bioengineering and Fluids Engineering Conference, Houston, Texas, June 20-22, 1983 , AMD Vol. 55, 1983.

43. Csanady, G.T., "Radial Forces in a Pump Caused by Volute Casing," Trans. ASME, J. of Eng. for Power, Vol. 84, pp. 337-340, October 1962.

44. Davis, W. R., and Millar, D. A. J., "A Comparison of the Matrix and Streamline Curvature Methods of Axial Flow Turbomachinery Analysis, From a User's Point of View," J. of Eng. for Power, pp. 549-560, Oct. 1975.

45. Dede, M.M., Dogan, M., and Holmes R., "Damping Capacity of a Sealed Squeeze Film Bearing," Third Workshop*, 1984.

46. Domm, U., and Hergt, P., "Radial Forces on Impeller of Volute Casing Pumps, Flow Research on Blading" (L.S. Dzung, ed.), Elsevier Pub. Co., The Netherlands, pp. 305-321, 1970.

47. Doyle, H.E., "Field Experiences with Rotordynamic Instability in High-Performance Turbomachinery," First Workshop*, 1980.

48. Ehrich, F.F., "The Dynamic Stability of Rotor/Stator Radial Rubs in Rotating Machinery," J. of Eng. for Industry, Vol. 91, pp.1025-1028, Nov. 1969.

49. Ehrich, F.F., "The Influence of Trapped Fluids on High Speed Rotor Vibration," Trans. of the ASME, J. of Eng. for Industry, pp. 806-812, Nov. 1967.

50. Ehrich, F., and Childs, S. D., "Self-Excited Vibrations in High Performance Turbomachinery," Mechanical Engineering, pp.66-79, May 1984.

51. Ek, M. C., "Solution of the Subsynchronous Whirl Problem in the High Pressure Hydrogen Trubomachinery fo the Space Shuttle Main Engine," Paper No. 78-1002, AIAA/SAE 14th Joint Propulsion Conference, Las Vegas, Nevada, July 25-28, 1978.

52. Emerick, M.F., "Vibration and Destabilizing Effects of Floating Ring Seals in Compressors," Second Workshop*, 1982.

53. Evans, B.F., and Smalley, A.J., "Subsynchronous Vibrations in a High-Pressure Centrifugal Compressor: A Case History," Third Workshop*, 1984.

54. Fenwick,J., DiJulio, R., Ek, M.C., Ehrgott, R., Green, H., and Shaolian, S., "Linear Force and Moment Equations for an Annular Smooth Shaft Seal Perturbed Both Angularly and Laterally," Second Workshop*, 1982.

55. Feranec, M., and Pliska, K., "Research of Radial Forces Acting Upon the Rotor of a Centrifugal Pump for Handling Hydraulic Mixtures," Czechoslovak Scientific Technical Monthly for Engineering and Heavy Industry, pp.40-47.

56. Fleming, D. P., "Damping in Ring Seals for Compressible Fluids," First Workshop*, 1980.

57. Fowlie,D.W.,and Miles, D.D., "Vibration Problems with High Pressure Compressors," ASME Paper 75-PET-28, Petroleum Mechanical Engineering Conference, Tulsa, Oklahoma, 1975.

58. Frigne, P., and Van Den Braembussche, R., "Comparative Study of Subsynchronous Rotating Flow Patterns in Centrifugal Compressors with Vaneless Diffusers," Second Workshop*, 1982.

59. Fritzen, C.P., and Nordmann, R., "Influence of Parameter Changes to Instability Behavior of Rotors," Second Workshop*, 1982.

60. Fujikawa, T., Ishiguro, N., and Ito, M., "Asynchronous Vibration Problem of Centrifugal Comrpsesor," First Workshop*, 1980.

61. Fulton, J.W., "Full Load Testing in the Platform Module Prior to Tow -Out : A Case History of Subsynchronous Instability," Third Workshop*, 1984.

62. Giberson, M.F., "Time Transient Non-Synchronous Rotor Response," Shock and Vibration Computer Programs-Reviews and Summaries, Shock and Vibration Monograph-10, Naval Research Laboratory, Washington, D.C., pp. 465-466, 1975.

63. Goggin, D.C., "Field Experiences with Rub Induced Instabilities in Turbo-machinery," Second Workshop*, 1982.

64. Gondhalekar, V., and Holmes, R., "Design of Electromagnetic Bearing for Vibration Control of Flexible Transmission Shaft," Third Workshop*, 1984.

65. Goulas, A., and Truscott, G.F., "The Effect of Cut-Water Clearance on Dynamic Hydraulic Loading on Centrifugal Pump Impellers".

66. Grabowski, B., "Shaft Vibrations in Turbomachinery Excited by Cracks," Second Workshop*, 1982.

67. Greitzer, E.M., "The Stability of Pumping Systems - The 1980 Freeman Scholar Lecture," Trans. of the ASME, J. of Fl. Eng., Vol. 103, pp. 193-242, June 1981.

68. Greitzer,E.M., and Strand, T., "Asymmetric Swirling Flows in Turbomachine Annuli," Trans. of the ASME, J. of Eng. for Power, Vol. 100, pp. 618-629, October 1978.

69. Gunter, E.J., Springer, H., and Humphris, R., "Influence of Unbalance on the Stability Characteristics of Flexible Rotor Bearing Systems," presented at the ASME/The Applied Mechanics, Bioengineering and Fluids Engineering Conference, Houston, Texas, June 20-22, 1983 , AMD Vol. 55, 1983.

70. Haley, P.J., "Gas Turbine Rotor/Case Structural Response to Rotating Stall: Experimental Documentation and Analytical Approach," Second Workshop*, 1982.

71. Hauck, L., "Measurement and Evaluation of Swirl-Type Flow in Labyrinth Seals of Conventional Turbine Stages," Second Workshop*, 1982.

72. Hergt, P., and Krieger, P., "Radial Forces in Centrifugal Pumps with Guide Vanes," Advance Class Boiler Feed Pumps, Proc. Inst. of Mechanical Engineers, Vol. 184, Pt 3N, pp. 101-107, 1969-1970.

73. Hergt, P., and Starke, J., "Flow Patterns Causing Instabilities in the Performance Curves of Centrifugal Pumps with Vaned Diffusers," Proc. of the Second International Pump Symposium, Houston,Texas, April 29 - May 2, 1985.

74. Holmes, R., "On the Role of Oil-Film Bearings in Promoting Shaft Instability: Some Experimental Observations," First Workshop*, 1980.

75. Holmes, R., and Dogan, M., "Investigation of Squeeze-Film Dampers in Flexible Support Structures," Second Workshop*, 1982.

76. Hori, Y., "A Theory of Oil Whip," ASME J. of Appl. Mech., Vol.26, pp. 189-198, June 1959.

77. Hudson, J. H., and Wittman, L. J., "Subsynchronous Instability of a Geared Centrifugal Compressor of Overhung Design," First Workshop *, 1980.

78. Imaichi, K., Tsujimoto, Y. , and Yoshida, Y., "A Two-Dimensional Analysis of the Interaction Effects of Radial Impeller in Volute Casing," IAHR/AIRH Symposium, Tokyo, Japan, pp. 635-647, 1980.

79. Isay, W-H., "Diestromung durchein schwingendes und rotierendes radiales schaufelgitter," Z. Flugwiss. 6, Heft II, pp. 319-328, 1958.

80. Iino, T., and Kaneko, H., "Hydraulic Forces Caused by Annular Pressure Seals in Centrifugal Pumps," First Workshop*, 1980.

81. Iversen, H. W., Rolling, R. E., and Carlson, J. J. K., "Volute Pressure Distribution, Radial Force on the Impeller, and Volute Mixing Losses of a Radial Flow Centrifugal Pump," Trans. ASME, J. of Eng. for Power, Vol. 82, pp. 136-144, April 1960.

82. Iwatsubo, T., "Evaluation of the Instability Forces of Labyrinth Seals in Turbines or Compressors," First Workshop*, 1980.

83. Iwatsubo, T., Kawai, R., Kagawa, N., Kakiuchi, T., and Takahara, K., "Analysis of Dynamic Characteristics of Fluid Force Induced by Labyrinth Seal," Third Workshop*, 1984.

84. Japikse, D., "Review-Progress in Numerical Turbomachinery Analysis," Trans. ASME, J. of Fluids Eng., Vol. 98, pp. 592-606, Dec. 1976.

85. Jery, B., Acosta, A.J., Brennen, C.E., and Caughey, T.K., "Hydrodynamic Impeller Stiffness, Damping, and Inertia in the Rotordynamics of Centrifugal Flow Pumps," Third Workshop*, 1984.

86. Jery, B., Brennen, C.E., Caughey, T.K., and Acosta, A.J., "Forces on Centrifugal Pump Impellers," Proc. of the Second International Pump Symposium, Houston, Texas, April 29 - May 2, 1985.

87. Jery, B., and Franz, R., "Stiffness Matrices for the Rocketdyne Diffuser Volute," Cal. Inst. of Tech., Pasadena, California, Technical Report No.E249.1 under NASA contract NAS 8-33108, Oct. 1982.

88. Kameoka, T., Abe, T., and Fujikawa, T., "Theoretical Approach to Labyrinth Seal Forces - Cross-Coupled Stiffness of a Straight-Through Labyrinth Seal," Third Workshop*, 1984.

89. Kamimoto, G., Ohshima, T., Mizutani, M., and Mizutani, H., "Applications of Singularity Method in Turbomachinery," IAHR/AIRH Symposium, Tokyo, Japan, pp.649-660, 1980.

90. Kasztejna, P.J., Heald, C.C., and Cooper, P., "Experimental Study of the Influence of Backflow Control on Pump Hydraulic-Mechanical Interaction," Proc. of the Second International Pump Symposium, Houston,Texas, April 29 - May 2, 1985.

91. Katsanis, T., "Use of Arbitrary, Quasi-Orthogonals for Calculating Flow Distribution in a Turbomachine," J. of Eng. for Power, pp. 197-202, April 1966.

92. Kawata, Y., Kanki, H., and Kawakami, T., "The Dynamic Radial Force on the Cavitating Centrifugal Impeller," The 12th IAHR Symposium on Hydraulic Machinery in the Energy -Related Industries, Stirling, Scotland, August 27-30, 1984, pp. 305-315, 1984.

93. Kimball, A.L., Jr., "Internal Friction Theory of Shaft Whirling," General Electric Review, Vol. 27, pp. 244-251, April 1924.

94. Kirk, R.G., and Donald, G.H., "Design Criteria for Improved Stability of Centrifugal Compressors," presented at ASME/The Applied Mechanics, Bioengineering and Fluids Engineering Conference, Houston, Texas, June 20-22, 1983 , AMD Vol. 55, 1983.

95. Kirk, R. G., and Gunter, E. J., "Transient Response of Rotor-Bearing Systems," Trans. of the ASME, pp. 682-693, May 1974.

96. Kirk, R.G., Mondy, R.E., and Murphy, R.C., "Instabilities of Geared Couplings-Theory and Practice," Second Workshop*, 1982.

97. Kirk, R.G., Nicholas, J.C., Donald, G.H., and Murphy, R.C., "Analysis and Identification of Subsynchronous Vibration For a High-Pressure Parallel Flow Centrifugal Compressor," First Workshop*, 1980.

98. Kurokawa, J., "Theoretical Determinations of the Flow Characteristics in Volutes," IAHR/AIRH Symposium , Tokyo, Japan, pp.623-634 ,1980.

99. Leader, M.E., "A Solution for Variable Speed Vertical Pump Vibration Problems," Proc. of the Second International Pump Symposium, Houston, Texas, April 29 - May 2, 1985.

100. Lee, O.W.K., Martinez-Sanchez, M., and Czajkowski, E., "Prediction of Force Coefficients for Labyrinth Seals," Third Workshop *, 1984.

101. Leie, B., and Thomas, H. J., "Self-Excited Rotor Whirl Due to Tip-Seal Leakage Forces," First Workshop*, 1980.

102. Leong, Y.M.M.S., and Brown, R.D., "Experimental Investigations of Lateral Forces Induced by Flow Through Model Labyrinth Glands,"Third Workshop*, 1984.

103. Lewis, D.W., Moore, J.W., Bradley, P.L., and Allaire, P.E., "Vibration Limiting of Rotors by Feedback Control," Second Workshop*, 1982.

104. Liess, C., "The Determination of Dynamic Radial Forces in Hydraulic Machines," Voith Research and Construction , Vol. 28e , 1982, Paper 3.

105. Liess, C., Jaeger, E.U., and Klemm, D., "Hydraulically Induced Radial Forces on Francis Turbines and Pump Turbines: Measurement, Evaluation and Results," The 12th IAHR Symposium on Hydraulic Machinery in the Energy-Related Industries, Stirling, Scotland, August 27-30, 1984, pp. 284-304, 1984.

106. Loret, G., Gopalakrishnan, S., "Interaction Between Impeller and Volute of Pumps at Off-Design Conditions," Performance of Hydraulic Turbines and Pumps, ASME Annual Winter Meeting, Fluids Engineering Division, Vol. 6, Nov. 1983.

107. Lund, J. W. , "Stability and Damped Critical Speeds of a Flexible Rotor in Fluid-Film Bearings," J. of Eng. for Industry, pp. 509-517, May 1974.

108. Makkay, E., "Centrifugal Pump Hydraulic Instability," CS-1445 Research Project 1266-18 prepared for EPRI, Palo Alto, CA by Energy Research and Consultants Corporation, May 1980 .

109. Malanoski, S. T., "Practical Experience with Unstable Compressors," First Workshop*, 1980.

110. Matsushita, O., Takagi, M., Kikuchi,K., and Kaga, M., "Rotor Vibration Caused by External Excitation and Rub," Second Workshop*, 1982.

112. McLean, L.J., and Hahn, E.J., "Sqeeze-Film Dampers for Turbomachinery Stabilization," Third Workshop*, 1984.

113. McNally, W.D., and Sockol, P.M., "Review - Computational Methods for Internal Flows with Emphasis on Turbomachinery," Transactions of the ASME, J. of Fl. Eng. , Vol. 107, pp. 6-22, March 1985.

114. Miller, E.H., and Vohr, J.H., "Preliminary Investigation of Labyrinth Packing Pressure Drops at Onset of Swirl-Induced Rotor Instability," Third Workshop*, 1984.

115. Moore, J.W.,Lewis, D.W., Heinzman, J., "Feasibility of Active Feedback Control of Rotordynamic Instability," First Workshop*, 1980.

116. Morton, P.G., "Aspects of Coulomb Damping in Rotors Supported on Hydrodynamic Bearings," Second Workshop*, 1982.

117. Nelson , C. D., "The Rotordynamic Coefficients of High-Pressure Annular Gas Seals," ASME Gas Turbine Conference Paper 84-GT-32, Amsterdam, The Netherlands, June, 1984.

118. Newkirk, B.L., "Shaft Whipping," General Electric Review, Vol. 27, pp. 169-178, March 1924.

119. Ng, S.L., "Dynamic Response of Cavitating Turbomachines," Ph. D. Thesis, Division of Engineering and Applied Sciences, California Institute of Technology, 1976.

120. Ng, S.L., and Brennen, C.E., "Experiments on the Dynamic Behaviour of Cavitating Pumps," J. of Fluid Engineering, Vol. 100, pp. 166-176, June 1978.

121. Nordmann, R., and Massman, H., "Identification of Dynamic Coefficients of Annular Turbulent Seals," Third Workshop*, 1984.

122. Ohashi, H., and Shoji, H., "Lateral Fluid Forces Acting on a Whirling Centrifugal Impeller in Vaneless and Vaned Diffuser," Third Workshop *, 1984.

124. Parszewski, Z., Krodkiewski, J., and Marynowski, K., "Parametric Instabilities of Rotor-Support Systems with Application to Industrial Ventilators," First Workshop*, 1980.

125. Pollman, E., Schwerdtfeger, H., and Termuehlen, H., "Flow-Excited Vibrations in High-Pressure Turbines (Steam Whirl)," J. of Eng. for Power , Vol.100, pp. 219-228, April 1978.

126. Rogers, G.W., Rau, C.A.,Jr., Kottke, J.J., and Menning, R.H."Analysis of a Turbine Rotor Containing a Transverse Crack at Oak Creek Unit 17," Second Workshop*, 1982.

127. San Andres, L., and Vance, J.M., "Effects of Fluid Inertia and Turbulence on Force Coefficients for Squeeze Film Dampers," Third Workshop*, 1984.

128. Sato, C., and Allaire, P., "Aerodynamic Forces on an Unbounded Centrifugal Impeller Undergoing Synchronous Whirl," Report No. UVA/643092/MAE82/196, School of Engineering and Applied Science, University of Virginia, June 1982.

129. Shen, S. F., and Mengle, V. G., "Non-Synchronous Whirling Due to Fluid-Dynamic Forces in Axial Turbomachinery Rotors," First Workshop*, 1980.

130. Shimura,T., and Kamijo, K., "A Study on Dynamic Characteristics of Liquid Oxygen Pumps for Rocket Engines (First Report)," Technical Report of National Aerospace Laboratory, Paper No. NAL TR-725 , 1982.

131. Shoji, H., and Ohashi, H., "Fluid Forces on Rotating Centrifugal Impeller with Whirling Motion," First Workshop*, 1980.

132. Simon, F., "On the Computation of the Dynamic Behavior of Shaft Systems in Hydro-electric Power Stations," Voith Research and Construction, Vol. 28e, 1982, Paper 4.

133. Sloteman, D.P., Cooper, P., and Dussourd, J.L., "Control of Backflow at the Inlets of Centrifugal Pumps and Inducers," Proceedings of the First International Pump Symposium, Texas A&M University, College Station, Texas, pp.9-22, May 1984.

134. Smalley, A.J., "Use of Elastomeric Elements in Control of Rotor Instability," First Workshop*, 1980.

135. Smith, D.R., and Wachel, J.C., "Experiences with Nonsynchronous Forced Vibration in Centrifugal Compressors," Third Workshop*, 1984.

136. Stafford, J. A. T., Ferguson, T. B., Hirst, E. S., and Asquith, R. W., "An Experimental Investigation Observing Some Unsteady Flows Induced by a Rotating Disc," Proc. of the 5th Conference on Fluid Machinery, Budapest, Vol.2, pp. 1071-1079, 1975.

137. Steck, E., "Berechnung Des Betriebsverhaltens Rotierender Radialgitter," Sonderdruck aus Stroemungsmechanik und Stroemungsmaschinen, 30-81, Mitteilungen des Instituts fuer Stroemungslehre und Stroemungsmaschinen, Universitaet Karlsruhe (TH).

138. Stepanoff, A.F., "Centrifugal and Axial Flow Pumps," Second Edition, Wiley, New York, 1957.

139. Stodola, A., "Steam and Gas Turbines," McGraw-Hill Book Co., New York, Translation of the Sixth German Edition, 1927.

140 Thomas, H. J., "Unstable Oscillations of Turbine Rotors Due to Steam Leakage in the Clearance of the Sealing Glands and the Buckets," Bulletin Scientifique, A.J.M., Vol. 71, 1958.

141. Thompson, W. E., "Fluid Dynamic Excitation of Centrifugal Compressor Rotor Vibrations," J. Fluid Engineering, Vol. 100, pp. 73-78, March 1978.

142. Thompson, W. E., "Vibration Exciting Mechanisms Induced by Flow in Turbomachine Stages," First Workshop*, 1980.

143. Tsujimoto, Y., "Theoretical Study of Fluid Forces on a Centrifugal Pump Impeller Rotating and Whirling in a Volute," Personal Communication on Future Paper, July 1985.

144. Tsujimoto, Y., Acosta, A.J., and Brennen, C.E., "Two-Dimensional Unsteady Analysis of Fluid Forces on a Whirling Centrifugal Impeller in a Volute," Third Workshop*, 1984.

145. Urlichs, K., "Clearance-Flow Generated Transverse Forces at the Rotors of Thermal Turbomachines," NASA TM-77292, Translation of Doctoral Dissertation, Technical University of Munich, W. Germany, 1975.

146. Vance, J.M., and Laudadio, F.J., "Experimental Measurement of Alford's Force in Axial Flow Turbomachinery," Second Workshop*, 1982.

147. Vance, J. M. , and Laudadio, F. J., "Experimental Results Concerning Centrifugal Impeller Excitations," First Workshop*, 1980.

148. Vance, J. M. and Laudadio, F. J., "Rotordynamic Instability in Centrifugal Compressors- Are All the Excitations Understood?," ASME Paper No. 80-GT-149, 1980.

149. Vance, J. M. and Tison, J. D., "Analysis and Interpretation of Nonsynchronous Whirling in Turbomachinery," Presented at the Energy Technology Conference & Exhibition, Houston, TX, Nov.5-9, 1978.

150. Veikos, N.M., Page, R.H., and Tornillo, E.J., "Control of Rotordynamic Instability in a Typical Gas Turbine's Power Rotor System," Third Workshop*, 1984.

151. Wachel, J.C., "Rotordynamic Instability Field Problems," Second Workshop*, 1982.

152. Wachel, J. C., and Szenasi, F. R., "Field Verification of Lateral-Torsional Coupling Effects on Rotor Instabilities in Centrifugal Compressors," First Workshop*, 1980.

153. Wachel,W.D., "Nonsynchronous Instability of Centrifugal Compressors," ASME Paper 75-PET-22, Petroleum Mechanical Engineering Conference, Tulsa, Oklahoma, 1975.

154. Warner, R. E., and Soler, A. I., "Stability of Rotor-Bearing Systems with Generalized Support Flexibility and Damping and Aerodynamic Cross-Coupling," J. of Lubrication Technology, July 1975, pp. 461-471.

155. Wohlrab, R., "Experimental Determination of Gap Flow-Induced Forces at Turbine Stages and Their Effect on the Running Stability of Simple Rotors," NASA TM-77293, Translation of Doctoral Dissertation, Munich, W. Germany, 1975.

156. Worster, R.C., "The Flow in Volutes and Its Effect on Centrifugal Pump Performance," Proc. Institution of Mech. Engineers, Vol. 177, No. 31, pp. 843-875, 1963.

157. Wright, D.V., "Labyrinth Seal Forces on a Whirling Rotor," Presented at ASME/The Applied Mechanics, Bioengineering and Fluids Engineering Conference, Houston, Texas, June 20-22, 1983 , AMD Vol. 55, 1983.

158. Zanetti, V., "La Poussee Radiale dans les Machines Hydrauliques: Experiences de Laboratoire," La Houille Blanche, pp. 237-245, March 1982.

159. Zeidan, F.Y., "Internal Hysteresis Experienced on a High Pressure Syn Gas Compressor," Third Workshop*, 1984.

160. Zorzi, E., and Walton, J., "Evaluation of Shear Mounted Elastomeric Damper," Second Workshop*, 1982.

APPENDIX A

SUMMARY OF THE SSME TURBOMACHINERY DESIGN AND PERFORMANCE DATA

As an illustration of current high performance turbomachine technology standards, this appendix presents a summary of the design and performance data of the rotating machinery in NASA's Space Shuttle Main Engines (SSME). It should be emphasized, however, that the problems addressed by this research work are of a fundamental nature and have been encountered in many turbomachine applications. They are not exclusive to the Shuttle turbomachines, although there is such a potential for exacerbating their underlying causes (owing to the unprecedented levels of specific speeds and power densities, see Fig. A.1-top). Other reasons for the choice of the SSME as an example are (i) familiarity of the author with the project, and (ii) availability of documentation[1], not to mention NASA's sponsorship of the present work.

Engine Description:

Design of the Space Shuttle Main Engines (SSME) started in the early 1970's, with Rocketdyne Division of Rockwell International as the main contractor. The George C. Marshall Space Flight Center administered the program for NASA. Each vehicle is equipped with three identical engines, providing 55% of the impulse needed to take the orbiter and the external tanks within 41 m/sec (135 ft /sec) of the orbital velocity. The external tanks are dropped after the engines are shut down. An important design feature is the reusability of the engines. They are designed for 55 flights (27,000 seconds of operation) between overhauls. Each engine develops 2,276 kN (512,000 lbs) of high altitude thrust, at a specific impulse of 455 seconds. Full Power Level (FPL) is 109% of Rated Power Level (RPL), with the possibility of throttling down to a Minimum Power Level (MPL) at about 65% of RPL. The total engine mass is 3,170 kg (7,000 lbm).

---

[1] Data and pictures presented in this appendix are courtesy of Rocketdyne Division, Rockwell International.

The engine is a liquid oxygen / hydrogen topping cycle operating at a mixture ratio of 6.0, and a chamber pressure of 22.5 MPa (3,270 Psia) at FPL. The inherent characteristics of the cycle dictated use of four turbopumps, two low pressure and two high pressure. This allows the high pressure pumps to be operated at high speeds (within the suction specific speed limits) for obvious gains in efficiency and weight. The picture in Fig. A.2 shows the arrangement of the engine powerhead components.

Description of Turbopumps:

Two turbopumps are required for each propellant. The engine must accept low inlet pressure, in order to minimize tank weight, and hence the requirement for a low speed, low pressure turbopump. On the other hand, the main combustor must operate at as high a pressure as possible in order to maximize the available energy. This requires high pump discharge pressures and hence high pump speed. Also, the engine must throttle, dictating pump operations over a wide range of flows. Centrifugal pumps are best suited for throttling. Both high pressure pumps are of this type. Other important design considerations include weight, stage and machine efficiency, dynamic seal life and efficiency, rotor axial (or thrust) balance, bearing life, rotor critical speed, rotor dynamic stability, rotor balancing capability, service in oxygen and service in high pressure hydrogen.

The following paragraphs include descriptions of the design choices for the four engine turbopumps. The problems encountered in their developement are briefly mentioned. The ones directly relevant to the current work, namely, those related to rotor vibrations, are described in more detail in Chapter 1, Section 1.3.

Low Pressure Oxygen Turbopump (LPOTP):

The pump has an axial flow inducer of the tandem blade row type, with four blades on the first row and twelve blades in the second. It operates at an inlet pressure of 689 kPa (100 psia), the minimum being 138 kPa (20 psi) above vapor pressure. The turbine is a full admission six-stage

impulse turbine, driven by fluid from the High Pressure Oxygen Turbopump. Axial forces from pump and turbine counteract each other. Rotor residual axial loads are carried by a thrust bearing. The turbopump operates below the rotor first critical speed[2]. The major problem encountered in the LPOTP was early degradation (due to ball wear) of the thrust bearing. It was solved by reducing the turbine labyrinth diameter and increasing the turbine load in the aft direction.

High Pressure Oxygen Turbopump (HPOTP):

Figure A.2 gives a summary of the key performance parameters of the HPOTP, together with a graphic description of (i) the overall turbopump arrangement, and (ii) the turbopump rotor assmbly.

The HPOTP features two pumps. The main pump has a double entry centrifugal impeller with an inducer on each side. The volute is of the constant velocity type and has a vaned diffuser. The discharge goes to the LPOTP turbine, the preburner (boost) pump and main combustor. The preburner (boost) pump has a single entry centrifugal impeller and boosts about 11% of engine flow to preburner pressures. These two pumps are driven by a two-stage reaction turbine. The difference in axial thrust between preburner and turbine is taken by a balance piston. The bearings do not carry the mainstage axial loads.

The most serious problems encountered in the HPOTP were:

(i) poor suction performance: remedied by the addition of inducers,

(ii) dynamic shaft seal life: solved by change of oxidizer seal design and turbine seal materials, and

(iii) bearing life due to poor rotor stability: problem and solution described in Chapter 1, Section1.3.

Low Pressure Fuel Turbopump (HPFTP):

The pump has an axial flow inducer with four full blades at the inlet and four partial blades at the exit. The nominal pump inlet pressure is 30 psia (minimum is 17 kPa, or 2.5 psi above vapor

[2] Refer to Chapter 1, Section 1.2 for definition of critical speed.

pressure), and the flow rate is 67 kg/sec (148 lbm/sec) at RPL. The pump is powered by a partial admission two-stage turbine, driven by heated hydrogen from part of the thrust chamber cooling circuit. This turbine operates below its first critical speed, a pair of thrust bearings balancing the residual axial loads from pump and turbine.

The LPFTP problems included:

(i) low pump performance: solved by reducing the number of vanes in the discharge diffuser and by eliminating a row of partial blades on the inducer, and

(ii) turbine labyrinth seal degradation caused by non-symmetrical arcs of admission (turbine changed from full to partial admission): corrected by incorporating symmetric arcs of admission.

High Pressure Fuel Turbopump (HPFTP):

The HPFTP has, by far, the highest power-to-weight ratio of any turbomachine ever built (over 166 kW/kg (100 HP/lbm) at FPL , see Fig. A.3 for performance data and graphic description). Its design features a three-stage centrifugal pump, with two high efficiency crossovers at the first two stages and a constant velocity diffuser volute at the third. Each blade on the 28 cm (11 inch) diameter, two-stage reaction turbine absorbs close to 527 kW (700 H.P). The unit's rotational speed is a staggering 37,000 rpm at FPL, resulting in rotor operation above the second critical speed. Angular contact duplex bearing pairs support the rotor and serve as thrust bearings for transient loads. The seals are of the pressure actuated lift-off type. The turbine thrust is directed against the pump thrust. The residual axial load is taken by a balancing piston. Refer to Chapter 1, Section 1.3, for a discussion of the severe rotor instability problems that plagued the early development of the HPFTP.

This concludes this appendix. The main point was to stress the adverse environment (extremes of pressure, temperature and speed) in which high performance turbomachine rotor components have to operate.

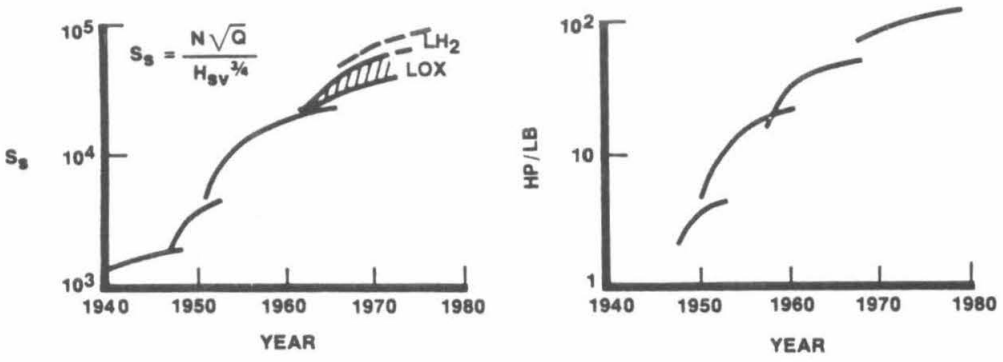

- TREND TOWARD HIGH P_C (SMALLER ENGINE/LB THRUST) PUSHED TURBOPUMP PRESSURES UPWARD
- ABILITY TO DEVELOP HIGH S_S ALLOWED HIGH SHAFT SPEED, SMALLER PUMPS
- HYDROGEN TECHNOLOGY REQUIRED EXTREME DEVELOPED HEAD

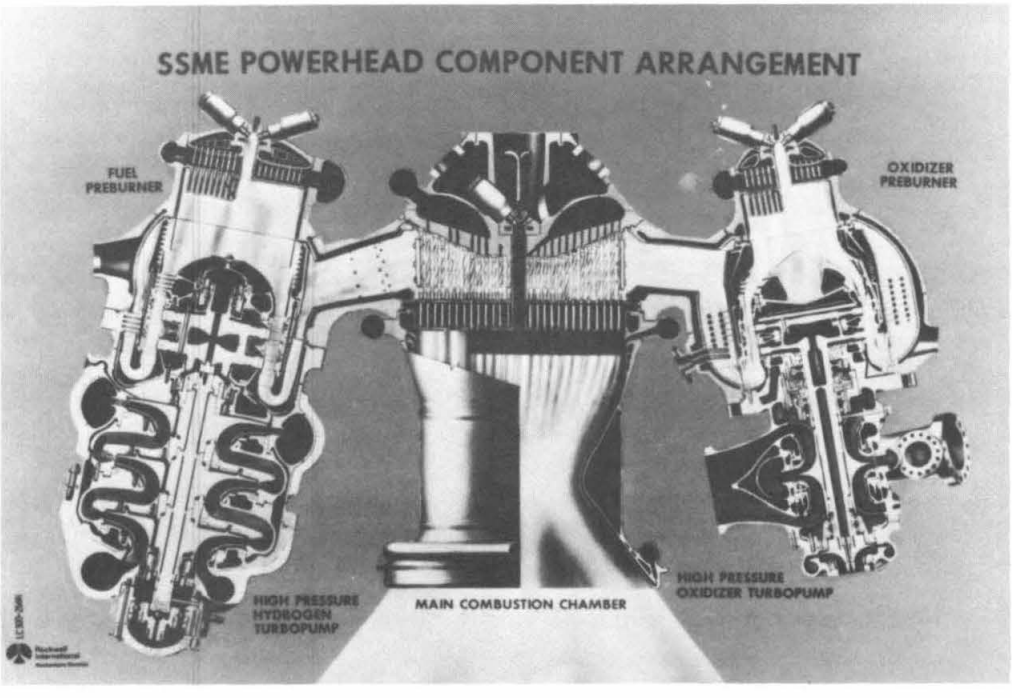

Fig. A.1 Top: Evolution of suction specific speeds and power densities in the turbomachinery of rocket engines over the period of four decades. Bottom: Arrangement of the Space Shuttle Main Engine (SSME) powerhead components.

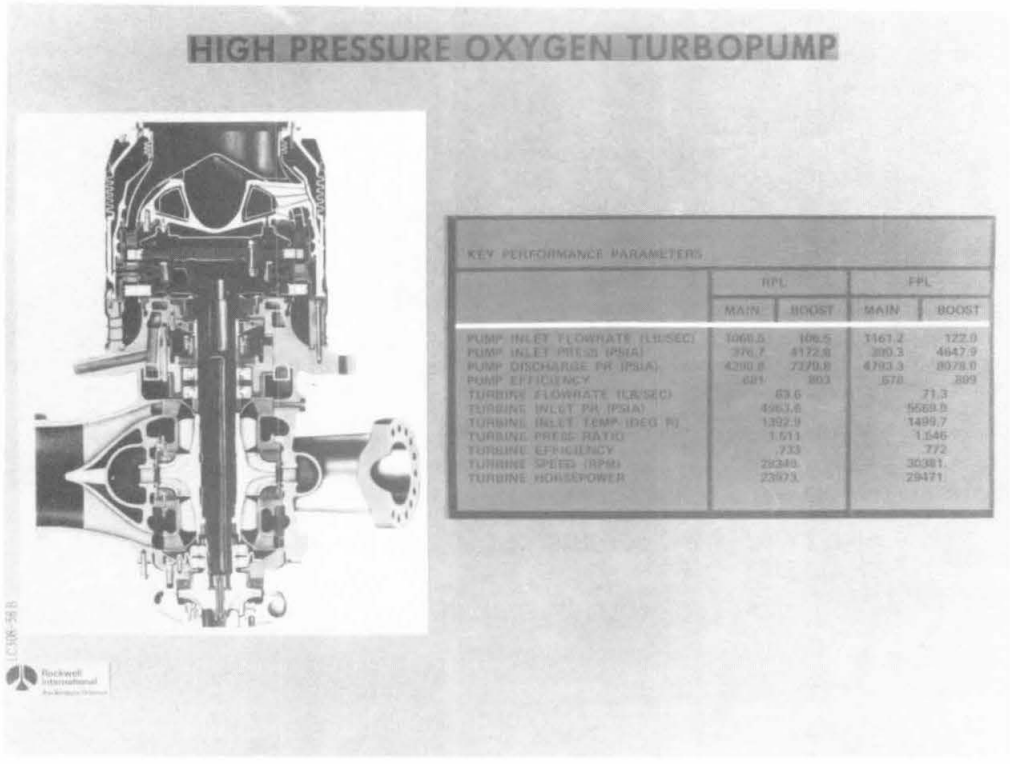

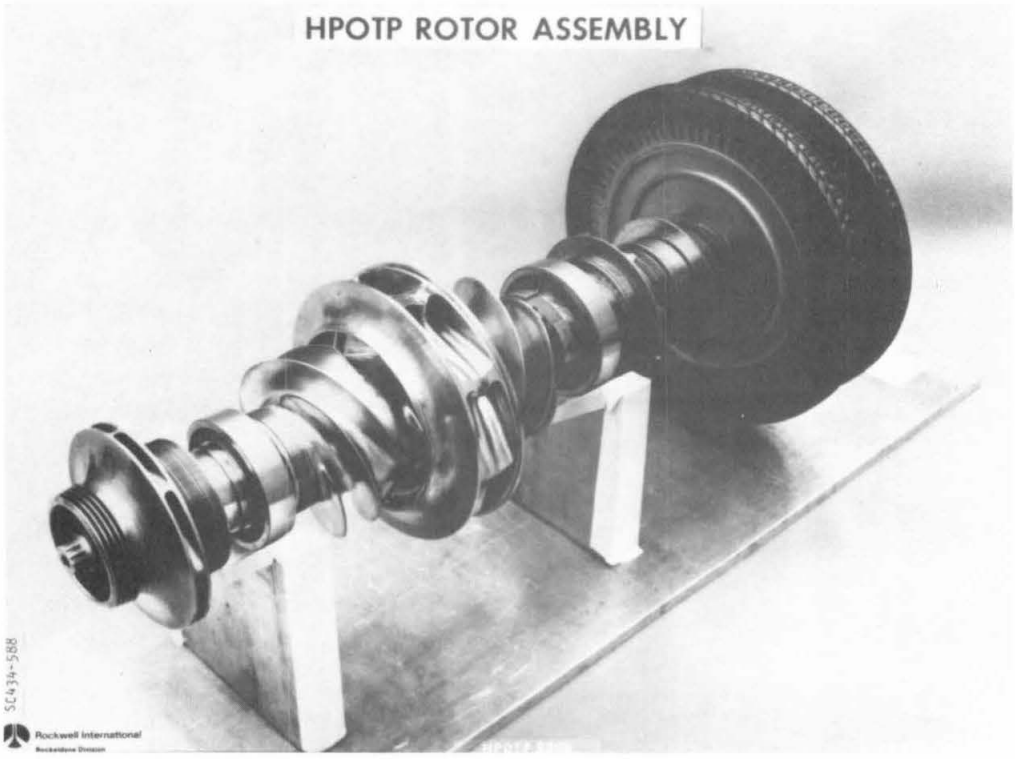

Fig. A.2 Top: Layout and performance data of the High Pressure Oxidizer Turbopump (HPOTP). Bottom: Photograph of the HPOTP rotor assembly.

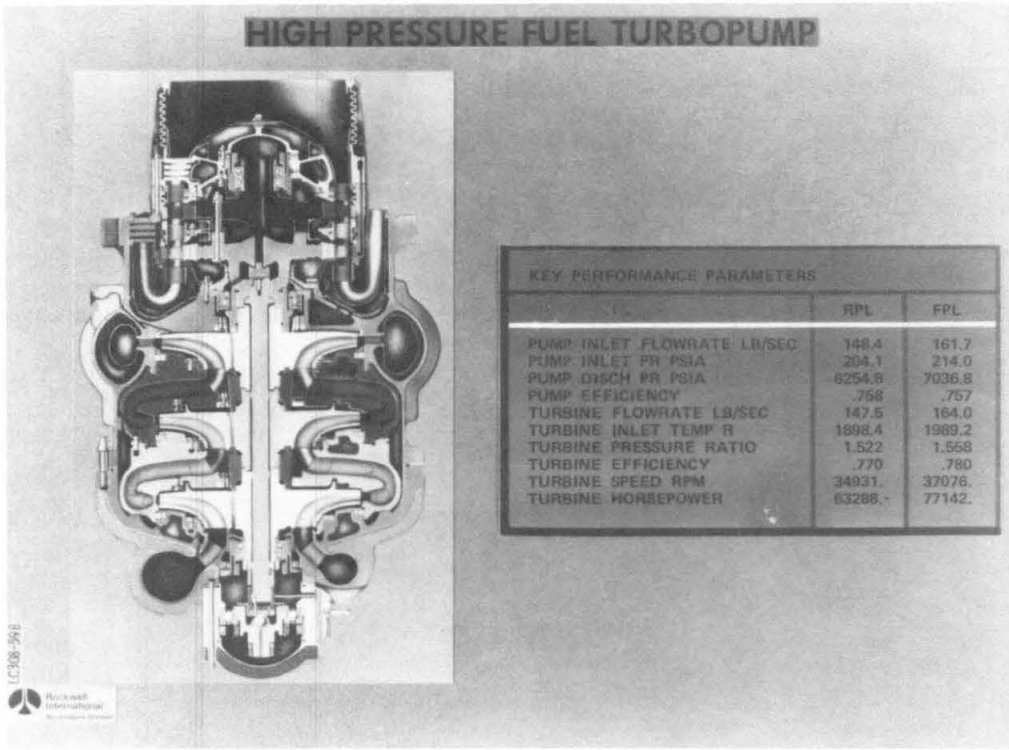

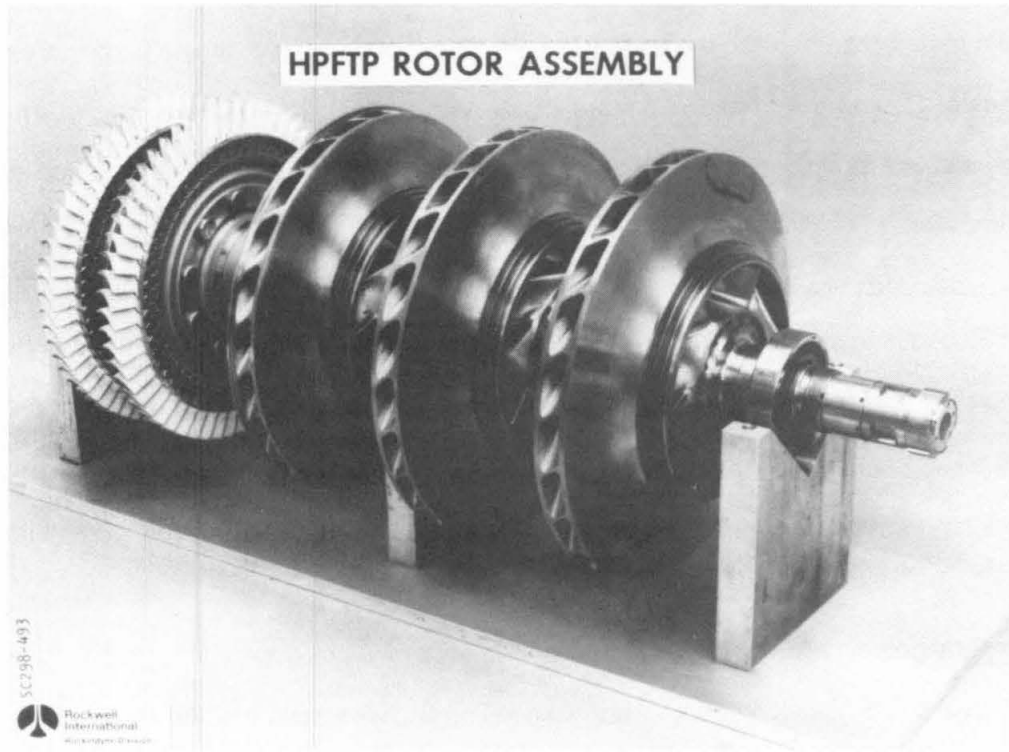

Fig. A.3 Top: Layout and performance data of the High Pressure Fuel Turbopump (HPFTP). Bottom: Photograph of HPFTP rotor assembly.

APPENDIX B

NOTES ON THE DESIGN OF THE ROTATING DYNAMOMETER

This appendix contains preliminary notes on the design of the rotating dynamometer. As mentioned in Chapter 3, this design had to necessarily be tentative, due to uncertainties in estimating the magnitudes and frequencies of the hydrodynamic forces. The primary information sought concerns (i) the raw signal level (sensitivity), and (ii) the dynamic characteristics of the dynamometer structure (natural frequencies).

Preliminary Design Choices:

The choice of the basic four-post configuration has already been commented upon. Presented in Fig. D.1 is a sketch of the four posts showing the location and naming convention of the strain gages, together with the choice of axes. The four posts have length L, they are placed at a radius, R, and they have a square cross section, with side dimensions, a. They are instrumented with strain gages in such a way as to record all six components of force and moment on the impeller.

It was decided to have two types of gages: a set of four gages to sense the axial thrust,P, and a set of 32 gages to sense the two lateral forces, F_1 and F_2, the torque,T, and the two bending moments, M_1 and M_2. The thrust gages are denoted M1 through M4, and are placed on the external faces of the posts, at mid-length. The other gages are placed at the quarter and three-quarter length points from the ends of the posts, that is to say, near the points of maximum curvature.

This arrangement allows 8 gages per post (2 on each face), or a total of 32. The arrangement of all 36 gages in Wheatstone bridges is shown in Fig. D2. Nine such bridges are formed. Bridge excitations are denoted Ei, i=1 to 9. Bridge output voltages are denoted Vi, i=1 to 9. With the

exception of the thrust bridge, all bridges are primarily sensitive to two force components (generalized force, that is), as indicated below the voltage symbols.

Design Factors:

For convenience denote the strains, ε, registered by the thrust gages with subscripts Mi, i=1 to 4. Denote the strains registered by the other gages with subscripts XKL, where X=A,B,C or D refers to the post, K=1,2,3 or 4 refers to the face of the post and L=1 or 2 refers, respectively, to the quarter and three-quarter locations. Also, let λ=L/a. The following relations are then readily determined:

$$F_1 = (E\,a^3 / 6\lambda)\ [(\varepsilon_{A22} - \varepsilon_{A21} - \varepsilon_{A42} + \varepsilon_{A41}) - (\varepsilon_{C22} - \varepsilon_{C21} - \varepsilon_{C42} + \varepsilon_{C41}) + (\varepsilon_{B12} - \varepsilon_{B11} - \varepsilon_{B32} + \varepsilon_{B31}) - (\varepsilon_{D12} - \varepsilon_{D11} - \varepsilon_{D32} + \varepsilon_{D31})]$$

$$F_2 = (E\,a^3 / 6\lambda)\ [(\varepsilon_{A11} - \varepsilon_{A12} + \varepsilon_{A32} - \varepsilon_{A31}) - (\varepsilon_{C11} - \varepsilon_{C12} + \varepsilon_{C32} - \varepsilon_{C31}) + (\varepsilon_{B22} - \varepsilon_{B21} + \varepsilon_{B41} - \varepsilon_{B42}) - (\varepsilon_{D22} - \varepsilon_{D21} + \varepsilon_{D41} - \varepsilon_{D42})]$$

$$P = (E\,a^2 / 4) \sum_{i=1}^{4} \varepsilon_{Mi}$$

$$M_1 = (E\,a^2 R/2)\,(1/4 + a^2 / 48R^2) \sum_{K=1}^{4} \left(\sum_{L=1}^{2} (\varepsilon_{AKL} - \varepsilon_{CKL}) \right)$$

$$M_2 = (E\,a^2 R/2)\,(1/4 + a^2 / 48R^2) \sum_{K=1}^{4} \left(\sum_{L=1}^{2} (\varepsilon_{BKL} - \varepsilon_{DKL}) \right)$$

$$T = (E\,a^3\,R / 6\lambda) \sum_{X=A}^{D} (\varepsilon_{x21} - \varepsilon_{x22} - \varepsilon_{x41} + \varepsilon_{x42})$$

The typical strains associated with the lateral force, thrust, moment and torque measurements, denoted here by ε_F, ε_P, ε_M and ε_T, respectively, are given by:

$$\varepsilon_F = 3\lambda F / 8Ea^2 \quad , \quad \varepsilon_P = P / 4Ea^2 \quad , \quad \varepsilon_M = M / 8Ea^2R \quad \text{and} \quad \varepsilon_T = 3\lambda T / 8Ea^2R.$$

Some of the compromises necessary in deciding on design values of R, a and λ follow from these expressions. Other design considerations include the natural frequencies of lateral motion, torsional motion and whirling motion of the impeller on the dynamometer. It is clear that increasing these frequencies generally decreases the dynamometer sensitivity, and hence some compromise is sought for which the natural frequencies are sufficiently above the excitation frequencies and yet reasonable sensitivity is maintained. The maximum whirl and shaft frequencies for which data are expected to be obtained are a little less than 60 Hz (3600 rpm).

If the natural frequencies are red-lined at some value such as 500 Hz, then the optimum conditions are achieved if both the torsional and whirl natural frequencies are both close to this value. This requires that the radius, R, of the posts be equal to the radius of gyration of the impeller and its added mass of water; under these conditions the lateral and whirl natural frequencies are equal. This radius can be expected to be of the order of 5 cm (2 in) or greater and hence the proposed value of R.

The next step is to observe that the natural frequencies depend on (a / λ^3). If this has a value of 4×10^{-3} cm (1.6×10^{-3} in), and if the mass of the impeller (plus added mass) is of the order of 5 kg (~10 lbs), the natural frequencies (lateral and whirl) are approximately 350 Hz. Consequently, a value of (a / λ^3) of 4×10^{-3} cm is proposed. Now one must decide on a value for a or λ and assess the sensitivities using the above expressions for ε_F, ε_P, ε_M and ε_T. For greatest sensitivity one requires the smallest a, and hence a small value of λ. However; the aspect ratio, λ, cannot be too small; otherwise the gage positions will be too close to the post ends in terms of number of thicknesses. The minimum λ was estimated to be about 5, leading to a value of a of 0.5 cm (~0.2 in) and a post length of 2.54 cm (1 in).The following typical sensitivities can then be expected:

Shear Force	Strain of 3×10^{-7} per N (~1.5×10^{-6} per lbf).
Thrust	Strain of 2×10^{-7} per N (~2×10^{-7} per lbf).
Moment	Strain of 4×10^{-7} per N.m (~5×10^{-8} per lbf. in).
Torque	Strain of 6×10^{-6} per N.m (~8×10^{-7} per lbf. in).

For example, if semi-conductor strain gages with a gage factor of 100 and an excitation of 5 volts are used, this leads to sensitivities in terms of output signal voltage per N (or per N.m) which are larger than the above numbers by a factor of 125, that is to say, for example, 40 mV per N of shear force.One measure of the possible magnitude of the forces to be expected is to estimate the simple centrifugal force on the impeller (5 kg) for a deliberate whirl amplitude of 1.5 mm (~1 /16 in). This would be of the order of 1 kN (~200 lbf) leading to a voltage output of 0.04 volts corresponding to shear force.

These preliminary steps led to the configuration presented in Fig. D.3 in the form of a machine drawing of the main rotating dynamometer structure. Most of the design estimations were later confirmed, and a redesign was not necessary.

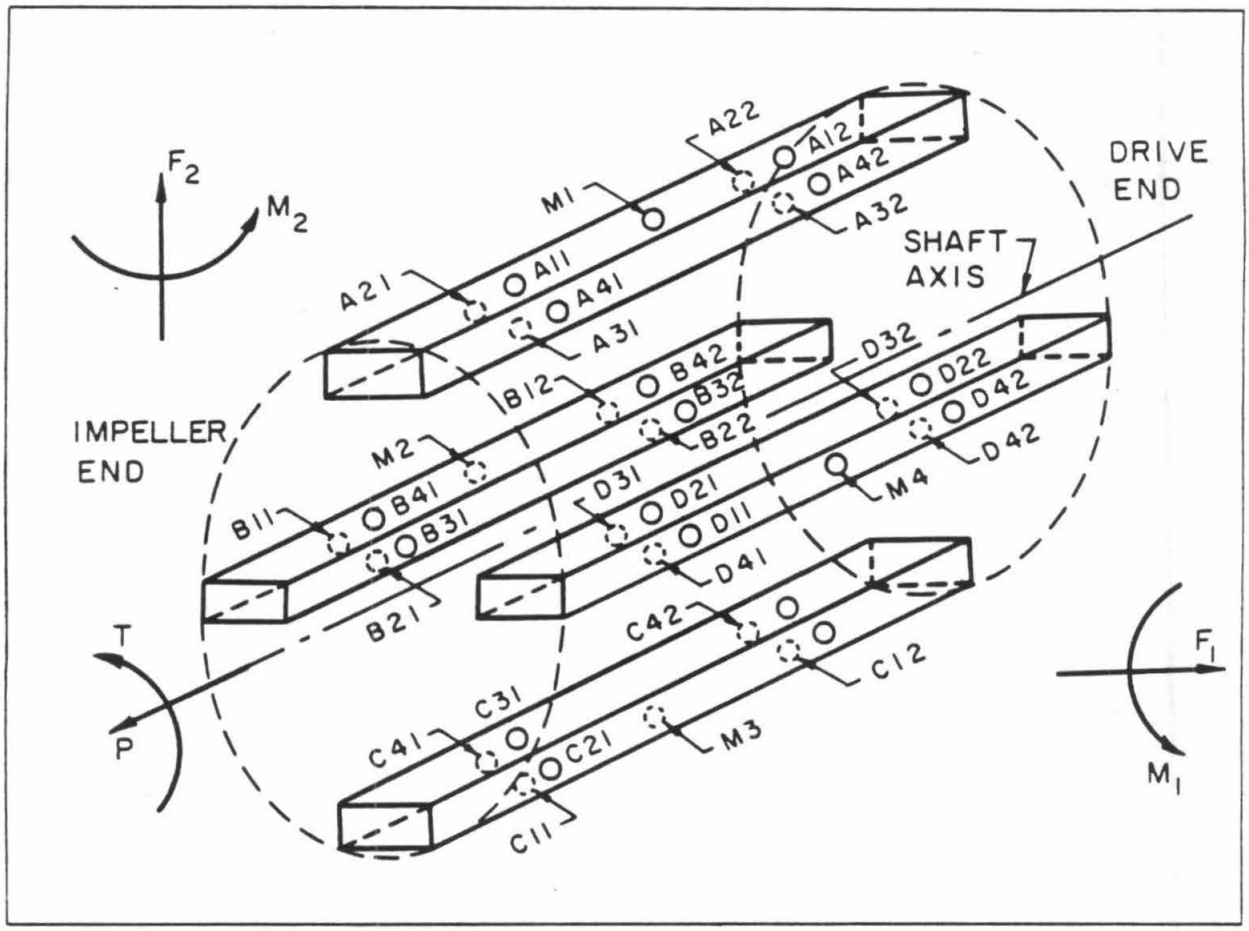

Fig. B.1 Sketch (distorted) of dynamometer measuring section consisting of four posts A,B,C and D and 9 gages per post: 4 at quarter-length, XK1, 1 at mid-length, MK, and 4 at three-quarter length, XK2. Forces and moments shown are defined as acting on the impeller, at the impeller end of the dynamometer.

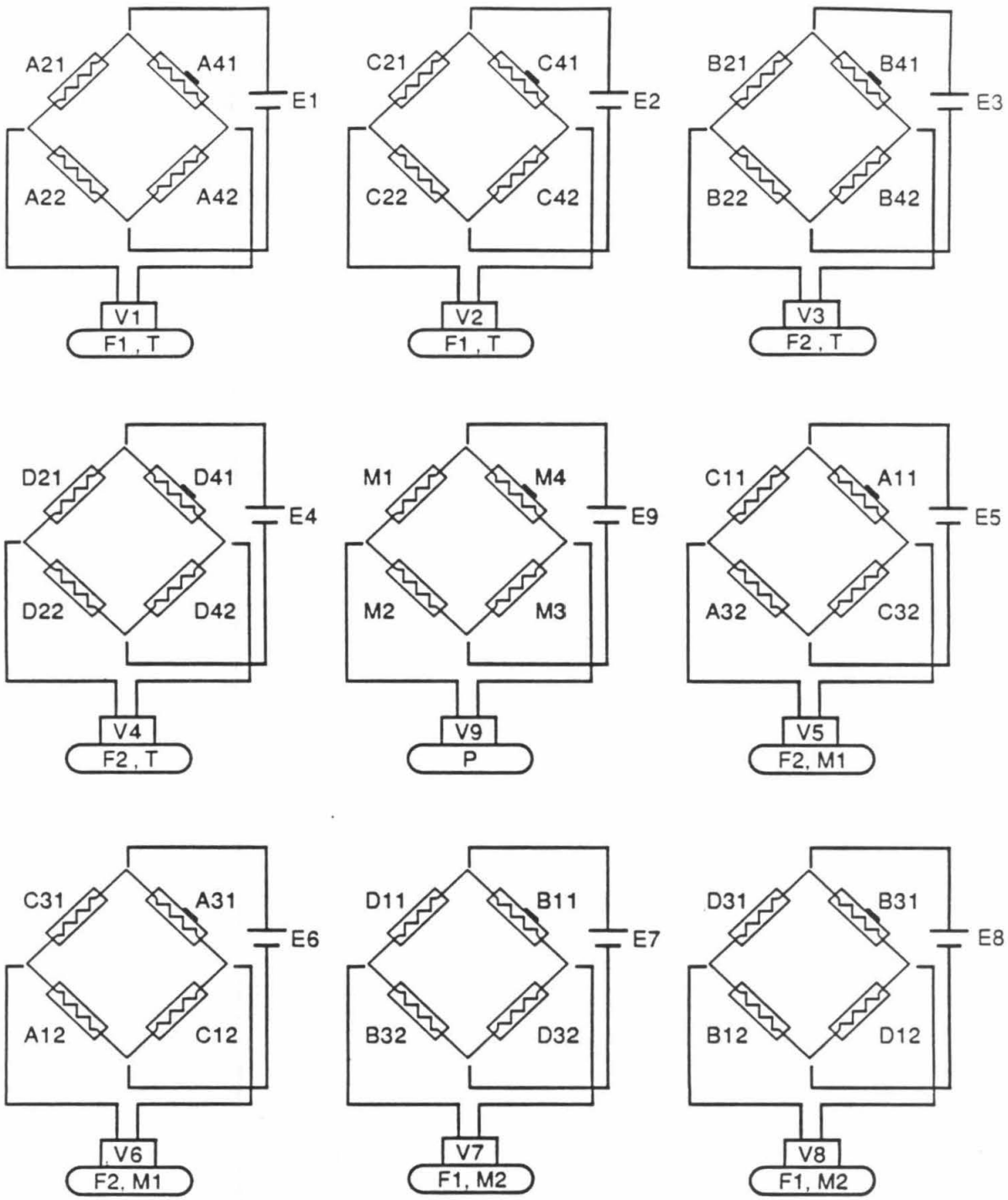

Fig. B.2 Arrangement of the 36 semi-conductor gages in nine Wheatstone bridges (see Fig. B.1 for gage designation), showing bridge excitation voltages, E1 through E9, and bridge output voltages, V1 throughV9. Each bridge is primarily sensitive to one or two components of the generalized force vector, as indicated in the oval box below the bridge output voltage symbol.

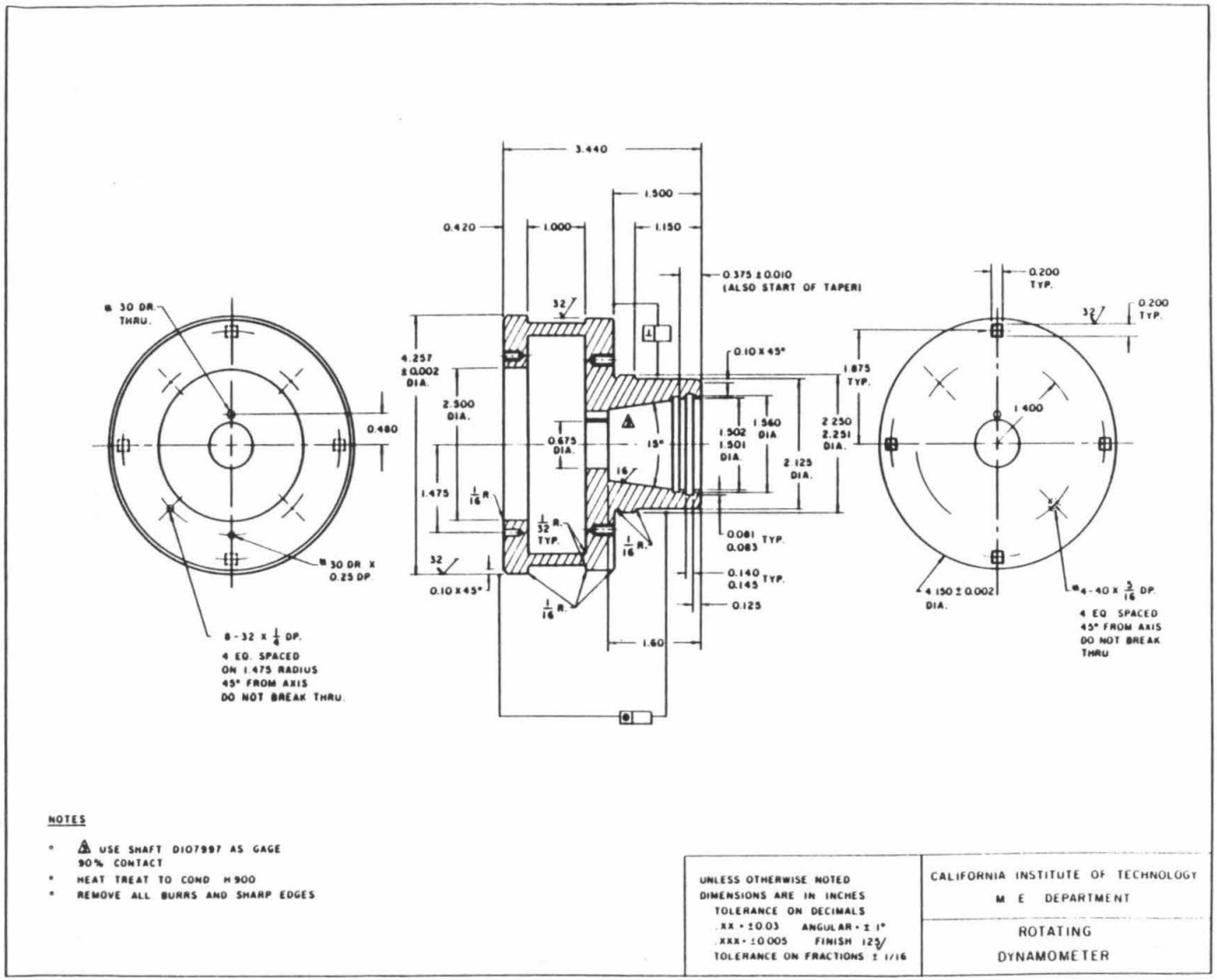

NOTES

* ⚠ USE SHAFT D107997 AS GAGE
  90% CONTACT
* HEAT TREAT TO COND H900
* REMOVE ALL BURRS AND SHARP EDGES

UNLESS OTHERWISE NOTED DIMENSIONS ARE IN INCHES TOLERANCE ON DECIMALS .XX ± 0.03 ANGULAR ± 1° .XXX ± 0.005 FINISH 125√ TOLERANCE ON FRACTIONS ± 1/16	CALIFORNIA INSTITUTE OF TECHNOLOGY M E DEPARTMENT ROTATING DYNAMOMETER

Fig. B.3 Machine drawing of the rotating dynamometer's main structure. This structure is machined out of a monolithic block of 17-4 PH stainless steel.

APPENDIX C

DERIVATION OF FORCES AND MATRICES

This appendix explains how the steady forces, F_{ox} and Foy, and the elements of the generalized stiffness matrix, $A(\Omega/\omega)$, are extracted from the raw data. As explained in Ch. 4, the raw data for a typical run consist of a set of 1024, 12-bit digital values stored in the RAM of the Shapiro Digital Signal Processor (SDSP). For each of the 16 measurement channels, the signals generated while the rotor is spinning at the rate ω and whirling at the rate Ω are sampled at 64 points equally spaced in the reference cycle.

Each one of these total 1024 points (16x64) corresponds to a specific location of the impeller center, O_i, on the circular whirl orbit (as defined by the angle Ωt), and to a specific spacial orientation of the rotating dynamometer (as defined by the angle ωt). Refer to Fig. C.1 for details. The beginning of the reference cycle (t=0) is chosen to correspond to the point in time where the impeller center is at the highest point on the orbit, which also coincides with the moment where the F_1-axis of the dynamometer frame, (1,2), is pointing vertically upward (in the laboratory frame, (H,V). The angle Φ_m relates this initial position of the dynamometer frame to the stationary volute frame (X,Y).

The reference cycle frequency is chosen so that each of the two motors (main motor and whirl motor) completes an integral number of rotations during the period of the cycle. In this manner (i) readings from several reference cycles (up to 4096) can be consistently accumulated and averaged (providing a very effective noise-filtering process), and (ii) the forces can be properly resolved within the various reference frames.

Experimental conditions:

The operator chooses two integers, I and J, to set the whirl-to-pump frequency ratio ($\Omega=\omega I/J$), and the number of cycles, N, for which data are to be gathered. Typically, keeping all other pump

operating parameters at the same setting, J is set equal to 10 and a dozen one-minute tests are run varying only I (from 1 to 11 for positive whirl, and from -11 to -1 for negative whirl). Thus:

main shaft frequency $= \omega$

whirl shaft frequency $= \Omega = \omega\, I / J$

reference frequency $= \omega / J$ (= orbit frequency when I =1)

number of cycles $= N$ (=100 typically, for 1000 rpm pump speed).

Analysis:

Essentially, the data processing is based on Fourier analysis of the two lateral force signals (after proper application of the full 6x6 calibration matrix). The following relation is implicit in the linear formulation of the problem:

$$\begin{pmatrix} F_x(t) \\ F_y(t) \end{pmatrix} = \begin{pmatrix} F_{ox} \\ F_{oy} \end{pmatrix} + \begin{bmatrix} & \\ A(\Omega/\omega) & \\ & \end{bmatrix} \begin{pmatrix} \varepsilon_x(t) \\ \varepsilon_y(t) \end{pmatrix} \qquad \text{(C.1)}$$

Referring to Fig. C.1, one can readily write

$$\begin{pmatrix} F_x(t) \\ F_y(t) \end{pmatrix} = \begin{pmatrix} F_1(t)\cos(\omega t + \phi_m) - F_2(t)\sin(\omega t + \phi_m) \\ F_1(t)\sin(\omega t + \phi_m) + F_2(t)\cos(\omega t + \phi_m) \end{pmatrix} \qquad \text{(C.2)}$$

where:

$$\begin{cases} \varepsilon_x(t) = \varepsilon\cos(I/J\,\omega t + \phi_m) \\ \varepsilon_y(t) = \varepsilon\sin(I/J\,\omega t + \phi_m) \end{cases} \quad ; \text{and} \quad \begin{bmatrix} & \\ A(\Omega/\omega) & \\ & \end{bmatrix} = \begin{bmatrix} a_{xx} & a_{xy} \\ a_{yx} & a_{yy} \end{bmatrix}$$

Now, F_1 and F_2 are extracted from the raw data in terms of their Fourier coefficients (subscripts P and Q refer to the in-phase and quadrature components, respectively; the superscript refers to the order of the coefficents, not to be confused with a power exponent):

$$\begin{cases} F_1(t) = F_1{}^0 + F_{1P}{}^1 \sin(\omega t/J) + F_{1Q}{}^1 \cos(\omega t/J) + F_{1P}{}^2 \sin(2\omega t/J) + F_{1Q}{}^2 \cos(2\omega t/J) + \ldots \\ F_2(t) = F_2{}^0 + F_{2P}{}^1 \sin(\omega t/J) + F_{2Q}{}^1 \cos(\omega t/J) + F_{2P}{}^2 \sin(2\omega t) + F_{2Q}{}^2 \cos(2\omega t/J) + \ldots \end{cases}$$

Let $\omega t/J = \theta$. Then from (C.1) and (C.2) one gets, dropping the 'm' from ϕ_m :

$$\begin{cases} \varepsilon a_{xx}\cos(l\theta+\phi) + \varepsilon a_{xy}\sin(l\theta+\phi) + F_{ox} = F_1(t)\cos(J\theta+\phi) - F_2(t)\sin(J\theta+\phi) \\ \varepsilon a_{yx}\cos(l\theta+\phi) + \varepsilon a_{yy}\sin(l\theta+\phi) + F_{oy} = F_1(t)\sin(J\theta+\phi) - F_2(t)\cos(J\theta+\phi) \end{cases}$$

and substituting for $F_1(t)$ and $F_2(t)$:

$$\begin{aligned} \varepsilon a_{xx}\cos(l\theta+\phi) + \varepsilon a_{xy}\sin(l\theta+\phi) + F_{ox} = {} & F_1{}^0\cos(J\theta+\phi) - F_2{}^0\sin(J\theta+\phi) \\ & + F_{1P}{}^1\sin\theta\cos(J\theta+\phi) - F_{2P}{}^1\sin\theta\sin(J\theta+\phi) \\ & + F_{1Q}{}^1\cos\theta\cos(J\theta+\phi) - F_{2Q}{}^1\cos\theta\sin(J\theta+\phi) \\ & \vdots \\ k^{th}\text{ harmonic} \rightarrow \quad & \begin{cases} + F_{1P}{}^k \sin k\theta\cos(J\theta+\phi) - F_{2P}{}^k\sin k\theta\sin(J\theta+\phi) \\ + F_{1Q}{}^k \cos k\theta\cos(J\theta+\phi) - F_{2Q}{}^k\cos k\theta\sin(J\theta+\phi) \end{cases} \\ & \vdots \\ & + F_{1P}{}^J\sin J\theta\cos(J\theta+\phi) - F_{2P}{}^J\sin J\theta\sin(J\theta+\phi) \\ & + F_{1Q}{}^J\cos J\theta\cos(J\theta+\phi) - F_{2Q}{}^J\cos J\theta\sin(J\theta+\phi) \\ & \vdots \\ & \infty \end{aligned}$$

and similarly for the y-component.

Solution scheme:

To solve for the a_{ij}'s, multiply both sides by appropriate sine or cosine function and integrate between appropriate limits (ex: to solve for a_{xx} multiply by cos lθ ...). To simplify the algebra, let $\phi=0$, with (X',Y') as a temporary reference frame. Later, one can perform a change of axes back to (X,Y). Use the interval [0,2Π] for integration. The following kinds of integrals will be encountered:

1) $\int_0^{2\Pi} \sin l\theta \sin J\theta \; d\theta$ 2) $\int_0^{2\Pi} \cos l\theta \cos J\theta \; d\theta$ 3) $\int_0^{2\Pi} \sin l\theta \cos J\theta \; d\theta$

4) $\int_0^{2\Pi} \sin k\theta \cos J\theta \cos l\theta \; d\theta = 1/2 \int_0^{2\Pi} \left(\sin (k-J)\theta \cos l\theta + \sin (k+J)\theta \cos l\theta \right) d\theta$

5) $\int_0^{2\Pi} \sin k\theta \cos J\theta \sin l\theta \; d\theta = 1/2 \int_0^{2\Pi} \left(\sin (k-J)\theta \sin l\theta + \sin (k+J)\theta \sin l\theta \right) d\theta$

6) $\int_0^{2\Pi} \sin k\theta \sin J\theta \cos l\theta \; d\theta = 1/2 \int_0^{2\Pi} \left(\cos (k-J)\theta \cos l\theta + \cos(k+J)\theta \cos l\theta \right) d\theta$

7) $\int_0^{2\Pi} \sin k\theta \sin J\theta \sin l\theta \; d\theta = 1/2 \int_0^{2\Pi} \left(\cos (k-J)\theta \sin l\theta + \cos(k+J)\theta \sin l\theta \right) d\theta$

8) $\int_0^{2\Pi} \cos k\theta \cos J\theta \cos l\theta \; d\theta = 1/2 \int_0^{2\Pi} \left(\cos (k-J)\theta \cos l\theta + \cos (k+J)\theta \cos l\theta \right) d\theta$

9) $\int_0^{2\Pi} \cos k\theta \cos J\theta \sin l\theta \; d\theta = 1/2 \int_0^{2\Pi} \left(\cos (k-J)\theta \sin l\theta + \cos (k+J)\theta \sin l\theta \right) d\theta$

10) $\int_0^{2\Pi} \cos k\theta \sin J\theta \cos l\theta \; d\theta = 1/2 \int_0^{2\Pi} \left(\sin (k-J)\theta \cos l\theta + \sin (k+J)\theta \cos l\theta \right) d\theta$

$$11)\ \int_0^{2\Pi} \cos k\theta \sin J\theta \sin l\theta \, d\theta \;=\; 1/2 \int_0^{2\Pi} \left(\sin (k-J)\theta \ \sin l\theta \ + \sin (k+J)\theta \ \sin l\theta \right) d\theta$$

Let

$$I_1(m,n) \equiv \int_0^{2\Pi} \sin mx \sin nx \ dx = \begin{cases} 0 & m \neq n \\ \Pi & m = n \neq 0 \\ 0 & m = n = 0 \end{cases}$$

$$I_2(m,n) \equiv \int_0^{2\Pi} \cos mx \cos nx \ dx = \begin{cases} 0 & m \neq n \\ \Pi & m = n \neq 0 \\ 2\Pi & m = n = 0 \end{cases}$$

$$I_3(m,n) \equiv \int_0^{2\Pi} \sin mx \cos nx \ dx = 0 \ ; \ \forall \ m, n.$$

Then:

$$1) = I_1(I,J) \qquad 2) = I_2(I,J) \qquad 3) = I_3(I,J) = 0$$

$$4) = [\ I_3(k-J, I) + I_3(k+J, I)\ ]/2 = 0 \qquad 5) = [\ I_1(k-J, I) + I_1(k+J, I)\ ]/2$$

$$6) = [\ I_2(k-J, I) - I_2(k+J, I)\ ]/2 \qquad 7) = [\ I_3(I, k-J) - I_3(I, k+J)\ ]/2 = 0$$

$$8) = [\ I_2(k-J, I) + I_2(k+J, I)\ ]/2 \qquad 9) = 1/2\ [\ I_3(I, k-J) + I_3(I, k+J)\ ]/2 = 0$$

$$10) = [\ I_3(J-k, I) + I_3(J+k, I)\ ]/2 = 0 \qquad 11) = 1/2\ [\ I_1(J-k, I) + I_1(J+k, I)\ ]/2.$$

Remember: all this is in the simpler frame of reference (X',Y'), where one has:

$$\begin{pmatrix} F_{x'} \\ F_{y'} \end{pmatrix} = \begin{pmatrix} F_{ox'} \\ F_{oy'} \end{pmatrix} + \begin{bmatrix} \\ A'(I/J) \\ \\ \end{bmatrix} \begin{pmatrix} \varepsilon \cos l\theta \\ \\ \varepsilon \sin l\theta \end{pmatrix}$$

Hence,

$$F_{ox'} = (1/2\Pi) \sum_{k=0}^{\infty} [\ -F_{2P}{}^k I_1(k,J) + F_{1Q}{}^k I_2(k,J)\ ] = 1/2\ (\ -F_{2P}{}^J + F_{1Q}{}^J\ )$$

$$F_{oy'} = (1/2\Pi) \sum_{k=0}^{\infty} [\ F_{1P}{}^{k}\, I_1(k,J) + F_{2Q}{}^{k}\, I_2(J,k)\ ] = 1/2\ (\ F_{1P}{}^{J} + F_{2Q}{}^{J}\ )$$

$$a_{xx'} = (1/\Pi\varepsilon)\ F_1{}^{0}\, I_2(J,I) - (1/2\Pi\varepsilon) \sum_{k=0}^{\infty} [\ (\ F_{2P}{}^{k} - F_{1Q}{}^{k}\ )\ I_2(J-k, I\ )\ ]$$

$$a_{xy'} = -(1/\Pi\varepsilon)\ F_2{}^{0}\, I_1(J,I) - (1/2\Pi\varepsilon) \sum_{k=0}^{\infty} [\ (\ F_{1P}{}^{k} + F_{2Q}{}^{k}\ )\ I_1(J-k, I\ )\ ]$$

$$a_{yx'} = (1/\Pi\varepsilon)\ F_2{}^{0}\, I_2(J,I) + (1/2\Pi\varepsilon) \sum_{k=0}^{\infty} [\ (\ F_{1P}{}^{k} + F_{2Q}{}^{k}\ )\ I_2(J-k, I\ )\ ]$$

$$a_{yy'} = (1/\Pi\varepsilon)\ F_1{}^{0}\, I_1(J,I) - (1/2\Pi\varepsilon) \sum_{k=0}^{\infty} [\ (\ F_{2P}{}^{k} - F_{1Q}{}^{k}\ )\ I_1(J-k, I\ )\ ].$$

Practical considerations :

1) J is integer and $J>0$

2) k is integer and $k\geq 0$

3) I is integer and $J \geq I \geq -J$.

Hence, the above results could be put in a much simpler form, namely:

$$F_{ox'} = (\ -F_{2P}{}^{J} + F_{1Q}{}^{J}\ )/2$$

$$F_{oy'} = (\ F_{1P}{}^{J} + F_{2Q}{}^{J}\ )/2$$

$$a_{xx'} = (1/\Pi\varepsilon) \sum_{k=0}^{\infty} [\, F_1^k - 1/2\,(F_{2P}^k - F_{1Q}^k)\,] \;\; I_2(J-k, I)$$

$$a_{xy} = (-1/\Pi\varepsilon) \sum_{k=0}^{\infty} [\, F_2^k + 1/2\,(F_{1P}^k + F_{2Q}^k)\,] \;\; I_1(J-k, I)$$

$$a_{yx'} = (1/\Pi\varepsilon) \sum_{k=0}^{\infty} [\, F_2^k + 1/2\,(F_{1P}^k + F_{2Q}^k)\,] \;\; I_2(J-k, I)$$

$$a_{yy'} = (1/\Pi\varepsilon) \sum_{k=0}^{\infty} [\, F_1^k - 1/2\,(F_{2P}^k - F_{1Q}^k)\,] \;\; I_1(J-k, I).$$

Here, the convention used is:

$$\begin{pmatrix} F_1^k \\ F_2^k \end{pmatrix} = \delta_{0k} \begin{pmatrix} F_1^0 \\ F_2^0 \end{pmatrix}$$

, $\delta_{0k} = 1$ if $k=0$, 0 otherwise (Kronecker symbol)

and: $F_{1P}^0 = F_{1Q}^0 = F_{2P}^0 = F_{2Q}^0 = 0$.

Specific results :

case 1 : $I = 0$

case 2a : $I = J$

case 2b : $I = -J$

case 3 : $|I| < J$

case 1: $l = 0 , J > 0 , k \geq 0$ (rotation without whirl)

$$F_{ox'} = -(F_{2P}{}^{J} - F_{1Q}{}^{J}) /2$$

$$F_{oy'} = (F_{1P}{}^{J} + F_{2Q}{}^{J}) /2$$

$$a_{xx'} = -(1/\varepsilon) (F_{2P}{}^{J} - F_{1Q}{}^{J})$$

$$a_{xy'} = 0$$

$$a_{yx'} = (1/\varepsilon) (F_{1P}{}^{J} + F_{2Q}{}^{J})$$

$$a_{yy'} = 0$$

case 2a: $l = J > 0 , k \geq 0$ (positive synchronous whirl)

$$F_{ox'} = -(F_{2P}{}^{J} - F_{1Q}{}^{J}) /2$$

$$F_{oy'} = (F_{1P}{}^{J} + F_{2Q}{}^{J}) /2$$

$$a_{xx'} = (1/\varepsilon) F_1{}^{0} - (1/2\varepsilon) (F_{2P}{}^{2J} - F_{1Q}{}^{2J})$$

$$a_{xy'} = -(1/\varepsilon) F_2{}^{0} + (1/2\varepsilon) (F_{1P}{}^{2J} + F_{2Q}{}^{2J})$$

$$a_{yx'} = (1/\varepsilon) F_2{}^{0} + (1/2\varepsilon) (F_{1P}{}^{2J} + F_{2Q}{}^{2J})$$

$$a_{yy'} = (1/\varepsilon) F_1{}^{0} + (1/2\varepsilon) (F_{2P}{}^{2J} - F_{1Q}{}^{2J})$$

case 2b: $l = -J < 0 , k \geq 0$ (negative, synchronous whirl)

$$F_{ox'} = -(F_{2P}{}^{J} - F_{1Q}{}^{J}) /2$$

$$F_{oy'} = (F_{1P}{}^{J} + F_{2Q}{}^{J}) /2$$

$$a_{xx'} = (1/\varepsilon) F_1{}^{0} - (1/2\varepsilon) (F_{2P}{}^{2J} - F_{1Q}{}^{2J})$$

$$a_{xy'} = (1/\varepsilon) F_2{}^{0} + (1/2\varepsilon) (F_{1P}{}^{2J} + F_{2Q}{}^{2J})$$

$$a_{yx'} = (1/\varepsilon) F_2{}^{0} + (1/2\varepsilon) (F_{1P}{}^{2J} + F_{2Q}{}^{2J})$$

$$a_{yy'} = -(1/\varepsilon) F_1{}^{0} - (1/2\varepsilon) (F_{2P}{}^{2J} - F_{1Q}{}^{2J})$$

case 3: $|l| < J$, $k \geq 0$ (subsynchronous whirl: general case)

$$F_{ox'} = -\left(F_{2P}^{J} - F_{1Q}^{J} \right)/2$$

$$F_{oy'} = \left(F_{1P}^{J} + F_{2Q}^{J} \right)/2$$

$$a_{xx'} = -\left[\left(F_{2P}^{(J-l)} - F_{1Q}^{(J-l)} \right) + \left(F_{2P}^{(J+l)} - F_{1Q}^{(J+l)} \right) \right]/2\varepsilon$$

$$a_{xy'} = -\left[\left(F_{1P}^{(J-l)} + F_{2Q}^{(J-l)} \right) - \left(F_{1P}^{(J+l)} + F_{2Q}^{(J+l)} \right) \right]/2\varepsilon$$

$$a_{yx'} = \left[\left(F_{1P}^{(J-l)} + F_{2Q}^{(J-l)} \right) + 1/2\varepsilon \left(F_{1P}^{(J+l)} + F_{2Q}^{(J+l)} \right) \right]/2\varepsilon$$

$$a_{yy'} = -\left[\left(F_{2P}^{(J-l)} - F_{2Q}^{(J-l)} \right) - \left(F_{2P}^{(J+l)} - F_{1Q}^{(J+l)} \right) \right]/2\varepsilon$$

Returning to the volute reference frame:

Let $$R = \begin{bmatrix} \cos\phi\, m & -\sin\phi\, m \\ \sin\phi\, m & \cos\phi\, m \end{bmatrix};$$

then

$$\begin{pmatrix} F_{ox} \\ F_{oy} \end{pmatrix} = R \begin{pmatrix} F_{ox'} \\ F_{oy'} \end{pmatrix}$$

and

$$[\, A(l/J)\,] = R\, [A'(l/J)]\, R^{T}.$$

Hence:

$$F_{x0} = F_{x0'} \cos\phi\, m - F_{y0'} \sin\phi\, m$$

$$F_{y0} = F_{x0'} \sin\phi\, m + F_{y0'} \cos\phi\, m$$

$$a_{xx} = a_{xx'} \cos^2\phi\, m + a_{yy'} \sin^2\phi\, m - \left(a_{xy'} + a_{yx'} \right) \cos\phi\, m \, \sin\phi\, m$$

$$a_{xy} = \left(a_{xx'} - a_{yy'} \right) \cos\phi\, m \, \sin\phi\, m + a_{xy'} \cos^2\phi\, m - a_{yx'} \sin^2\phi\, m$$

$$a_{yx} = \left(a_{xx'} - a_{yy'} \right) \cos\phi\, m \, \sin\phi\, m - a_{xy'} \sin^2\phi\, m + a_{yx'} \cos^2\phi\, m$$

$$a_{yy} = a_{xx'} \sin^2\phi\, m + a_{yy'} \cos^2\phi\, m + \left(a_{xy'} + a_{yx'} \right) \cos\phi\, m \, \sin\phi\, m.$$

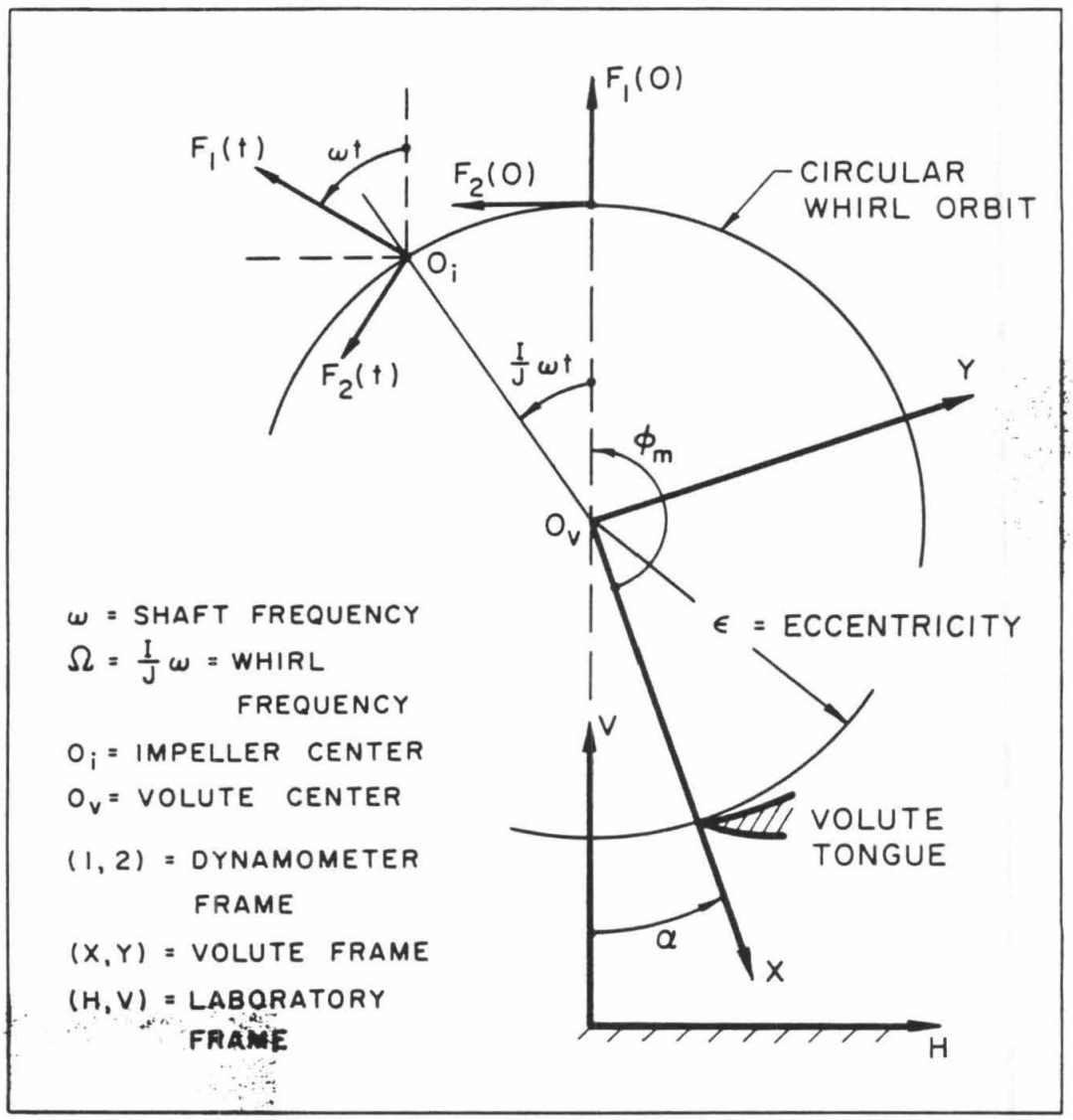

Fig. C.1 Schematic showing the relation between the lateral forces in the stationary (X,Y) frame and the rotating (1,2) frame of the dynamometer.

APPENDIX D

SAMPLE ROTORDYNAMIC CALCULATIONS USING CAL-TECH ROTORDYNAMIC COEFFICIENTS

by

Dara W. Childs
Director, Turbomachinery Laboratories
Department of Mechanical Engineering
Texas A&M University
College Station, Texas

and

David S. Moyer
Space Shuttle Systems Engineer
McDonell Douglas Technical Services Company
Houston, Texas

INTRODUCTION:

Engineers may well be curious as to the influence of the impeller-diffuser forces on the rotordynamic characteristics of an actual piece of turbomachinery. As a partial answer to this point, some calculated results are presented for the HPOTP (High Pressure Oxygen Turbopump) of the SSME (Space Shuttle Main Engine). The rotating assembly for this unit is illustrated in Fig. D.1. The high operating speed range of 20,900-30,380 rpm and the relatively high specific gravity of liquid oxygen (1.137) are obviously not typical of commercial equipment; however, the results do show the very significant influence of the impeller rotordynamic coefficients.

IMPELLER ROTORDYNAMIC MODEL:

The Cal-Tech data presented in Table 1 define the following constant-coefficient face-displacement model:

$$-\begin{Bmatrix} F_x \\ F_y \end{Bmatrix} = \begin{bmatrix} K_{xx} & K_{xy} \\ K_{yx} & K_{yy} \end{bmatrix} \begin{Bmatrix} X \\ Y \end{Bmatrix} + \begin{bmatrix} C_{xx} & C_{xy} \\ C_{yx} & C_{yy} \end{bmatrix} \begin{Bmatrix} X \\ Y \end{Bmatrix} + \begin{bmatrix} M_{xx} & M_{xy} \\ M_{yx} & M_{yy} \end{bmatrix} \begin{Bmatrix} X \\ Y \end{Bmatrix}. \qquad (D.1)$$

However, an inspection of the data in this table shows that the matrices are approximately symmetric; hence, for the results presented here, the following simplified model is used:

$$-\begin{Bmatrix} F_x \\ F_y \end{Bmatrix} = \begin{bmatrix} K & k \\ -k & K \end{bmatrix} \begin{Bmatrix} X \\ Y \end{Bmatrix} + \begin{bmatrix} C & c \\ -c & C \end{bmatrix} \begin{Bmatrix} \dot{X} \\ \dot{Y} \end{Bmatrix} + \begin{bmatrix} M & m \\ -m & M \end{bmatrix} \begin{Bmatrix} \ddot{X} \\ \ddot{Y} \end{Bmatrix}. \qquad (D.2)$$

The dimensional entries of (D.2) are related to the non-dimensional entries of Table 1 as follows:

$$K = (K^*_{XX} + K^*_{YY})C_1\omega^2/2$$

$$k = (K^*_{XX} - K^*_{XY})C_1\omega^2/2$$

$$C = (C^*_{XX} + C^*_{YY})C_1\omega/2$$

$$c = (C^*_{XY} - C^*_{YX})C_1\omega/2$$

$$M = (M^*_{XX} + M^*_{YY})C_1/2$$

$$m = (M^*_{XY} - M^*_{YX})C_1/2$$

where * denotes the non-dimensional entries of Table 1. Further,

$C_1 = \rho\Pi b_2 r_2^2$

ρ = fluid density

r_2 = impeller discharge radius

b_2 = impeller discharge width.

For the main impeller of the HPOTP, r_2 = 85mm, and b_2 = 25.4 mm, while for the boost impeller, r_2 = 66mm, and b_2 = 6.9 mm. The fluid density for both impellers is approximately 1100 kg/m^3.

Most computer codes in use today for pump rotordynamics analysis do not account for the added-mass coefficients of Eq.(D.2). The authors of this addendum extended the procedure of [36] to account for added mass terms in carrying out the calculations presented here.

ROTORDYNAMIC CALCULATIONS:

Over the past several years, the HPOTP has experienced excessive subsynchronous motion at a frequency associated with a second critical speed mode shape. The zero-running-speed undamped modes are illustrated for the first and second rotor bending modes in Fig. D.2. Observe that the first critical speed mode shape involved primarily the overhung turbine mode with relatively small bearing deflections, while the second mode involved large deflections at the main impeller and large bearing deflections. Hence, the first mode response is expected to be insensitive to impeller forces, while the second mode would be quite sensitive.

The addendum authors recently published the result of a rotordynamic analysis concerning subsynchronous vibration problems of the HPOTP [39] when operating at high speeds. The rotordynamics model used in [39] included a structural dynamics model for the rotor and the housing. For linear analysis, the bearings were modelled as linear springs. Liquid seals at the boost impeller were modelled according to Equation (D.2) using the analysis procedure of [37]. Gas seals in the turbine area were accounted for by a model similar to Equation (D.2), except that the mass matrix was dropped. Seal coefficients were calculated based on Nelson's analysis [117]. The turbine clearance excitation forces used the model of Thomas[140] and Alford [6].

The obvious point of interest here is the influence that the impeller coefficients had on the rotordynamic characteristics of the HPOTP. This point is addressed by calculating the OSI (Onset Speed of Instability) and synchronous bearing reactions for the following impeller models:

- Stiffness Coefficients only. This was the first "static-only" data published by Chamieh et al. [35] and was used in [39].
- Full model, including stiffness, damping and added-mass coefficients.
- Reduced model, obtained by dropping the added-mass terms.
- Reduced model, obtained by dropping the added-mass terms and the cross-coupled damping terms.

The nondimensional data for Volute A, Φ=0.092 of row 4 in Table 1 are used.

The synchronous reactions for bearings 1 and 4 due to rotating imbalance based on only the stiffness-matrix model for the impellers are illustrated in Fig. D.3.The bearing reaction response was dominated by first and second critical speeds at approximately 13,500 rpm and 31,170 rpm, respectively. Some smaller peaks are evident, due to housing resonances. The calculated OSI for this configuration are approximately 30,500 rpm. The cross-coupled stiffness coefficient from the main impeller was the source of the instability, and the OSI was arbitrarily set to the calculated value by adding direct damping at the main impeller. The OSI of 30,500 rpm was chosen to yield agreement with field data.

The results presented in Fig. D.4 illustrate the predicted synchronous-response characteristics including the stiffness, damping and added-mass terms. The second critical speed was calculated to lie at 33,060 rpm, while the predicted OSI was greater than 55,000 rpm.

The results presented in D.5 illustrate the calculated bearing reactions if the stiffness and damping matrices are included, but the mass matrix is dropped. The second critical speed was seen to be heavily damped and was elevated to approximately 39,000 rpm. For this impeller model, the OSI was also greater than 55,000 rpm. By comparison with Fig. D.4, the obvious conclusion is that the mass-matrix contribution cannot be neglected, and rotordynamics-analysis procedures for pumps, which are not able to account for the added-mass matrix at impellers, should be avoided.

The cross-coupled-damping coefficients in the models of Eqs. (D.1) and (D.2) act as "gyroscopic-stiffening" elements to raise the rotor's critical speed, and the Cal-Tech cross-coupled damping coefficients are relatively high. The direct mass coefficients tend to compensate for the cross-coupled damping coefficients in depressing the rotor critical speeds, and this explains the sharp elevation of the second critical speed from Fig. D.4 to Fig. D.5 after the mass matrix has been dropped. From this reasoning, one could expect that dropping both the mass matrix and the cross-coupled damping matrix might yield a simplified, but still reasonable, model. The synchronous response prediction for this type of impeller model is illustrated in D.6. The

second critical speed is predicted to be at 32,340 cpm, which is in reasonable agreement with the results of Fig. D.6 for the complete impeller model; however, the second critical speed is much more heavily damped and the predicted OSI is now in excess of 75,000 cpm. Clearly, the proposed simplified model is inadequate.

CONCLUSIONS:

The sample calculations presented herein support the following conclusions:

(a) Impeller-diffuser forces have a very significant impact on the calculated rotordynamic characteristics of pumps, particularly with respect to damping and stability

(b) The complete model for the impeller, *specifically including the mass terms*, must be included in rotordynamic calculations to achieve reasonable results.

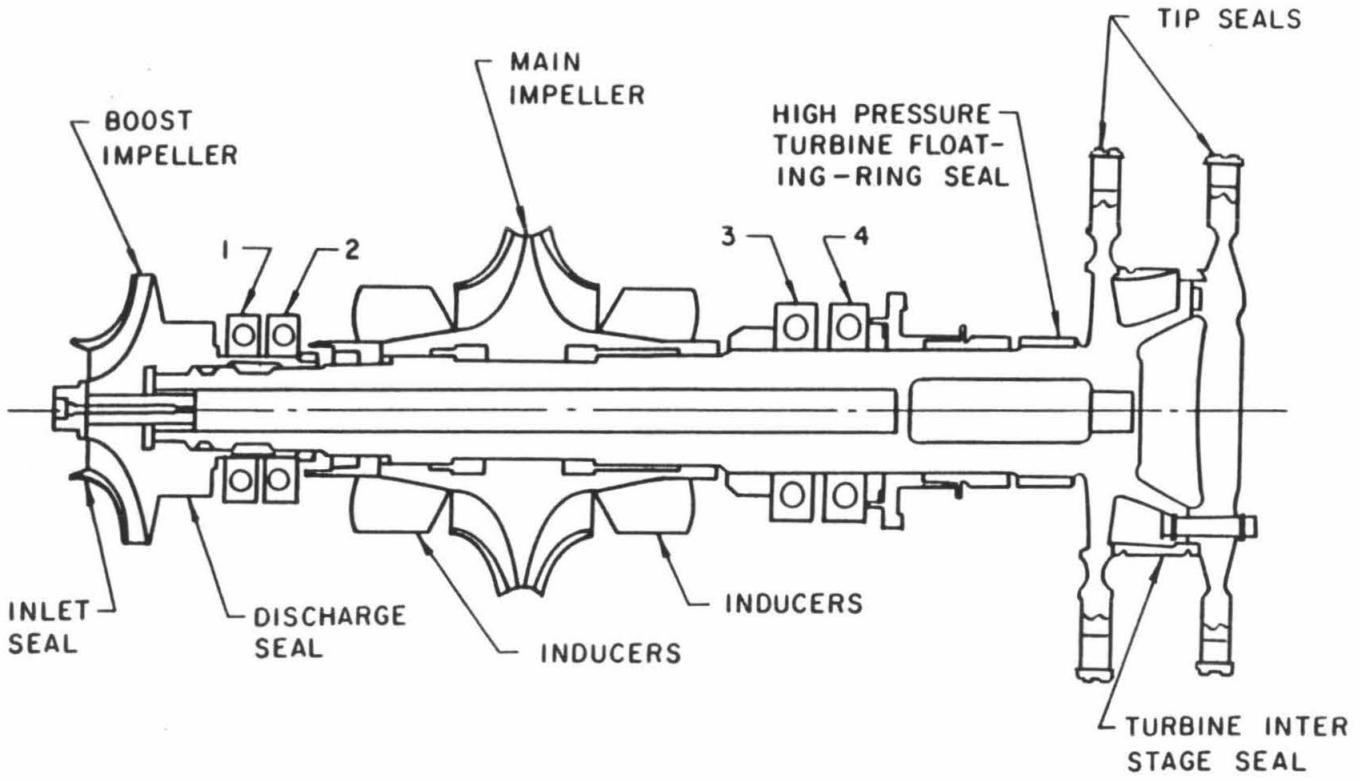

Fig. D.1 Schematic highlighting the major components of the SSME's High Pressure Oxidizer Turbopump (HPOTP).

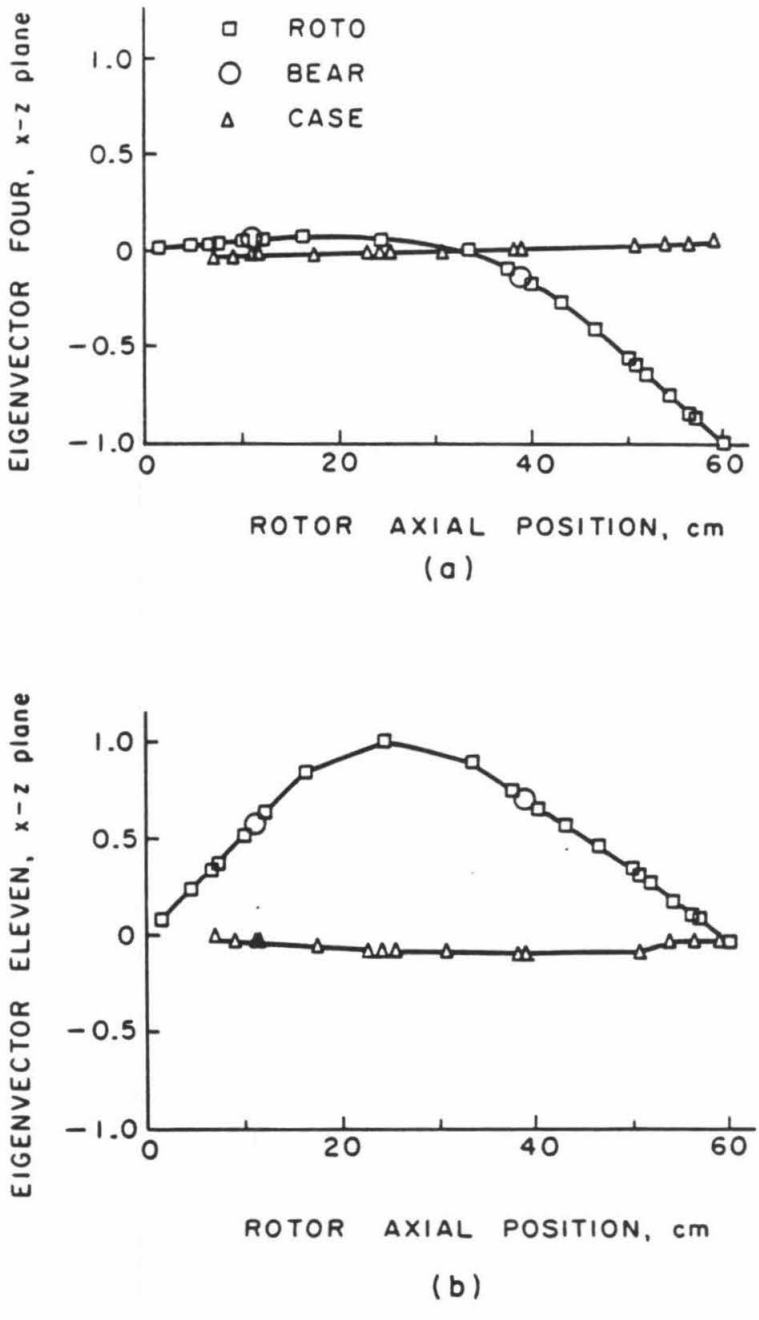

Fig. D.2 Undamped, zero-running-speed, rotor-housing modes associated with the first (top) and second (bottom) rotor critical speeds.

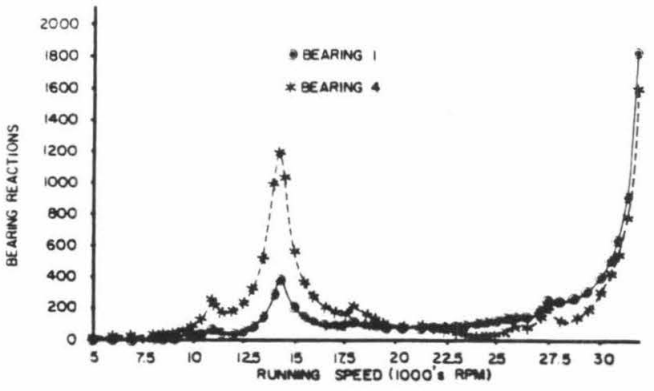

Fig. D.3 Calculated bearing reactions for stiffness-matrix-only impeller models.

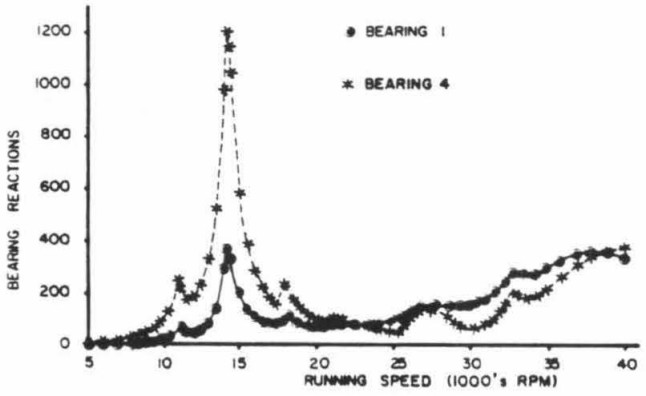

Fig. D.4 Calculated bearing reactions for full impeller models including stiffness, damping, and added-mass matrices.

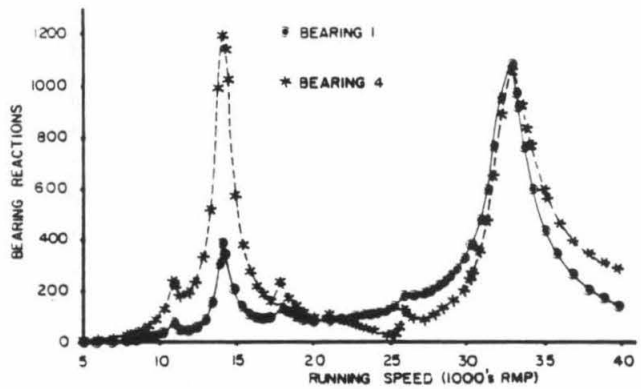

Fig. D.5 Calculated bearing reactions for reduced impeller models with the mass matrix dropped.

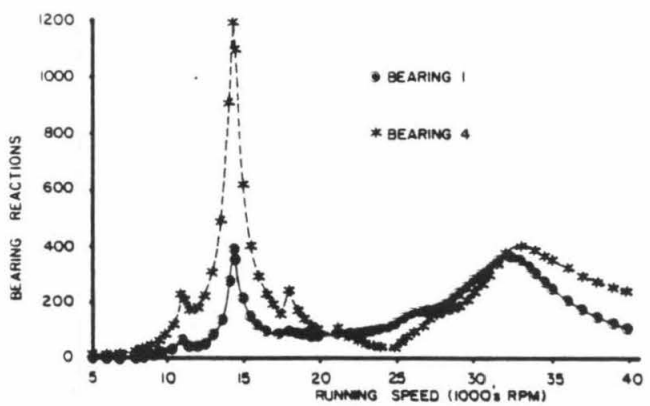

Fig. D.6 Calculated bearing reactions for a reduced impeller model including the stiffness matrix and the direct-damping coefficients.

VOLTE SPEED	IMPEL. PHI	Kxx Kyx	Kxy Kyy	Cxx Cyx	Cxy Cyy	Mxx Myx	Mxy Myy
A 500	X 0.092	-2.375 -1.094	1.100 -2.640	2.934 -8.141	7.685 3.341	6.906 0.358	-0.697 6.127
A 1000	X 0.092	-2.681 -1.220	1.011 -2.532	2.894 -8.477	8.568 3.660	6.106 0.294	-0.774 6.382
A 1500	X 0.092	-2.541 -1.078	0.901 -2.398	2.877 -8.704	8.709 3.116	6.979 0.628	-1.114 6.761
A 2000	X 0.092	-2.687 -1.239	1.062 -2.596	2.807 -9.006	9.108 3.009	6.928 0.648	-0.693 7.110
E 1000	X 0.000	-1.893 -0.133	0.145 -1.387	3.449 -7.279	7.835 3.350	6.183 -0.923	0.433 7.483
E 1000	X 0.060	-2.805 -0.992	1.043 -2.710	3.662 -9.421	9.647 3.811	6.581 1.021	-0.998 7.259
E 1000	X 0.092	-2.699 -0.967	1.104 -2.592	3.728 -8.846	9.071 3.871	6.222 0.926	-0.880 6.978
E 1000	X 0.145	-2.546 -1.157	1.169 -2.343	4.101 -7.770	8.090 4.127	5.624 0.437	-0.661 6.774
N 1000	X 0.060	-0.646 -0.739	0.611 -0.462	1.135 -3.575	3.627 1.337	4.249 -2.090	1.265 4.507
D 1000	X 0.060	-2.996 -1.165	1.069 -2.725	2.626 -9.193	9.290 2.992	6.254 -0.102	-0.401 6.603
F 1000	X 0.060	-3.454 -1.325	1.386 -3.337	3.490 -9.538	9.484 3.781	6.130 0.541	-0.904 6.357
G 1000	X 0.060	-3.469 -1.239	1.357 -3.220	3.314 -9.229	8.991 3.532	5.380 0.195	-0.589 6.122
H 1000	X 0.060	-3.523 -1.317	1.349 -3.323	3.568 -10.351	10.329 3.932	6.991 0.485	-0.819 7.482
E 1000	Y 0.092	-2.900 -0.776	0.922 -2.714	3.269 -8.331	8.724 3.403	5.250 0.724	-0.763 5.745
A 1000	S 0.000	-0.628 -0.516	0.302 -0.213	1.685 -3.874	3.739 2.057	6.282 -0.161	-0.237 6.802

Table 1 Summary of numeric values of rotordynamic coefficients (stiffness, K_{ij}, damping, C_{ij}, and inertia, M_{ij}) obtained from least-squares quadratic fits to the elements of the generalized hydrodynamic stiffness matrix [$A(\Omega/\omega)$].

(deg) VOL IMP RPM PHI	Kxx Kxy Kyx Kyy	Cxx Cxy Cyx Cyy	Mxx Mxy Myx Myy
(2) E X 1000 .000	-1.893 0.145 -0.133 -1.387	3.449 7.835 -7.279 3.350	6.183 0.433 -0.923 7.483
(3) E X 1000 .000	-1.688 -0.100 0.117 -1.406	1.457 6.166 -7.435 1.310	6.895 -0.418 -0.052 7.417
(5) E X 1000 .000	-1.243 -0.492 0.459 -1.112	0.677 8.372 -6.986 1.050	11.295 -5.084 3.896 10.874
(2) E X 1000 .030	-2.869 0.764 -0.153 -2.909	3.909 10.317 -10.282 3.939	6.911 -1.620 2.190 7.055
(3) E X 1000 .030	-2.87 0.624 -0.010 -3.071	2.770 10.381 -11.600 2.777	6.884 -2.106 2.686 6.492
(5) E X 1000 .030	-2.197 0.435 0.683 -2.757	1.818 10.740 -11.858 1.218	14.479 -4.517 10.985 9.974
(2) E X 1000 .060	-2.805 1.043 -0.992 -2.710	3.662 9.647 -9.421 3.811	6.581 -0.998 1.021 7.259
(3) E X 1000 .060	-2.701 0.824 -0.759 -2.723	1.878 8.802 -9.525 1.910	6.942 -1.759 1.833 7.214
(5) E X 1000 .060	-2.228 0.756 -0.583 -2.339	1.207 9.466 -9.119 1.341	12.100 -2.720 3.986 11.677
(2) E X 1000 .092	-2.699 1.104 -0.967 -2.592	3.728 9.071 -8.846 3.871	6.222 -0.880 0.926 6.98
(2) E X 1000 .011	-2.676 1.168 -0.991 -2.578	3.823 8.848 -8.539 3.919	6.206 -0.722 0.725 6.852
(2) E X 1000 .132	-2.546 1.169 -1.157 -2.343	4.101 8.098 -7.770 4.127	5.624 -0.661 0.437 6.774

Table 2 Summary of numeric values of rotordynamic coefficients (stiffness, K_{ij}, damping, C_{ij}, and inertia, M_{ij}) obtained from second, third, and fifth order polynomial fits to the elements of the generalized hydrodynamic stiffness matrix [$A(\Omega/\omega)$].